

METHANOL: A DIAGNOSTIC TOOL FOR STAR FORMATION

Dissertation

zur

Erlangung des Doktorgrades (Dr. rer. nat.)

der

Mathematisch-Naturwissenschaftlichen Fakultät

der

Rheinischen Friedrich-Wilhelms-Universität Bonn

vorgelegt von

Silvia Leurini

aus

Rom

Bonn, Dezember 2004

Angefertigt mit Genehmigung der Mathematisch-Naturwissenschaftlichen Fakultät der Rheinischen Friedrich-Wilhelms-Universität Bonn

1. Referent: Prof. Dr. K. M. Menten

2. Referent: Prof. Dr. U. Klein

Tag der Promotion: 22 Dezember 2004

Diese Dissertation ist auf dem Hochschulschriftenserver der ULB Bonn http://hss.ulb.uni-bonn.de/diss_online elektronisch publiziert

Contents

Introduction	1
I Methanol excitation	5
1 Methanol as a diagnostic tool of interstellar clouds:	
Model calculations and application to molecular clouds	7
1.1 Excitation of CH ₃ OH	7
1.1.1 Infrared pumping mechanism	9
1.1.2 CH ₃ OH-He collisional rates	11
1.1.3 First test – dark clouds	13
1.1.4 CH ₃ OH as a probe of interstellar physical conditions	13
1.2 Analysis technique	18
1.3 Conclusions	24
2 Class I methanol masers	29
2.1 Introduction	29
2.2 Phenomenology of class I methanol masers	29
2.3 Statistical equilibrium calculations	32
2.3.1 Class I methanol masers.	33
2.3.2 Anti-inversion in the $2_0 \rightarrow 3_1 - E$, $5_1 \rightarrow 6_0 - A^+$ methanol transitions.	35
2.4 Outlook	37
II Methanol in the early stages of star formation	39
3 Modelling of high mass star forming regions	41
3.1 Selection of the sample	41
3.2 Line selection	42
3.3 Observations	43
3.3.1 Effelsberg 100 m	43
3.3.2 IRAM 30 m	43

3.3.3	Caltech Submillimeter Observatory (CSO)	44
3.4	CH ₃ OH Analysis	45
3.5	Model Results	49
3.5.1	Infrared Dark Clouds	55
3.5.2	High Mass Protostellar Objects	58
3.6	Highlights	66
4	IRAS 05358+3543: a high mass star forming cluster.	105
4.1	Introduction	105
4.2	Observations with the Plateau de Bure Interferometer (PdBI)	106
4.3	Observational results	106
4.4	Physical parameters	116
4.5	Conclusion	119
5	Highlights and prospects	123
5.1	Summary	123
5.2	Future plans	125
	Conclusions	128
	Appendices	129
A	CH₃OH-para H₂ collisional rates.	129
	List of publications	137
	Bibliography	138

Introduction

The early stages of star formation are known to occur in dense ($n(H_2) \geq 10^4 \text{ cm}^{-3}$) interstellar clouds, whose chemical composition is dramatically affected by the interaction with the embedded Young Stellar Objects (hereafter YSOs) through all their evolution. As the chemical composition of a source is intimately related to its evolutionary stage and history, the analysis of chemical abundances in star forming regions can give important information on the region and, once a large database of sources in different states of evolution is available, shed light on the details of star formation process. Chemical models (e.g. Charnley et al. 1992; Caselli et al. 1993) indeed agree in dividing molecules in two categories:

- primary molecules, which form on the dust grains, by grain-surface chemistry, and are then released to the gas phase by evaporation processes (among others NH_3 , CH_3OH , H_2CO);
- secondary molecules, which are produced, from the primary molecules, by gas-phase chemistry (e.g. CH_3CN , CH_3OCH_3).

Although gas-phase chemistry includes different types of reactions, each characterised by its own lifetime, it is typically fast and leads to a rapidly changing in the molecular abundances of secondary to primary molecules, that can be used as chemical clocks, once these processes are properly understood. Other important information comes from the study of the excitation mechanisms of chemical species found in the interstellar medium (ISM), since this is a powerful tool to investigate the physical conditions and the processes going on in the region: once the pumping mechanisms of the energy levels of a molecule are well understood, by observing transitions of that molecular species in a cloud, one can derive the kinetic temperature and spatial density of the source. These are fundamental parameters for our understanding of the physical processes and of the evolutionary sequence in star formation. Eventually, the dynamics and kinematics of a cloud can also be studied by observing maser transitions at high spatial resolution, as recent interferometric studies have shown (e.g. Moscadelli et al. 2000; Torrelles et al. 2003).

Observational evidences support a scenario in which low-mass stars ($M < 8 M_\odot$) form via collapse of dense molecular clumps, giving birth to an embedded protostar which accretes material from the parent cloud (Shu et al. 1987). The protostellar phase involves accretion via protostellar disks and leads to the production of bipolar outflows which, very collimated

in their early phases, spread out with time, (for a review of low-mass star formation see, e.g. André et al. 2000). Observations of high-mass stars ($M \geq 8 M_{\odot}$) are more complicated than for the low-mass case. These objects have short lifetime (a few million years for an object of $10 M_{\odot}$, Schaller et al. 1992, while typical low-mass stars have timescales of 10 billion years); they are rare and statically found on an average distance of a few kpc. Finally, they mainly form in clustered mode and not in isolated small cores as low-mass stars. Therefore, although they exert a deceive influence on the morphology and evolution of galaxies, the physical processes involved in their formation are still far less understood than those of their low-mass counterparts.

In recent years, a major observational effort has been made to identify the very earliest stages in the evolution of massive stars, prior to forming an ultracompact HII region (Molinari et al. 1996, 1998, 2000; Sridharan et al. 2002; Beuther et al. 2002b,c,d). These studies have shown that, at least from a qualitative point of view, a scenario similar to the one described for low-mass stars applies to the formation of massive stars as well. Several sources do show clear evidence of bipolar outflow morphologies (Shepherd & Churchwell 1996; Cesaroni et al. 1997; Zhang et al. 2001; Beuther et al. 2002a,c) and indications of accretion disks exist (Cesaroni et al. 1997, 1999; Beuther et al. 2004a). However, a proper understanding of the physical processes, and therefore of the physical conditions, which characterise the early evolutionary sequence of high-mass stars, is still missing. As discussed at the beginning of this section, a powerful diagnostic tool of interstellar clouds is found in the analysis of their molecular spectra, which can be seen as fingerprints of a star forming region. Moreover, molecules mainly emit at millimeter and submillimeter wavelengths, where extinction from the dust and gas around young massive protostars is low.

Since the main gas-phase molecular component, H_2 , is not directly observable under “normal” conditions, one has to rely on other molecules to trace the physical state of an interstellar cloud. Often, traditionally symmetric rotors such as NH_3 are used to probe a cloud’s kinetic temperature (Walmsley & Ungerechts 1983; Danby et al. 1988), while linear molecules, e.g. CS, are used to determine its density (e.g., Snell et al. 1984; Beuther et al. 2002b). However, different spatial distributions of the tracers (“chemistry”) often complicate the picture, (see, e.g., Tafalla et al. 2002) as they often trace physically different and spatially non-coexisting gas components. It is thus desirable to trace all relevant physical parameters with a single molecule. Promising candidates exist among slightly asymmetric rotors, which have properties qualifying them as tracers for physical conditions. Since they are almost symmetric, they share a strong sensitivity to kinetic temperature with symmetric molecules, but they also allow determinations of spatial density (for a detailed discussion of H_2CO , see Mundy et al. 1987; Mangum & Wootten 1993). Methanol, CH_3OH , a slightly asymmetric rotor, is a proven tracer of high-density environments (e.g. Menten et al. 1988b); moreover it is particularly well suited for high mass star forming regions (Leurini et al. 2004), as it is ubiquitously found in different regimes of star formation, from quiescent, cold ($T \sim 10$ K), dark clouds, where its abundance relative to H_2 is only $\sim 10^{-9}$ (Friberg et al. 1988), to “hot core”

sources near high-mass (proto)stellar objects, where $[\text{CH}_3\text{OH}]/[\text{H}_2]$ values $\sim 10^{-7} - 10^{-6}$ are observed (Menten et al. 1986, 1988b). However, up to now an extremely poor knowledge of the CH_3OH collisional rates and of their propensity rules has prevented realistic systematic studies exploiting methanol's full potential as an interstellar tracer. Recently, this situation has changed with the calculation of collisional rate coefficients by Pottage et al. (2001, 2002). **Part I** of this thesis is a pilot study dedicated to the analysis of the excitation of CH_3OH in the interstellar medium and to its tracing properties in the centimeter, millimeter and sub-millimeter spectrum; in chapter 1 the new collisional rates by Pottage et al. (2001, 2002) have been integrated in a "standard" Large Velocity Gradient program aimed at modelling methanol excitation. Since the new calculations on collisional rates have been initially computed only for the torsional ground state, the study discussed in this first part is limited to those sources in which the only external radiation field is the cosmic background radiation, in order to avoid any effect due to infrared pumping. An innovative way of analysing CH_3OH spectra, which is based on a simultaneous fitting of all the lines observed towards a given position, will be also discussed, together with its application to two sources, G19.30P1 and G79.3P1. They belong to a population of infrared-dark clouds, identified by Egan et al. (1998) using the Galactic plane survey from the SPIRIT III telescope aboard the Midcourse Space Experiment, MSX. They typically show an average value of $T \leq 20$ K and $n(\text{H}_2) \geq 10^5 \text{ cm}^{-3}$; therefore the CH_3OH level populations are expected to be governed by collisions and the assumption that any external radiation field but the cosmic background is negligible is expected to be plausible. Chapter 2 is dedicated to the analysis of the pumping mechanism of class I CH_3OH masers and to the information on the physical parameters of an interstellar cloud that can be derived by observing these transitions. Several class I CH_3OH masers are indeed detected throughout the centimeter and millimeter spectrum and the analysis of their excitation conditions reveals two main patterns, with the $4_{-1} \rightarrow 3_0 - E$ and the $5_{-1} \rightarrow 4_0 - E$ masers, for example, quenched at high density ($n(\text{H}_2) \geq 10^7 \text{ cm}^{-3}$) and the $J_2 \rightarrow J_1 - E$ band masing in the same regime. Observations of lines in both these two groups can be therefore used as a density indicator of a region.

Part II is dedicated to the application of the analysis and the technique discussed in Part I to high-mass star forming regions. In chapter 3, a sample of 13 sources in the early stages of star formation is analysed by single dish observations of centimeter and millimeter CH_3OH lines. All the sources are in the earliest stages of star formation, prior to forming an ultracompact HII region, and have been selected among the infrared dark clouds studied by Carey et al. (1998) and the High Mass Protostellar Objects (hereafter HMPO) studied in the last years by Sridharan et al. (2002) and Beuther et al. (2002b). The two main criteria for our selection are that the sources have a homogenous distance to the solar system and show strong CH_3OH emission at least in the less excited lines we observed. Detection of complex molecules (e.g. CH_3OH , CH_3CN Sridharan et al. 2002; Schilke, unpublished data) towards some of HMPOs in our sample indicates an ongoing hot core formation in the sources. Therefore, the analysis described in chapter 1, limited to the first 100 levels ($(J,k)=9$) in the torsional ground state,

is extended in chapter 3 to include all the levels up to ($J=14, k=13$) in the torsional ground state and up to (J,k)=9 for the first torsionally excited state, using extrapolated collisional rates.

CH_3OH observations at high spatial resolution are discussed in chapter 4; the High Mass Protostellar Object IRAS 05358+3543 has been mapped in the $5_{-1} \rightarrow 4_0 - E$ $v_t=0$ band at 241.7 GHz with the Plateau de Bure Interferometer, reaching a resolution of $2.6'' \times 1.36''$. The source is part of the sample of very young massive star-forming regions studied by our group in detail over recent years (Sridharan et al. 2002; Beuther et al. 2002b,a) both in single-dish and interferometric mode. The main result of these studies is that the previously observed single-dish outflow splits up into at least 3 molecular outflows, one of them being one of the most collimated massive molecular outflow observed today. Also located near the main mm-condensation are two mid-infrared sources observed with Keck, a H_2O maser feature, and the deeply embedded source found by polarimetric infrared observations (Yao et al. 2000). Detection of complex molecules (CH_3OH , CH_3CN Sridharan et al. 2002; Leurini, unpublished data) indicates an ongoing hot core formation in the region.

Our observations reveal indeed a hot, dense phase around the main millimeter dust condensations, still unresolved with our resolution, with detection of torsionally excited lines. The technique discussed in chapter 1 for the analysis of methanol data is here applied to some positions around the millimeter continuum peak. Although some lines in our spectra show an unexpected extension and are heavily corrupted by negative features caused by missing spacings, their analysis on the central position leads to typical hot-core parameter: $T=240$ K, $N(\text{CH}_3\text{OH})=1.2 \times 10^{17} \text{ cm}^{-2}$, $n(\text{H}_2)=5 \times 10^7 \text{ cm}^{-3}$, $X(\text{CH}_3\text{OH})=1 \times 10^{-7}$.

Our data also confirm the property of methanol of tracing the core emission as well as the outflows already discussed in the low-mass star case by Bachiller et al. (1995, 1998) and in the high-mass stars regime by Liechti & Walmsley (1997).

Part I

Methanol excitation

Chapter 1

Methanol as a diagnostic tool of interstellar clouds: Model calculations and application to molecular clouds

The content of this chapter is based on Leurini, S., Schilke, P., Menten, K. M., et al. 2004, A&A, 422, 573

1.1 Excitation of CH₃OH

Methanol, CH₃OH, is a slightly asymmetric rotor, capable of hindered internal rotation: the hydroxyl group (OH) may rotate around the methyl (CH₃) symmetry axis, as shown in Fig. 1.1. Due to the threefold symmetry of its hindering potential, CH₃OH occurs as *A*– and *E*– symmetry states. The *E*– type, $-J \leq k \leq J$, is vibrationally doubly degenerate: the E_1 , $k \geq 0$, states are degenerate with E_2 , $k \leq 0$. In the *A*– type, $0 \leq K \leq J$, for $K \geq 0$ there are doublets split by asymmetry which are labelled A^+ and A^- (Lees & Baker 1968). For radiative transport purposes, its *A*– and *E*–type symmetry states can be considered as two different molecules, since interconversion can happen only through proton exchange reactions, which happen on timescales so long that the excitation is unaffected. Transitions between A^+ and A^- levels occur.

CH₃OH is potentially a promising candidate for probing the physical conditions of interstellar clouds. First, it is slightly asymmetric: as discussed by several authors in the case of H₂CO (Mundy et al. 1987; Mangum & Wootten 1993), slightly asymmetric rotors share a strong sensitivity to kinetic temperature with symmetric molecules **and** they also allow determinations of spatial density. Moreover, CH₃OH is ubiquitous and associated with different regimes of star formation, from quiescent, cold ($T \sim 10$ K), dark clouds, where its abundance relative to H₂ is only $\sim 10^{-9}$ (Friberg et al. 1988), to “hot core” sources near high-mass (proto)stellar objects, where [CH₃OH/H₂] values $\sim 10^{-7} - 10^{-6}$ are observed (Menten et al.

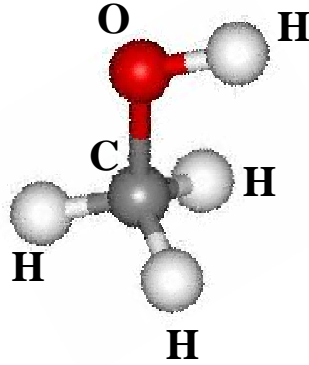


Figure 1.1: Structure of the methanol molecule. The O-H bond may rotate about the axis with respect to the CH₃ group, but this rotation is hindered by mutual interaction (figure from Cologne Database for Molecular Spectroscopy)

1986, 1988b). Studies on the chemistry of CH₃OH toward regions of massive star formation (Menten et al. 1986, 1988b) interpret the enhancement of CH₃OH in warmer sources as due to evaporation of icy grain mantles. At temperatures ≤ 100 K, production of CH₃OH in the gas phase is governed by the radiative association reaction $\text{CH}_3 + \text{H}_2\text{O} \rightarrow \text{CH}_3\text{OH}_2^+ + h\nu$ followed by electronic recombination to CH₃OH (50%) and H₂CO (50%) (Lee et al. 1996). Because radiative association is slow, the reaction set yields abundances of only $\sim 10^{-11}$ relative to H₂ and it is inefficient in explaining the observed abundances; therefore it has been concluded that CH₃OH is produced by grain chemistry, a scenario supported by finding that CH₃OH is one of the most abundant species residing on interstellar grains (Grim et al. 1991; Dartois et al. 1999a,b; Pontoppidan et al. 2004). Recent studies on abundance profiles of CH₃OH and H₂CO toward massive young stars (van der Tak et al. 2000; Maret 2004) indicate that the excitation and abundance of CH₃OH are useful evolutionary indicators during the embedded stage of star formation. In their study on several massive star formation sites, they find three different types of abundance profiles: $[\text{CH}_3\text{OH}/\text{H}_2] \sim 10^{-9}$ in the coldest sources, a jump from $[\text{CH}_3\text{OH}]/[\text{H}_2] \sim 10^{-9}$ to $[\text{CH}_3\text{OH}]/[\text{H}_2] \sim 10^{-7}$ in the warmer and a few $\sim 10^{-6}$ in hot cores. They locate this “*jump*” at ≤ 100 K, that is the temperature at which the evaporation of CH₃OH from the mantles happens. Theoretical models of hot cores (Nomura & Millar 2004) do predict this observed step function in the abundance of methanol.

A practical advantage in using methanol as tracer of interstellar conditions is that, because of its complex energy level structure, it has groups of several transitions close together in wavelength space throughout the millimeter and submillimeter region that can be observed simultaneously, thus minimizing relative pointing and calibration uncertainties, and a multitude of its transitions is observable with ground-based telescopes.

Methanol has in the past been used as a probe of spatial density in dense molecular clouds,

(cf. Friberg et al. 1988; Walmsley et al. 1988; Menten et al. 1988b; Kalenskii et al. 1997; Bachiller et al. 1998; Sutton et al. 2004); however, uncertainties in the derived densities are expected since these authors modelled the CH₃OH excitation using collisional rates based upon the experiments by Lees & Haque (1974) for CH₃OH colliding with He, for low states (up to $k \leq 2$) of CH₃OH-*E* only.

The CH₃OH spectrum up to 500 GHz is shown in Fig. 1.2 for two different sets of physical parameters typical for the ISM calculated with our LVG program (see §1.1.2). Rest frequencies are from the Cologne Database for Molecular Spectroscopy, (<http://www.cdms.de>, Müller et al. 2001), which includes new measurements by Xu & Lovas (1997).

1.1.1 Infrared pumping mechanism

In steady state, level populations are fixed by a balance among spontaneous and induced radiative processes, with characteristic rates described by the Einstein coefficients, and collisional excitation and deexcitation. Radiative transitions are constrained by selection rules which, in the case of methanol, are as follows:

$$\begin{array}{lll}
 \Delta v_t = 0 & \Delta J = 0 & \Delta K = 0 \text{ (for A), } \pm 1 \\
 & \Delta J = \pm 1 & \Delta K = 0, \pm 1 \\
 \Delta v_t = 1, 2, \dots & \Delta J = 0 & \Delta K = \pm 1 \\
 & \Delta J = \pm 1 & \Delta K = \pm 1
 \end{array}$$

In the following discussion, only $\Delta v_t=0,1$ transitions will be analysed.

The populations approach the Boltzmann distribution at the kinetic temperature when the downward collisional decays from a given level exceed its spontaneous radiative decay rates. Level thermalization happens when the density of the system is greater than the critical density of the level, defined by the above condition

$$n_{i_{cr}} = \frac{\sum_j A_{ij}}{\sum_j C_{ij}}$$

Because of the high Einstein coefficients in the $v_t=1$ levels, collisional excitation does not play a major role in the pumping mechanism of the torsionally excited states and critical densities are usually of the order of $10^{10} - 10^{11} \text{ cm}^{-3}$. Radiative transitions, on the other hand, can significantly affect the level populations not only in the $v_t=1$ levels, but also in the torsional ground state.

Assuming only radiative level changes and the CH₃OH -A molecule in its ground state, (J, k, v_t)=0, absorption of an infrared photon can excite the system to the ($J=1, k=0, v_t=1$) or ($J=1, k=1, v_t=1$). Assuming that the molecule has been excited to ($J=1, k=1, v_t=1$), from there the system can decay down to the starting level, with no effective change in its excitation, or

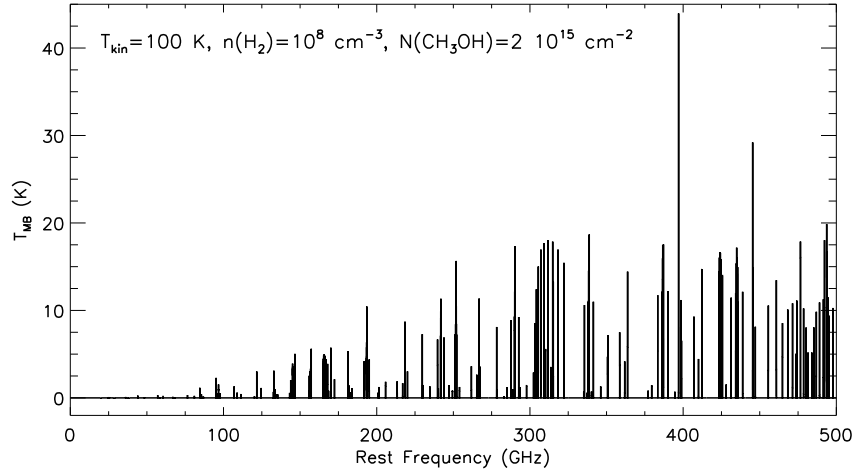
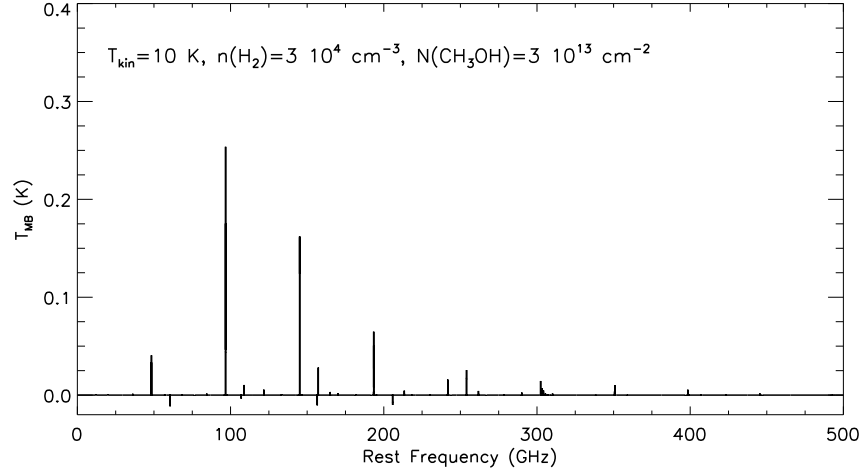


Figure 1.2: Synthetic CH_3OH spectra, (source size= $20''$, telescope diameter=30 m), up to $(J, k) = 9$ for the torsional ground state, calculated using our LVG model.

can decay down to other levels, $(J=1, k=0, v_t=0)$, $(J=2, k=2, v_t=0)$ and $(J=2, k=0, v_t=0)$, which can absorb other infrared photons and be excited again to the $v_t=1$ levels before they cascade back down. If the infrared pumping rate is not fast enough to compete with the rotational decays, then the IR excitation leads to a closed loop without affecting the population of high rotational levels. When, on the other hand, the infrared rate is faster than rotational decays, level populations in low energy states can be efficiently transferred to more excited states. The net result is that IR pumping can mimic the effect of collisional pumping, introducing

a degeneracy between H₂ density and IR field (for CS see Carroll & Goldsmith (1981); Hauschildt et al. (1993); for CH₃OH see discussion in § 3.4).

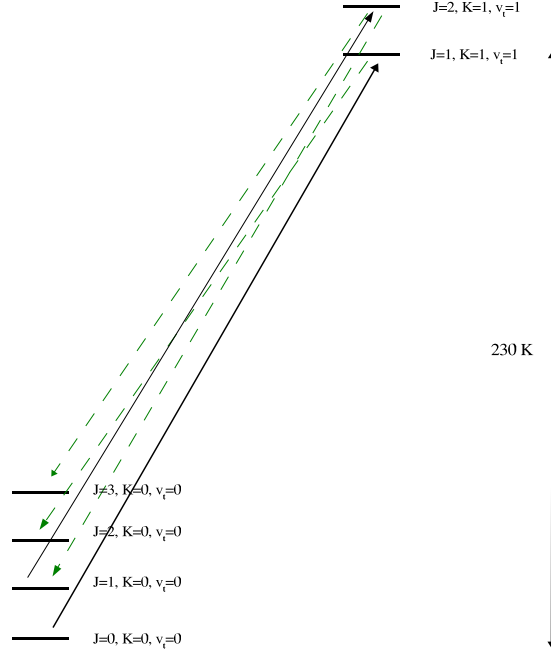


Figure 1.3: Methanol excitation through absorption of infrared photons. For the sake of clearness, only few levels are displayed and only few transitions are taken into account. Black, solid lines indicate absorptions of a photon to the $v_t=1$ band; dashed, green lines decays to the torsional ground state.

1.1.2 CH₃OH-He collisional rates

Only recently (see Pottage et al. 2001, 2002), rate coefficients for collisions of methanol with helium, for both CH₃OH-A and CH₃OH-E, have been computed for levels up to $(J, k^1) = 9$ at kinetic temperatures up to 200 K. Calculations of rate coefficients for collisions with para-H₂, for a limited set of energy levels, have recently been made available and comparisons of our results with this new dataset will be analysed in appendix A.

With this new set of collisional rates, we have performed statistical equilibrium calculations on both A- and E-types for the torsional ground state, using the Large Velocity Gradient (LVG) method with spherical geometry in the derivation of de Jong et al. (1975). Since the new calculations on collisional rates have been computed only for the torsional ground state,

¹The projection of the angular momentum quantum number k runs from $-J$ to $+J$ for E-type CH₃OH. For A-type CH₃OH a capital K is used, with $0 < K \leq J$. When referring in one expression to levels from both species, lowercase k is used.

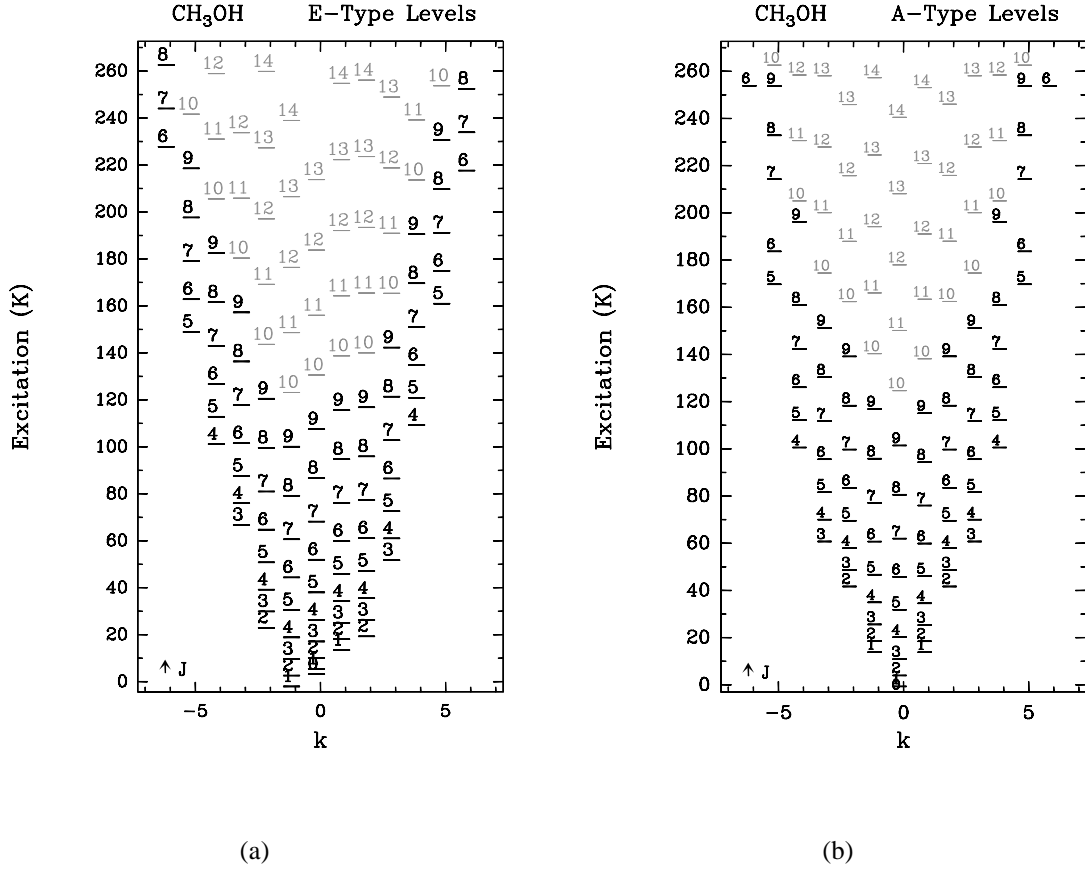


Figure 1.4: Energy levels for the E - and A -symmetry states of CH_3OH in the torsional ground state with an excitation energy of less than 260 K and $J < 9$, (black), $9 < J < 14$, (grey). Levels for $\text{CH}_3\text{OH-A}^+$ and $\text{CH}_3\text{OH-A}^-$ have been included in the same diagram: $k < 0$ indicate levels from $\text{CH}_3\text{OH-A}^-$, $k > 0$ levels from $\text{CH}_3\text{OH-A}^+$.

we limit our study at this point to those sources in which the only external radiation field is the cosmic background radiation, in order to avoid any effect due to infrared pumping. We estimate differences in the interaction potentials between He and H_2 to be likely more important than those due to their different reduced masses and did not scale the $\text{CH}_3\text{OH-He}$ collisional rates by any factor related to the masses (Flower, priv. comm.).

Our calculations are extended to the first 100 levels for each state, for which the collisional rates from Pottage et al. (2001, 2002) are available; the coverage in energy is thus incomplete above 100 K, (see 1.4(a)-1.4(b)), and does not allow a reliable estimation of the partition function at high temperatures. We compared our LTE values for the partition function with the one obtained with a more complete set of levels, ($J \leq 26, k \leq 14$), for which energies are calculated using global fit parameters reported in Xu & Hougen (1995), and we expect no significant uncertainties in our results up to 50 K, where the deviation from the most accurate value of Q is close to 10%. Since our sample of sources is not expected

to show temperatures higher than 50 K, the inaccuracy in the partition function should not affect our calculations. All allowed radiative transitions for the levels up to $(J, k) = 9$ have been included in our model, even the weak $\Delta k \geq 2$ lines. Line strengths are from Mekhtiev et al. (1999).

1.1.3 First test – dark clouds

Pottage et al. (2001) have compared their results with the ones from Lees & Haque (1974) and tested the accuracy of their collisional rates by modelling the $2_0 \rightarrow 3_{-1}$ E transition at 12.18 GHz. They find a generally good agreement with the measurements of Lees & Haque (1974), with exceptions, for example, in the $\Delta k = 3m$ transitions, (where m is an integer). We extended the tests to other transitions observed in dark clouds, where any external radiation field but the cosmic background is negligible and level populations are expected to be governed by collisions. Fig. 1.5 shows the model results for the $2_0 \rightarrow 3_{-1}$ E line at 12.18 GHz and the $2_{-1} \rightarrow 1_{-1}$ E and $2_0 \rightarrow 1_0$ A transitions near 96 GHz; typical dark clouds parameters, $n(\text{H}_2) = 10^3 - 10^8 \text{ cm}^{-3}$, $T = 10 \text{ K}$, were assumed in order to model the lines and compare the predictions with the observations from Walmsley et al. (1988) and Friberg et al. (1988). L134N has been selected as test source, since detailed multi-transition studies on it exist (see Swade 1989; Dickens et al. 2000). Dickens et al. (2000) find an average density along several lines of sight of $\sim 2 \cdot 10^4 \text{ cm}^{-3}$, from HC_3N , N_2H^+ and CS , while NH_3 observations give a kinetic temperature of 10 K. Assuming an A/E abundance ratio equal to 1, they derive a CH_3OH column density in the range $10^{13} - 10^{14} \text{ cm}^{-2}$. Following Walmsley et al. (1988), the $2_0 \rightarrow 3_{-1}$ E data towards L134N have been corrected by a factor 0.5 due to an offset position of $3'$ relative to the $2_0 \rightarrow 1_0$ A peak from Friberg et al. (1988). Our results are shown in Fig. 1.5: all three lines indicate a H_2 density in the range $\sim 3 - 4 \cdot 10^4 \text{ cm}^{-3}$ that is in good agreement with the “average” density toward various lines of sight in this source ($\sim 2 \cdot 10^4 \text{ cm}^{-3}$) determined by Dickens et al. (2000) from a variety of molecules.

Our results are generally in good agreement with old models of methanol excitation and suggest that estimates of spatial density based on Lees & Haque (1974) collisional rates are generally reliable. However our tests regard only the 12.18 GHz line and the quartet at 96 GHz and we did not carry out a systematic comparison of the dependence on spatial density and kinetic temperature of the CH_3OH transitions computed with the collisional rates from Pottage et al. (2001, 2002) and with the ones based on the experiment by Lees & Haque (1974).

1.1.4 CH₃OH as a probe of interstellar physical conditions

The richness of the CH_3OH spectrum prevents us from a systematic study of all its transitions: taking into account only the energy levels with $(J, k) \leq 9$, the E state alone has more than 300 lines, (see Fig. 1.2(a)–1.2(b)). Therefore, we restricted our study to only some bands observable from ground based telescope and not showing any maser action: the

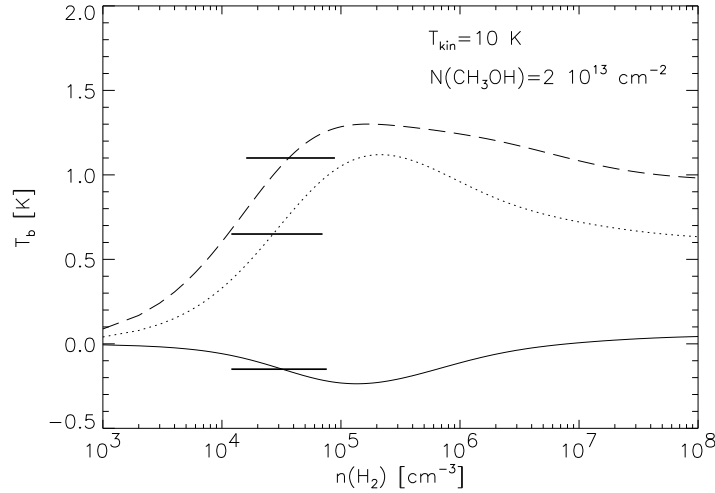


Figure 1.5: Results of statistical equilibrium calculations. We show the $2_0 \rightarrow 3_{-1}$ *E*, (full line), the $2_{-1} \rightarrow 1_{-1}$ *E*, (dotted line) and the $2_0 \rightarrow 1_0$ *A*, (long dashed line), line temperatures as a function of H_2 density. Superimposed on the plot, the observed values towards L134N from Walmsley et al. (1988), and Friberg et al. (1988) are indicated by horizontal lines.

$2_k \rightarrow 1_k$ -*A* and -*E*-type lines near 96 GHz, the $5_k \rightarrow 4_k$ -*A* and -*E* lines near 241 GHz, the $7_k \rightarrow 6_k$ -*A* and -*E* lines near 338 GHz. Even if promising candidates to trace kinetic temperature are in the submillimeter bands, with current collisional rates, we cannot reliably analyse higher transitions because the level set is incomplete above 100 K, (see Fig. 1.4(a)- 1.4(b)).

As a first step, we analysed line ratios from transitions close together in frequency space, in order to find diagnostic tools of kinetic temperature and density which are not affected by beam-size differences, pointing and absolute calibration uncertainties. A slight asymmetry in the abundances of the *A* and *E* subspecies, due to a difference in their ground state energies, has been suggested and indeed observed (see Friberg et al. 1988; Menten et al. 1988b). Since their relative abundance can vary from 0.69 in dark clouds, (Friberg et al. 1988), to 2 in OMC-2, (Menten et al. 1988b), comparisons between CH_3OH -*E* and -*A* lines are not taken into account to avoid any uncertainties in deriving physical parameters due to an inaccurate knowledge of the *A/E* ratio.

From the CH_3OH -*E* selected transitions, we found several ratios to be calibration - independent tracers of density: the $T_R(2_1 \rightarrow 1_1)/T_R(2_{-1} \rightarrow 1_{-1})$ and the $T_R(2_0 \rightarrow 1_0)/T_R(2_{-1} \rightarrow 1_{-1})$ in the 96 GHz band (Fig. 1.6); the $T_R(5_0 \rightarrow 4_0)/T_R(5_{-1} \rightarrow 4_{-1})$ (Fig. 1.7), the $T_R(5_1 \rightarrow 4_1)/T_R(5_{-1} \rightarrow 4_{-1})$, the $T_R(5_2 \rightarrow 4_2)/T_R(5_{-1} \rightarrow 4_{-1})$, and the $T_R(5_{-2} \rightarrow 4_{-2})/T_R(5_{-1} \rightarrow 4_{-1})$ in the 241 GHz band. They all also show a dependence on temperature in the range 5 – 15 K that suggest their use as temperature tracer in dark clouds. However, no line ratios in the 1 mm and the 3 mm bands show a pure dependence on the kinetic temperature, while for several ratios in the 1 mm band we found a strong sensitivity to both density and temperature.

The submillimeter band we analysed, the $7_k \rightarrow 6_k$ at 338 GHz, shows a behaviour very

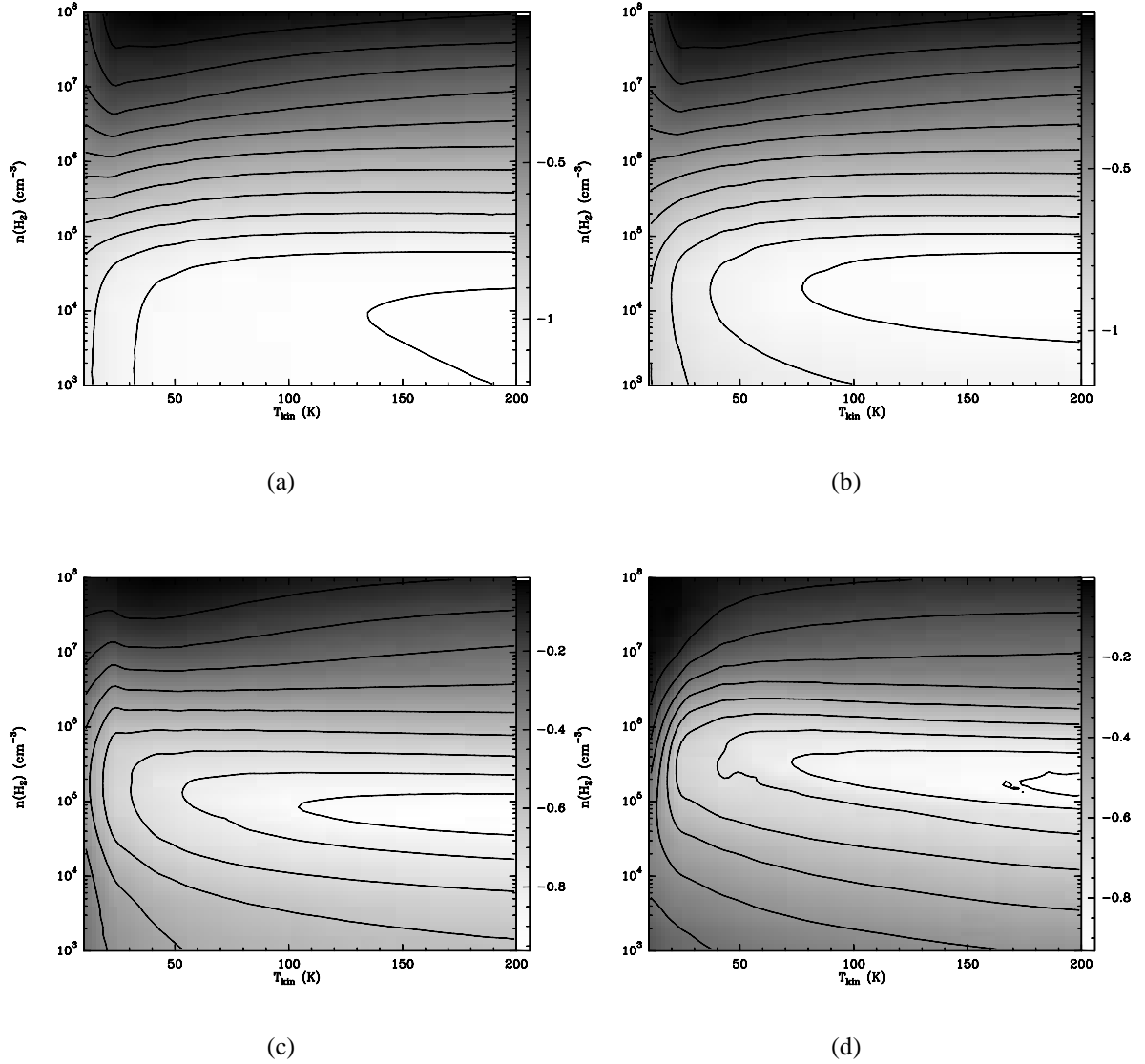


Figure 1.6: Results of statistical equilibrium calculations for CH₃OH-*E*. The $T_R(2_0 \rightarrow 1_0)/T_R(2_{-1} \rightarrow 1_{-1})$ line ratio is shown in logarithmic scale, as function of H₂ density and temperature at $N(\text{CH}_3\text{OH})/\Delta\nu=10^{13}$, **a**), $N(\text{CH}_3\text{OH})/\Delta\nu=10^{14}$, **b**), $N(\text{CH}_3\text{OH})/\Delta\nu=10^{15}$, **c**) and $N(\text{CH}_3\text{OH})/\Delta\nu=10^{16} \text{ cm}^{-2}/(\text{km s}^{-1})$, **d**). The black contours range from -1.5 to 0 by steps of 0.1. Line intensities, at all densities and temperatures, are strong enough to make the whole T- n plane is accessible to observations.

similar to the 1 mm series, with several line ratios being sensitive to both kinetic temperature and spatial density. However, some line ratios can be used as calibration-independent tracers of density, [e.g. the $T_R(7_0 \rightarrow 6_0)/T_R(7_{-1} \rightarrow 6_{-1})$ and the $T_R(7_1 \rightarrow 6_1)/T_R(7_{-1} \rightarrow 6_{-1})$]. A pure dependence on kinetic temperature is found in line ratios with $|k| \geq 3$, but mainly at low density ($n(\text{H}_2) \leq 10^5 \text{ cm}^{-3}$) where these lines are very weak (see Fig.1.8(a)–1.8(b)). However, given the sensitivity to both kinetic temperature and spatial density of several line

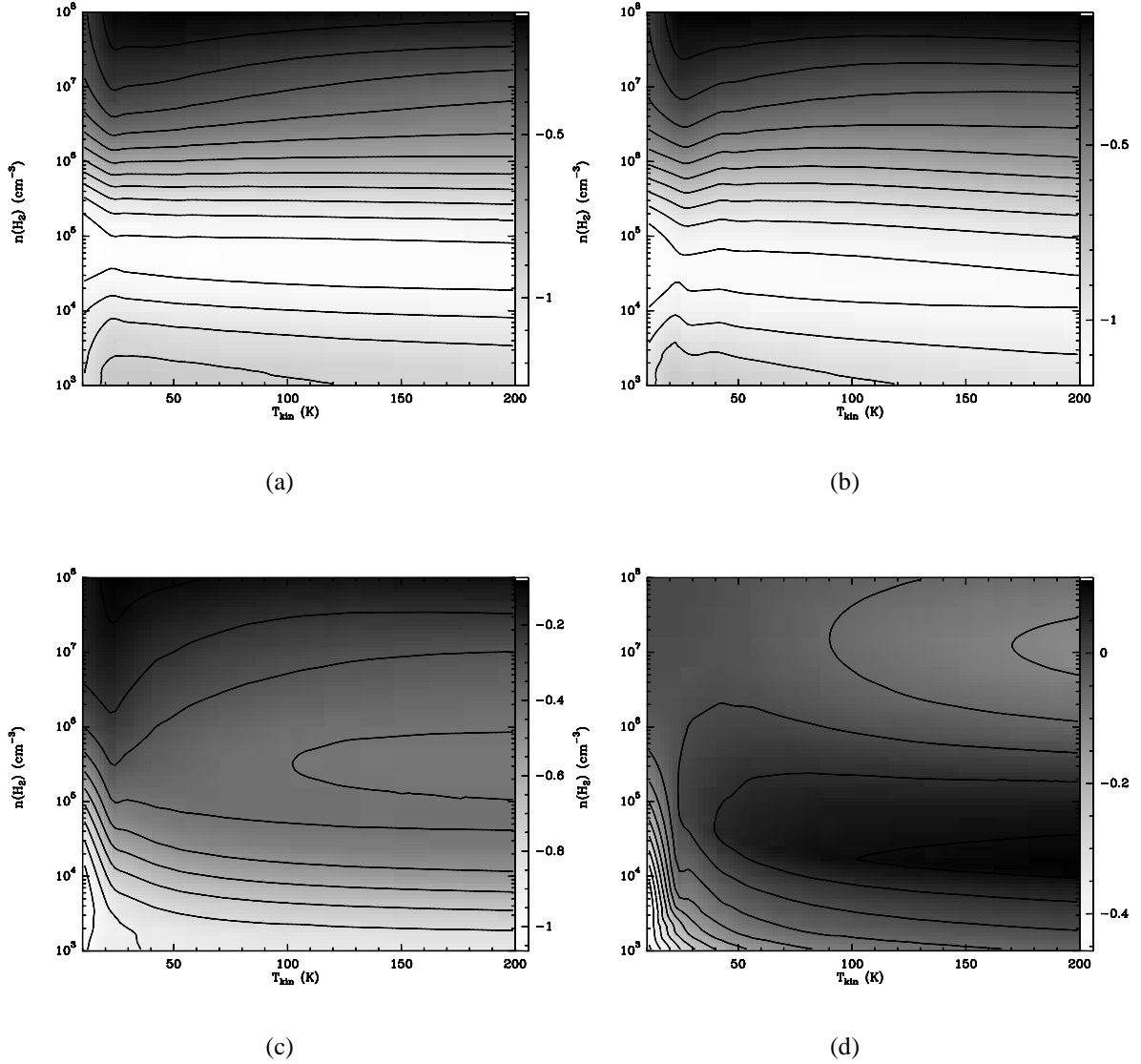


Figure 1.7: Results of statistical equilibrium calculations for $\text{CH}_3\text{OH-E}$. The $T_R(5_0 \rightarrow 4_0)/T_R(5_{-1} \rightarrow 4_{-1})$ line ratio in logarithmic scale is shown as function of H_2 density and temperature at $N(\text{CH}_3\text{OH})/\Delta\nu=10^{13}$, **a**), $N(\text{CH}_3\text{OH})/\Delta\nu=10^{14}$, **b**), $N(\text{CH}_3\text{OH})/\Delta\nu=10^{15}$, **c**) and $N(\text{CH}_3\text{OH})/\Delta\nu=10^{16} \text{ cm}^{-2}/(\text{km s}^{-1})$, **d**). The black contours range from -1.5 to 0 by steps of 0.1 in **a**), **b**) and **c**); from -0.5 to 0.1 by steps of 0.05 in **d**). The whole T - n plane is accessible to observations.

ratios in the $5_k \rightarrow 4_k$ and $7_k \rightarrow 6_k$ bands and the pure dependence on density of others, the simultaneous observations of several lines from these series allows determining both the physical parameters.

Fig. 1.6, 1.7 and 1.8 show LVG model predictions for line ratios in logarithmic scale as function of density and temperature at different column densities. The submillimeter bands are studied only at high column densities (10^{14} - $10^{16} \text{ cm}^{-2}/(\text{km s}^{-1})$) where their brightness

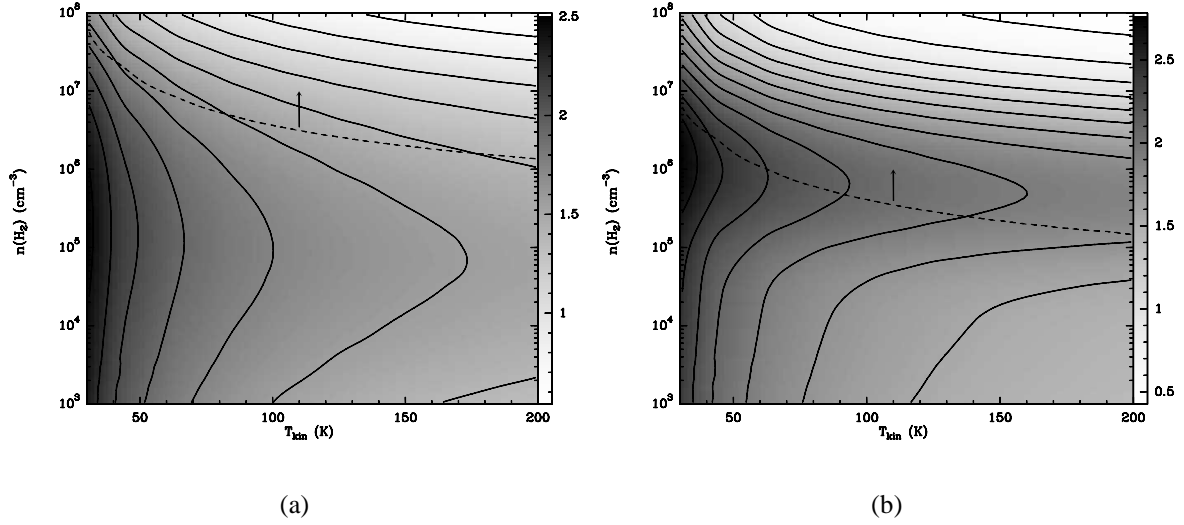


Figure 1.8: Results of statistical equilibrium calculations for CH₃OH-*E*. **a)** The $T_R(7_{-3} \rightarrow 6_{-3}) / T_R(7_5 \rightarrow 6_5)$ line ratio in logarithmic scale, as function of H₂ density and temperature at $N(\text{CH}_3\text{OH})/\Delta v = 10^{15}$ and, **b)**, at $10^{16} \text{ cm}^{-2}/(\text{km s}^{-1})$. The black contours range from 0 to 2.5 by steps of 0.2. The black dashed line corresponds to a $7_5 \rightarrow 6_5$ line intensity of 0.01 K; a black arrow shows how the $T_R(7_5 \rightarrow 6_5)$ increases with spatial density; the plane below the black dashed line is therefore inaccessible to observations.

temperatures become significant. Our results are summarized in the following guidelines:

- line ratios in the $2_k \rightarrow 1_k$ and the $5_k \rightarrow 4_k$ bands at 96 and 241 GHz are usually tracers of densities higher than 10^5 cm^{-3} , with a weak dependence on temperatures up to 15 K;
- some line ratios in the $5_k \rightarrow 4_k$ at 241 GHz and $7_k \rightarrow 6_k$ at 338 GHz are sensitive to kinetic temperature and spatial density, with some examples of pure density tracers;
- information on kinetic temperature is recovered when lines with an excitation temperature close to the expected kinetic temperature of the source are observed.

The main result we found is that, for all the analysed millimeter bands, ratios between lines in the same band are strongly sensitive to density, with a weaker dependence on temperature. This is explained by the high probability of the *a*-type² radiative transitions to occur, ($A_{ij} \propto \mu^2$, $\mu_a = 0.896$, $\mu_b = 1.412$, Sastry et al. 1981). Even if CH₃OH is only slightly asymmetric, ($\kappa = -0.98$ for CH₃OH, while $\kappa = -1$ for a prolate symmetric rotor, where κ is the Ray's asymmetry parameter, Ray 1932; Townes & Schawlow 1996), the $\Delta k \neq 0$ radiative lines are strongly allowed and not mainly dependent on the collisions as the structural similarity of

²Using standard asymmetric rotor nomenclature, *a*-type transitions have $\Delta k = 0$, while *b*-type transitions have $\Delta k = \pm 1$.

asymmetric molecules with symmetric rotors would suggest. However, in the submillimeter regime, several transitions show a strong dependence on the kinetic temperature in the range up to 100 – 150 K. Nevertheless, since several line ratios in the $5_k \rightarrow 4_k$ and in the $7_k \rightarrow 6_k$ band are strongly dependent on kinetic temperature and spatial density, both the parameters can be derived when a rich CH_3OH spectrum is available, with lines in different frequency and excitation ranges. Intraband line ratios from the $5_k \rightarrow 4_k$ band with the $7_k \rightarrow 6_k$ series show a dependence on temperature up to 50-80 K, at high density, $n(\text{H}_2) \geq 10^6 \text{ (cm}^{-3}\text{)}$, (see Fig. 1.9(a)–1.9(b)), since they have different excitation energies.

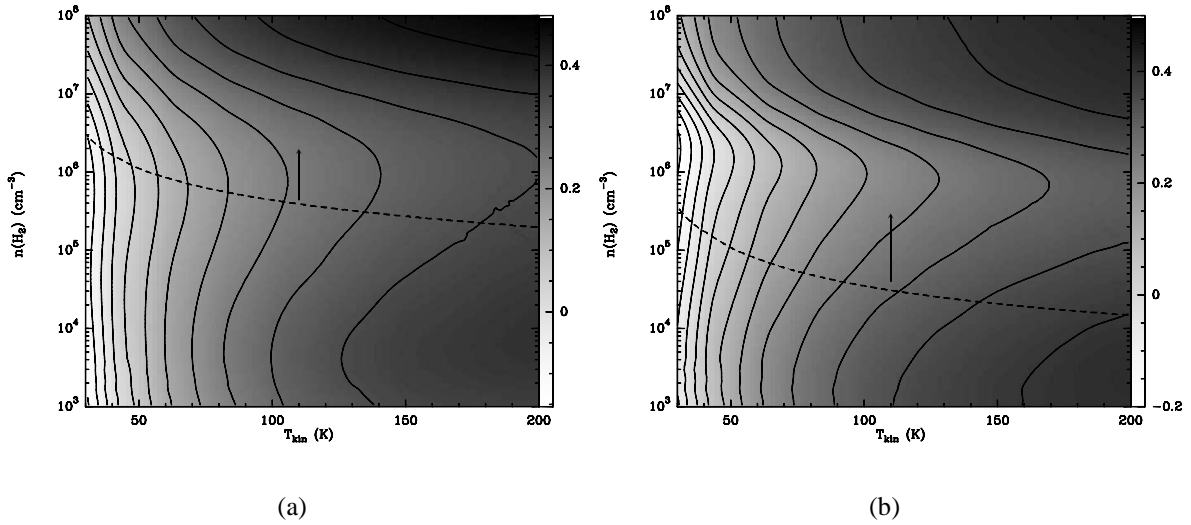


Figure 1.9: Results of statistical equilibrium calculations for $\text{CH}_3\text{OH-E}$. **a)** The $T_R(5_{-3} \rightarrow 4_{-3})/T_R(7_{-4} \rightarrow 6_{-4})$ line ratio in logarithmic scale, as function of H_2 density and temperature at $N(\text{CH}_3\text{OH})/\Delta v \ 10^{15}$ and, **b)**, at $10^{16} \text{ cm}^{-2}/(\text{km s}^{-1})$. The black contours range from -0.3 to 1 by steps of 0.05. The black dashed contour corresponds to a $7_5 \rightarrow 6_5$ line intensity of 0.01 K; a black arrow shows how the $T_R(7_5 \rightarrow 6_5)$ increases with spatial density; the plane below the black dashed line is therefore inaccessible to observations.

1.2 Analysis technique

The traditional approach for deriving physical parameters such as kinetic temperature and spatial density from an observed spectrum involves “by-hand” Gaussian fitting of the lines with multiple components and χ^2 analysis comparing the measured quantities with statistical equilibrium calculations (see Olmi et al. 1993; Mangum & Wootten 1993). Better results are obtained if the analysed quantities are ratios between lines close together in frequency space and observed simultaneously with the same receiver, because uncertainties due to absolute pointing, calibration and to the beam filling factor are minimized. The main drawback is the loss of information on the column density. On the other hand, when working with line intensities, uncertainties due to absolute calibration and to the beam filling factor play a major

role in making the determination of physical parameters less reliable. In general, this kind of analysis also ignores upper limits on lines too weak to be detected, because of the non-physical fitting procedure. For complex sources, the technique also requires decomposing line profiles, a tedious and, for strongly blended lines, very unreliable process. When applied to large multi-line datasets, like line surveys of a source or systematic multi-frequency studies of a molecule, by-hand fitting is impractical. With sensitive receivers available nowadays and in view of the next generation of instruments, which will provide copious amounts of data in a short time, new methods of data analysing and modelling are required.

An innovative technique to handle the problem, proposed by Schilke et al. (1999) and recently improved by Comito et al. (2004), is based on the simultaneous fit of all the lines in a spectrum with a synthetic spectrum computed under Local Thermodynamic Equilibrium (LTE) conditions. Here we propose an extension to this technique using the LVG approximation: this development is necessary and fully justifies the computing-time involved in such an analysis because we expect prominent departures from LTE in the sources of our sample and in many other astrophysical scenarios. To allow for complexity in the physical conditions along a line of sight, our model handles multiple components, which are assumed not to interact, i.e. the intensities simply add up. The free parameters for each component are kinetic temperature, molecular hydrogen density, source size and column density. To take into account the possibly different abundance between *A* and *E* states, CH₃OH-*A* and CH₃OH-*E* column densities are treated as two independent free parameters. Line width, Δv , and LSR velocity, v_{LSR} , are fixed parameters and assumed to be the same for all the lines in each component. The fitting is done by minimizing the χ^2 between the data and the model spectrum using the Levenberg-Marquardt method from Press et al. (1992). The χ^2 analysis is however not trivial, given the high number of fitted channels. We assume the degrees of freedom to be given by $\nu_d = N_o - N_f$, where N_o , the number of observed quantities, is here the number of *all* the channels in which CH₃OH transitions fall, even if not detected, plus the observed velocity and line width of each components. N_f is the number of free parameters. Frequencies for the line identification are from the Cologne Database for Molecular Spectroscopy. In the current implementation, 100 000 lines can be fitted simultaneously and data from different telescopes can be combined easily.

All the levels for which the collisional rates from Pottage et al. (2002) are available are used for the calculations; however, at low temperatures ($T_{\text{kin}} \leq 30$ K) the program runs into numerical problems due to the depopulation of the most excited levels in this regime. Therefore, only a subset of transitions is used in this range.

We assume the following representation of the spectrum:

$$T_v = \sum_c \eta(\theta^c) [\tilde{J}(T_{ex_v}^c) - J(T_{bg})] (1 - e^{-\tilde{\tau}_v^c}) \quad (1.1)$$

$$\tilde{\tau}_v^c = \sum_l \tau_l^c = \sum_l \frac{c^3}{8\pi\nu_l^3} A_l \frac{N_{\text{CH}_3\text{OH}}^c}{\Delta\nu^c} \left(n_{\text{low}}^c \frac{g_{\text{up}}}{g_{\text{low}}} - n_{\text{up}}^c \right) \phi^{l,c} \quad (1.2)$$

$$\tilde{J}(T_{ex_v}^c) = \frac{\sum_l J(T_{ex_l}^c) \tau_l^c}{\sum_l \tau_l^c} \quad (1.3)$$

where T_{ex} and τ are given by the LVG results, η is the beam filling factor and ϕ the line profile. The sums are computed on both A and E states; the indices l and c correspond to lines and spatial components. In eq. 1.2, n_{low}^c and n_{up}^c are the fractional populations of the lower and upper levels for the transition l in the component c and depend on the set of levels used for the calculations.

An implicit assumption, when solving the radiative transport equation with the escape probability method, is that different lines do not overlap locally. This is not true for molecules with a complex spectrum, especially for CH_3OH , whose A and E transitions are often very close in the frequency space. Following Cesaroni & Walmsley (1991), we define an average optical depth and brightness temperature by means of the previous expressions eq. 1.2-1.3 when lines have a frequency separation

$$\nu_i - \nu_j \leq \Delta\nu_i + \Delta\nu_j \quad (1.4)$$

Eq. 1.3 is equivalent to eq. 13 of Cesaroni & Walmsley (1991) in units of temperature. In the optically thin limit, eq. 1.3 is equal to the traditional approach of convolving a line with several Gaussians. On the other hand, it better describes situations in which both optically thin and optically thick lines are present: photons emitted from the optically thin transition are locally absorbed by the optically thick emission. The intensities of the lines do not simply add up like in the optically thin limit, but the intensity at the overlapping frequencies is mainly described by the optically thick emission. In the simplest case of one component and two transitions, both optically thin, eq. 1.1 can be approximated by

$$T_v = \eta(\theta^c) [J(T_{ex_1}^c) - J(T_{bg})] \tau_1^c + \eta(\theta^c) [J(T_{ex_2}^c) - J(T_{bg})] \tau_2^c \quad (1.5)$$

while when one of the two lines, e.g. line 1, is optically thick

$$\begin{aligned} T_v &= \frac{1}{\tau_1^c + \tau_2^c} \eta(\theta^c) [J(T_{ex_1}^c) - J(T_{bg})] \tau_1^c \\ &\quad + \frac{1}{\tau_1^c + \tau_2^c} \eta(\theta^c) [J(T_{ex_2}^c) - J(T_{bg})] \tau_2^c \\ &\simeq \eta(\theta^c) [J(T_{ex_1}^c) - J(T_{bg})] \end{aligned} \quad (1.6)$$

Tests on the convergence criterion

Although the simultaneous fit of a spectrum has been demonstrated to be a powerful technique to derive physical parameters (Comito et al. 2004), it does imply several approximations. The assumption behind the analysis is that the CH₃OH emission can be reasonably well approximated by a small number of non-interacting components, thus ignoring any alignments between them. This assumption is fully justified when no information on the morphology is available, but it fails in well reproducing the observed spectra if the components are related, leading, for example, to overestimate line intensities when self-absorption happens. The LVG approach adds other uncertainties to the obtained results, since it assumes only one set of physical parameters for each component used for fitting the source and implicitly neglects any local and non-local overlap between the lines; a more detailed model, including density and temperature distributions within each component, would be desirable. However, fitting large datasets with a Monte Carlo synthetic spectrum and minimizing all the free parameters would involve an enormous amount of computing time and it is practically impossible to be applied to a sample of sources. In fact, most (if not all) published Monte Carlo fits used manual fitting of the parameters, with no control over reaching a globally best fit, or assessment to the uniqueness of the fit (e.g. Hogerheijde & van der Tak 2000). Moreover, since several spectral windows can be fitted simultaneously, calibration uncertainties still render the determination of physical parameters less reliable. Another drawback is the uniqueness of the χ^2 minimization, which is not *a priori* guaranteed. Indeed the minimum found occasionally depends on the input parameters. A better control on the fit results is assured when plausible input parameters are used. Particularly important is the information on the source size, which helps in solving the degeneracy between source size, temperature and column density for certain parameter ranges. In the worst situation, no information at all is available in the literature on the source to be modelled and the number of free parameters is $5 \times N_c$, where N_c the number of components. To investigate whether the found solution is local or global, an analysis of the χ^2 distribution as function of the different free parameters in an interval reasonably close to the minimum is desirable.

However, one should be aware of the limits in determining the physical parameters of a source which are intrinsic to this technique. Unless lines with $\tau \ll 1$ and $\tau \gg 1$ are available, solving the degeneracy between source size and column density in the optically thin limit, ($T(\nu) = \sum \eta [J(T_{ex}^c) - J(T_{bg})] \tau$), where the information on the temperature is recovered when several optically thin lines are available, or between temperature and source size, in the optically thick case, ($T(\nu) = \sum \eta [J(T_{ex}^c) - J(T_{bg})]$), is impossible. Plotting the optical depth for each fitted line gives a better idea on which of the obtained parameters is more affected by uncertainties. Also, fitting CH₃OH spectra assures a reliable determination of kinetic temperature only when many lines are fitted, thus covering different excitation ranges, and/or when millimeter *and* submillimeter data are available, (see §1.1.4).

Observations of the $2_k \rightarrow 1_k$ -A and -E lines near 96 GHz, the $J_0 \rightarrow J_{-1}$ -E lines at 157 GHz, the $5_k \rightarrow 4_k$ -A and -E near 241 GHz were obtained towards a sample of more than 60

sources during a systematic program on CH₃OH in high-mass star forming regions at the IRAM 30 m telescope during summer 2002-winter 2003. Details on the observations and analysis of the data are given in chapter 3.

We here discuss the application of our method to two sources of our sample, G19.30P1 and G79.3P1. They both belong to a population of infrared-dark clouds, (hereafter IRDCs), identified by Egan et al. (1998) using the Galactic plane survey from the SPIRIT III telescope aboard the Midcourse Space Experiment, MSX. LVG calculations on H₂CO, (Carey et al. 1998), give an average value of $T \leq 20$ K, $n(\text{H}_2) \geq 10^5 \text{ cm}^{-3}$ and $N(\text{H}_2\text{CO}) \sim 10^{13}-10^{14} \text{ cm}^{-2}$ for IRDCs. Pillai et al. (2005) derive a kinetic temperature of 17 K for G19.30P1 and 15 K for G79.3P1 from NH₃ (1,1),(2,2) data; typical values for H₂ column densities are $10^{22}-10^{23} \text{ cm}^{-2}$ (Carey et al. 2000).

G79.3P1 shows CH₃OH emission only from the lowest energy levels in each band. The CH₃OH spectrum towards G19.30P1 is instead characterized by lines from levels higher in energy, ($2_1 \rightarrow 1_1 -E$; $6_0 \rightarrow 6_{-1}$ and $5_0 \rightarrow 5_{-1} -E$; $5_1 \rightarrow 4_1$, $5_{-2} \rightarrow 4_{-2}$ and $5_2 \rightarrow 4_2 -E$), which suggest a denser medium. Moreover the ground state lines ($k=0$ for *A* state and $k=-1$ for *E*) show Gaussian-like profiles with red and blueshifted wings.

G79.3P1 is, thus, an example of a simple source, to be fitted by a single component, while the more complex G19.30P1 region, needs at least a second component to fit the non-Gaussian profiles. As input values, we used typical IRDC values, $T = 20$ K and $n(\text{H}_2)=10^5 \text{ cm}^{-3}$. $N(\text{CH}_3\text{OH})$ for *A*- and *E*-states have been chosen equal to 10^{14} cm^{-2} using $N(\text{H}_2)=10^{23} \text{ cm}^{-2}$ and assuming $[\text{CH}_3\text{OH}/\text{H}_2]=10^{-9}$. The sizes of the CH₃OH regions are based on BIMA maps of CH₃OH at 3mm (Wyrowski 2005), $32''$ for G79.3P1 and $12''$ for G19.30P1. Figs. 1.12(a)-1.12(c) show the fitted spectra overlaid on the real data toward G19.30P1.

	$\Delta\nu$ (km s ⁻¹)	T_K (K)	$n(\text{H}_2)$ (cm ⁻³)	$N(\text{CH}_3\text{OH-A})$ (cm ⁻²)	$N(\text{CH}_3\text{OH-E})$ (cm ⁻²)	source size ('')	$\chi^2_{\nu d}$
best fit							
G19.30P1							3
core	3.0	44	10^6	7.5×10^{15}	3×10^{15}	5	
outflow	10.0	24	1.8×10^5	2×10^{15}	2×10^{15}	12	
1 σ fit range							
G19.30P1							
core		25–320	$1.2 \times 10^5 - 3 \times 10^6$	$3.6 \times 10^{15} - 1.6 \times 10^{16}$	$2 \times 10^{15} - 5 \times 10^{15}$		
outflow		18–61	$4.5 \times 10^4 - 3 \times 10^5$	$1.4 \times 10^{15} - 3 \times 10^{15}$	$1 \times 10^{15} - 2.5 \times 10^{15}$		
best fit							
G79.3P1							0.2
	2.0	17	2.5×10^5	7.9×10^{13}	5.7×10^{13}	32	
1 σ fit range							
G79.3P1							
		12–52	$4 \times 10^4 - 7 \times 10^5$	$5 \times 10^{13} - 1.3 \times 10^{14}$	$3.6 \times 10^{13} - 8.1 \times 10^{13}$		

Table 1.1: CH₃OH model results.

Table 1.1 lists the best fit results and the 1 σ fit range for our estimates of T_K , $n(\text{H}_2)$, $N(\text{CH}_3\text{OH})$ -*A* and *E* towards the two sources; for both sources, the fit gives temperatures higher than what found by (Pillai et al. 2005) from NH₃ (2,2), (1,1), which trace only the cooler, extended envelope, thus resulting in underestimate of T_K . Besides the satisfactory agreement between data and fit ($\chi_{\nu d} = 3$ for G19.30P1, $\chi_{\nu d} = 0.2$ for G79.3P1), some lines,

transition	ν	τ		T_{ex}		τ	T_{ex}
	(GHz)	core	outflow	core (K)	outflow (K)		(K)
G19.30P1						G79.3P11	
$2_{-1} \rightarrow 1_{-1} - E$	96.739	-8.8×10^{-1}	-7.2×10^{-2}	-13.2	-8.0	-5.8×10^{-1}	-162.0
$2_0 \rightarrow 1_0 - A$	96.741	1.0	4.7×10^{-1}	34.3	20.3	1.7×10^{-1}	13.0
$2_0 \rightarrow 1_0 - E$	96.744	5.2×10^{-1}	2.3×10^{-1}	16.3	7.9	3.7×10^{-2}	8.4
$2_1 \rightarrow 1_1 - E$	96.755	7.2×10^{-2}	2.3×10^{-2}	34.7	9.4		
$6_0 \rightarrow 6_{-1} - E$	157.048	3.1	2.8×10^{-1}	7.0	2.9		
$5_0 \rightarrow 5_{-1} - E$	157.179	3.9	8.1×10^{-1}	7.4	2.9	5.2×10^{-2}	9.6
$4_0 \rightarrow 4_{-1} - E$	157.246	4.3	2.1	7.7	3.1	1.5×10^{-1}	3.3
$1_0 \rightarrow 1_{-1} - E$	157.270	6.2×10^{-1}	9.7×10^{-1}	26.0	6.5	1.8×10^{-1}	6.8
$3_0 \rightarrow 3_{-1} - E$	157.272	4.1	1.6	8.0	3.6	2.8×10^{-1}	3.8
$2_0 \rightarrow 2_{-1} - E$	157.276	3.5	2.1	8.1	4.2	3.7×10^{-1}	4.5
$5_0 \rightarrow 4_0 - E$	241.700	6.8×10^{-1}	9.7×10^{-2}	37.4	11.5	1.4×10^{-2}	9.9
$5_{-1} \rightarrow 4_{-1} - E$	241.767	1.6	9.4×10^{-1}	41.3	13.7	1.2×10^{-1}	11.3
$5_0 \rightarrow 4_0 - A$	241.791	2.8	9.7×10^{-1}	42.4	13.8	1.7×10^{-1}	11.4
$5_4 \rightarrow 4_4 - A$	241.806	7.6×10^{-3}	3.4×10^{-6}	10.2	8.1		
$5_{-4} \rightarrow 4_{-4} - A$	241.806	8.5×10^{-3}	3.7×10^{-6}	9.4	7.6		
$5_{-4} \rightarrow 4_{-4} - E$	241.813	8.6×10^{-4}	1.8×10^{-6}	12.6	10.5		
$5_4 \rightarrow 4_4 - E$	241.829	1.8×10^{-4}	9.7×10^{-7}	17.2	12.6		
$5_3 \rightarrow 4_3 - A$	241.832	1.3×10^{-1}	7.8×10^{-4}	19.8	13.2		
$5_3 \rightarrow 4_3 - A$	241.833	2.9×10^{-2}	6.4×10^{-4}	11.6	17.8		
$5_2 \rightarrow 4_2 - A$	241.842	3.3×10^{-1}	4.1×10^{-4}	17.6	12.6		
$5_3 \rightarrow 4_3 - E$	241.843	1.6×10^{-2}	1.2×10^{-4}	17.2	12.1		
$5_{-3} \rightarrow 4_{-3} - E$	241.852	2.8×10^{-3}	2.6×10^{-5}	19.4	14.2		
$5_1 \rightarrow 4_1 - E$	241.879	3.1×10^{-1}	1.3×10^{-2}	30.7	10.6		
$5_2 \rightarrow 4_2 - A$	241.887	2.2×10^{-1}	3.4×10^{-4}	24.0	14.7		
$5_{-2} \rightarrow 4_{-2} - E$	241.902	1.3×10^{-1}	2.1×10^{-2}	23.3	10.7		
$5_2 \rightarrow 4_2 - E$	241.904	3.9×10^{-1}	1.9×10^{-3}	28.4	9.3		

Table 1.2: Line parameters.

mostly the $2_k \rightarrow 1_k$ band, are underestimated in intensities. This behaviour is more marked for G19.30P1, for which the χ^2 S. analysis does not allow a reliable estimate of temperature due to the shallow property of the minimum. The source also shows a more complex structure than G79.3P1. Therefore, we attribute these discrepancies mainly to the fact that real sources are more complex than our model can represent, with a finite number of non-interacting components, thus ignoring alignment, self-absorption, a gradual gradient of the parameters within the source.

G79.3P1 offers, instead, a better agreement of the fit with the data, probably due to a less complex structure. All the lines are well fitted by our model, even the $2_{-1} \rightarrow 1_{-1} - E$ which

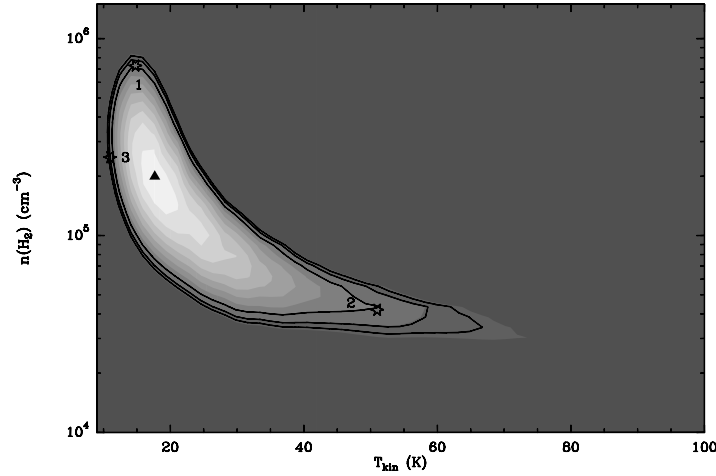


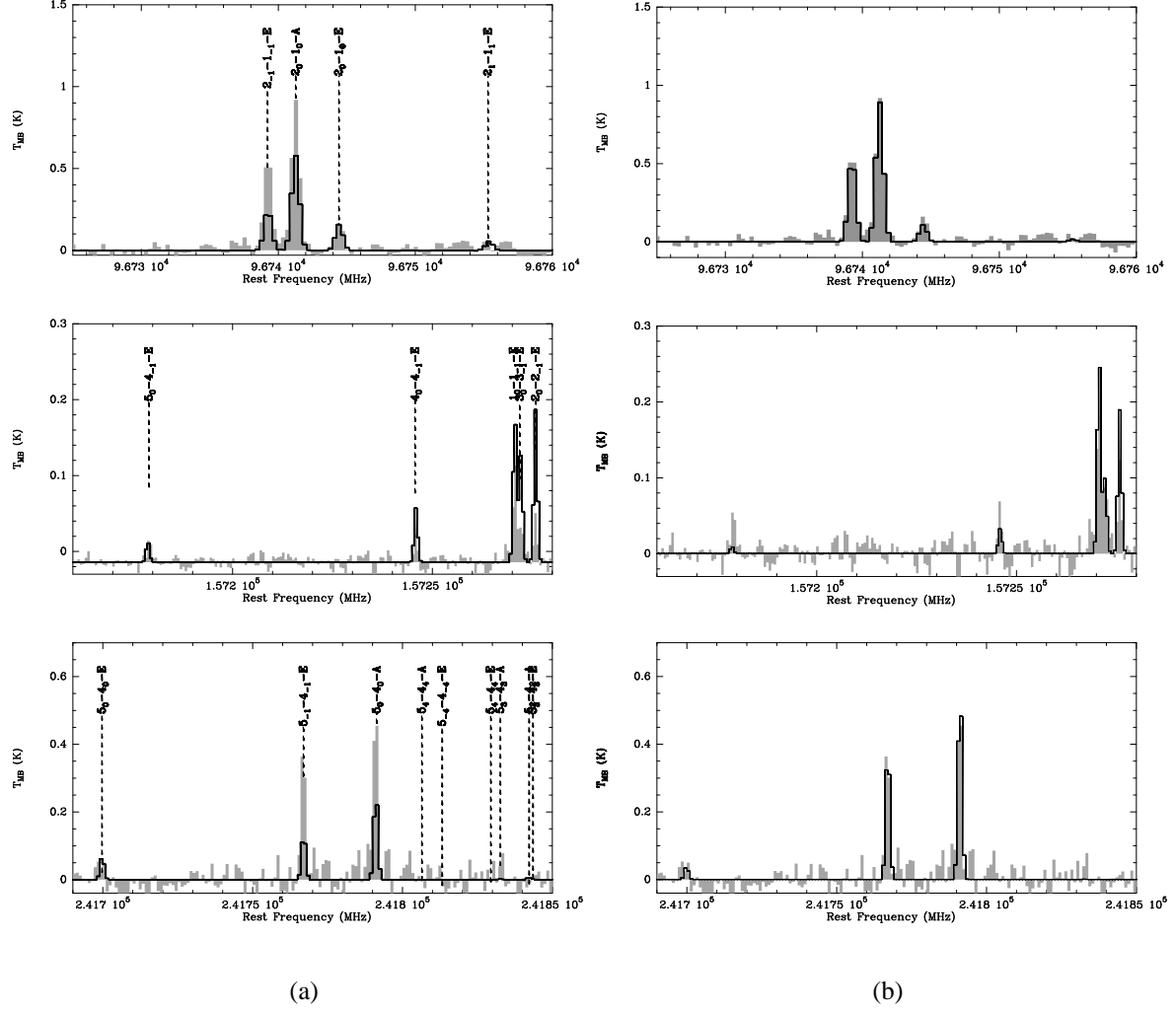
Figure 1.10: χ^2 square distribution in the $[T_{kin}, n(\text{H}_2)]$ plane toward G79.3P1. A black triangle marks the minimum position, $T_{kin}=17$ K, $n(\text{H}_2)=2.5 \times 10^5 \text{ cm}^{-3}$; stars mark the positions at which spectra of Fig. 1.13 are taken, which are also labelled by numbers. Overlaid in black the 3σ , 2σ and 1σ confidence contours.

shows an unusual excitation.

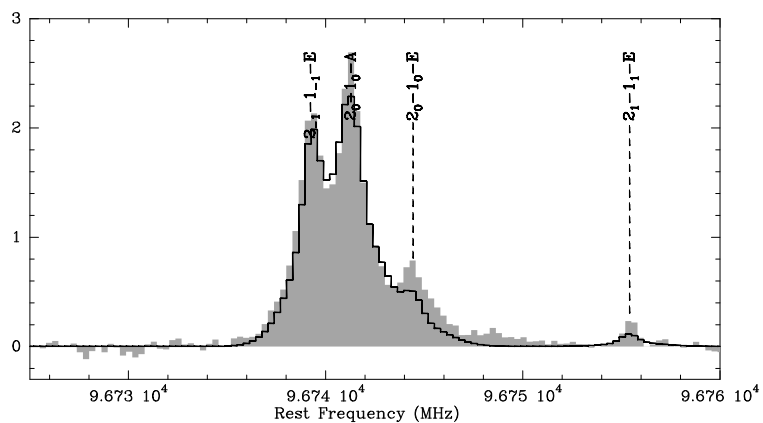
Fig. 1.10 shows the χ^2 distribution for G79.3P1 in the $(T_{kin}, n(\text{H}_2))$ plane at the column densities derived for *A*- and *E*-species; 1, 2 and 3 σ confidence contours, computed from the incomplete gamma function (see Press et al. 1992), are shown. Black stars mark the positions within the 1σ confidence contour for which spectra are shown in Fig. 1.13 along with the best fit; even if the fits within the 1σ range are still pretty good, major deviations from the observations, mainly at 3 mm and 2 mm, occur. Since the fit solution falls in the temperature range in which both the $2_k \rightarrow 1_k$ and the $5_k \rightarrow 4_k$ bands show a dependence on density and temperature, for G79.3P1 the estimates of T_K and $n(\text{H}_2)$ and their uncertainties correlate. This is not true at higher temperature, as in G19.30P1, where the bands have a pure dependence on density. In the case of G79.3P1 we have also compared our LVG results with a similar analysis under the LTE assumption. The agreement between data and LTE fit is usually less satisfactory than in the LVG case, with $\chi_{\nu_d}=7$, particularly in the $J_0 \rightarrow J_{-1}$ -*E* band at 157 GHz, which is a known Class II maser series of lines, where the predicted spectrum differs significantly from the measured data. The best fit under the LTE approximation is found at $T = 10$ K and for similar values for column densities. The LTE fit overlaid on the data is shown in Fig. 1.11.

1.3 Conclusions

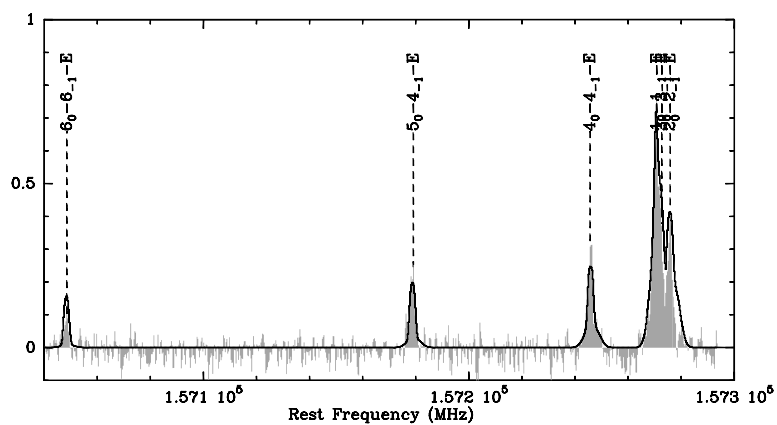
Using a spherical LVG model to describe the molecular excitation, we have carried out a detailed analysis of the tracing properties of CH_3OH in the millimeter and submillimeter



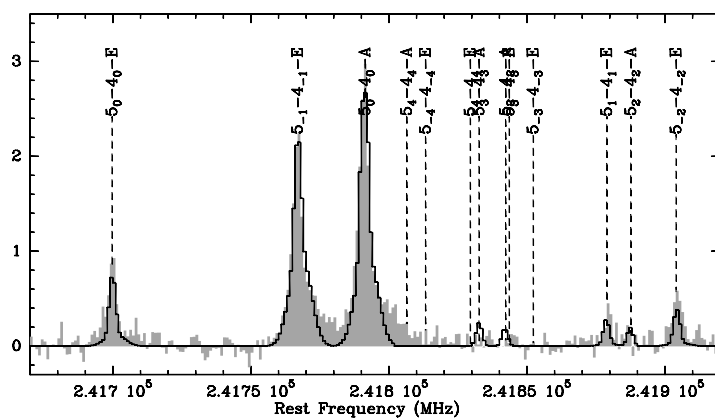
a simultaneous fitting of all the lines observed towards a given position. The application of this technique to two IRDCs, G19.30P1 and G79.3P1, has been discussed.



(a)



(b)



(c)

Figure 1.12: Spectra toward G19.30P1 (J2000 coordinates: R.A. = $18^h 25^m 58^s.5$, decl. = $-12^\circ 03' 59''$), taken with the IRAM 30m telescope. The 2mm and 1mm data are smoothed for the difference in the beam size with the 3mm data. Overlaid in black the synthetic spectra resulting from the fit.

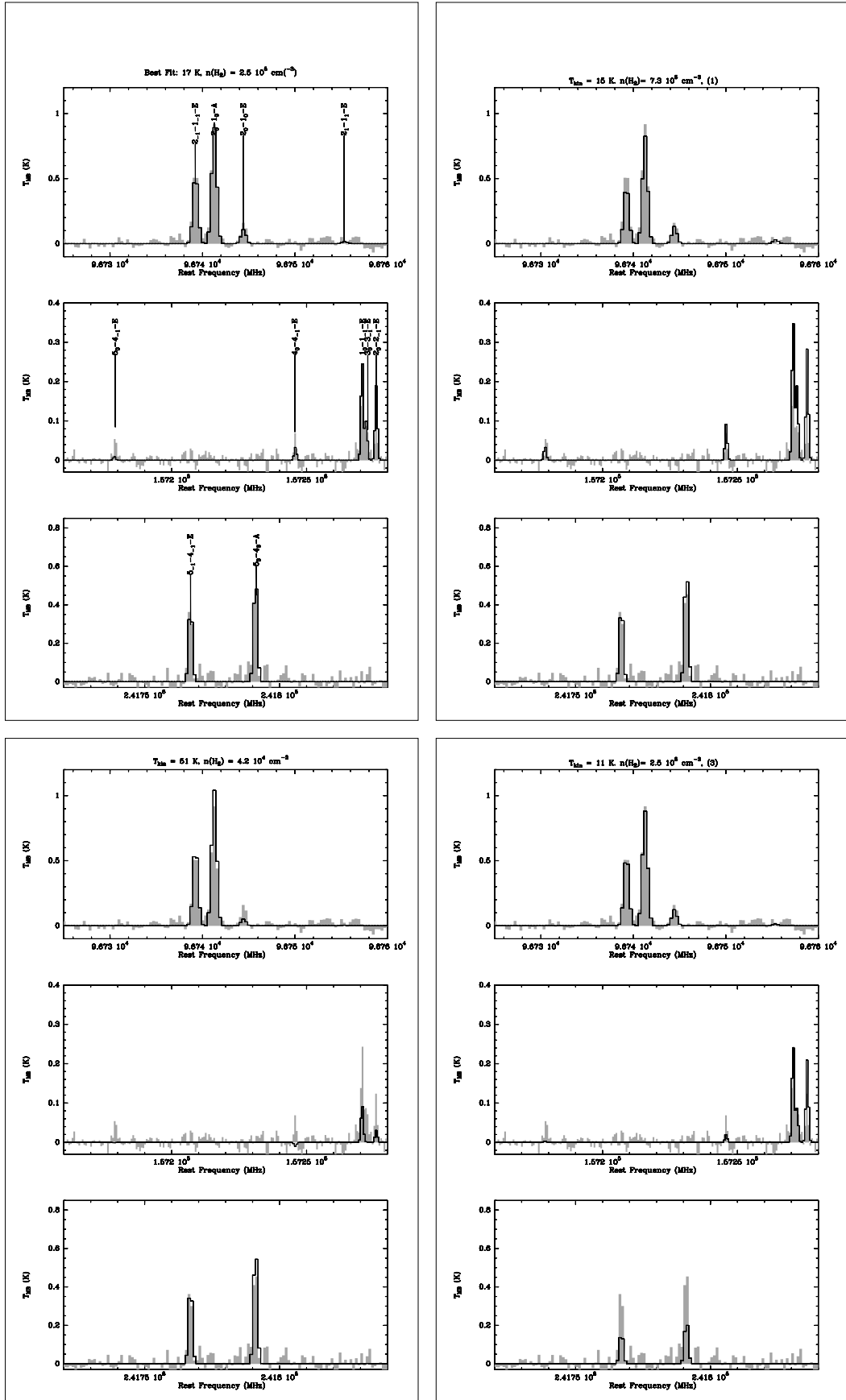


Figure 1.13: Synthetic spectra corresponding to different positions within the 1σ confidence surface overlaid on the spectra observed toward G79.3P1. For comparison, the best fit spectrum is also shown. Major deviations in the 3 mm and 2 mm lines occur in the fits at the 1σ level.

Chapter 2

Class I methanol masers

The content of this chapter is based on Leurini, S., Menten, K. M., Schilke, P. to be submitted to A&A

2.1 Introduction

Recent progress in the calculation of collisional rate coefficients has resulted in numbers that now allow meaningful modelling of methanol (CH_3OH) excitation over a wide range of interstellar conditions (Pottage et al. 2001, 2002). The preceding paper in this series (Leurini et al. 2004) describes model calculations we made using these coefficients. A Large Velocity Gradient (LVG) method was employed to reproduce CH_3OH observations of dark clouds and constrain temperature, density, and CH_3OH abundance in such regions.

Here we describe calculations using the same program that were aimed to explain the pumping of class I methanol masers (cIMMs). In the following section we give a review of cIMMs, followed by a description of our calculations. We then discuss the physical conditions implied by the maser observations in the context of our modelling results.

2.2 Phenomenology of class I methanol masers

Basic properties

As first realized by Batrla et al. (1987), CH_3OH masers come in two varieties, termed class I and II by Menten (1991a,b). Class II methanol masers (cIIMMs) are closely associated with young high-mass (proto)stellar objects and arise from the same regions of hot molecular cores as hydroxyl (OH) masers, and are, like these (Cesaroni & Walmsley 1991), most likely pumped by far-infrared radiation in dense ($n \sim 10^7 \text{ cm}^{-3}$), warm ($T \sim 150 \text{ K}$) gas. For class II CH_3OH masers various, sometimes intricate, pumping schemes have been proposed (Sobolev & Deguchi 1994a,b; Sobolev et al. 1997). We consider their inferred density and temperature information as uncertain, since the excitation of these masers is likely to involve radiative and collisional excitation to torsionally excited levels and their calculations were

made *before* the newly calculated rate coefficients from (Pottage et al. 2001, 2002, 2004b) were available. In contrast, as discussed in § 2.3, cIMMs¹ can be explained from basic properties of the CH₃OH molecule. For example, the propensity for $\Delta k = 0$ over $\Delta k = 1$ collisions causes molecules to preferentially de-excite down a k stack (see Fig. 2.1), leading to a situation where, say, the lower levels in the $k = -1$ stack are overpopulated relative to those in the $k = 0$ stack, resulting in maser action in the $J_k = 4_{-1} \rightarrow 3_0 - E$ and $5_{-1} \rightarrow 4_0 - E$ transitions and enhanced absorption in the $2_0 \rightarrow 3_{-1} - E$ line, which in turn is the second most prominent class II *maser* line (see Fig. 2.2).

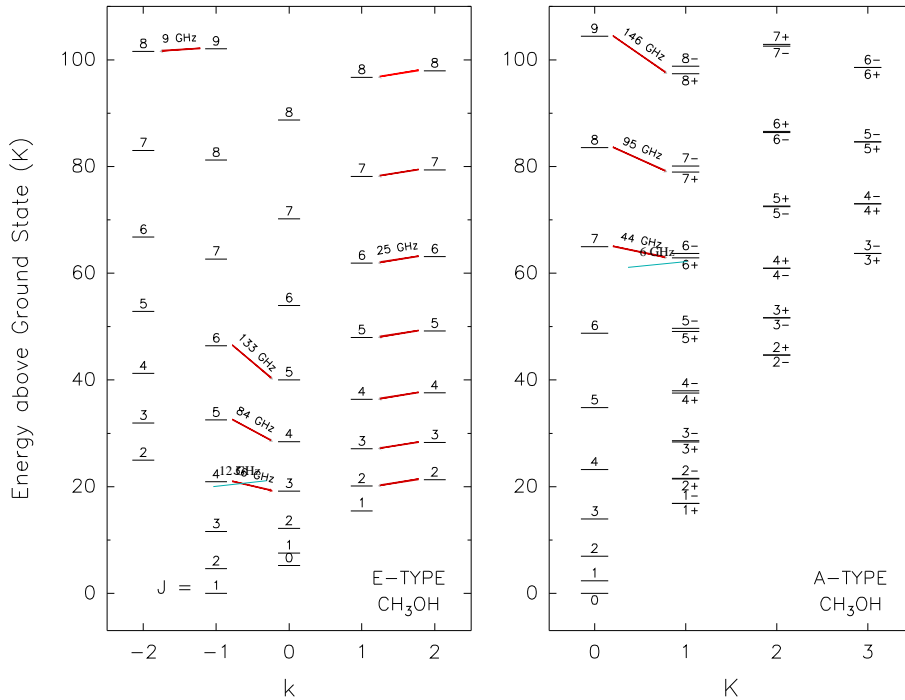


Figure 2.1: Partial rotational level diagram of *E*-type (left) and *A*-type methanol (right). Known class I maser transitions are connected by red arrows with frequencies indicated; cyan arrows connect anti-inverted transitions. Note that all of the maser lines originating in the $J = 2$ *E* stack have frequencies near 25 GHz. Higher J $J_{k=2} \rightarrow J_{k=1} E$ lines (with higher frequencies) have also found to be masing (see Table 2.1) but are not shown here. The projection of the total angular momentum J on the molecular axis quantum number is upper case K ($0 \leq K \leq J$) for *A*-type CH₃OH and lower case k ($-J \leq k \leq +J$ for the *E* species).

Occurrence of class I methanol masers

cIMMs CH₃OH masers are frequently found in the general vicinity of intermediate and high-mass star formation, but often significantly offset (up to a parsec) from prominent centers of activity, such as infrared sources or compact radio sources (Menten et al. 1986). In some

¹We loosely use the term “class I methanol masers” for, both, the maser transitions in question as well as for the sources from which the emission arises.

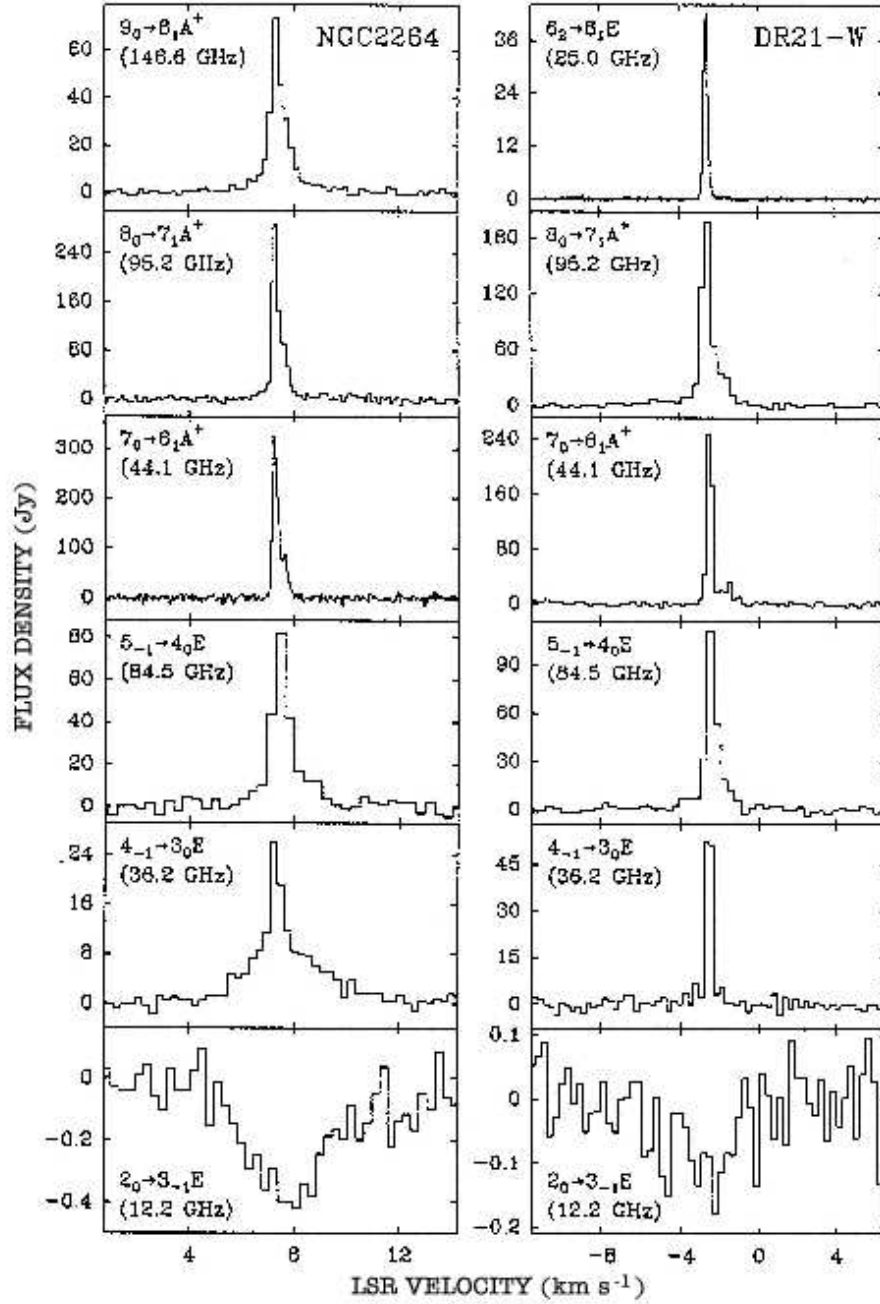


Figure 2.2: For both NGC 2264 (left) and DR21-W (right) the lowest spectrum shows absorption in the CH₃OH $2_0 \rightarrow 3_{-1} - E$ line, while the other spectra show various maser transitions taken with differing velocity resolutions and a number of telescopes (see Table 2.1 for reference. Some spectra have not yet been published elsewhere.

regions, on parsec scales, masers of both types are found, which has led to some confusion when studied at low spatial resolution with single-dish telescopes. However, in all such cases interferometric observations clearly separate class I from class II maser regions (see Mehringer & Menten 1997, for the case of Sgr B2).

Low-mass star-forming regions (SFRs) seem to be largely devoid of class I *and* class II (Minier et al. 2003) methanol masers, although few such regions have been searched (see below). The methanol-rich outflow in the L 1157 region, which is powered by an object of luminosity, L , of $11L_{\odot}$, where Kalenskii et al. (2001) detect maser emission in the $5_{-1} - 4_0E$ transition, is an exception and motivates further searches in such regions.

The dearth of methanol masers in low-mass SFRs regions may be caused by the low abundance of methanol; Friberg et al. (1988) found $[\text{CH}_3\text{OH}/\text{H}_2] \sim 10^{-9}$ in cold ($T \sim 10$ K), quiescent dark clouds, prohibiting the build-up of large enough gain-lengths for strong maser emission.

In the case of class II masers the high CH_3OH abundances, implied by analysis of thermal transitions, are thought to result from evaporation of CH_3OH off icy dust grain mantles. These are known to contain large quantities of this molecule which are desorbed into the gas phase at $T \gtrsim 120$ K (Sandford & Allamandola 1993).

In one source, DR 21, the class I masers are found in what appears to be the interaction region between a powerful molecular outflow traced by shocked molecular hydrogen and a dense clump traced by CS emission (Plambeck & Menten 1990). In the Orion-KL region, too, the CH_3OH masers show the same general distribution as shocked H_2 (Johnston et al. 1992).

A location in the (swept-up) interaction region of outflows with ambient material may be a natural explanation for some of the observed properties of cIMMs. For once, the elevated temperatures of the shocked material evaporate methanol off ice mantles, producing the elevated CH_3OH column densities necessary for observable maser emission. Moreover, the facts that no high velocity cIMM emission is ever observed and the (generally few) observed features are always clustered within a few km s^{-1} around a region's LSR velocity, v_{LSR} , are explained by the fact that paths moving perpendicular to the line-of-sight have the longest velocity-coherent gain length and have, naturally, velocities close to v_{LSR} .

2.3 Statistical equilibrium calculations

Up to now all previous studies on CH_3OH made use of collisional rates based on experimental results by Lees & Oka (1969) and Lees & Haque (1974). The selection rules they derive show a propensity for $\Delta k = 0$ collisions and a dependence upon ΔJ as $1/\Delta J$.

The $\Delta k = 0$ collisional selection rule and the spontaneous decays of the $k = -1$ ladder being much slower than $J_{-1} \rightarrow (J-1)_{-1}$ radiative transitions overpopulate the $k = -1$ levels relative to levels in the close k ladders and are responsible for the anti-inversion to occur in the $2_0 \rightarrow 3_1 - E$ transition at 12.18 GHz, (Walmsley et al. 1988), and for the class I masers

$4_{-1} \rightarrow 3_0 - E$, 36 GHz, and $5_{-1} \rightarrow 4_0 - E$, 84 GHz (see Fig. 2.1 ; Lees (1973), and the references given in Table 2.1). Similar effects lead to an overpopulation of the $k = 0$ levels in the A-state and explain the $7_0 \rightarrow 6_1 - A$, $8_0 \rightarrow 7_1 - A$ and $9_0 \rightarrow 8_1 - A$ masers at 44, 95 and 146 GHz. However, the collisional rates from Walmsley et al. (1988) cannot reproduce the class I maser series $J_2 \rightarrow J_1 - E$ at 25 GHz without an additional preference for the $\Delta k = 3$ collisions, suggested by the threefold symmetry of methanol, and the assumption that $\Delta k = 2$ collisions are forbidden, (Johnston et al. 1992).

We now describe the application of our model on the excitation of cIMMs.

2.3.1 Class I methanol masers.

As already discussed by Pottage et al. (2001), the calculations of the $\text{CH}_3\text{OH-He}$ collisional rates confirm a propensity for the $\Delta k = 0$ collisions, hence yielding to the same pumping mechanism proposed by Lees (1973) for the A-type $k = 0 \rightarrow k = 1$ and E-type $k = -1 \rightarrow k = 0$ masers. However, the $\Delta k = 3$ and $\Delta k = 2$ selection rules suggested by Johnston et al. (1992) are not reproduced and the $\Delta k = 2$ collisions are almost as strong as the $\Delta k = 3$ (see Fig. 2.3).

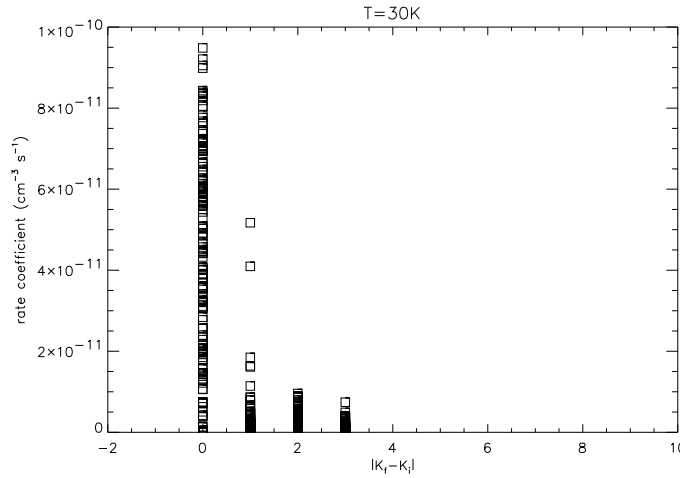


Figure 2.3: Scatter plot showing the rate coefficients for de-excitation transitions in the ground state of E-type at 30 K, as function of $|\Delta K| = |K_f - K_i|$.

To explain the maser action in the $J_2 \rightarrow J_1 E$ at 25 GHz, we have performed a deeper study on these transitions; the simplest system in which inversion of the $2_2 \rightarrow 2_1 E$ line occurs is a four level-system involving the 1_{-1} , 2_0 , 2_1 and $2_2 E$ levels, (see Fig. 2.4), where only collisions and spontaneous decays are taken into account. Although collisions from the ground state equally populate the 2_1 and $2_2 E$ levels, the lower level is more fastly depopulated by spontaneous decays than the upper, (as a direct consequence of the dependence of the Einstein coefficients on the frequency, $A_{ij} \propto \nu_{ij}^3$, spontaneous decay from the 2_1 level to the 2_0 is several times stronger than that from 2_2 to 2_1), resulting in the inversion of the

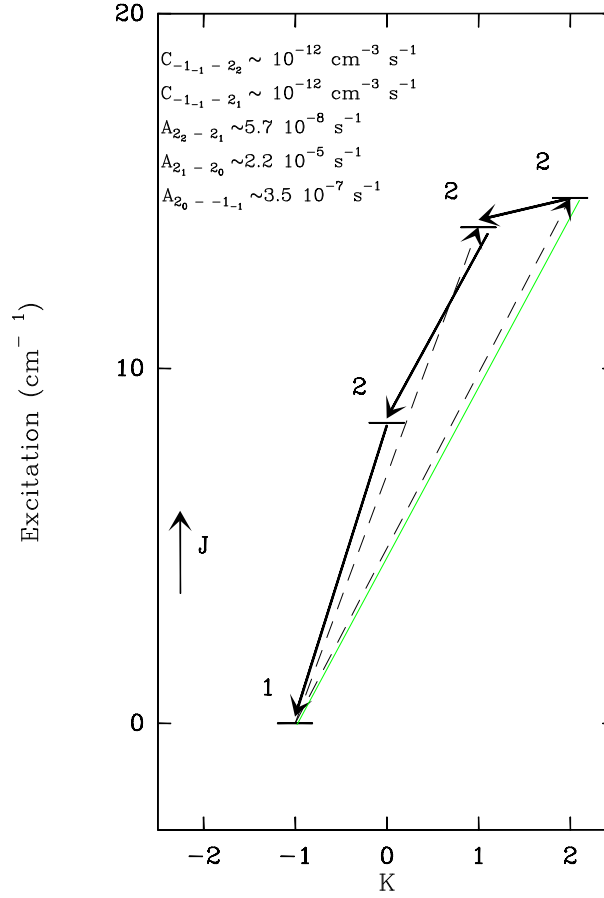
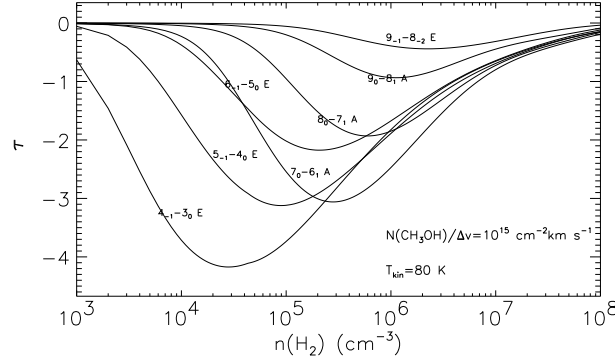


Figure 2.4: Pumping mechanism of the $2_2 \rightarrow 2_1 E$ class I maser. The dashed lines mark collisional transitions, the full lines the radiative ones. A green line connects the levels involved in the maser line. Collisional rates and Einstein coefficients taken into account in the calculations are also listed.

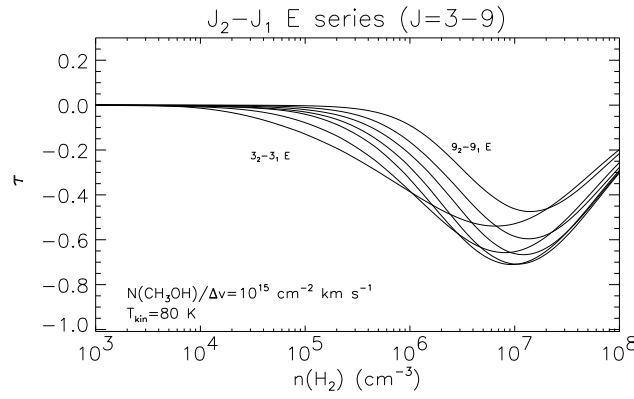
$2_2 \rightarrow 2_1 E$ transition. The same consideration is valid for the other $J_2 \rightarrow J_1 E$ lines.

Extending the calculations to the levels up to $(J, K) = 9$, we have modelled several observed class I masers in a range of physical parameters typical of interstellar clouds. Results at a kinetic temperature, T_{kin} , of 80 K and a methanol column density, $N(\text{CH}_3\text{OH})$, of 10^{15} cm^{-2} are shown in Fig. 2.5(a)–2.5(b). A quite interesting result of our calculations is that, while the maser action in the $J_2 \rightarrow J_1 - E$ series has a maximum around 10^7 cm^{-3} and at densities higher than 10^8 cm^{-3} is quenched, the other class I methanol transitions maser at lower densities (10^4 – 10^6 cm^{-3}) and are then quenched. Hence the detection of maser action in the class I maser transitions can be used as a density indicator.

Similar results are found at different temperatures and methanol column densities: the dependence on the spatial density in the maser action does not change; however, their intensities decrease with the temperature and the column density.



(a)



(b)

Figure 2.5: **a**: Line optical depths of several class-I maser transitions of *A*- and *E*-type CH_3OH as function of density; **b**: line optical depths of the $J_{k=2} \rightarrow J_{k=1}E$ series of class-I maser transitions of *E*-type CH_3OH as a function of density.

2.3.2 Anti-inversion in the $2_0 \rightarrow 3_1 - E$, $5_1 \rightarrow 6_0 - A^+$ methanol transitions.

Several observations (Batra et al. 1987; Walmsley et al. 1988; Whiteoak & Peng 1989; Menten 1991b) reveal that the $2_0 \rightarrow 3_1 - E$ at 12.18 GHz and the $5_1 \rightarrow 6_0 - A^+$ at 6.67 GHz, strong class II methanol masers, can be anti-inverted. Absorption in these two lines can happen not only in sources with a significant continuum, but also against the microwave background. Walmsley et al. (1988) therefore concluded that high kinetic temperatures and a strong infrared radiation field are prerequisites for maser inversion in class II masers. Models of class II lines (e.g. Cragg et al. 2002) confirm this idea.

We have carried out statistical equilibrium calculations for both the lines, to investi-

gate their excitation mechanism; as already noticed by (Walmsley et al. 1988), at least the 12.18 GHz line, can be a tracer of dense, cold dark clouds.

Figs.2.6(a)-2.6(d) show the line temperature as function of the H_2 density for different methanol column densities, at 10 and 50 K, for both the $2_0 \rightarrow 3_1 - E$ transition, left panels, and the $5_1 \rightarrow 6_0 - A^+$ line, right panels. The anti-inversion in the $2_0 \rightarrow 3_1 - E$ line happens at low densities; thermalization starts around 10^6 cm^{-3} . The absorption temperature increases with methanol abundance and kinetic temperature.

The absorption in the $5_1 \rightarrow 6_0 - A^+$ line has the same behaviour of the $2_0 \rightarrow 3_1 - E$ line as function of temperature and methanol column density. However the anti-inversion happens at higher densities ($n(H_2) > 10^4 \text{ cm}^{-3}$).

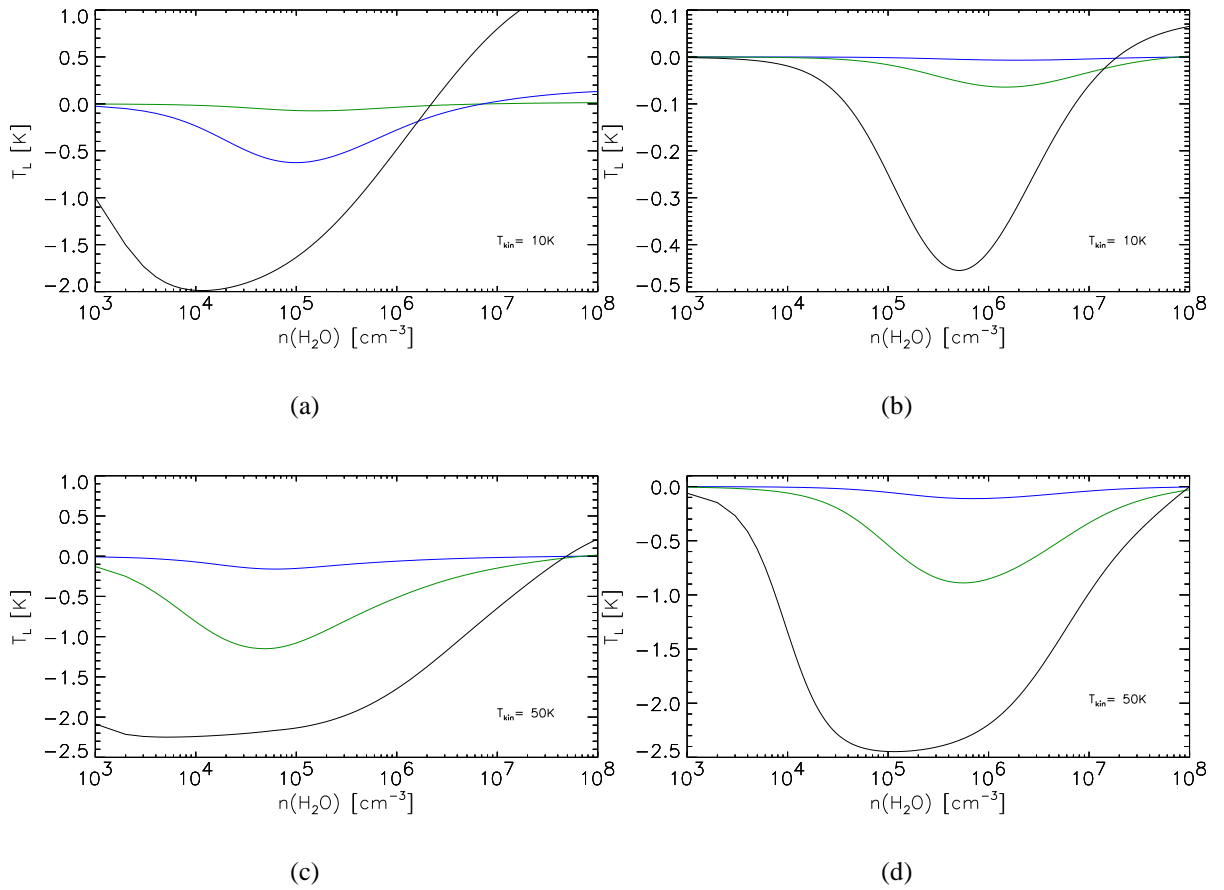


Figure 2.6: The brightness temperature of the $2_0 \rightarrow 3_1 - E$ transition (a,c) and of the $5_1 \rightarrow 6_0 - A^+$ one (b,d) as function of the H_2 density at 10 and 50 K. The blue solid line shows the results of our calculations for $N(\text{CH}_3\text{OH})/\Delta\nu=2 \cdot 10^{13} \text{ cm}^{-2}/(\text{kms}^{-1})$, the green one for $N(\text{CH}_3\text{OH})/\Delta\nu=2 \cdot 10^{14} \text{ cm}^{-2}/(\text{kms}^{-1})$, the black one for $N(\text{CH}_3\text{OH})/\Delta\nu=2 \cdot 10^{15} \text{ cm}^{-2}/(\text{kms}^{-1})$.

2.4 Outlook

A pragmatist might ask “But what are these maser good for?” Having line luminosities around a few 10^{43} photon \times s $^{-1}$, cIMMs clearly are completely unimportant energetically. Possibly their most important “use” is the signpost effect, marking the chemically interesting interaction regions of high velocity outflows and dense ambient material. Apart from that, if a one-to-one relation of cIMMs and outflows could be established, the former would be efficient outflow tracers, not affected by interstellar extinction, which has dramatic effects in embedded sources as the high mass star forming regions and renders, e.g., the central portion of the DR21 outflow invisible even at (near-)IR wavelengths.

Historically speaking, outflow activity in SFRs was first postulated to explain high velocity H₂O maser emission (Strel'nitskii & Sunyaev 1972), long before high velocity CO (Snell et al. 1980) or H₂ (Beckwith et al. 1978) outflows were detected. That an outflow interpretation was not proposed earlier for the Orion cIMMs, may be caused by their low (radial) velocities.

Finally let us ask, whether it would be possible to measure cIMM proper motions, which would unequivocally prove their outflow nature. For the case of Orion-KL, let us assume (1) transverse velocities of 200 km s $^{-1}$ (which Herbig-Haro-objects associated with the outflow have; Jones & Walker (1985), (2) that the maser spots NW of the outflow centroid move in the opposite direction as those to the SE of it, and (3) that one repeated the A-Array observations made by Johnston et al. (1997) in 1990 now, 14 years later. Then these groups of maser spots would appear with a $2 \times 200 \times 86400 \times 365 \times 12 = 1.5 \times 10^{11}$ kms, or 1009 AU, larger separation. At Orion's distance, D , of 450 pc, this corresponds to an increase in the angular separation of 2.''2, which would be very easy to measure.

Transition	Frequency (MHz)	Lab. Ref.	Astronomical Reference
$9_{-1} \rightarrow 8_{-2} - E$	9936.202(4)	L2	A28
$3_2 \rightarrow 3_1 - E$	24928.700(50)	L1	A12,A20
$4_2 \rightarrow 4_1 - E$	24933.468(2)	L1	A1,A6,A8,A12,A20
$2_2 \rightarrow 2_1 - E$	24934.38295)	L1	A7,A12,A17,A20
$5_2 \rightarrow 5_1 - E$	24959.080(2)	L1	A1,A6,A12,A17,A20, A24
$6_2 \rightarrow 6_1 - E$	25018.123(2)	L1	A1, A2,A3,A17,A20 A4* ,A5,A6,A7,A8, A9 ,A12, A13 ,A17,A20,A24, A26* ,A36, A38* ,
$7_2 \rightarrow 7_1 - E$	25124.873(2)	L1	A1, A2, A3,A17,A20
$8_2 \rightarrow 8_1 - E$	25294.411(3)	L1	A1,A6,A17
$9_2 \rightarrow 9_1 - E$	25541.398(50)	L3	A12,A32
$12_2 \rightarrow 12_1 - E$	26847.237(50)	L3	A32
$14_2 \rightarrow 14_1 - E$	28169.47(50)	L3	A32
$15_2 \rightarrow 15_1 - E$	28905.812(50)	L3	A32
$16_2 \rightarrow 16_1 - E$	29636.940(50)	L3	A32
$4_{-1} \rightarrow 3_0 - E$	36169.262(50)	L3	A4 , A9 ,A10, A13 ,A19,A25, A26 ,A27,A33
$7_0 \rightarrow 6_1 - A^+$	44069.49(5)	L3	A4 , A9 , A10, A13 ,A21,A22, A26 ,A30,A34,A37
$5_{-1} \rightarrow 4_0 - E$	84521.21(5)	L3	<i>A14</i> , A26 , A41
$8_0 \rightarrow 7_1 - A^+$	95169.44(5)	L3	A11,A18,A23, A26 ,A29,A31
$6_{-1} \rightarrow 5_0 - E$	132890.79(5)	L3	A26 ,A35,A39
$9_0 \rightarrow 8_1 - A^+$	146618.82(5)	L3	A26

NOTES – References are in chronological order. Numbers in parentheses appended to laboratory references are uncertainties in the last significant digit(s). Laboratory references are: L1: 1974ApJ...191L..99G; L2: Breckenridge & Kukolich (1995); L3: Xu & Lovas (1997), retrieved from the Cologne Database for Molecular Spectroscopy (Müller et al. (2001); <http://www.ph1.uni-koeln.de/vorhersagen/>). Astronomical references presenting interferometric observations are given in *italics*, theoretical papers in **boldface**. Theoretical references discussing various of the $J_2 \rightarrow J_1 - E$ transitions are only listed for the $6_2 \rightarrow 6_1 E$ transition and are marked by an asterisk. Astronomical references are: A1: Barrett et al. (1971); A2: Chui et al. (1974); A3: Hills et al. (1975); **A4***: Pelling (1975); A5: Barrett et al. (1976) (*VLBI*); A6: Barrett et al. (1975); A7: Buxton et al. (1977); A8: Matsakis et al. (1980); **A9**: Sobolev & Strelnitskii (1983); A10: Morimoto et al. (1985); A11: Nakano & Yoshida (1986); A12: Menten et al. (1986); Zeng et al. (1987); A14: Batrla & Menten (1988); A17: Menten et al. (1988b,a); A18: Plambeck & Wright (1988); A19: Haschick & Baan (1989); A20: Menten & Batrla (1989); A21: Haschick et al. (1990); A22: Bachiller et al. (1990); A23: Plambeck & Menten (1990); A24: Johnston et al. (1992); A25: Kalenskii et al. (1992); **A26*** Cragg et al. (1992); A27: Haschick & Baan (1989); A28: Slysh et al. (1993); A29: Kalenskii et al. (1994); A30: Slysh et al. (1994); A31: Val'ts et al. (1995); A32: Wilson et al. (1996); A33: Liechti & Wilson (1996); A34: Mehringer & Menten (1997); A35: Slysh et al. (1997); A36: Johnston et al. (1997); A37: Kogan & Slysh (1998); **A38**: Sobolev et al. (1998); A39: Slysh et al. (1999); A40: Val'ts et al. (2000); A41: Kalenskii et al. (2001)

Table 2.1: Known interstellar class I methanol maser transitions. (2003 May).

Part II

Methanol in the early stages of star formation

Chapter 3

Modelling of high mass star forming regions

The content of this chapter is based on Leurini, S., Schilke, P., Wyrowski, F. and Menten, K. M. to be submitted to A&A

3.1 Selection of the sample

As discussed at the beginning of this thesis, the earliest stages of high-mass star formation are still poorly understood. One of the main open question is which densities and temperatures characterize the different evolutionary stages. In chapter 1, the tracing properties of CH_3OH have been discussed, reaching the conclusion that CH_3OH is indeed very useful as a prober of physical conditions in star forming regions in all mass regimes.

However, given the formation in cluster mode of high-mass stars and their average distance of a few kpc, in order to investigate this problem and to get around the confusion of the cluster, investigations at high resolution and high frequency are essential, to zoom in the innermost regions of high mass star forming cluster and to investigate the individual protostellar dust condensations in the continuum and the hot, dense gas within the evolving cores in molecular line emission. Studies of a few samples of HMPOs (Molinari et al. 1996, 1998, 2000; Sridharan et al. 2002; Beuther et al. 2002b,c,d) had been recently very successful in discovering objects in the, so far, earliest phases of massive star formation and are beginning to shed light on the details of star formation process; however not being homogeneous in distance, few sources of these databases are good candidates for high spatial resolution studies. Current interferometers are indeed limited in resolution to $\sim 0.5''$, that corresponds to 500 AU at a distance of 1kpc, which is about the size of massive protostellar disks one expects.

With these two problems in mind, investigating the physical conditions of high-mass star forming regions and defining a sample of sources well suited for interferometric follow-up observations, we have selected 13 sources from two databases of protostellar candidates, the infrared-dark clouds sources studied by Carey et al. (1998) and the HMPOs sources

from Sridharan et al. (2002). The infrared dark clouds have been chosen on the basis of the largest extinction. For the HMPOs sources from Sridharan et al. (2002), preliminary CH₃OH observations had already been performed by these authors: we therefore selected sources with strong CH₃OH emission. The final sample for our CH₃OH multi-frequency study is presented in Table 3.1. With few exceptions (G28.34+0.06 and G33.71–0.01, IRAS 23139+5939, IRAS 18310–0825 and IRAS 18182–1433), the sources are at less than 4 kpc and are therefore an interesting sample for follow-up interferometric observations.

source	R.A. [J2000]	Dec. [J2000]	R.A. offset [']	Dec. offset ['']	v_{lsr} [km/s]	d [kpc]
Infrared Dark Clouds						
G11.11–0.12 P1	18 10 28.40	–19 22 29.0	0	0	29	3.6 ^a
G19.30+0.07 P1	18 25 58.50	–12 03 59.0	0	0	26	2.2 ^a
G28.34+0.06 P1	18 42 50.70	–04 03 16.0	0	0	78	4.8 ^a
G33.71–0.01	18 52 59.10	+00 42 32.0	0	0	104	7.2 ^a
G79.34+0.3 P1	20 32 21.80	+40 20 00.8	0	0	0.1	1 ^a
High Mass (Proto)stellar Objects						
18089–1732	18 11 51.3	–17 31 29.0	3.2 ^b	0.1 ^b	34	3.6 ^c
18151–1208	18 17 57.1	–12 07 22.0	13.2 ^b	–4.9 ^b	33	3.0 ^d
18182–1433	18 21 07.9	–14 31 53.0	19.0 ^b	4.2 ^b	59	4.5 ^c
18264–1152	18 29 14.3	–11 50 26.0	5.1 ^b	3.7 ^b	44	3.5 ^c
18310–0825	18 33 47.2	–08 23 35.0	10.9 ^b	–10.6 ^b	84.4	4.9 ^c
19410+2336	19 43 11.4	+23 44 06.0	–6.8 ^b	4.0 ^b	22	2 ^c
20126+4104	20 14 26.0	+41 13 32.0	–1.5 ^b	2.0 ^b	–4	1.7 ^e
23139+5939	23 16 09.3	+59 55 23.0	–2.7 ^b	–10.1 ^b	–45	4.8 ^c

^a Carey et al. (1998)

^b Beuther et al. (2002b)

^c Bontemps, priv. comm.

^d Sridharan et al. (2002)

^e Wilking et al. (1989)

Table 3.1: The sample

3.2 Line selection

In § 1.1.4, we have analysed several CH₃OH transitions and determined their properties as tracers of physical conditions in the interstellar medium. Our main results are that transitions in the centimeter and millimeter spectrum are mainly density probes; however, when sub-millimeter lines are available, or when complete bands of lines with different energies and

excitation ranges are observed, information on kinetic temperature can be obtained. In chapter 1, only transitions where no maser action has been detected or predicted by excitation models have been studied. However, important informations on the physical conditions of a source can be derived also by observing masing transitions, as discussed in § 2.3. Moreover, in § 3.4 we will discuss how the torsionally excited lines are fundamental probes of kinetic temperature in sources where infrared radiation fields are not negligible.

Therefore, we performed observations towards the sources in our sample in the:

- $J_2 \rightarrow J_{-1}$ band at 25 GHz, which is sensitive to the spatial density;
- $J_0 \rightarrow J_{-1}$ band at 157 GHz;
- $2_k \rightarrow 1_k$ and the $5_k \rightarrow 4_k$ bands at 96.7 and 241.7 GHz, which are mainly tracers of densities higher than $\times 10^5 \text{ cm}^{-3}$ and have a weak dependence on temperatures up to 15 K;
- $7_k \rightarrow 6_k$ at 338 GHz, which is sensitive to both kinetic temperature and spatial density, with some examples of pure density tracers ($k = 0, \pm 1$);
- $2_k \rightarrow 1_k \text{ } v_t=1$ and the $5_k \rightarrow 4_k \text{ } v_t=1$ bands at 96.5 and 241.2 GHz, which are sensitive to the radiation field and therefore to the kinetic temperature;
- $2_k \rightarrow 1_k$, $J_0 \rightarrow J_{-1}$ and $J_3 \rightarrow J_2$ $^{13}\text{CH}_3\text{OH}$ series at 94.4 GHz, 156 GHz and 255 GHz, respectively, to have a reliable estimate of the optical depth.

3.3 Observations

3.3.1 Effelsberg 100 m

The $J_2 \rightarrow J_{-1} - E$ band at 25 GHz was observed during winter 2001 and autumn 2002 with the MPIfR 100 m telescope near Effelsberg, in frequency switching mode. Conversion factors from counts to antenna temperature are provided by the receiver group at different frequencies; corrections for elevation are taken into account using the gain elevation curve by Dr. Alex Kraus. The flux calibration was checked measuring W3(OH) and NGC7027.

3.3.2 IRAM 30 m

The IRAM 30 m telescope was used in summer 2002 and January 2003 to observe our sample at 96 GHz, 157 GHz and 241 GHz in the $2_k \rightarrow 1_k$, $J_0 \rightarrow J_{-1}$ and $5_k \rightarrow 4_k$ CH_3OH series; this setup allows also the simultaneous observation of the $2_{k,v_t=1} \rightarrow 1_{k,v_t=1}$ at 96.5 GHz. Nine-point maps with a spacing of $6''$ were performed toward each source to cover the 3 mm beam of the telescope with the 2 mm and 1 mm beams (at 96 GHz the resolution of the 30 m telescope is approximately $25''$, $15''$ at 157 GHz and $10''$ at 241.7 GHz). The observations

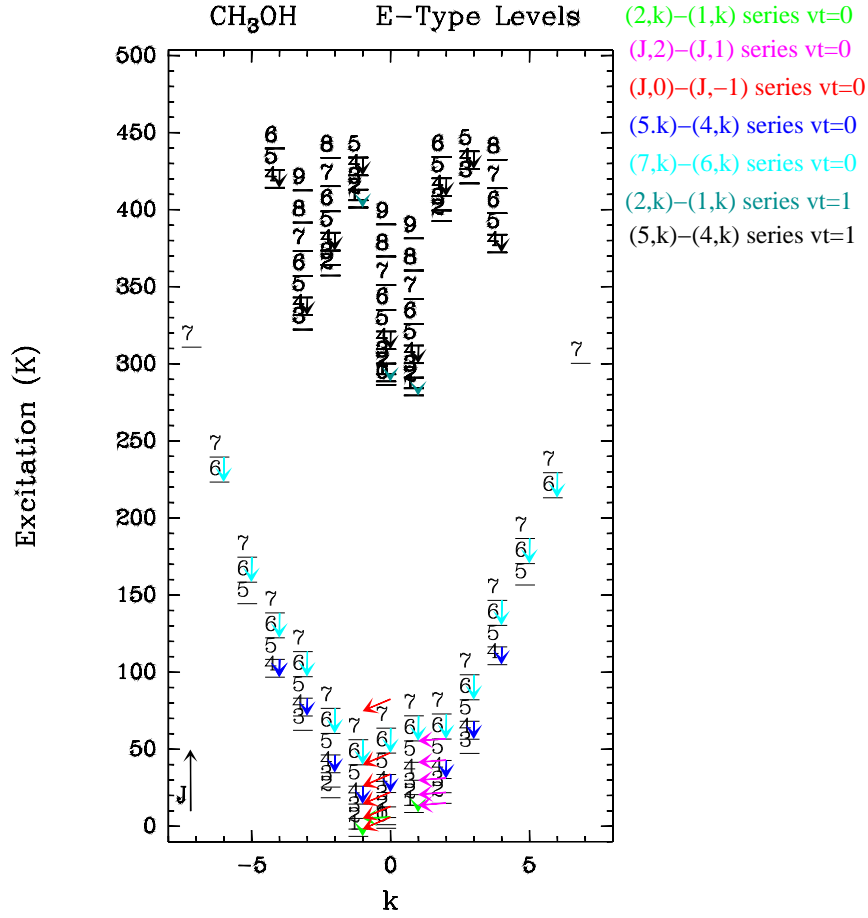


Figure 3.1: Partial energy level diagram for $\text{CH}_3\text{OH} -E$, with $v_t=0,1$ levels. Transitions observed during our observations are marked.

were done in the wobbler switching mode, with the wobbler switching in azimuth of $240''$ between the ON and OFF positions. To have a reliable estimate of the optical depth, the $J_3 \rightarrow J_2$ $^{13}\text{CH}_3\text{OH}$ series at 255 GHz has also been observed, simultaneously with the main isotopologue. For IRAS 18089–1732, additional data in the $5_k \rightarrow 4_k$ CH_3OH series in the first torsionally excited level have been taken with the same observing strategy as for the ground state lines, simultaneously with the $2_k \rightarrow 1_k$, $J_0 \rightarrow J_{-1}$ $^{13}\text{CH}_3\text{OH}$ series, at 94.4 GHz and 156 GHz, respectively.

3.3.3 Caltech Submillimeter Observatory (CSO)

In May 2004, the CSO 10.4 m telescope on Mauna Kea, Hawaii, was used to observe the $7_k \rightarrow 6_k$ CH_3OH series at 338 GHz. However, due to very poor weather conditions, only observations toward one of the sources, IRAS 18089–1732, were performed. Flux calibration is obtained by observing URANUS.

CH ₃ OH							
source	$J_2 - J_{-1}$	$2_k^1 - 1_k^1$	$2_k^0 - 1_k^0$	$J_0 - J_{-1}$	$5_k - 4_k$	$7_k - 6_k$	$5_k^1 - 4_k^1$
G11.11–0.12 P1		–	+	+	+		
G19.30+0.07 P1	+	–	+	+	+		
G28.34+0.06 P1	–	–	+	+	+		
G33.71–0.01	–	–	+	+	+		
G79.3+0.3 P1		–	+	+	+		
18089–1732	+	+	+	+	+	+	+
18151–1208	+	?	+	+	+		
18182–1433	+	–	+	+	+		
18264–1152	+	–	+	+	+		
18310–0825		–	+	+	+		
19410+2336		–	+	+	+		
20126+4104	–	–	+	+	+		
23139+5939	–	–	+	+	+		
¹³ CH ₃ OH							
source	$2_k - 1_k$	$J_0 - J_{-1}$	$J_3 - J_2$				
G11.11–0.12 P1			–				
G19.30+0.07 P1			–				
G28.34+0.06 P1			–				
G33.71–0.01			–				
G79.3+0.3 P1			–				
18089–1732	+	+	+				
18151–1208			–				
18182–1433			+				
18264–1152			+				
18310–0825			–				
19410+2336			–				
20126+4104			–				
23139+5939			–				

Table 3.2: Overview of the observations: + shows detections, – non-detections and ? tentative detections. Empty space indicates non-observations.

3.4 CH₃OH Analysis

Recently, Leurini et al. (2004) have investigated the diagnostic properties of CH₃OH over a range of physical parameters typical of high-mass star-forming regions, finding CH₃OH to be a good tracer of high-density environments and sensitive to the kinetic temperature. However, the level dataset is incomplete in energy above 100 K and does not ensure reliable results for sources with temperatures higher than 50 K. We here extend their calculations to a dataset better suited to the study of more evolved sources, as some HMPOs in our sample do show signs of hot core formation, indicated by the detection of typical hot core

molecules (CH_3OCH_3 and HCOOCH_3 , Leurini & Schilke 2005). Our new analysis includes all the levels up to $(J=14, k=13)$ in the torsional ground state and up to $(J,k)=9$ for the first torsionally excited state. The new level dataset is shown in Fig. 3.2 for energies up to 700 K.

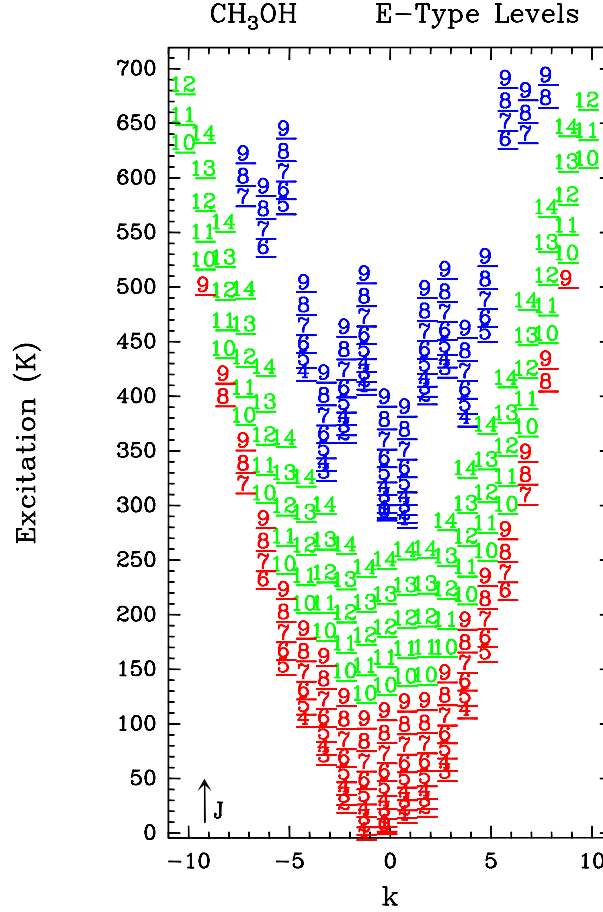


Figure 3.2: Energy levels for the E -symmetry state of CH_3OH with an excitation energy of less than 700 K: in red, levels for which CH_3OH -He collisional rates have been computed by (Pottage et al. 2002) for the $v_t=0$; in green, levels for which CH_3OH -He collisional rates have been extrapolated; in blue, $v_t=1$ levels for which collisional rates have been computed by Pottage et al. (2004b) at 20 K and which have been then extrapolated at higher temperatures.

Transitions within the $v_t=1$ state are included as well as transitions between the $v_t=1$ and the ground state. Collisional rates for $(J,k)>9$, $v_t=0$ have been extrapolated from the results of (Pottage et al. 2002), using the propensity rules derived from the $(J,k)\leq 9$ levels. Collisional coefficients for CH_3OH -A and -E species in $v_t=1$ with He have been recently computed by (Pottage et al. 2004b) at low temperature. They found the cross sections for the torsionally inelastic transitions ($\Delta v_t \pm 1$) to be typically two orders of magnitude smaller

than for torsionally elastic transitions ($\Delta v_t = 0$) and characterised by no propensities rules. We scaled their results for torsionally elastic collisions to higher temperatures by a factor $(T/T_0)^{1/2}$ (Flower, priv. comm.) and assumed the torsionally inelastic collisions to be two orders of magnitude smaller than rotationally inelastic transitions within $v_t=0$. The Large Velocity Gradient (LVG) method with spherical geometry, in the derivation of de Jong et al. (1975), has been used for solving the radiative transfer equations. An external radiation field, described by a diluted grey-body, equation 3.1, has been included in the model, since infrared pumping plays a major role in the excitation of the torsionally excited levels.

$$J_{ext} = w \times J(T_d)(1 - e^{-\tau_{dv}}) \quad (3.1)$$

with

$$\tau_{dv} = \tau_{d0} \times \left(\frac{\nu}{\nu_0} \right)^\beta \quad (3.2)$$

$J(T_d) = [\exp(h\nu/kT_d) - 1]^{-1}$ and w is a dilution factor. The optical depth of the dust, τ_d , is given by a power law of the frequency, (see equation 3.2); β is known to range between 1.75 and 2.5 between the Orion photo-dominated region and the ridge (Lis et al. 1998), while a mean value of 2 is found in massive star forming regions (Molinari et al. 2000). However, recently several authors (Natta et al. 2004; Beuther et al. 2004b; Natta et al. 2004) have reported β lower than the canonical value of 2 in HMPOs.

Since an external radiation field has been used only for the hottest, probably more evolved, sources of our sample, a fix value of 2 has been adopted for our model when no other informations from the literature were available. Following Krügel & Walmsley (1984), dust and gas are assumed to be coupled at high density, ($n > 10^5 \text{ cm}^{-3}$).

Even if several CH₃OH lines show sensitivity only to spatial density and others to temperature, with several cases of dependence on both, when zooming into the inner regions of a cloud, close to the central massive protostars, infrared radiation fields are not negligible and degeneracy between collisions and the IR radiation field in the pumping of the energy levels is a known phenomenon (for CS see Carroll & Goldsmith 1981; Hauschildt et al. 1993): IR vibrational pumping is shown to mimic the effect of excitation by collisions (see Fig. 3.3(a)). However, a promising way to break the degeneracy is by observation of vibrationally or torsionally excited lines, as, with very high critical densities (10^{10} - 10^{11} cm^{-3}) and high level energies ($T \geq 300 \text{ K}$ in the case of CH₃OH), they are hardly populated by collisions (Fig. 3.3(b)), but trace the IR field instead. Therefore, for the hotter sources of our samples, reliable determinations of density and kinetic temperature are possible only when observations of $v_t=1$ bands are available.

Another problem of degeneracy is found in the IR radiation field, when fitting the spectral energy distribution of the dust. Here the degeneracy happens between the dilution factor w , the dust temperature T_d , the spectral index β and the reference optical depth of the dust at $100\mu\text{m}$. Our data, the CH₃OH $v_t=1$ transitions, are sensitive only to the dust spectrum around

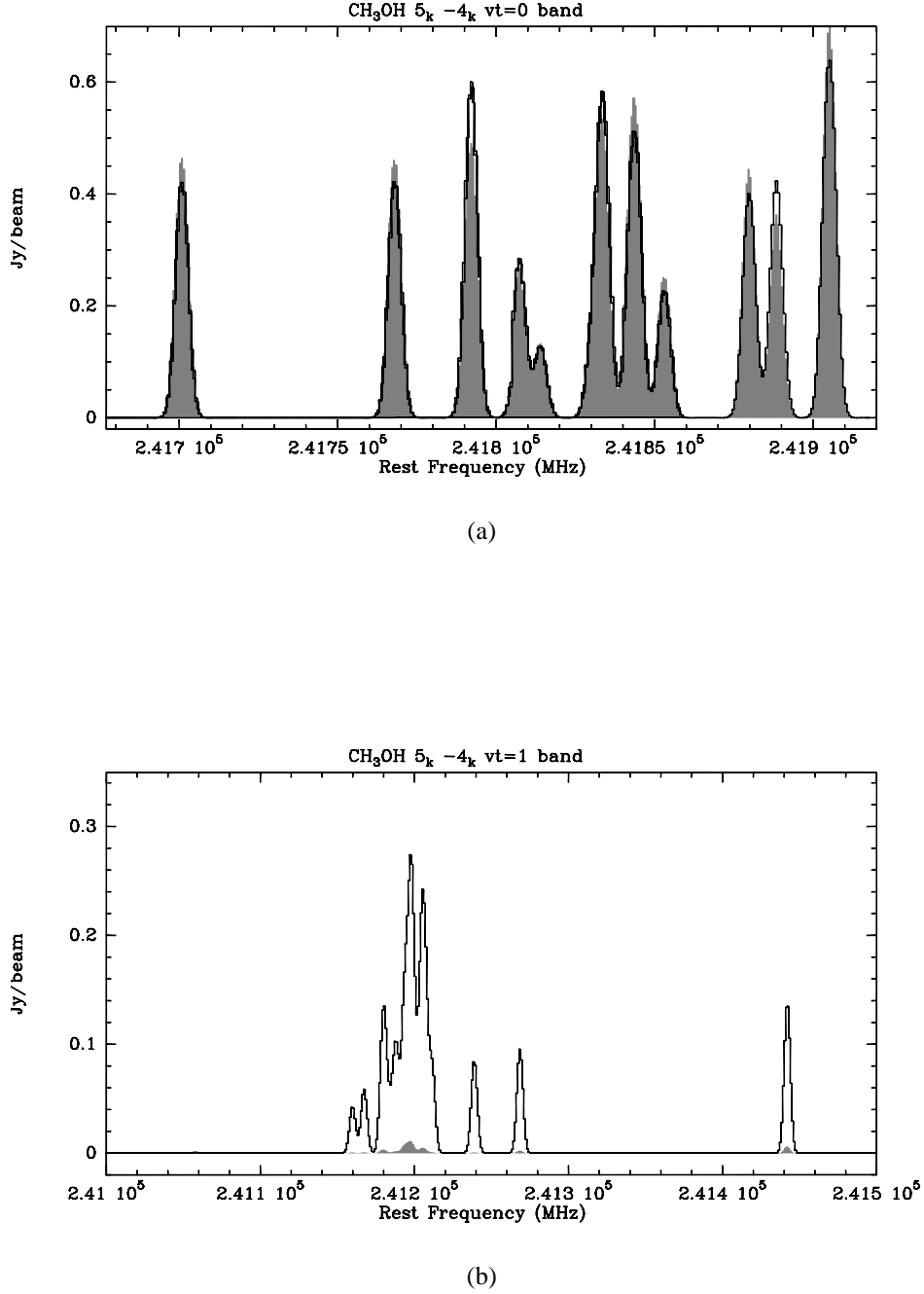


Figure 3.3: Fig. 3.3(a)- 3.3(b) illustrate how excitation by collisions mimics the effect of IR vibrational pumping in populating the $v_t=0$ CH₃OH levels. In grey scale synthetic spectra when pure collisional pumping ($n(\text{H}_2)=10^8 \text{ cm}^{-3}$, no radiation field) is populating the $v_t=0$ levels (a) and the $v_t=1$ levels (b); the black line shows the synthetic spectra for the same levels when only the IR radiation field is pumping the system, ($n(\text{H}_2)=10^3 \text{ cm}^{-3}$, radiation field given by a diluted grey-body, $wJ(T_d)(1 - \exp[\tau_{100\mu\text{m}}(v/v_{100\mu\text{m}})^\beta])$, $T_d=190 \text{ K}$, $w=1$, $\tau_{100\mu\text{m}}=1.5$, $\beta=1.8$). While the ground-state spectra are virtually indistinguishable, the $v_t=1$ spectra show how inefficiently the pure collisional pumping excites the torsionally excited levels.

40 μ m and, even though for some sources of the sample several observations throughout the millimeter/infrared spectrum are available, combining data with such different beam sizes is not easy. Solving the degeneracy between these factors is therefore impossible and changing these parameters in the model has the only physical meaning of changing the number of photons which excite the torsional levels.

The fitting procedure used to analyse the CH₃OH data is described in Leurini et al. (2004); free parameters are the kinetic temperature and the spatial density of the gas, the CH₃OH-*E* and -*A* column densities and source sizes. Source sizes from interferometric CH₃OH data are used when available, otherwise sizes from dust emission maps are taken as initial guesses. For sources for which we have ¹³CH₃OH data, these data have been included in the fit assuming a fixed abundance ratio between the isotopologues. For the warmest sources of the sample, lines are expected to be optically thick, at least in the less excited transitions. By fitting optically thick lines, the derived physical parameters are the ones where the gas becomes opaque, while optically thin lines will reflect the conditions in an inner region. Therefore, when ¹³CH₃OH and ¹²CH₃OH $v_t=1$ are observed, results from their fit are expected to be more relevant to the source interiors than what derived from the analysis of ¹²CH₃OH optically thick lines.

¹³CH₃OH level populations and its spectra are computed with the same technique described for ¹²CH₃OH; line strengths and rest frequencies are from the Cologne Database for Molecular Spectroscopy, (<http://www.cdms.de>, Müller et al. 2001), which includes new measurements by Xu & Lovas (1997). Collisional rates for ¹³CH₃OH are not available, therefore the coefficients for ¹²CH₃OH have been used for the calculations. Relative abundance of ¹²CH₃OH and ¹³CH₃OH has been estimated using the isotopic ratio ¹²C/¹³C listed by Wilson & Rood (1994) as function of the distance from the Galactic center and range from 89 in the Solar system to 20 in the Galactic center region.

3.5 Model Results

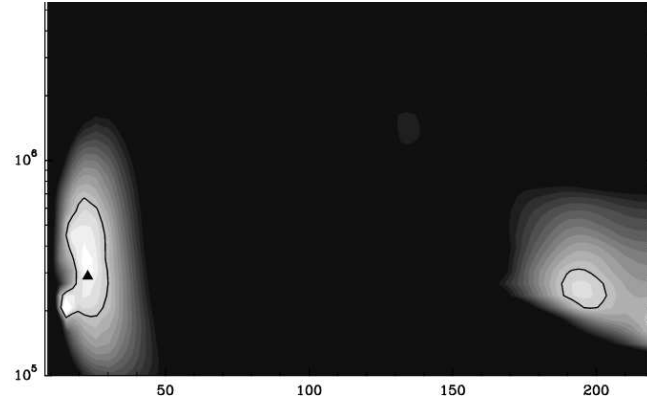
In the following sections our model results are discussed within the context of the known properties of each source. Using the Stefan-Boltzmann formula and a spherical geometry, best fit model results have been used to compute gas mass, H₂ column density, CH₃OH abundance and luminosity for each component along the line of sight for all the sources. In order to compare our results with literature, H₂ column density and CH₃OH abundance are given as sum over the components, weighted by the different beam filling factor. Estimation of luminosities and gas masses needs some knowledge on the morphology of the source; if the different components simply happen to be in the beam of the telescope but do not radiatively interact, then each component has its own luminosity and gas mass which do not depend on the others. On the other hand, if they interact radiatively, having for example a concentric structure, the masses of the outer components have to be corrected for the contribution from

the inner part. For the luminosity, this correction is even more complicated as the inner region heats the rest of the sources. Therefore luminosities, masses and methanol abundances derived from our CH₃OH analysis listed in Table 3.4 are given for each component without any corrections for the others.

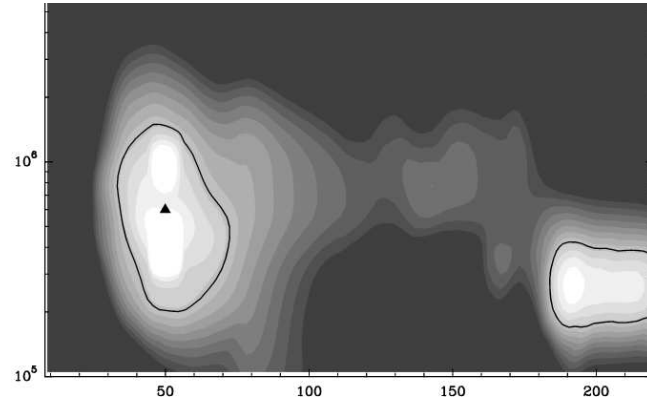
Table 3.3 lists the physical parameters obtained for each component in each source. At the end of this section, the methanol synthetic spectra obtained from our models are overlaid on the observations. Optical depths and brightness temperatures for each line in each component are also listed. In Table 3.5, the 1σ range for our estimates of T_K , $n(\text{H}_2)$, $N(\text{CH}_3\text{OH} - A)$ and $N(\text{CH}_3\text{OH} - E)$ are given. Ranges for H₂ mass and column density, luminosity and methanol abundance are derived from these values and listed in Table 3.5. Fig. 3.4 show the χ^2 distribution in the $[T_K, n(\text{H}_2)]$ plane for IRAS 18264, for each component. As discussed in chapter 1, sources in which only the less excited transitions are detected do not allow a good estimation of temperature, while the analysis on the CH₃OH spectra give reliable values of the spatial density. Fig. 3.4(a)- 3.4(b) show how the χ^2 distribution for the first two components fitted in IRAS 18264 has a strong dependency on the density, but at least two solutions, at different temperatures, can be found. Here, the second minima at 200 K can be excluded because the derived luminosities would be much higher than what observed ($L \sim 6 \times 10^7 L_\odot$). On the other hand, the χ^2 distribution of the third component has no dependence at all on the density, but only on the kinematic temperature.

	Δv (km s ⁻¹)	T_K (K)	$n(\text{H}_2)$ (cm ⁻³)	$N(\text{CH}_3\text{OH-A})$ (cm ⁻²)	$N(\text{CH}_3\text{OH-E})$ (cm ⁻²)	source size ('')	$\chi^2_{\nu_d}$
G11.11-0.12 P1							2.2
1 comp.	4.7	16.0	1.5×10^5	8.6×10^{14}	8.1×10^{14}	12.4	
2 comp.	1.7	40.0	3.0×10^5	6.0×10^{15}	6.0×10^{15}	3.0	
G19.30+0.07 P1							1.7
1 comp.	15.0	15.4	1×10^5	2.7×10^{15}	2.7×10^{15}	12.5	
2 comp.	3.5	59.3	2×10^5	8.6×10^{15}	7.5×10^{15}	6.0	
G28.34+0.06 P1							4.4
1 comp.	2	10	4×10^4	2.2×10^{14}	2.2×10^{14}	19	
2 comp.	9	37	3.5×10^4	1.5×10^{15}	1.5×10^{15}	13	
3 comp.	2.5	37	47.5×10^5	2.8×10^{15}	1.6×10^{15}	8	
G33.71-0.01							4.3
1 comp.	8.0	14.7	6.4×10^4	5.5×10^{14}	5.5×10^{14}	19	
2 comp.	2.8	31	6.7×10^5	8.9×10^{14}	7.7×10^{14}	11	
G79.34+0.3 P1							1.4
1 comp.	2.0	17.2	$2. \times 10^5$	7.8×10^{13}	7.6×10^{13}	32.0	
18089-1732							2.1
1 comp.	4.0	20.8	3.2×10^6	3.5×10^{15}	3.0×10^{15}	8.5	
2 comp.	3.1	60	9.0×10^7	4.0×10^{17}	4.0×10^{17}	1.7	
3 comp.	3.2	300	1.0×10^8	9.0×10^{17}	9.0×10^{17}	0.7	
18151-1208							1.7
1 comp.	3.1	29	5.7×10^5	1.9×10^{14}	1.9×10^{14}	20.0	
2 comp.	3.2	66	6.9×10^6	4.2×10^{15}	4.0×10^{14}	3.2	
18182-1433							1.7
1 comp.	9.0	19.1	3.8×10^5	3×10^{14}	$3. \times 10^{14}$	24	
2 comp.	2.8	32.1	1.7×10^6	8.4×10^{14}	8.4×10^{14}	13.4	
3 comp.	3.2	56.7	4×10^6	7.4×10^{16}	7.4×10^{16}	3.0	
18264-1152							3.8
1 comp.	7.5	22.8	2.9×10^5	1×10^{15}	8×10^{14}	17	
2 comp.	2.5	50	6×10^5	3.2×10^{15}	3.2×10^{15}	9	
3 comp.	3.6	90	2.5×10^6	1.3×10^{16}	1.3×10^{16}	4	
18310-0825							1.9
1 comp.	2.4	17	2×10^5	2.7×10^{14}	2.2×10^{14}	18.5	
19410+2336							3.7
1 comp.	3.0	18.6	1.7×10^5	4.6×10^{14}	4.0×10^{14}	20.0	
2 comp.	3.2	52.8	5.0×10^5	4.7×10^{15}	4.7×10^{15}	5.0	
20126+4104							1.4
1 comp.	4.4	36.4	1.7×10^6	2.5×10^{14}	2.4×10^{14}	15.0	
2 comp.	6.0	77.8	1.9×10^7	2.0×10^{17}	1.9×10^{17}	1.2	
23139+5939							2.4
1 comp.	10.0	17	2.1×10^5	3.7×10^{14}	2.7×10^{14}	19.5	
2 comp.	3.7	37	2.7×10^5	1.9×10^{15}	1.9×10^{15}	8	

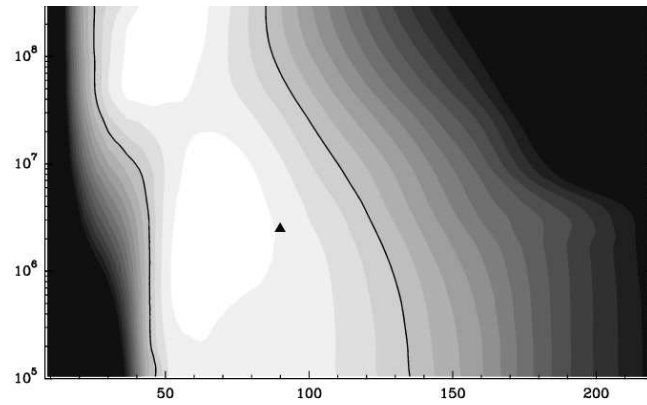
Table 3.3: CH₃OH model results.



(a)



(b)



(c)

Figure 3.4: In grey scale the χ^2 distribution in the $[T_K, n(\text{H}_2)]$ plane for the three components in IRAS 18264 (first component in **a**, second in **b**, third in **c**). The black contour show the 1σ confidence contours; a black triangle mark the best fit position.

source	L ($10^4 L_\odot$)	M (M_\odot)	N(H ₂) 10^{23} cm^{-2}	[CH ₃ OH]/[H ₂]
G11.11–0.12 P1				
1 comp.	0.1	39	1	2×10^{-8}
2 comp.	0.3	1	0.5	3×10^{-7}
G19.30+0.07 P1				
1 comp.	0.0	6	0.4	1×10^{-7}
2 comp.	2.2	1	0.4	4×10^{-7}
G28.34+0.06				
1 comp.	0.1	89	0.5	9×10^{-9}
2 comp.	7.7	26	0.3	9×10^{-8}
3 comp.	2.8	124	4	1×10^{-8}
G33.71–0.01				
1 comp.	0.9	480	1	8×10^{-9}
2 comp.	5.9	974	8	2×10^{-9}
G79.34+0.3 P1				
1 comp.	0.1	24	1	1×10^{-9}
18089–1732				
1 comp.	0.2	268	15	4×10^{-9}
2 comp.	0.5	60	82	1×10^{-7}
3 comp.	52.3	5	38	5×10^{-7}
18151–1208				
1 comp.	2.6	360	5	7×10^{-10}
2 comp.	1.8	18	10	8×10^{-9}
18182–1433				
1 comp.	1.6	1401	6	1×10^{-9}
2 comp.	3.9	1091	15	1×10^{-9}
3 comp.	1.9	29	8	2×10^{-7}
18264–1152				
1 comp.	1.0	179	3	7×10^{-9}
2 comp.	6.3	55	3	2×10^{-8}
3 comp.	13.1	20	5	5×10^{-8}
18310–0825				
1 comp.	0.7	417	3	2×10^{-9}
19410+2336				
1 comp.	0.2	32	1	9×10^{-9}
2 comp.	0.8	15	8	1×10^{-8}
20126+4104				
1 comp.	1.2	83	7	7×10^{-10}
2 comp.	0.2	1	6	6×10^{-7}
23139+5939				
1 comp.	0.8	504	3	2×10^{-9}
2 comp.	3.0	45	2	3×10^{-8}

Table 3.4: Luminosity, gas mass, H₂ column density and CH₃OH abundance derived from the analysis on the CH₃OH spectra.

source	T_K (K)	$n(\text{H}_2)$ (cm^{-3})	$N(\text{CH}_3\text{OH-A})$ (cm^{-2})	$N(\text{CH}_3\text{OH-E})$ (cm^{-2})	L ($10^4 L_\odot$)	M (M_\odot)	$N(\text{H}_2)$ 10^{23} cm^{-2}	$[\text{CH}_3\text{OH}]/[\text{H}_2]$
G11.11-0.12								
1 comp.	11-45	$2 \times 10^4 - 3 \times 10^5$	$4 \times 10^{14} - 1 \times 10^{15}$	$3 \times 10^{14} - 1 \times 10^{15}$	0.03-8	5-	0.1-78	$1 \times 10^{-8} - 5 \times 10^{-8}$
2 comp.	14-69	-	$9 \times 10^{13} - 1 \times 10^{17}$	$4 \times 10^{14} - 4 \times 10^{16}$	0.01-3	-	-	-
G19.30+0.07 P1								
1 comp.	10-36	$2 \times 10^4 - 2 \times 10^5$	$7 \times 10^{14} - 6 \times 10^{15}$	$7 \times 10^{14} - 4 \times 10^{15}$	0.01-1.3	1-12	0.1-0.8	$5 \times 10^{-8} - 3 \times 10^{-7}$
2 comp.	-	$2 \times 10^4 - 2 \times 10^6$	$3 \times 10^{15} - 3 \times 10^{16}$	$4 \times 10^{15} - 1 \times 10^{16}$	-	0.1-13	0.03-4	$1 \times 10^{-7} - 2 \times 10^{-6}$
G28.34+0.06								
1 comp.	11-40	$9 \times 10^3 - 1 \times 10^5$	$1 \times 10^{14} - 7 \times 10^{14}$	$1 \times 10^{14} - 7 \times 10^{14}$				
2 comp.	19-78	$1 \times 10^4 - 9 \times 10^4$	$1 \times 10^{15} - 3 \times 10^{15}$	$1 \times 10^{15} - 4 \times 10^{15}$	0.5 - 151	7.4-67	0.1-0.9	$8 \times 10^{-9} - 2 \times 10^{-7}$
3 comp.	21-45	$2 \times 10^5 - 3 \times 10^6$	$1 \times 10^{15} - 5 \times 10^{15}$	$9 \times 10^{14} - 3 \times 10^{15}$	0.3-6	17-500	0.6-17	$5 \times 10^{-9} - 3 \times 10^{-8}$
G33.71-0.01								
1 comp.	11-70	$1 \times 10^4 - 1 \times 10^5$	$5 \times 10^{14} - 1 \times 10^{15}$	$2 \times 10^{14} - 8 \times 10^{14}$	0.3-460	150-750	0.4-2	$4 \times 10^{-9} - 9 \times 10^{-8}$
2 comp.	6-63	$2 \times 10^5 - 2 \times 10^6$	$5 \times 10^{14} - 1 \times 10^{15}$	$5 \times 10^{14} - 1 \times 10^{15}$	0.01-100	291-2900	2.4-23	$5 \times 10^{-10} - 8 \times 10^{-9}$
G79.34+0.3 P1								
1 comp.	12-30	$6 \times 10^4 - 4 \times 10^5$	$4 \times 10^{13} - 9 \times 10^{13}$	$4 \times 10^{13} - 9 \times 10^{13}$	0.02-0.8	6-38	1-2	$9 \times 10^{-10} - 3 \times 10^{-9}$
18089-1732								
1 comp.	10-30	$5 \times 10^5 - 6 \times 10^6$	$1 \times 10^{15} - 6 \times 10^{15}$	$1 \times 10^{15} - 5 \times 10^{15}$	0.01-0.8	42-503	2-	$1 \times 10^{-9} - 9 \times 10^{-9}$
2 comp.	-	$1 \times 10^6 - 1 \times 10^8$	$7 \times 10^{16} - 8 \times 10^{17}$	$7 \times 10^{16} - 8 \times 10^{17}$	-	0.7-67	0.9-91	$1 \times 10^{-7} - 2 \times 10^{-6}$
3 comp.	150-320	-	$4 \times 10^{17} - 1 \times 10^{18}$	$4 \times 10^{17} - 1 \times 10^{18}$	3-68	-	-	-
18151-1208								
1 comp.	17-47	$2 \times 10^5 - 2 \times 10^6$	$1 \times 10^{14} - 4 \times 10^{14}$	$1 \times 10^{14} - 3 \times 10^{14}$	0.3-18	127-1260	2-18	$1 \times 10^{-10} - 1 \times 10^{-9}$
2 comp.	27-180	-	$1 \times 10^{13} - 7 \times 10^{15}$	$2 \times 10^{15} - 8 \times 10^{15}$	0-100	-	-	$2 \times 10^{-9} - 1 \times 10^{-8}$
18182-1433								
1 comp.	8-30	$1 \times 10^5 - 1 \times 10^6$	$1 \times 10^{14} - 6 \times 10^{14}$	$1 \times 10^{14} - 5 \times 10^{14}$	0.02-3	64-642	0.9-9	$1 \times 10^{-8} - 2 \times 10^{-9}$
2 comp.	8-40	$9 \times 10^4 - 2 \times 10^6$	$1 \times 10^{14} - 9 \times 10^{14}$	$1 \times 10^{14} - 9 \times 10^{14}$	0.05-30	332-7300	1.5-32	$5 \times 10^{-10} - 3 \times 10^{-9}$
3 comp.	32-71	$5 \times 10^4 - 1 \times 10^8$	$7 \times 10^{15} - 8 \times 10^{17}$	$3 \times 10^{16} - 3 \times 10^{17}$	0.2-5	0.4-720	0.1-201	$4 \times 10^{-6} - 5 \times 10^{-8}$
18264-1152								
1 comp.	4-31	$2 \times 10^5 - 7 \times 10^5$	$6 \times 10^{14} - 2 \times 10^{15}$	$6 \times 10^{14} - 1 \times 10^{15}$	0-3	123-432	2-6	$5 \times 10^{-9} - 1 \times 10^{-8}$
2 comp.	34-65	$2 \times 10^5 - 1 \times 10^6$	$2 \times 10^{15} - 7 \times 10^{15}$	$2 \times 10^{15} - 4 \times 10^{15}$	1-18	18-92	1-5	$1 \times 10^{-8} - 4 \times 10^{-8}$
3 comp.	30-122	-	$2 \times 10^{15} - 3 \times 10^{16}$	$8 \times 10^{15} - 2 \times 10^{16}$	0.2-44	-	-	$2 \times 10^{-8} - 1 \times 10^{-7}$
18310-0825								
1 comp.	12-27	$7 \times 10^4 - 4 \times 10^5$	$1 \times 10^{14} - 4 \times 10^{14}$	$1 \times 10^{14} - 3 \times 10^{14}$	0.2-4	153-870	0.9-5	$1 \times 10^{-9} - 7 \times 10^{-9}$
19410+2336								
1 comp.								
2 comp.	27-87	$3 \times 10^5 - 3 \times 10^8$	$2 \times 10^{15} - 9 \times 10^{15}$	$3 \times 10^{15} - 6 \times 10^{15}$	0.1-6	1-878	0.4-448	$1 \times 10^{-10} - 3 \times 10^{-7}$
20126+4104								
1 comp.	20-	$2 \times 10^5 - 1 \times 10^7$	$1 \times 10^{13} - 1 \times 10^{15}$	$9 \times 10^{13} - 4 \times 10^{14}$	0.1-	10-	0.9-	1×10^{-8}
2 comp.	45-	-	$4 \times 10^{16} - 4 \times 10^{18}$	$4 \times 10^{16} - 4 \times 10^{18}$	0.02-	-	-	-
23139+5939								
1 comp.	-52	$3 \times 10^4 - 1 \times 10^6$	$2 \times 10^{14} - 5 \times 10^{14}$	$1 \times 10^{14} - 5 \times 10^{14}$	-65	72-2400	0.4-14	$7 \times 10^{-10} - 7 \times 10^{-9}$
2 comp.	18-45	$1 \times 10^5 - 6 \times 10^6$	$9 \times 10^{14} - 3 \times 10^{15}$	$1 \times 10^{15} - 4 \times 10^{15}$	0.2-6	17-995	0.6-34	$2 \times 10^{-9} - 1 \times 10^{-7}$

Table 3.5: CH₃OH model results: 1 σ range.

3.5.1 Infrared Dark Clouds

Infrared Dark Clouds (IRDCs) are a population of several thousand molecular clouds which have been identified by their mid-infrared extinction in MSX (Midcourse Space Experiment) images by Egan et al. (1998). They concluded that IRDCs have a visual extinction in excess of 170 mag and contain large column density of cold dust. Millimeter/submillimeter line observations reveal typical temperatures of $T \leq 20$ K and densities $n(\text{H}_2) \geq 10^5 \text{ cm}^{-3}$ (Carey et al. 2000). Submillimeter continuum observations suggest that high-mass star formation may be occurring in IRDCs Carey et al. (2000). Moreover, the sources exhibit non-Gaussian line profiles in several molecular species (H_2CO , see Carey et al. 1998; HCO^+ , see Redman et al. 2003), which could be explained by infall (Redman et al. 2003) or outflow events. Recent SiO observations (Feldman et al. 2004) reveal the first bipolar outflow detected in IRDCs, thus suggesting that the non-Gaussian wings found in other molecules in several IRDCs are also due to outflows.

G11.11–0.12 P1

G11.11–0.12 is a filamentary cloud, as revealed by the $8\mu\text{m}$ MSX extinction map by Carey et al. (1998); continuum observations at $850\mu\text{m}$ (Carey et al. 2000) and in molecular tracers such as H_2CO (Carey et al. 1998) and NH_3 (Pillai et al. 2005) show very similar morphologies. From the analysis of the continuum, Carey et al. (2000) derive a dust temperature ranging between 25 and 43 K, depending on the spectral index used for modelling the dust emissivity, and a total mass between 67 and $150 M_\odot$ (Carey et al. 2000). A gradient from the outer to the inner core is seen in the kinetic temperature traced by the NH_3 (1,1) and (2,2) lines, whose peaked value is 13.7 K (Pillai et al. 2005). However, detection of the NH_3 (3,3) transition suggests a higher temperature, (Pillai, priv. comm.).

Recently, Pillai et al. (2004) have reported the discovery of maser action in the $2_0 \rightarrow 3_{-1}$ $\text{CH}_3\text{OH} -E$ transition at 6.7 GHz towards the region, a pretty unexpected result for such a cold cloud, as class II CH_3OH masers are usually found in dense ($n \sim 10^7 \text{ cm}^{-3}$), hot ($T \sim 150$ K) active high mass star forming regions. The maser emission coincides with the SCUBA dust continuum peak; however, given the low resolution of SCUBA ($14''$ at $850 \mu\text{m}$), high resolution studies of the continuum are essential to confirm this, otherwise, first unequivocal detection of high-mass star formation in IRDCs.

Our CH_3OH observations show non-Gaussian profiles in the $2_k \rightarrow 1_k$ and $5_k \rightarrow 4_k$ $k = 0, -1$ lines. A two components model has been used to fit the data, with one component to fit the wings and one for the core emission. Initial values for the source size come from our nine point maps. Results are listed in table 3.3; the synthetic spectra overlaid on the data are shown in Figures 3.7(a)-3.7(c).

The first component, $12''$ in size, responsible for the broad line width, traces average infrared dark cloud parameter, while the second one, of $3''$ size, is warmer ($T_{\text{kin}} = 40$ K) and in agreement with the results found in NH_3 . However the physical conditions we find for this

second component are well below typical class II CH₃OH maser conditions. This could be explained by pointing errors in our observations.

The gas mass derived by our results is 23 M_⊙ and the total H₂ column density 6.2×10^{22} cm⁻². The values given are averaged over the 1 mm beam. The reduced χ^2 is 2.2.

G19.30+0.07 P1

G19.30+0.07 P1 belongs to the infrared dark cloud G19.30+0.07, which, seen in absorption by MSX at 8 μ m by Carey et al. (1998), splits into two cores in emission at 850 μ m with SCUBA (Carey et al. 2000). The analysis of the continuum leads to dust temperatures between 14 and 25 K and masses in the range 33-93 M_⊙; estimations of gas temperatures and density have been done by Pillai et al. (2005) on NH₃ data and by Leurini et al. (2004) based on CH₃OH. The former found a kinetic temperature of ~ 17 K, which is probably a lower limit as only the (1,1) and (2,2) lines have been analysed; the analysis of the CH₃OH data led to higher temperatures, ~ 24 K in what seems to be an outflow and ~ 44 in the inner core, and typical IRDC spatial densities ($n \sim 10^5 - 10^6$ cm⁻³). However an erroneous calibration of the 1.3 mm and 2 mm data has caused wrong results in the fit. Our new analysis on the re-calibrated data is performed with two components, one to fit the non Gaussian wings, the other for the main emission. In chapter 1, the red wings in the $5_k \rightarrow 4_k$ had not been fitted, as these profiles could be caused by emission in HNC(11-10). However, similar non Gaussian profiles are found in all the $k = 0, k = -1$ lines, at 3 mm and 2 mm; we therefore believe it is more reasonable to assume that the 1 mm profiles too are due to a broader component, 15 km/s, shifted in velocity, -2.5 km/s, respect to the main emission. A maser component is detected in the $6_2 \rightarrow 6_1 - E$ transition at 25.018 GHz, shifted by 3.3 km s⁻¹ from the parent cloud velocity; since this component is not detected in any other transition, it is not included in the model.

The spectra are well reproduced by the fit; however, the agreement between the model and the data, given by the reduced χ^2 , is not extremely good, with a value of 3.3. This is partly due to the quartet of lines at 3 mm, for which our model overestimates the intensities in the broad line component, and to the $J_0 \rightarrow J_{-1}$ lines. As already noticed in § 1.2, these transitions can be class II masers, therefore pumped by infrared radiation. A first problem in fitting this band is that, the IRDCs being cold, no external radiation field has been used in the model and therefore the excitation of these lines can not be well reproduced. However, another problem comes from the line widths in the J=1,2,3, which are narrower than what modeled. Since they have excitation conditions similar to the $2_k \rightarrow 1_k$ $k = 0, \pm 1$ and $5_k \rightarrow 4_k$ $k = 0, \pm 1$, we assume that the difference in the observed widths of these lines are not real, but due to bad signal to noise.

Results are listed in Table 3.3 and the spectra are shown in Figures 3.9(a)-3.9(c). The first component has typical physical conditions for IRDCs, while the kinetic temperature derived for the second one is higher than expected for this populations of sources. Methanol abundance relative to H₂ is in both cases higher than the typical dark cloud values, 10^{-9} . The H₂

column density derived from our analysis is $3.4 \times 10^{22} \text{ cm}^{-2}$ and the gas mass $3.9 M_{\odot}$.

G28.34+0.06 P1

G28.34+0.06 P1 belongs to the IRDC G28.34+0.06; observations at $850\mu\text{m}$ with SCUBA (Carey et al. 2000) reveal three subcores in emission, the strongest of which, P2, is associated with the IRAS source 18402–0403. P1 has a kinetic temperature of $\sim 16 \text{ K}$ as derived from the NH_3 (1,1) and (2,2) inversion lines (Pillai et al. 2005); the continuum data lead to a dust temperature between 12 and 18 K, depending on the spectral index used for modelling the dust emissivity, and a total mass between 120 and $400 M_{\odot}$ (Carey et al. 2000).

Methanol emission is strong in all the millimeter bands observed, but highly excited lines are not detected. Non-Gaussian wings are detected in the $5_{-1} \rightarrow 4_{-1} - E$ and $5_0 \rightarrow 4_0 - A$ at 1 mm. We therefore model the source with three components. The first, cold, extended and not very dense, is mainly responsible for the Gaussian emission at 3 mm; the second one reproduces the emission in the wings, the third the bulk emission. Source sizes are estimated from our nine points map.

Results are listed in Table 3.3 and the spectra are shown in Figures 3.10(a)-3.10(c). The $\chi^2_{\nu_d}$ is 4.4. Total gas mass is $131 M_{\odot}$ and H_2 column density $2 \times 10^{23} \text{ cm}^{-2}$.

G33.71–0.01

G33.71–0.01 is an infrared dark cloud detected by the MSX satellite at $8\mu\text{m}$. The source has been mapped in NH_3 (1,1) and (2,2) by Pillai et al. (2005); they derive a kinetic temperature of $\sim 21 \text{ K}$.

The methanol spectrum towards the source is characterised by weak non-Gaussian wings at 3 mm and 1 mm, in the $k=0,-1$ lines. No highly excited lines are detected in any band. The modelling of the source has been therefore performed with two components, one to model the wings and the other for the bulk emission.

Results are listed in Table 3.3 and the spectra are shown in Figures 3.11(a)-3.11(c). The reduced χ^2 is high, 4.3, and mainly due to a failure in reproducing the wing emission both at 3 mm, where they are overestimated, and at 1 mm, where on the other hand they are underestimated. However, physical parameters are typical of infrared dark clouds. The total gas mass is $883 M_{\odot}$ and the H_2 column density is $5 \times 10^{23} \text{ cm}^{-2}$.

G79.3+0.3 P1

G79.3+0.3 P1 belongs to the larger infrared dark cloud G79.34+0.33, at a distance of $\sim 1 \text{ kpc}$; the region shows several indications of star formation activity, with the HII region DR 15 lying behind it and with spots of warm dust emission between the different sub-cores, which are suggestive of deeply embedded hot stars. P1 is the most prominent condensation of the region; Gemini mid-infrared observations by Redman et al. (2003) reveal three YSOs within the cloud and BIMA 3 mm data suggest the brightest of these to be a Herbig A/Be

star. Interaction with the IRDC is expected and probably responsible for blue wings seen in HCO^+ (3-2). BIMA observations at 96 GHz (Wyrowski 2005) show that CH_3OH does not peak at the continuum position determined by the SCUBA data (Carey et al. 2000), but it is off by $\sim -23''$ in declination. Unfortunately this information was not available at the time the observations were performed and our data were taken towards the SCUBA peak position. The source does show a simple CH_3OH spectrum, with detection only in the less excited lines. Line profiles are Gaussian. A single component model has been used for the source. Results are listed in Table 3.3 and the spectra are shown in Figures 3.12(a)-3.12(c). Physical parameters are typical of infrared dark clouds. The $\chi^2_{\nu_d}$ is 1.4. Total gas mass is $22 M_\odot$ and H_2 column density $1 \times 10^{23} \text{ cm}^{-2}$.

3.5.2 High Mass Protostellar Objects

A sample of 69 HMPOs has been studied in detail over recent years by Sridharan et al. (2002) and Beuther et al. (2002b,c,d), in the continuum and in the several molecular tracers. The sources, selected, among other criteria, to be bright in the infrared and not associated to any evolved region, have:

- no cm free-free emission down to 1 mJy, with VLA, which suggests they are in the earliest evolutionary phases;
- bolometric luminosities between $10^{3.5}$ and $10^{5.6} L_\odot$;
- average kinetic temperature of 20 K, as derived from NH_3 (1,1) and (2,2);
- average spatial density of 10^6 cm^{-3} .

Some of the HMPOs in our sample have been mapped with BIMA by Wyrowski et al. (2005). For these sources, from the 3 mm continuum fluxes and the source sizes they observed, we derived gas masses and column densities assuming that the mm continuum emission is mainly due to optically thin dust (Hildebrand 1983):

$$M_{H_2} = \frac{1.3 \times 10^{-3}}{J_\nu(T_d)} \frac{a}{0.1 \mu_m} \frac{\rho}{3 \text{ g cm}^{-3}} \frac{R}{100} \frac{F_\nu}{Jy} \times \left(\frac{D}{kpc} \right)^2 \left(\frac{\nu}{2.4 \text{ THz}} \right)^{-3-\beta} [\text{M}_\odot] \quad (3.3)$$

$$N_{H_2} = \frac{7.8 \times 10^{10}}{J_\nu(T_d) \Omega} \frac{a}{0.1 \mu_m} \frac{\rho}{3 \text{ g cm}^{-3}} \frac{R}{100} \frac{F_\nu}{Jy} \times \left(\frac{\nu}{2.4 \text{ THz}} \right)^{-3-\beta} [\text{cm}^{-2}] \quad (3.4)$$

where $J_\nu(T_d) = [\exp(h_\nu/kT_d)]$, T_d the temperature of the cold dust component, Ω the beam solid angle, a the grain size, ρ the grain mass density, R the gas to dust ration and β the grain

emissivity index. Following Beuther et al. (2002b), we used for T_d the values they list and $0.1 \mu m$, 3 g cm^{-3} , 100 and 2 for a , ρ , R and β respectively. Results are listed in table 3.6. They will be used for comparison with our results in the following discussion. For the sources for which these data are not available, the results from Beuther et al. (2002b), based on 1 mm bolometer observations, will be used.

Source	maj. \times min. (")	M_{H_2} (M_\odot)	N_{H_2} (10^{25} cm^{-2})
IRAS 18089–1732	6.7 \times 4.3	2980	2.6
IRAS 18151–1208	15.8 \times 13.0	1382	0.2
IRAS 18182–1433	5.7 \times 4.0	1864	1.3
IRAS 18264–1152	8.4 \times 3.0	2094	2.0

Table 3.6: Gas masses of the HMPOs in our sample, from 3 mm BIMA data.

IRAS 18089–1732

IRAS 18089–1732, located at a distance of 3.6 kpc, has been extensively studied in the last few years at millimeter and submillimeter wavelengths. With a bolometric luminosity of $10^{4.5} L_\odot$ and a massive core, $M > 2000 M_\odot$ (Sridharan et al. 2002), IRAS 18089 shows several probes of intense high mass star formation activity, with H_2O and CH_3OH maser emission and outflows detected in different molecular tracers (Beuther et al. 2004c). A recent line survey at 217 GHz and 344 GHz with the Submillimeter Array (SMA) (Beuther et al. 2004c) shows an outgoing hot core formation in the source, with the detection of complex molecules like CH_3OCH_3 and $HCOOCH_3$. CH_3CN is detected with BIMA (Beuther et al. 2002b). A velocity gradient across the core is found in the $HCOOCH_3$ data, that Beuther et al. (2004a) interpret as originating from a rotating disk.

The results from our CH_3OH analysis are shown in Table 3.3; the best fit, overlaid on the data, is shown in Fig. 3.13(a)- 3.16(c). Parameters for the external radiation field are taken from Wyrowski et al. (2005, in prep.), who extended the analysis on the radial distribution of the continuum at 1.2 mm by Beuther et al. (2002b) to BIMA data at 3 mm and found the best fit to the data corresponding to a dust opacity index of 1.75 and $\tau_{100\mu m} = 1$. Our CH_3OH analysis is done using three components along the line of sight, as the detection of several high excited lines in our data, and in data by other authors (Beuther et al. 2004c, 2002b), suggest hot core formation going on. Limits on the size of this component come from its luminosity and from CH_3CN data (Wyrowski et al. 2005, in prep.). A second, slightly bigger, component is mainly responsible for the emission in the 25 GHz lines and in $^{13}CH_3OH$. Finally, a third, more extended region is seen in emission in CH_3OH by Wyrowski et al. (2005, in prep.) at 107 GHz and by Beuther et al. (2004c) at 217 GHz. The source size derived by these authors is used as input value for the third extended component used in our model.

In § 3.4, we discussed how optically thick lines can play a role in the reliability of the physical parameters derived from a fit and how the more excited lines and the $^{13}\text{CH}_3\text{OH}$ lines can be used as a better probe in hot, complex sources. IRAS 18089 is an example of such a complex source, in which several $v_t=0$ lines of the main isotopologue are optically thick. When all lines are fitted simultaneously and using the same weight, the solution the program finds is not adequate for the $v_t=1$ and the $^{13}\text{CH}_3\text{OH}$ lines. Moreover, the $v_t=1$ are not affected by the degeneration in the pumping mechanism between collisions and the IR radiation field, as discussed in § 3.4, and trace the kinetic temperature. Limits on the density come from the $J_2 \rightarrow J_{-1} - E$ band, where we clearly do not detect any strong maser action: high densities are required to have quenching of these lines. Therefore, when modelling IRAS 18089, we have used a weighted fitting procedure with more weight given to the CH_3OH torsionally excited lines, to the $J_2 \rightarrow J_{-1} - E$ band and to $^{13}\text{CH}_3\text{OH}$, even if, since they do not have a not very good signal to noise, this leads to a reduced chi square of 2.1. Absolute calibration uncertainties and the uncertainty in the $^{12}\text{C}/^{13}\text{C}$ value can play a role in the goodness of the fit and deriving the true value of this ratio from our data is not straightforward given all the free parameters in our model.

Table 3.4 lists luminosities, gas masses, H_2 column densities and methanol abundances for each component used in the model, as derived from our results. The luminosity of the source is dominated by the the third component and it is in agreement with its IRAS luminosity. Moreover, the methanol abundance of this component is typical of hot cores. Adding masses and column densities from all the three components and convolving them to the $10''$ beam of the IRAM 30 m telescope at 1 mm, the total mass of the source is $M_2=109 M_\odot$ and its H_2 column density $N_2=8.2 \times 10^{23} \text{ cm}^{-2}$, values that are in good agreement with those found in the continuum observations by Wyrowski et al. (2005).

IRAS 18151–1208

IRAS 18151–1208 ($d \sim 3 \text{ kpc}$, $L \sim 10^{4.3} L_\odot$) belongs to the sample of HMPOs studied by Sridharan et al. (2002) and Beuther et al. (2002b,c,d). Its dust continuum map at 1.3 mm reveals three massive cores, with masses ranging from $\sim 60 M_\odot$ to $\sim 1100 M_\odot$. CH_3OH maser emission is associated with core 1, which is the sub-source we refer to in our analysis. At least two separated outflows are seen in CO and H_2 (Davis et al. 2004), with a high degree of collimation. Its radial distribution of the continuum is fitted by Wyrowski et al. (2005) with $\tau_{100\mu\text{m}} = 0.6$, $\beta=1.5$.

The CH_3OH spectrum toward the source is rather simple, with no highly excited lines indicating a hot component. However, the $k = \pm 2, \pm 3$ lines in the $5_k \rightarrow 4_k$ band, with a lower level energy in the $\sim 60 - 70 \text{ K}$ range, are detected. These lines can be well fitted by a single component model only at densities higher than the limits given by the H_2 column densities derived by Beuther et al. (2002b). Therefore a model with two components along the line of sight is used for our analysis.

The $2_0 \rightarrow 1_0 - A$ line shows a non-Gaussian profile with blueshifted wing. A similar pro-

file is also detected at 1.3 mm, in the $5_{-1} \rightarrow 4_{-1} - E$ line; however, given the fact that no deviations from a Gaussian line profile are seen in the $5_0 \rightarrow 4_0 - A$, which have the same excitation conditions as the $k = -1 - E$ transition, and that overlap with the HNCO (11-10) series ($E_{low} \sim 58$ K) could lead to the same profile, no outflow component is used in the model.

The results from our CH₃OH analysis are shown in Table 3.3; the best fit, overlaid on the data, is shown in Fig. 3.17(a)- 3.17(c). Luminosities and masses for each component are listed in Table 3.4; methanol abundances (see Table 3.4) are pretty low, almost typical of dark clouds. Total mass and H₂ column density are $104 M_{\odot}$ and $3.3 \times 10^{23} \text{ cm}^{-2}$.

IRAS 18182–1433

IRAS 18182–1433 ($d \sim 4.5$ kpc, $L \sim 10^{4.3} L_{\odot}$) belongs to the sample of HMPOs studied over the last years by Sridharan et al. (2002) and Beuther et al. (2002b,c,d); its bolometric luminosity and its mass, $M \sim 3000 M_{\odot}$, together with the detection of complex molecules like CH₃CN, CH₃OCH₃ (Leurini & Schilke 2005, in prep.), suggest that the source shows early stages of a massive hot core. Wyrowski et al. (2005, in prep.) modelled the continuum combining information at different frequencies and found that a dust opacity index of 1.8 and $\tau_{100\mu\text{m}} = 3.4$ fit the data well.

The CH₃OH spectrum shows Gaussian-like profiles with red and blueshifted wings in the $k=-1,0$ lines, probably associated with the outflow detected in CO by Beuther et al. (2002c), as CH₃OH has been observed in outflows in low mass star forming regions (Bachiller et al. 1995, 1998) and in HMPOs (Beuther et al. 2002b); emission from highly excited lines ($5_4 \rightarrow 4_4 - A, E$ with energies of the lower levels of ~ 100 K) is also detected, but no torsionally excited lines are found. Therefore, three components have been used to model the source: one for the outflow, one for the main core and one for the hotter emission.

The results from our CH₃OH analysis are shown in Table 3.3; the best fit, overlaid on the data, is shown in Fig. 3.18(a)- 3.20(b). The agreement between the data and the fit is very good ($\chi_{\nu_d}=1.7$) in the millimeter ¹²CH₃OH lines; however deviation from the observations are seen in the centimeter band and in the ¹³CH₃OH lines.

The predictions from our model for the $J_2 \rightarrow J_1 - E$ transitions at 25 GHz are reasonably close to our data, given that the lines are class II masers. Geometrical symmetries play a role in the amplification mechanism of maser lines and fitting them is therefore more problematic than in the case of (sub)-thermal transitions.

For the ¹³CH₃OH two considerations have to be made:

- an erroneous value for the isotopic ratio ¹²C/¹³C could lead to underestimate line intensities;
- the level dataset we use in our calculations is incomplete in energy.

As discussed for IRAS 18089–1732, deriving the ¹²C/¹³C ratio from our data is not feasible. The relation between ¹²C/¹³C and the galactocentric distance from Wilson & Rood (1994)

gives average values and deviation from it are found. Henkel et al. (1985) found $^{12}\text{C}/^{13}\text{C} < 50$ in the inner galactic disk; one of their source (G19.6-0.2, see their tables 1 and 2) is close to IRAS 18182–1433 and have a similar velocity. Therefore, in our model, we use the value they found, $^{12}\text{C}/^{13}\text{C}=41$. This can also contribute to underestimate intensities.

The last point that can give wrong predictions in these transitions is the level dataset we used in the calculations that is complete in quantic number up to $(J,k)=9$, but not in energy, as shown in Figure 3.5. This can result in an erroneous distribution of the population among the levels and thus to a not correct model of the transitions.

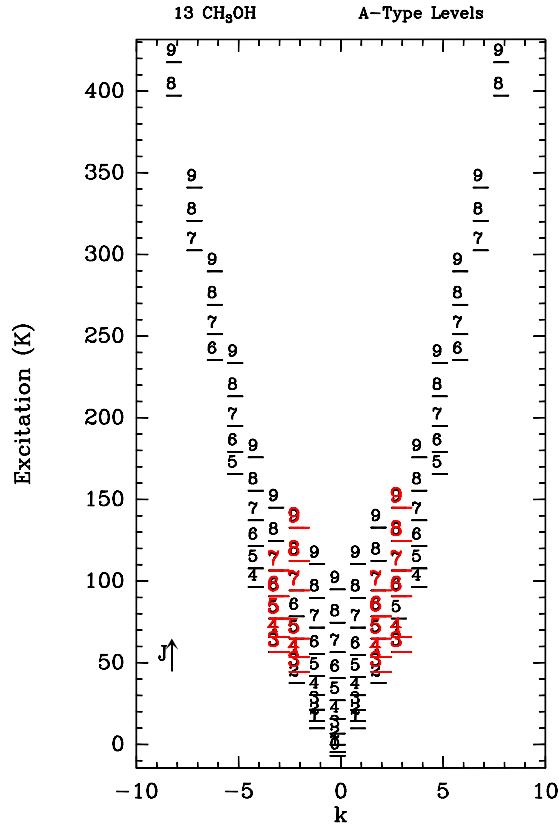


Figure 3.5: Partial energy level diagram for $^{13}\text{CH}_3\text{OH}$ -A. The levels involved in the observed transitions are marked in red.

IRAS 18264–1152

IRAS 18264–1152 ($d \sim 3.5$ kpc, $L \sim 10^4 L_\odot$), part of the sample studied by Sridharan et al. (2002) and Beuther et al. (2002b,c,d), shows several indicators of high mass star formation. CO observations show a massive outflow (Beuther et al. 2002c) centered on the mm dust peaks; both CH_3OH and H_2O maser spots are observed (Beuther et al. 2002d). Detection

of complex molecular species (CH_3OH , CH_3CN , Sridharan et al. 2002; CH_3OH_3 Leurini & Schilke 2005) may indicate hot core formation going on in the source.

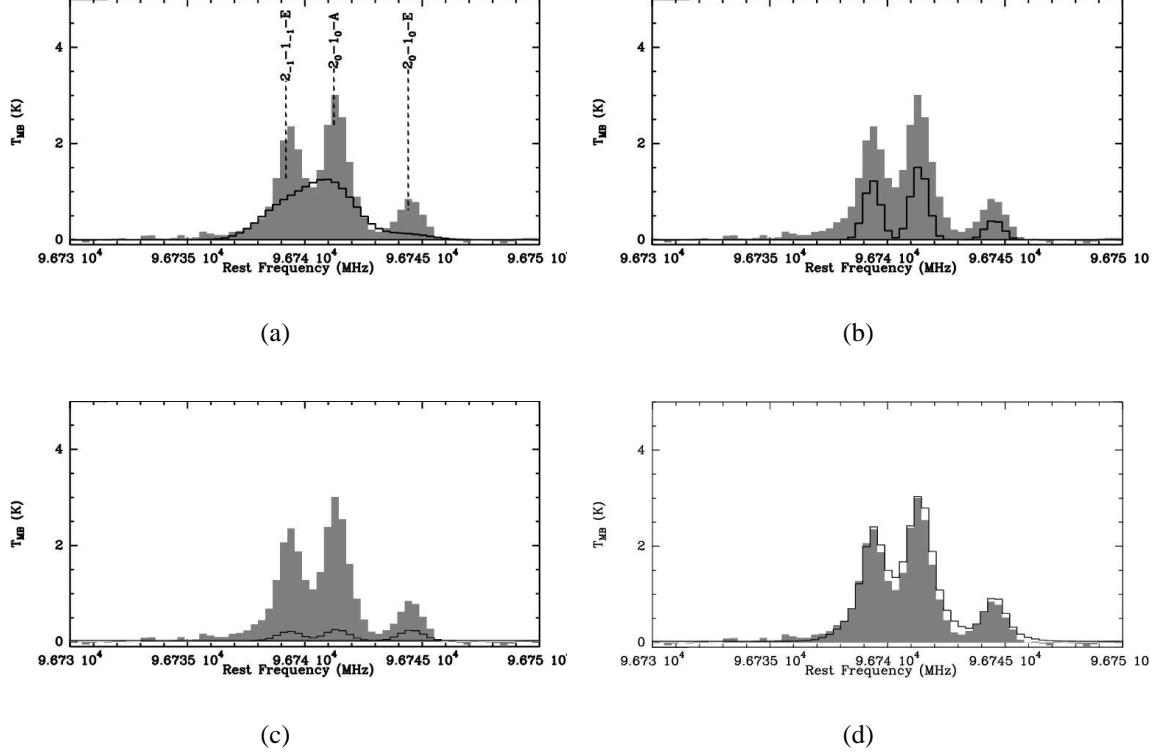


Figure 3.6: In grey, the observed methanol spectrum towards IRAS 18264–152 at 3 mm (**a**, **b**, **c**, **d**) is shown; overlaid in black, the contribution to the total emission from component 1 (**a**), component 2 (**b**), component 3 (**c**) and their sum (**d**).

Wyrowski et al. (2005, in prep.) modelled the continuum combining information at different frequencies and found a dust opacity index of 1.3 and $\tau_{100\mu\text{m}} = 2.4$ to well fit the data. Methanol spectra are strong in emission in almost all the lines in the millimeter bands; however, no torsionally excited lines are detected. Blue non-Gaussian wings are detected in the $k = 0, -1$ lines. Maser emission is detected 2 km s^{-1} from the system velocity of the source in the centimeter band in $J=5,6,7$ lines, together with broader sub-thermal emission. Since no other methanol emission is detected at that velocity and masing components are more difficult to be modelled, the $J_2 \rightarrow J_1 - E$ series is not included in our χ^2 analysis of the source. However, synthetic spectra at the best fit solution are shown in Fig. 3.21(a)- 3.22(a) overlaid on the observations, to show that the broad thermal components are pretty well represented by our model.

Three components are used to model the CH_3OH spectra: one for the non-Gaussian emission; a second one for the bulk emission in the less excited lines and third one for the highly excited lines. Fig. 3.6 shows the contribution of each component to the total emission at 3 mm. The agreement between the data and the model is not extremely satisfying, $\chi_{\nu_d} = 3.8$;

however, the synthetic spectra at the best fit solution well reproduce the data.

Summing over the three components and smearing over the 1 mm beam, the total gas mass predicted by our model is $156 M_{\odot}$ and the H_2 column density 4×10^{23} .

IRAS 18310–0825

IRAS 18310–0825 ($d \sim 4.9$ kpc, $L \sim 10^{4.1} L_{\odot}$) belongs to the population of HMPOs studied by Sridharan et al. (2002) and Beuther et al. (2002b,c,d) over the last years. A class II methanol maser at 6.7 GHz is detected by Walsh et al. (1998) offset from the mm dust condensation. Single dish observations reveal outflows in CO, but no high resolution data are available.

The CH_3OH spectra we collected on the source shows emission only in less excited lines in each band. Wings are tentatively detected in the 3 mm lines, but the signal-to-noise ratio is very low. Therefore, we model the spectrum with one component along the line of sight. The results from our analysis are shown in Table 3.3, while the spectra and the fit are given in Figure 3.24(a)- 3.24(c).

The agreement between our model and the data is pretty good ($\chi_{\nu_d}=1.9$). The luminosity of the source is in good agreement with the IRAS luminosity; the methanol abundance is typical of cold clouds. Averaging over the beam, we derive a gas mass of $317 M_{\odot}$ and a H_2 column density of $2 \times 10^{23} \text{ cm}^{-2}$.

IRAS 19410+2336

IRAS 19410+2336 ($\sim 10^4 L_{\odot}$ Beuther et al. 2002b) shows H_2O and CH_3OH maser emission at the very center of the core, where a weak cm continuum source has also been detected. Beuther et al. (2002d) assume it to be optically thin free-free emission and suggest that a recently ignited, not very evolved massive object is at the cluster center. High-spatial resolution observations (Beuther et al. 2003) reveal four sub-cores in the 2.6 mm continuum, while the CO data resolve at least seven bipolar outflows. Gas masses derived from the 2.6 mm continuum data range from 30 to $110 M_{\odot}$, while H_2 column densities are in the $\times 10^{24}$ regime.

The CH_3OH spectrum towards IRAS 19410 does not show any torsionally excited transition. However, all the lines in the $5_k \rightarrow 4_k$ are clearly detected. Therefore we use a model with two components, one for the bulk emission and a second one responsible of the emission in the more excited lines and in the $J_2 \rightarrow J_1 - E$ band. Line profiles are well represented by a Gaussian shape.

The results from our CH_3OH analysis ($\chi_{\nu_d}=3.7$) are shown in Table 3.3; the best fit, overlaid on the data, is shown in Fig. 3.25(a)- 3.26(c). Luminosities and masses for each component are listed in Table 3.4, together with methanol abundances. Averaging the masses and column densities from each component over the 1 mm beam, we derive $28 M_{\odot}$ and $2.2 \times 10^{23} \text{ cm}^{-2}$, that are in good agreement with what found by Beuther et al. (2003).

IRAS 20126+4104

IRAS 20126+4104 ($d \sim 1.7$ kpc, $L \sim 10^4 L_\odot$) has been studied in great detail over the last years by Cesaroni et al. (1997, 1999) in several molecular tracers at different angular resolutions. They have identified an extended region, $\sim 15''$ in size, with single dish observations, while, at higher spatial resolution, they have been able to resolve the inner part of a bipolar outflow and detect a hot core at the center of it, with temperature ~ 200 K and mass $\sim 10 M_\odot$, of 1500 AU. H_2O masers coincide with the compact core position (Tofani et al. 1995). Methanol thermal emission is associated with both the extended source and the hot core. Moreover, a study on CH_3CN lines reveals a probable Keplerian disk, collapsing towards a central object with mass $\sim 24 M_\odot$.

The CH_3OH spectrum towards the source is strong in all the observed transitions, even if there is no evidence for emission in the torsionally excited lines. However, lines from only a few, very highly excited levels are in the band we observed and we did not perform any observations on the less excited lines in the $v_t=1$ band. Lines show a velocity gradient along the spectrum, as already noticed by Cesaroni et al. (1999), probably due to the disk. This affects our fit, as all the lines emitted by a single component are assumed to have the same velocity and line width. Given the evolved stage of the source, we interpret the features on the red-wing of the $5_{-1} \rightarrow 4_{-1} - E$ line as due to $HNCO(11-10)$ and not to methanol.

Our model takes into account two components: one for the bulk emission, $\sim 15''$ in size as measured by Cesaroni et al. (1999) with the PdBI in several molecular tracers, among which CH_3OH , and one for the hot core.

The results from our CH_3OH analysis are shown in Table 3.3; the best fit, overlaid on the data, is shown in Fig. 3.27(a)- 3.27(c). The agreement between the data and the fit is not extremely good ($\chi_{\nu_d}=3.5$), but this is probably due to velocity gradient in the lines that cannot be reproduced by our model. From the results of our fit, the inner component has an abundance typical of hot core; its luminosity is in agreement with the IRAS luminosity and the values found for the gas mass and the H_2 column density are in the high-mass protostar regime, $56 M_\odot$ and $4.4 \times 10^{23} \text{ cm}^{-2}$.

IRAS 23139+5939

IRAS 23139+5939 ($d \sim 4.8$ kpc, $L \sim 10^{4.4} L_\odot$) has been studied in different molecular tracers and in the continuum (Sridharan et al. 2002; Beuther et al. 2002b,c). Wouterloot et al. (1988) mapped the cloud in NH_3 (1,2) and (2,2) lines and reported a temperature of 29 K; CO observations reveal bipolar outflow (Wouterloot et al. 1989; Shepherd & Churchwell 1996; Beuther et al. 2002c). Beuther et al. (2002c) find strong wing emission in the CO (2-1), but no lobe separation between the blue and the red lobes; therefore, they conclude that the outflow is along the line of sight. Beuther et al. (2002d) report several H_2O masers spots associated to the mm dust continuum peak, but no CH_3OH maser emission. Gas mass and H_2 column density come from the single dish continuum observations at 1.2 mm: $1759 M_\odot$.

and $4.0 \times 10^{23} \text{ cm}^{-2}$ (Beuther et al. 2002b).

3.6 Highlights

With the Effelsberg 100 m telescope, the IRAM 30 m telescope and the Caltech Submillimeter Observatory, we have carried out a multi-frequency observational program on methanol in high mass protostellar candidates. Our main results are:

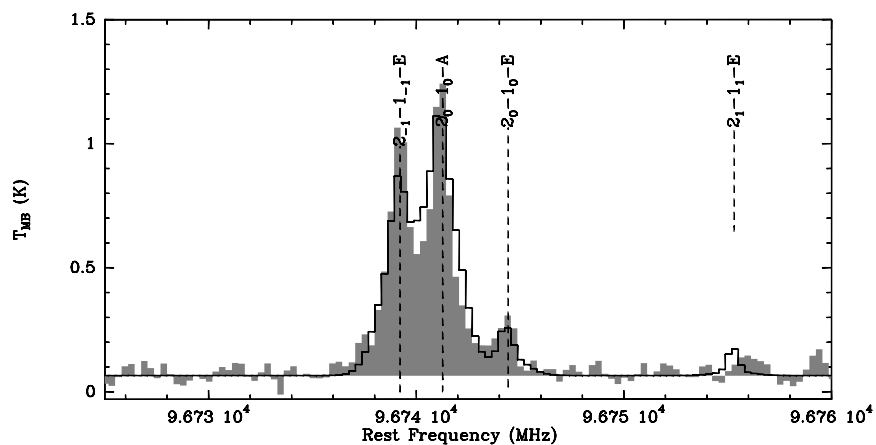
- we successfully applied the technique discussed in § 1.2 to a sample of 13 sources in the early stages of high mass star formation. Although for some sources the reduced χ^2 is not extremely satisfying (e.g. G28.34+0.06 P1, G33.71–0.01, 18264–1152, 19410+2336), our models usually reproduce the observations well. High values of $\chi^2_{\nu_d}$ are probably mainly due to the complexity of the sources, which is not really represented by our simple model; moreover, calibration uncertainties can still play a role in our analysis.
- Methanol has been successfully detected in all the sources of our sample; non-Gaussian profiles have been found in several sources in the infrared dark clouds sub-sample, in the $k = 0, \pm 1$ lines. Since SiO observations (Feldman et al. 2004) and other molecular tracers (Carey et al. 1998) hint outflows can be a common phenomenon in these population of sources, line shapes detected in CH₃OH can be explained as due to outflows. Another point supporting this scenario is that methanol is well known to be found in outflows in the low-mass star formation regime (Bachiller et al. 1995, 1998); however, the high-mass stars case is still poorly studied.
- Among HMPOs a variety of different methanol spectra has been detected; IRAS 18310 shows narrow lines (2.4 km s^{-1}) and only the less excited lines in each band are detected. On the other hand, IRAS 18089 has a very rich CH₃OH spectrum; several $\nu_t=1$ lines are detected and linewidths are typically around 5 km s^{-1} . Therefore, our analysis confirms methanol to be a good indicator of the physical conditions in star forming regions.
- Together with the detection of other complex molecules (for IRAS 18089, IRAS 18264, see Leurini & Schilke 2005; for IRAS 20126, Cesaroni et al. 1997, 1999), our CH₃OH observations suggest hot core formation in some sources of the sample. In hot, dense sources like hot cores, the kinetic temperature and the spatial density of the sources can be derived once $\nu_t=0$ **and** $\nu_t=1$ transitions are observed; if only ground states lines are available, then the degeneracy between the IR pumping and the collisions can lead

to ambiguous results, while, when only $v_t=1$ transitions are observed, the density is not traced.

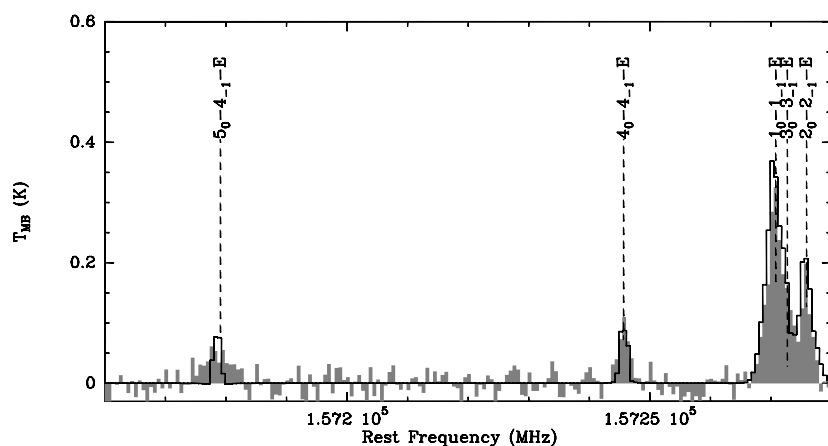
- The methanol abundances relative to H_2 range in the sources of our sample between 10^{-9} and 10^{-7} , as already reported by other authors (Menten et al. 1986; Friberg et al. 1988; van der Tak et al. 2000). In some of them (G19.30P1, IRAS 18089, IRAS 18182, IRAS 20126) a jump in CH_3OH abundance is required.

G11.11P1					
transition	ν (GHz)	τ	T_b	τ	T_b
		1 comp.		2 comp.	
$2_{-1} \rightarrow 1_{-1} - E$	96.739	4.6e-01	3.1e+00	1.1e+00	2.1e+01
$2_0 \rightarrow 1_0 - A$	96.741	6.5e-01	4.5e+00	1.8e+00	2.4e+01
$2_0 \rightarrow 1_0 - E$	96.744	2.8e-01	4.8e-01	2.0e+00	9.2e+00
$2_1 \rightarrow 1_1 - E$	96.755	3.2e-02	9.5e-02	4.3e-01	8.1e+00
$6_0 \rightarrow 6_{-1} - E$	157.048	7.2e-02	-6.6e-03	5.4e+00	5.3e+00
$5_0 \rightarrow 5_{-1} - E$	157.179	2.8e-01	-1.6e-02	7.3e+00	5.9e+00
$4_0 \rightarrow 4_{-1} - E$	157.246	7.5e-01	1.8e-02	8.4e+00	6.2e+00
$1_0 \rightarrow 1_{-1} - E$	157.270	1.2e+00	1.4e+00	3.8e+00	1.2e+01
$3_0 \rightarrow 3_{-1} - E$	157.272	1.3e+00	2.0e-01	8.4e+00	6.5e+00
$2_0 \rightarrow 2_{-1} - E$	157.276	1.6e+00	6.1e-01	7.1e+00	7.2e+00
$5_0 \rightarrow 4_0 - E$	241.700	3.8e-02	1.5e-01	2.4e+00	2.3e+01
$5_{-1} \rightarrow 4_{-1} - E$	241.767	5.2e-01	2.1e+00	4.4e+00	2.8e+01
$5_0 \rightarrow 4_0 - A$	241.791	6.1e-01	2.4e+00	5.0e+00	2.9e+01
$5_4 \rightarrow 4_4 - A$	241.806	4.7e-07	9.8e-07	4.9e-03	4.1e-02
$5_4 \rightarrow 4_4 - E$	241.829	2.2e-08	1.0e-07	7.7e-04	1.1e-02
$5_3 \rightarrow 4_3 - A$	241.832	1.6e+00	6.1e-01	7.1e+00	7.2e+00
$5_3 \rightarrow 4_3 - E$	241.833	2.1e-04	1.1e-03	1.3e-01	1.6e+00
$5_2 \rightarrow 4_2 - A$	241.842	1.0e-04	5.3e-04	3.2e-01	4.0e+00
$5_3 \rightarrow 4_3 - E$	241.843	1.1e-05	3.8e-05	5.1e-02	7.6e-01
$5_{-3} \rightarrow 4_{-3} - E$	241.852	2.4e-06	1.1e-05	1.4e-02	2.4e-01
$5_1 \rightarrow 4_1 - E$	241.879	7.6e-03	2.9e-02	1.5e+00	1.6e+01
$5_2 \rightarrow 4_2 - A$	241.887	1.1e-04	5.0e-04	3.2e-01	3.9e+00
$5_{-2} \rightarrow 4_{-2} - E$	241.904	5.2e-04	1.8e-03	4.6e-01	6.7e+00
$5_2 \rightarrow 4_2 - E$	241.905	1.8e-02	6.9e-02	1.4e+00	1.4e+01

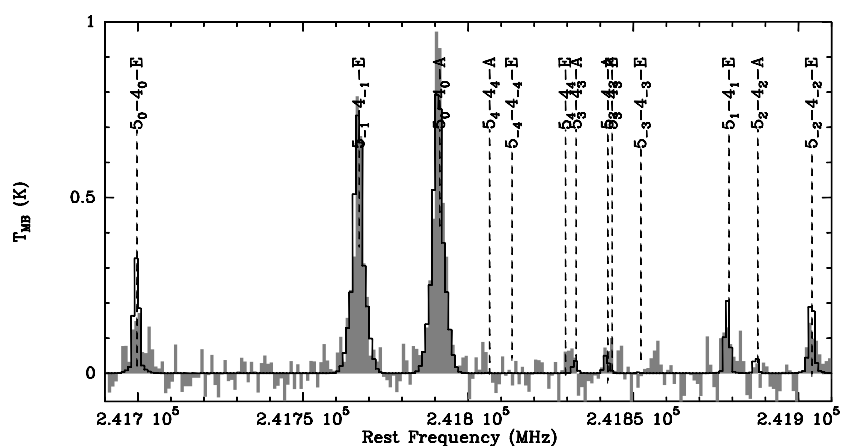
Table 3.7: Line parameters: G11.11P1.



(a)



(b)

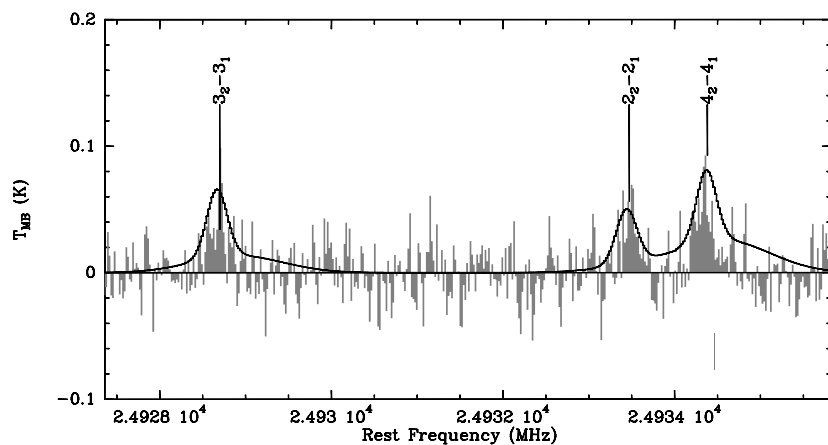


(c)

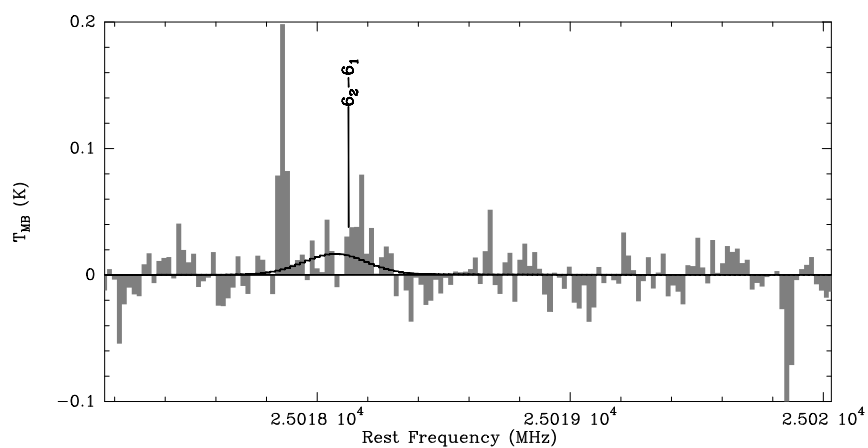
Figure 3.7: Spectra toward G11.11P1 taken with the IRAM 30 m telescope. The 1 mm and 2 mm data smoothed to the resolution of the 3 mm spectra (Fig. 3.7(a)). All observed lines are labelled. Overlaid in black the synthetic spectra resulting from the fit.

G19.30P1					
transition	ν (GHz)	τ	T_b	τ	T_b
		1 comp.		2 comp.	
$2_{-1} \rightarrow 1_{-1} - E$	96.739	7.7e-01	3.9e+00	6.3e-01	2.0e+01
$2_0 \rightarrow 1_0 - A$	96.741	9.5e-01	5.3e+00	7.3e-01	2.7e+01
$2_0 \rightarrow 1_0 - E$	96.744	4.2e-01	5.4e-01	1.7e+00	5.2e+00
$2_1 \rightarrow 1_1 - E$	96.755	4.2e-02	9.6e-02	1.3e-01	2.8e+00
$6_0 \rightarrow 6_{-1} - E$	157.048	6.5e-02	-9.8e-03	6.4e+00	2.9e+00
$5_0 \rightarrow 5_{-1} - E$	157.179	3.1e-01	-3.8e-02	8.3e+00	3.1e+00
$4_0 \rightarrow 4_{-1} - E$	157.246	9.6e-01	-4.0e-02	9.2e+00	3.2e+00
$1_0 \rightarrow 1_{-1} - E$	157.270	1.9e+00	1.5e+00	3.7e+00	7.2e+00
$3_0 \rightarrow 3_{-1} - E$	157.272	1.8e+00	1.2e-01	9.0e+00	3.2e+00
$2_0 \rightarrow 2_{-1} - E$	157.276	2.3e+00	5.5e-01	7.3e+00	3.5e+00
$5_0 \rightarrow 4_0 - E$	241.700	4.2e-02	1.3e-01	1.2e+00	2.2e+01
$5_{-1} \rightarrow 4_{-1} - E$	241.767	7.1e-01	2.1e+00	3.3e+00	3.3e+01
$5_0 \rightarrow 4_0 - A$	241.791	7.7e-01	2.2e+00	3.3e+00	3.9e+01
$5_4 \rightarrow 4_4 - A$	241.806	2.9e-07	5.6e-07	1.3e-03	7.5e-03
$5_4 \rightarrow 4_4 - E$	241.829	1.3e-08	5.5e-08	3.7e-05	4.9e-04
$5_3 \rightarrow 4_3 - A$	241.832	2.3e+00	5.5e-01	7.3e+00	3.5e+00
$5_3 \rightarrow 4_3 - E$	241.833	1.5e-04	7.5e-04	3.2e-02	5.5e-01
$5_2 \rightarrow 4_2 - A$	241.842	7.4e-05	3.5e-04	5.9e-02	1.0e+00
$5_3 \rightarrow 4_3 - E$	241.843	7.8e-06	2.5e-05	4.0e-03	3.8e-02
$5_{-3} \rightarrow 4_{-3} - E$	241.852	1.7e-06	7.6e-06	1.3e-03	1.9e-02
$5_1 \rightarrow 4_1 - E$	241.879	6.4e-03	2.1e-02	4.4e-01	6.8e+00
$5_2 \rightarrow 4_2 - A$	241.887	7.9e-05	3.3e-04	6.1e-02	9.3e-01
$5_{-2} \rightarrow 4_{-2} - E$	241.904	5.9e-04	1.6e-03	1.2e-01	1.9e+00
$5_2 \rightarrow 4_2 - E$	241.905	1.6e-02	5.1e-02	4.7e-01	5.8e+00

Table 3.8: Line parameters: G19.30P1.

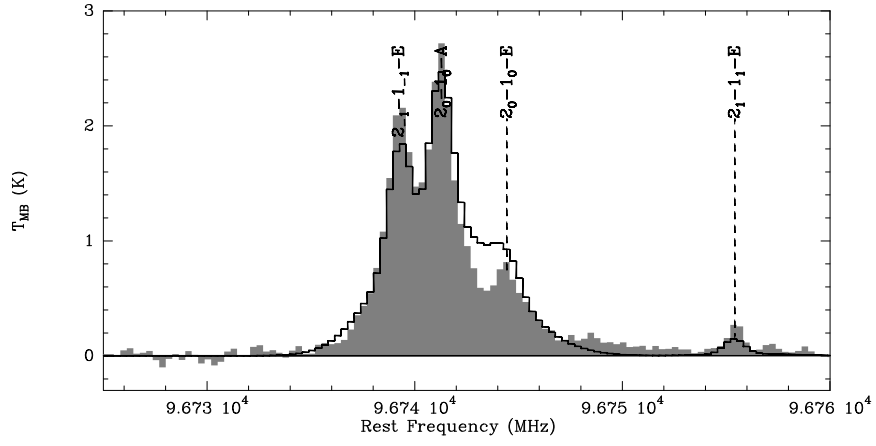


(a)

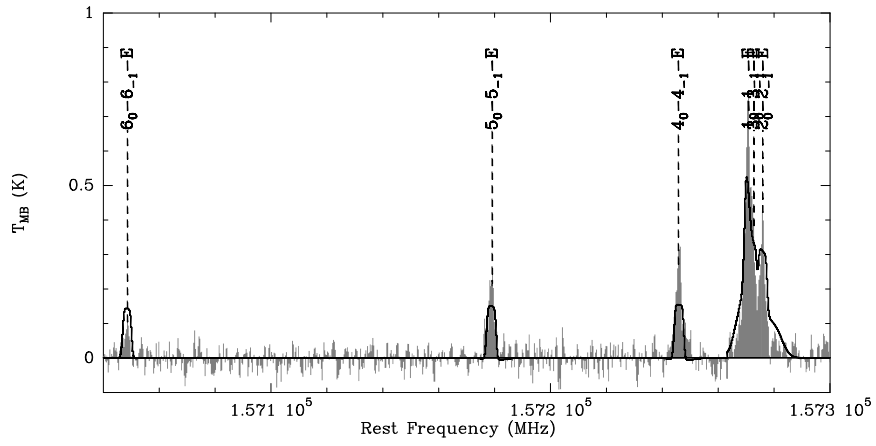


(b)

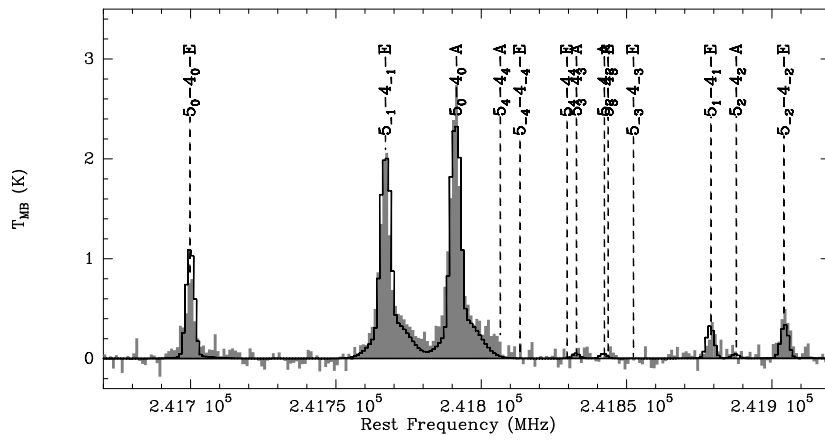
Figure 3.8: Spectra toward G19.30P1 the 100 m telescope, in frequency switching. All observed lines are labelled. Overlaid in black the synthetic spectra resulting from the fit.



(a)



(b)

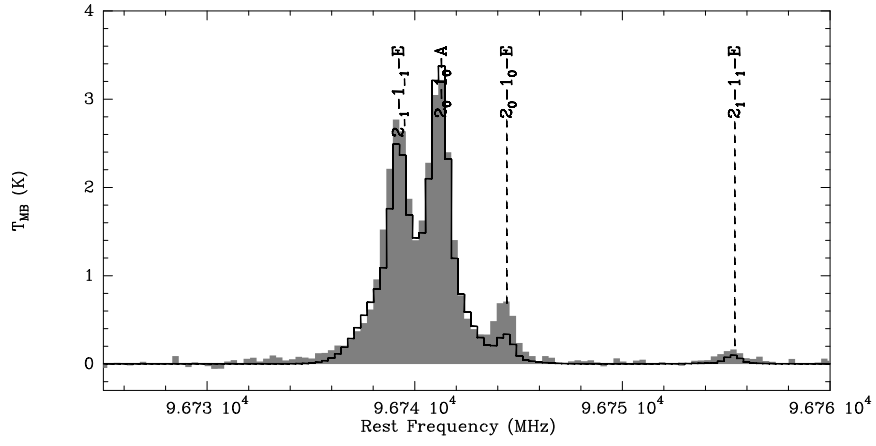


(c)

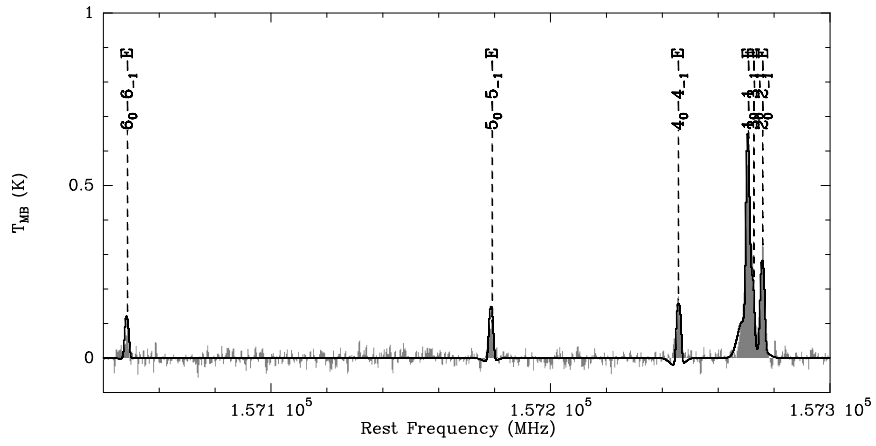
Figure 3.9: Spectra toward G19.30P1 taken with the IRAM 30 m telescope. The 1 mm and 2 mm data smoothed to the resolution of the 3 mm spectra (Fig. 3.9(a)). All observed lines are labelled. Overlaid in black the synthetic spectra resulting from the fit.

G28.34							
transition	ν (GHz)	τ	T_b	τ	T_b	τ	T_b
		1 comp.		2 comp.		3 comp.	
$2_{-1} \rightarrow 1_{-1} - E$	96.739	1.2e+00	2.2e+00	5.0e-01	4.3e+00	5.0e-01	4.3e+00
$2_0 \rightarrow 1_0 - A$	96.741	1.6e+00	3.02e+00	5.0e-01	6.2e+00	5.0e-01	6.2e+00
$2_0 \rightarrow 1_0 - E$	96.744	2.4e-01	1.9e+00	2.5e-01	2.9e-01	2.5e-01	2.9e-01
$2_1 \rightarrow 1_1 - E$	96.755	1.7e-02	1.2e-02	2.1e-02	4.4e-02	2.1e-02	4.4e-02
$6_0 \rightarrow 6_{-1} - E$	157.048	2.5e-03	-6.8e-04	1.2e-01	-1.9e-02	1.2e-01	-1.9e-02
$5_0 \rightarrow 5_{-1} - E$	157.179	2.4e-02	-6.0e-03	4.3e-01	-7.0e-02	4.3e-01	-7.0e-02
$4_0 \rightarrow 4_{-1} - E$	157.246	1.8e-01	-3.8e-02	1.2e+00	-1.3e-01	1.2e+00	-1.3e-01
$1_0 \rightarrow 1_{-1} - E$	157.270	2.3e+00	4.2e-01	1.8e+00	7.7e-01	1.8e+00	7.7e-01
$3_0 \rightarrow 3_{-1} - E$	157.272	8.4e-01	-8.3e-02	2.0e+00	-1.1e-01	2.0e+00	-1.1e-01
$2_0 \rightarrow 2_{-1} - E$	157.276	1.9e+00	6.3e-02	2.3e+00	9.0e-02	2.3e+00	9.0e-02
$5_0 \rightarrow 4_0 - E$	241.700	5.5e-03	6.2e-03	3.3e-02	1.5e-01	3.3e-02	1.5e-01
$5_{-1} \rightarrow 4_{-1} - E$	241.767	2.9e-01	5.5e-0	7.9e-01	2.8e+00	7.9e-01	2.8e+00
$5_0 \rightarrow 4_0 - A$	241.791	2.0e-01	2.4e-01	8.4e-01	3.1e+00	8.4e-01	3.1e+00
$5_4 \rightarrow 4_4 - A$	241.806			1.3e-06	5.2e-06	1.3e-06	5.2e-06
$5_4 \rightarrow 4_4 - E$	241.829			7.1e-08	6.4e-07	7.1e-08	6.4e-07
$5_3 \rightarrow 4_3 - A$	241.832	3.0e-06	8.5e-06	2.3e+00	9.0e-02	2.3e+00	9.0e-02
$5_3 \rightarrow 4_3 - E$	241.833			3.2e-04	3.1e-03	3.2e-04	3.1e-03
$5_2 \rightarrow 4_2 - A$	241.842	1.4e-05	3.3e-05	1.2e-04	1.5e-03	1.2e-04	1.5e-03
$5_3 \rightarrow 4_3 - E$	241.843	9.9e-07	2.7e-06	7.5e-06	4.4e-05	7.5e-06	4.4e-05
$5_{-3} \rightarrow 4_{-3} - E$	241.852			6.6e-06	7.7e-05	6.6e-06	7.7e-05
$5_1 \rightarrow 4_1 - E$	241.879	4.1e-04	5.5e-04	3.8e-03	2.2e-02	3.8e-03	2.2e-02
$5_2 \rightarrow 4_2 - A$	241.887	1.9e-06	3.1e-06	1.4e-04	1.4e-03	1.4e-04	1.4e-03
$5_{-2} \rightarrow 4_{-2} - E$	241.904	5.4e-05	5.9e-05	5.9e-04	2.6e-03	5.9e-04	2.6e-03
$5_2 \rightarrow 4_2 - E$	241.905	1.1e-03	1.5e-03	1.0e-02	5.1e-02	1.0e-02	5.1e-02

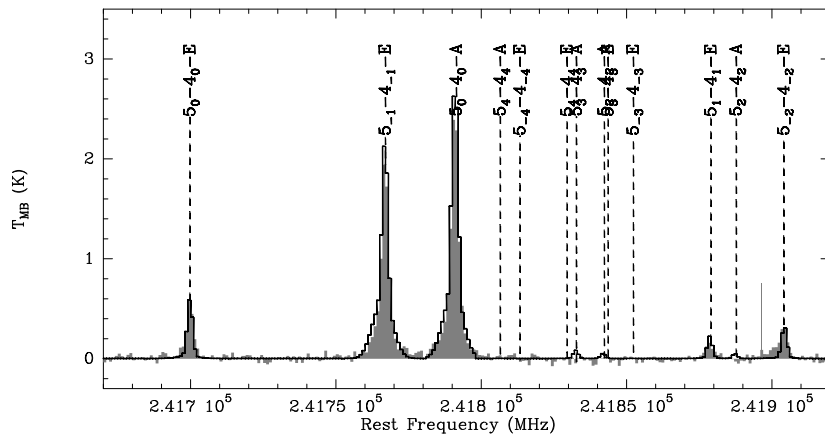
Table 3.9: Line parameters: G28.34.



(a)



(b)

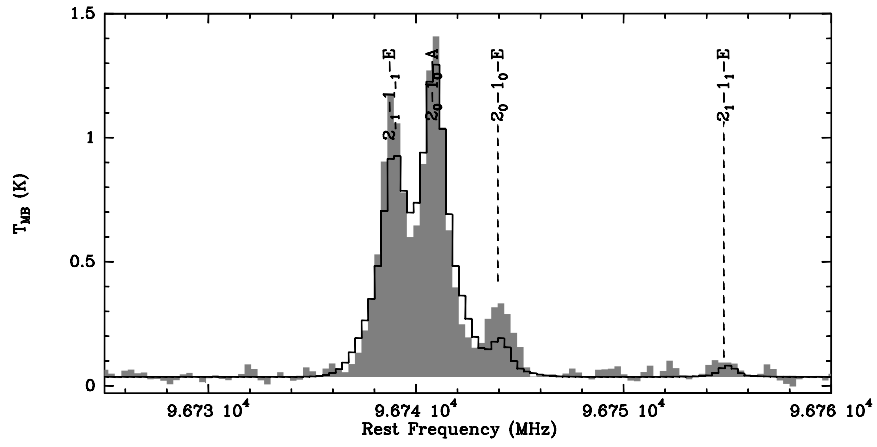


(c)

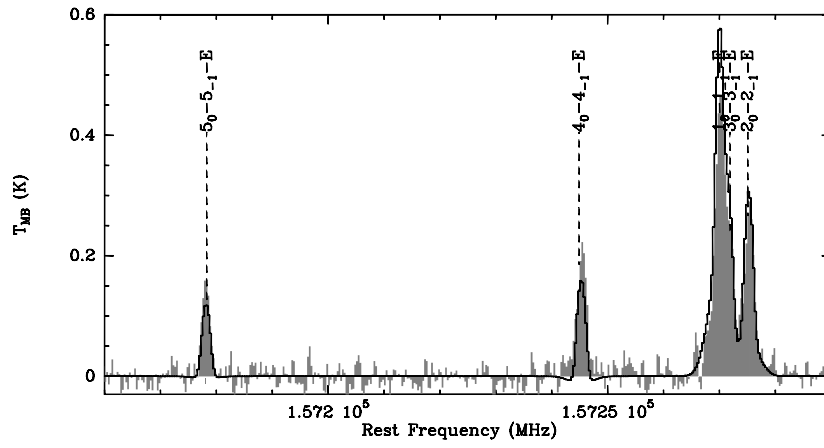
Figure 3.10: Spectra toward G28.34 taken with the IRAM 30 m telescope. The 1 mm and 2 mm data smoothed to the resolution of the 3 mm spectra (Fig. 3.10(a)). All observed lines are labelled. Overlaid in black the synthetic spectra resulting from the fit.

G33.71					
transition	ν (GHz)	τ	T_b	τ	T_b
		1 comp.		2 comp.	
$2_{-1} \rightarrow 1_{-1} - E$	96.739	4.7e-01	2.2e+00	1.7e-01	4.1e+00
$2_0 \rightarrow 1_0 - A$	96.741	5.5e-01	2.9e+00	3.9e-01	6.6e+00
$2_0 \rightarrow 1_0 - E$	96.744	1.5e-01	2.0e-01	3.5e-01	1.1e+00
$2_1 \rightarrow 1_1 - E$	96.755	1.5e-02	2.4e-02	3.7e-02	4.3e-01
$6_0 \rightarrow 6_{-1} - E$	157.048	1.5e-02	-3.2e-03	7.7e-01	5.1e-01
$5_0 \rightarrow 5_{-1} - E$	157.179	7.9e-02	-1.6e-02	1.2e+00	8.5e-01
$4_0 \rightarrow 4_{-1} - E$	157.246	3.2e-01	-5.1e-02	1.5e+00	1.2e+00
$1_0 \rightarrow 1_{-1} - E$	157.270	1.2e+00	5.7e-01	7.3e-01	3.1e+00
$3_0 \rightarrow 3_{-1} - E$	157.272	8.0e-01	-4.1e-02	1.6e+00	1.5e+00
$2_0 \rightarrow 2_{-1} - E$	157.276	1.2e+00	1.6e-01	1.4e+00	1.8e+00
$5_0 \rightarrow 4_0 - E$	241.700	1.0e-02	2.6e-02	1.7e-01	2.4e+00
$5_{-1} \rightarrow 4_{-1} - E$	241.767	2.5e-01	6.4e-01	6.5e-01	1.0e+01
$5_0 \rightarrow 4_0 - A$	241.791	2.6e-01	6.7e-01	8.7e-01	1.2e+01
$5_4 \rightarrow 4_4 - A$	241.806	3.9e-08	7.2e-08	1.4e-04	5.8e-04
$5_4 \rightarrow 4_4 - E$	241.829	1.9e-09	7.5e-09	6.2e-06	5.8e-05
$5_3 \rightarrow 4_3 - A$	241.832	1.2e+00	1.6e-01	1.4e+00	1.8e+00
$5_3 \rightarrow 4_3 - E$	241.833	3.2e-05	1.5e-04	8.3e-03	9.9e-02
$5_2 \rightarrow 4_2 - A$	241.842	1.4e-05	6.2e-05	5.7e-03	6.6e-02
$5_3 \rightarrow 4_3 - E$	241.843	1.4e-06	4.2e-06	5.3e-04	4.3e-03
$5_{-3} \rightarrow 4_{-3} - E$	241.852	3.3e-07	1.4e-06	1.9e-04	2.0e-03
$5_1 \rightarrow 4_1 - E$	241.879	1.4e-03	3.9e-03	6.5e-02	8.7e-01
$5_2 \rightarrow 4_2 - A$	241.887	1.6e-05	6.1e-05	6.0e-03	6.3e-02
$5_{-2} \rightarrow 4_{-2} - E$	241.904	1.2e-04	3.0e-04	8.1e-03	7.8e-02
$5_2 \rightarrow 4_2 - E$	241.905	4.0e-03	1.1e-02	1.1e-01	1.4e+00

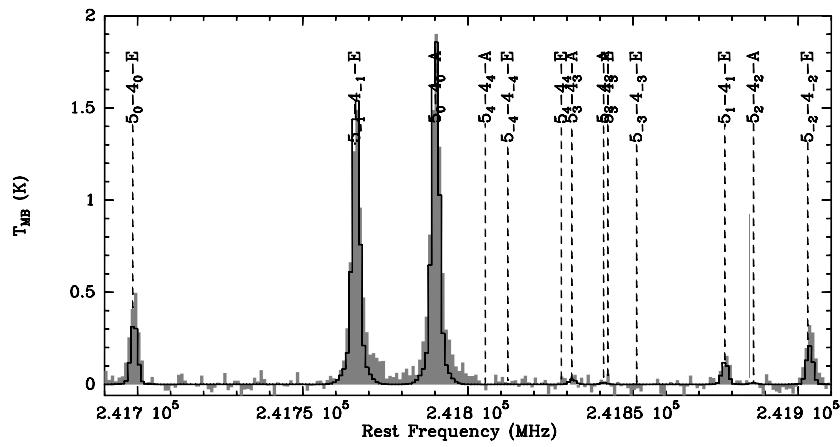
Table 3.10: Line parameters: G33.71.



(a)



(b)

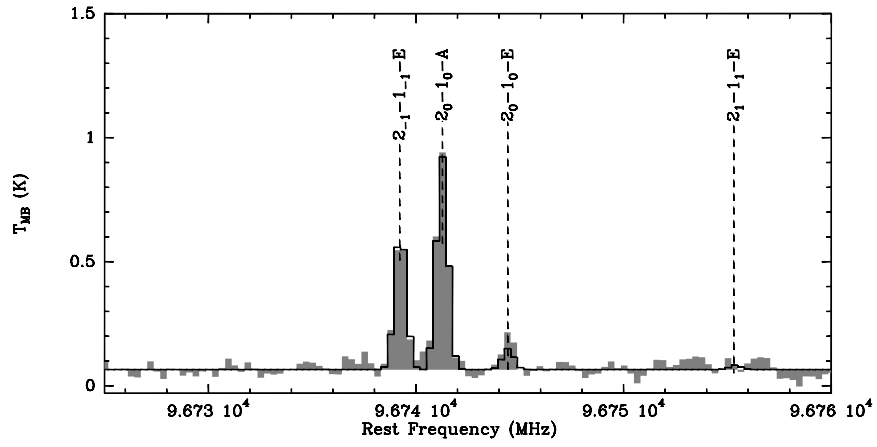


(c)

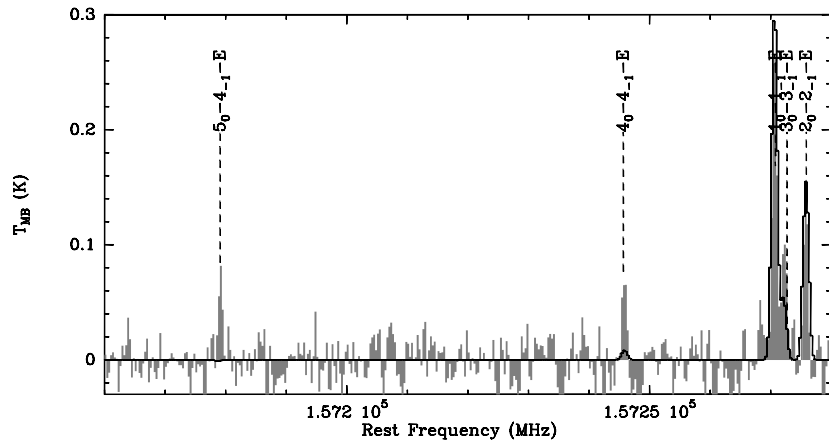
Figure 3.11: Spectra toward G33.71 taken with the IRAM 30 m telescope. The 1 mm and 2 mm data smoothed to the resolution of the 3 mm spectra (Fig. 3.11(a)). All observed lines are labelled. Overlaid in black the synthetic spectra resulting from the fit.

G79.34P1			
transition	ν (GHz)	τ	T_b
		1 comp.	
$2_{-1} \rightarrow 1_{-1} - E$	96.739	1.1e-01	1.0e+00
$2_0 \rightarrow 1_0 - A$	96.741	1.7e-01	1.6e+00
$2_0 \rightarrow 1_0 - E$	96.744	7.0e-02	1.6e-01
$2_1 \rightarrow 1_1 - E$	96.755	8.7e-03	3.2e-02
$6_0 \rightarrow 6_{-1} - E$	157.048	2.8e-02	-1.5e-03
$5_0 \rightarrow 5_{-1} - E$	157.179	9.6e-02	-1.8e-03
$4_0 \rightarrow 4_{-1} - E$	157.246	2.3e-01	1.5e-02
$1_0 \rightarrow 1_{-1} - E$	157.270	3.4e-01	5.4e-01
$3_0 \rightarrow 3_{-1} - E$	157.272	3.8e-01	9.3e-02
$2_0 \rightarrow 2_{-1} - E$	157.276	4.4e-01	2.7e-01
$5_0 \rightarrow 4_0 - E$	241.700	1.2e-02	5.6e-02
$5_{-1} \rightarrow 4_{-1} - E$	241.767	1.5e-01	8.6e-01
$5_0 \rightarrow 4_0 - A$	241.791	1.7e-01	9.4e-01
$5_4 \rightarrow 4_4 - A$	241.806	2.1e-07	4.8e-07
$5_4 \rightarrow 4_4 - E$	241.829	1.4e-08	7.1e-08
$5_3 \rightarrow 4_3 - A$	241.832	4.4e-01	2.7e-01
$5_3 \rightarrow 4_3 - A$	241.833	1.0e-04	5.9e-04
$5_2 \rightarrow 4_2 - A$	241.842	4.6e-05	2.7e-04
$5_3 \rightarrow 4_3 - E$	241.843	4.6e-06	2.0e-05
$5_{-3} \rightarrow 4_{-3} - E$	241.852	1.2e-06	6.4e-06
$5_1 \rightarrow 4_1 - E$	241.879	3.0e-03	1.4e-02
$5_2 \rightarrow 4_2 - A$	241.887	5.0e-05	2.5e-04
$5_{-2} \rightarrow 4_{-2} - E$	241.904	1.4e-04	6.4e-04
$5_2 \rightarrow 4_2 - E$	241.905	7.1e-03	3.3e-02

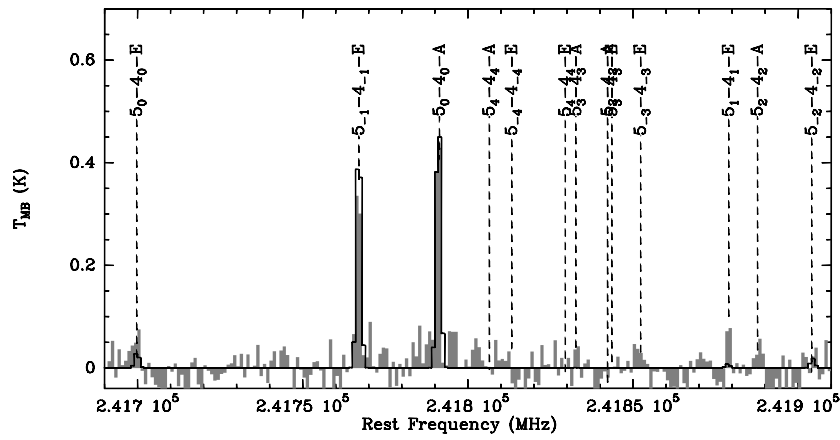
Table 3.11: Line parameters: G79.34P1.



(a)



(b)



(c)

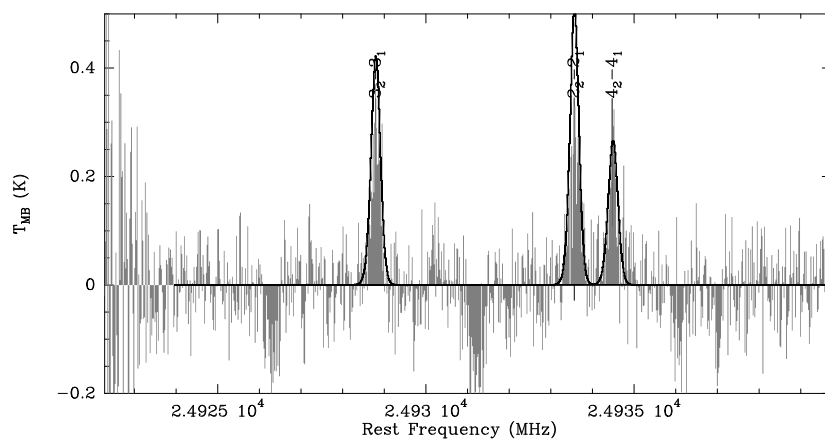
Figure 3.12: Spectra toward G79.34P1 taken with the IRAM 30 m telescope. The 1 mm and 2 mm data smoothed to the resolution of the 3 mm spectra (Fig. 3.12(a)). All observed lines are labelled. Overlaid in black the synthetic spectra resulting from the fit.

IRAM 18089–1732							
transition	ν (GHz)	τ	T_b	τ	T_b	τ	T_b
		1 comp.		2 comp.		3 comp.	
$3_2 \rightarrow 3_1 - E$	24.929	-3.2e-01	2.4e+00	-4.8e-01	1.5e+02	-2.7e-01	6.2e+01
$4_2 \rightarrow 4_1 - E$	24.934	-2.7e-01	2.0e+00	-2.4e-01	8.6e+01	-8.5e-02	3.2e+01
$2_2 \rightarrow 2_1 - E$	24.933	-2.8e-01	2.1e+00	-6.9e-01	2.1e+02	-3.9e-01	8.9e+01
$5_2 \rightarrow 5_1 - E$	24.959	-1.9e-01	1.4e+00	-8.2e-01	2.3e+02	-4.5e-01	1.1e+02
$6_2 \rightarrow 6_1 - E$	25.018	-1.2e-01	7.8e-01	-8.9e-01	2.4e+02	-4.5e-01	1.3e+02
$7_2 \rightarrow 7_1 - E$	25.125	-6.2e-02	3.7e-01	-9.3e-01	2.2e+02	-4.4e-01	1.5e+02
$2_{-1} \rightarrow 1_{-1} -^{13}E$	94.405	-3.6e-03	2.7e-01	-6.2e-02	8.1e+00	-8.0e-02	5.8e+00
$2_0 \rightarrow 1_0 -^{13}A$	94.407	3.2e-02	4.6e-01	1.9e-01	9.4e+00	2.7e-02	6.8e+00
$2_0 \rightarrow 1_0 -^{13}E$	94.411	1.6e-02	1.3e-01	2.0e-01	7.0e+00	9.6e-02	5.8e+00
$2_1 \rightarrow 1_1 -^{13}E$	94.421	3.3e-03	4.6e-02	9.9e-02	4.8e+00	1.8e-02	4.4e+00
$2_1 \rightarrow 1_1 - E, v_t=1$	96.492	6.8e-07	7.3e-06	3.5e-02	2.5e+00	2.7e-02	3.7e+01
$2_0 \rightarrow 1_0 - E, v_t=1$	96.494	3.8e-07	6.0e-06	5.4e-02	2.9e+00	2.1e-01	4.5e+01
$2_{-1} \rightarrow 1_{-1} - E, v_t=1$	96.501	1.6e-09	1.6e-08	5.2e-03	2.6e-01	2.6e-02	2.4e+01
$2_{-1} \rightarrow 1_{-1} - A, v_t=1$	96.589	8.3e-08	1.1e-06	2.7e-02	1.4e+00	1.7e-01	3.1e+01
$2_{-1} \rightarrow 1_{-1} - E$	96.739	5.7e-01	7.7e+00	5.2e+00	5.7e+01	4.2e-01	8.1e+01
$2_0 \rightarrow 1_0 - A$	96.741	1.1e+00	1.1e+01	7.5e+00	5.7e+01	4.7e-01	1.1e+02
$2_0 \rightarrow 1_0 - E$	96.744	8.2e-01	4.0e+00	6.0e+00	5.7e+01	2.4e-01	1.1e+02
$2_1 \rightarrow 1_1 - E$	96.755	1.8e-01	2.2e+00	4.1e+00	5.5e+01	4.9e-01	7.5e+01
$6_0 \rightarrow 6_{-1} -^{13}E$	156.187	1.8e-02	4.8e-02	9.5e-01	1.5e+01	6.7e-01	2.2e+01
$5_0 \rightarrow 5_{-1} -^{13}E$	156.299	6.2e-03	1.5e-01	6.1e-01	1.9e+01	2.7e-01	2.5e+01
$4_0 \rightarrow 4_{-1} -^{13}E$	156.356	4.8e-02	1.9e-01	7.8e-01	1.9e+01	3.3e-01	2.2e+01
$1_0 \rightarrow 1_{-1} -^{13}E$	156.374	2.3e-02	3.1e-01	2.3e-01	1.2e+01	5.4e-03	9.9e+00
$3_0 \rightarrow 3_{-1} -^{13}E$	156.378	6.9e-02	3.1e-01	7.9e-01	1.3e+01	3.1e-01	1.3e+01
$2_0 \rightarrow 2_{-1} -^{13}E$	156.379	6.9e-02	3.1e-01	7.9e-01	1.3e+01	3.1e-01	1.3e+01
$8_0 \rightarrow 8_{-1} - E$	156.489	1.7e-01	4.2e-01	1.4e+01	4.5e+01	2.2e+00	2.6e+02
$6_0 \rightarrow 6_{-1} - E$	157.048	8.5e-01	2.3e+00	2.1e+01	4.6e+01	3.4e+00	1.7e+02
$5_0 \rightarrow 5_{-1} - E$	157.179	1.4e+00	3.5e+00	2.3e+01	4.6e+01	3.3e+00	1.6e+02
$4_0 \rightarrow 4_{-1} - E$	157.246	2.0e+00	4.5e+00	2.3e+01	4.6e+01	3.0e+00	1.5e+02
$1_0 \rightarrow 1_{-1} - E$	157.270	1.4e+00	7.8e+00	1.1e+01	4.7e+01	1.6e+00	8.8e+01
$3_0 \rightarrow 3_{-1} - E$	157.272	2.4e+00	5.1e+00	2.1e+01	4.6e+01	2.7e+00	1.4e+02
$2_0 \rightarrow 2_{-1} - E$	157.276	2.4e+00	5.6e+00	1.7e+01	4.7e+01	2.2e+00	1.2e+02
$5_4 \rightarrow 4_4 - E, v_t=1$	241.159	2.1e-09	2.0e-08	3.0e-02	1.4e+00	2.8e-01	7.0e+01
$5_3 \rightarrow 4_3 - E, v_t=1$	241.166	7.9e-10	1.1e-08	1.8e-02	9.4e-01	4.2e-01	9.7e+01
$5_{-3} \rightarrow 4_{-3} - E, v_t=1$	241.180	4.9e-08	5.5e-07	1.0e-01	4.9e+00	5.5e-01	1.3e+02
$5_{-4} \rightarrow 4_{-4} - E, v_t=1$	241.184	1.7e-10	1.6e-09	1.0e-02	5.7e-01	1.8e-01	6.4e+01
$5_{-2} \rightarrow 4_{-2} - E, v_t=1$	241.187	1.6e-08	2.4e-07	5.8e-02	3.0e+00	6.7e-01	1.4e+02
$5_1 \rightarrow 4_1 - E, v_t=1$	241.204	1.0e-06	1.4e-05	2.4e-01	1.2e+01	9.2e-01	1.8e+02
$5_0 \rightarrow 4_0 - E, v_t=1$	241.206	6.8e-07	9.5e-06	2.2e-01	1.1e+01	9.9e-01	1.8e+02
$5_2 \rightarrow 4_2 - E, v_t=1$	241.211	3.0e-09	3.9e-08	2.8e-02	1.4e+00	5.6e-01	1.2e+02
$5_{-1} \rightarrow 4_{-1} - E, v_t=1$	241.238	2.2e-09	2.9e-08	2.4e-02	1.3e+00	5.8e-01	1.3e+02
$5_{-1} \rightarrow 4_{-1} - A, v_t=1$	241.441	1.6e-07	2.1e-06	1.3e-01	6.6e+00	9.0e-01	1.6e+02

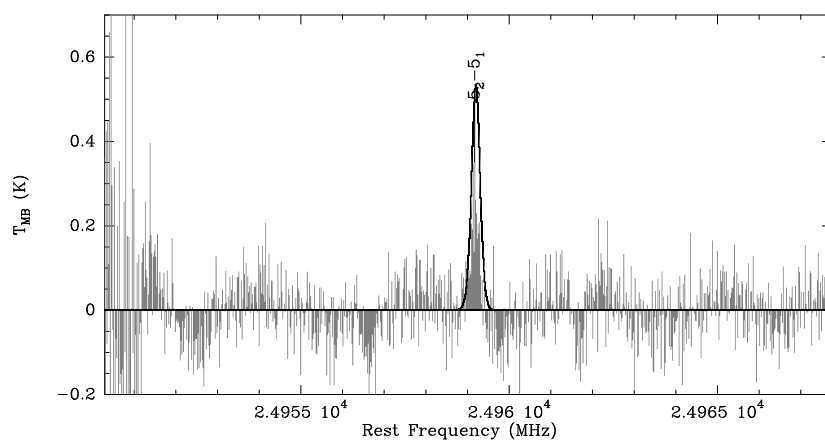
Table 3.12: Line parameters: IRAS 18089–1732.

transition	ν (GHz)	τ	T_b	τ	T_b	τ	T_b
		1 comp.		2 comp.		3 comp.	
$5_0 \rightarrow 4_0 - E$	241.700	7.0e-01	6.7e+00	2.5e+01	5.3e+01	2.4e+00	2.7e+02
$5_{-1} \rightarrow 4_{-1} - E$	241.767	1.5e+00	1.2e+01	2.8e+01	5.4e+01	2.6e+00	2.6e+02
$5_0 \rightarrow 4_0 - A$	241.791	2.0e+00	1.3e+01	3.1e+01	5.4e+01	2.5e+00	2.8e+02
$5_4 \rightarrow 4_4 - A$	241.806	2.0e-03	1.3e-02	2.9e+00	5.1e+01	6.7e-01	1.5e+02
$5_4 \rightarrow 4_4 - E$	241.829	2.6e-04	2.6e-03	2.2e+00	4.7e+01	6.2e-01	1.5e+02
$5_3 \rightarrow 4_3 - A$	241.832	2.4e+00	5.6e+00	1.7e+01	4.7e+01	2.2e+00	1.2e+02
$5_3 \rightarrow 4_3 - A$	241.833	4.2e-02	4.4e-01	8.7e+00	5.4e+01	1.3e+00	2.2e+02
$5_2 \rightarrow 4_2 - A$	241.842	8.5e-02	8.0e-01	1.4e+01	5.3e+01	2.0e+00	2.4e+02
$5_3 \rightarrow 4_3 - E$	241.843	1.7e-02	1.8e-01	9.0e+00	5.4e+01	1.4e+00	2.2e+02
$5_{-3} \rightarrow 4_{-3} - E$	241.852	3.7e-03	4.1e-02	6.8e+00	5.3e+01	1.3e+00	2.2e+02
$5_1 \rightarrow 4_1 - E$	241.879	3.5e-01	3.9e+00	2.2e+01	5.3e+01	2.4e+00	2.6e+02
$5_2 \rightarrow 4_2 - A$	241.887	1.0e+00	7.7e+00	3.9e+01	5.1e+01	4.7e+00	2.8e+02
$5_{-2} \rightarrow 4_{-2} - E$	241.904	1.3e-01	1.4e+00	1.7e+01	5.4e+01	1.9e+00	2.6e+02
$5_2 \rightarrow 4_2 - E$	241.905	4.1e-01	4.4e+00	1.8e+01	5.4e+01	2.1e+00	2.5e+02
$7_{-3} \rightarrow 7_2 -^{13}A$	254.959	-8.2e-05	4.0e-03	1.5e-01	1.7e+01	-1.7e-01	5.3e+01
$6_{-3} \rightarrow 6_2 -^{13}A$	255.050	1.0e-07	6.4e-03	1.9e-01	1.7e+01	-1.2e-01	4.5e+01
$5_{-3} \rightarrow 5_2 -^{13}A$	255.121	-2.8e-04	1.5e-02	1.4e-01	1.8e+01	-1.7e-01	4.0e+01
$4_{-3} \rightarrow 4_2 -^{13}A$	255.173	-5.3e-04	2.3e-02	1.2e-01	1.6e+01	-1.7e-01	3.0e+01
$5_{-3} \rightarrow 5_{-2} -^{13}A$	255.192	-2.8e-04	1.5e-02	2.6e-01	1.6e+01	-5.6e-02	3.6e+01
$6_3 \rightarrow 6_{-2} -^{13}A$	255.194	-1.3e-04	8.5e-03	1.4e-01	1.8e+01	-2.4e-01	5.1e+01
$4_3 \rightarrow 4_{-2} -^{13}A$	255.204	-5.1e-04	2.3e-02	1.2e-01	1.6e+01	-1.7e-01	3.0e+01
$3_{-3} \rightarrow 3_2 -^{13}A$	255.211	-7.9e-04	2.7e-02	7.3e-02	1.1e+01	-1.2e-01	1.7e+01
$7_3 \rightarrow 7_{-2} -^{13}A$	255.215	-3.9e-05	3.8e-03	1.5e-01	1.6e+01	-1.5e-01	5.3e+01
$3_3 \rightarrow 3_{-2} -^{13}A$	255.221	-1.7e-03	3.9e-02	7.9e-02	1.1e+01	-9.8e-02	1.7e+01
$8_3 \rightarrow 8_{-2} -^{13}A$	255.266	-1.4e-05	1.5e-03	1.2e-01	1.4e+01	-1.5e-01	5.7e+01
$9_3 \rightarrow 9_{-2} -^{13}A$	255.356	-9.7e-06	5.1e-04	6.9e-02	1.2e+01	-2.5e-01	6.4e+01
$7_0 \rightarrow 6_0 - E$	338.125	3.3e-01	2.8e+00	3.1e+01	5.1e+01	4.4e+00	2.8e+02
$7_{-1} \rightarrow 6_{-1} - E$	338.345	7.9e-01	6.5e+00	3.5e+01	5.1e+01	4.7e+00	2.7e+02
$7_6 \rightarrow 6_6 - E$	338.405	2.0e-07	1.7e-06	4.4e-01	1.8e+01	6.0e-01	1.5e+02
$7_0 \rightarrow 6_0 - A$	338.409	1.0e+00	7.7e+00	3.9e+01	5.1e+01	4.7e+00	2.8e+02
$7_{-6} \rightarrow 6_{-6} - E$	338.431	1.3e-07	1.0e-06	3.3e-01	1.4e+01	5.2e-01	1.4e+02
$7_6 \rightarrow 6_{-6} - A$	338.442	2.9e-07	2.7e-06	3.9e-01	1.7e+01	6.3e-01	1.3e+02
$7_{-5} \rightarrow 6_{-5} - E$	338.457	1.2e-05	1.1e-04	2.3e+00	4.6e+01	1.5e+00	2.2e+02
$7_5 \rightarrow 6_5 - E$	338.475	7.4e-06	7.9e-05	1.9e+00	4.3e+01	1.5e+00	2.1e+02
$7_{-5} \rightarrow 6_{-5} - A$	338.486	1.3e-05	1.5e-04	1.9e+00	4.3e+01	1.4e+00	2.2e+02
$7_{-4} \rightarrow 6_{-4} - E$	338.504	3.3e-04	3.5e-03	6.1e+00	5.1e+01	2.4e+00	2.5e+02
$7_{-4} \rightarrow 6_{-4} - A$	338.513	2.9e-02	2.6e-01	1.9e+01	5.1e+01	3.8e+00	2.7e+02
$7_{-2} \rightarrow 6_{-2} - A$	338.513	8.2e-04	8.5e-03	6.8e+00	5.1e+01	2.7e+00	2.3e+02
$7_4 \rightarrow 6_4 - E$	338.530	1.6e-04	1.8e-03	5.0e+00	5.0e+01	2.2e+00	2.5e+02
$7_3 \rightarrow 6_3 - A$	338.540	1.9e-02	1.8e-01	1.4e+01	5.1e+01	3.2e+00	2.7e+02
$7_{-3} \rightarrow 6_{-3} - A$	338.543	1.9e-02	1.8e-01	1.4e+01	5.1e+01	3.2e+00	2.7e+02
$7_{-3} \rightarrow 6_{-3} - E$	338.560	1.7e-03	1.8e-02	1.1e+01	5.1e+01	3.1e+00	2.7e+02
$7_3 \rightarrow 6_3 - E$	338.583	7.7e-03	8.8e-02	1.4e+01	5.1e+01	3.3e+00	2.7e+02
$7_1 \rightarrow 6_1 - E$	338.615	1.6e-01	1.5e+00	3.1e+01	5.1e+01	4.4e+00	2.7e+02
$7_2 \rightarrow 6_2 - A$	338.640	3.0e-02	2.6e-01	1.9e+01	5.1e+01	3.7e+00	2.8e+02
$7_2 \rightarrow 6_2 - E$	338.722	2.1e-01	1.9e+00	2.5e+01	5.1e+01	4.1e+00	2.7e+02
$7_{-2} \rightarrow 6_{-2} - E$	338.345	5.3e-02	5.1e-01	2.3e+01	5.1e+01	3.9e+00	2.8e+02

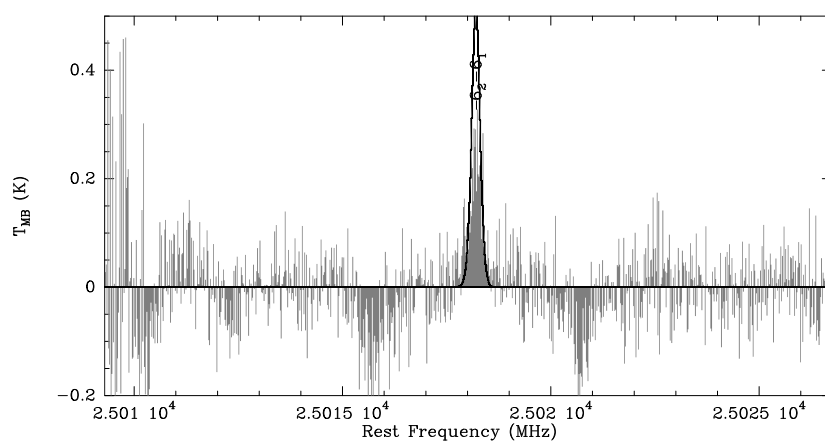
Table 3.12: Line parameters: IRAS 18089–1732 (continued).



(a)



(b)



(c)

Figure 3.13: Spectra toward IRAS 18089–1732 taken with the 100 m telescope, in frequency switching. All observed lines are labelled. Overlaid in black the synthetic spectra resulting from the fit.

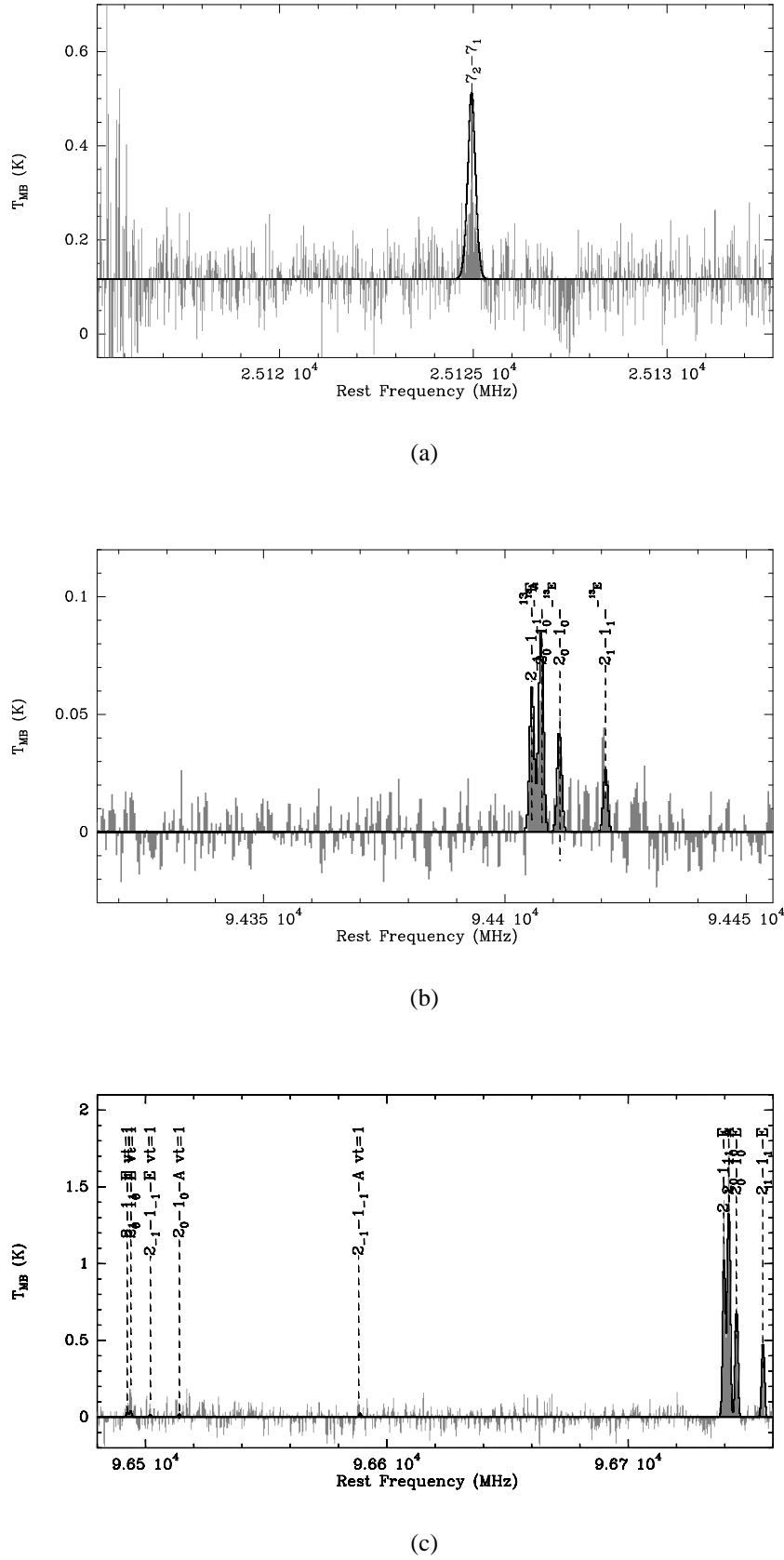
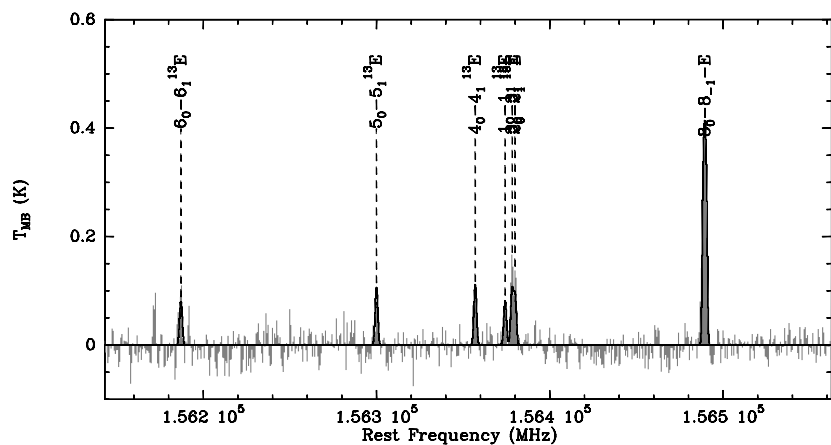
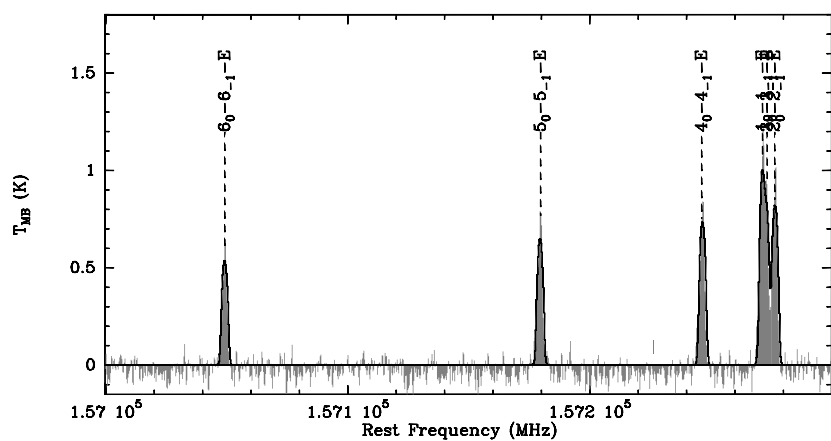


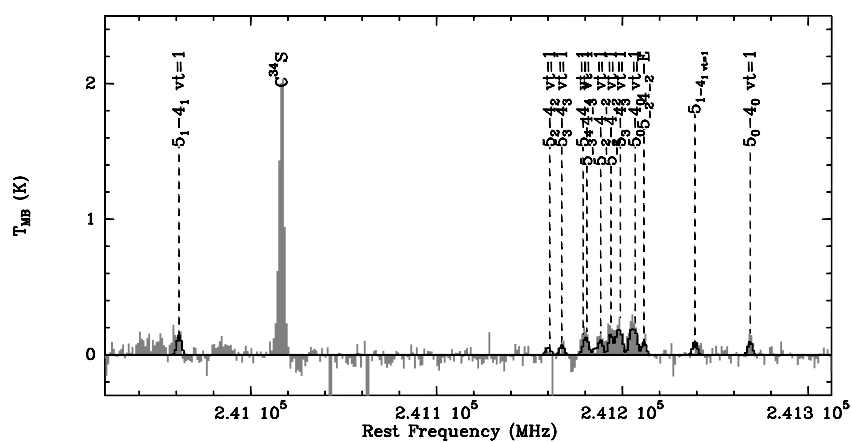
Figure 3.14: Spectra toward IRAS 18089–1732 taken with the 100 m telescope (3.14(a)), in frequency switching, and with the IRAM 30 m telescope (3.14(b)- 3.14(c)); the 2mm data are smoothed to the resolution of the 3 mm spectra. All observed lines are labelled. Overlaid in black the synthetic spectra resulting from the fit.



(a)

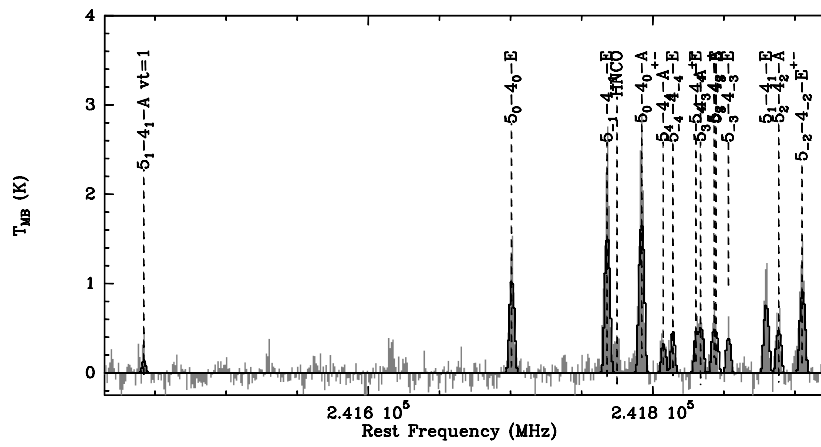


(b)

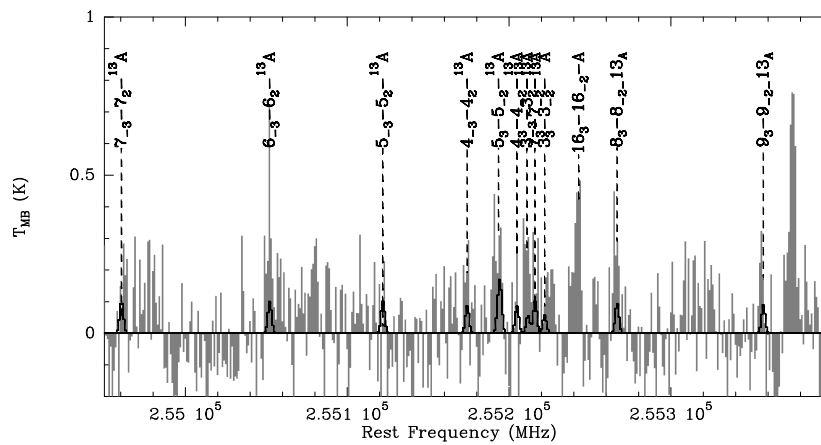


(c)

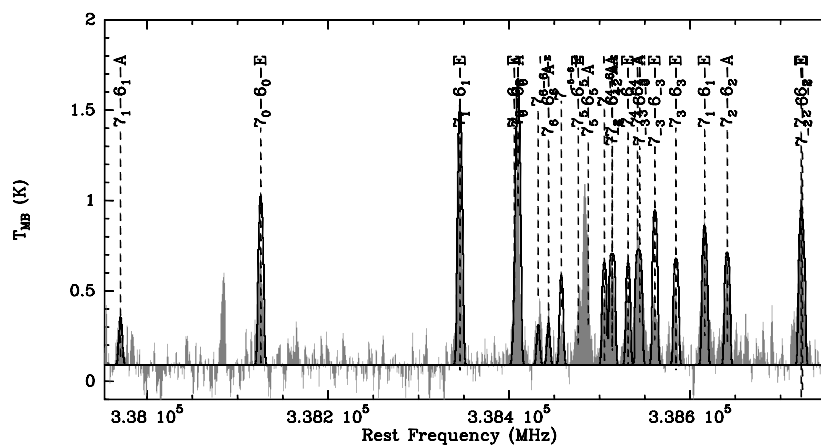
Figure 3.15: Spectra toward IRAS 18089–1732 taken with the IRAM 30 m telescope, smoothed to the resolution of the 3 mm spectra (Fig. 3.14(b)- 3.14(c)). All observed lines are labelled. Overlaid in black the synthetic spectra resulting from the fit.



(a)



(b)

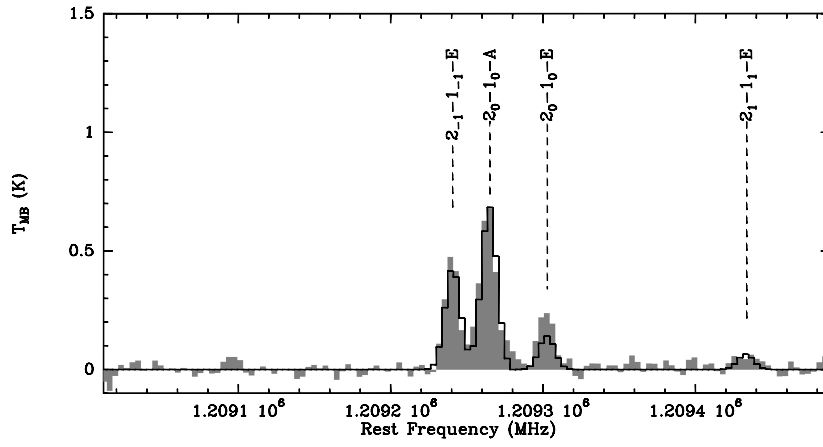


(c)

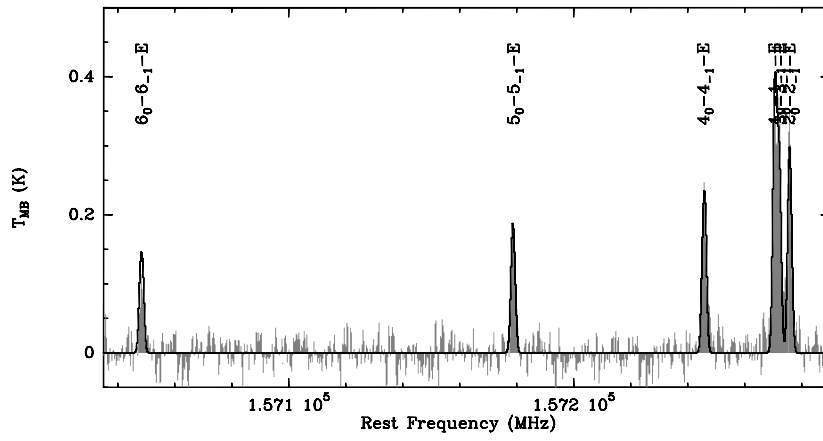
Figure 3.16: Spectra toward IRAS 18089–1732 taken with the IRAM 30 m telescope (Fig. 3.16(b)) and with the CSO (Fig. 3.16(c)), smoothed to the resolution of the 3 mm spectra (Fig. 3.14(b)–3.14(c)). All observed lines are labelled. Overlaid in black the synthetic spectra resulting from the fit.

IRAM 18151-1208					
transition	ν (GHz)	τ	T_b	τ	T_b
		1 comp.		2 comp.	
$2_{-1} \rightarrow 1_{-1} - E$	96.739	4.7e-02	1.1e+00	5.1e-02	3.7e+00
$2_0 \rightarrow 1_0 - A$	96.741	1.0e-01	1.8e+00	5.1e-02	4.7e+00
$2_0 \rightarrow 1_0 - E$	96.744	8.4e-02	2.5e-01	8.1e-02	3.7e+00
$2_1 \rightarrow 1_1 - E$	96.755	8.8e-03	8.5e-02	4.3e-02	2.5e+00
$6_0 \rightarrow 6_{-1} - E$	157.048	1.7e-01	7.7e-02	5.2e-01	8.2e+00
$5_0 \rightarrow 5_{-1} - E$	157.179	2.9e-01	1.6e-01	5.4e-01	9.1e+00
$4_0 \rightarrow 4_{-1} - E$	157.246	3.9e-01	2.8e-01	5.1e-01	9.4e+00
$1_0 \rightarrow 1_{-1} - E$	157.270	2.1e-01	8.6e-01	2.0e-01	5.5e+00
$3_0 \rightarrow 3_{-1} - E$	157.272	4.3e-01	4.1e-01	4.5e-01	8.9e+00
$2_0 \rightarrow 2_{-1} - E$	157.276	3.7e-01	5.3e-01	3.5e-01	7.6e+00
$5_0 \rightarrow 4_0 - E$	241.700	3.4e-02	4.1e-01	2.9e-01	1.3e+01
$5_{-1} \rightarrow 4_{-1} - E$	241.767	1.7e-01	2.8e+00	3.4e-01	1.7e+01
$5_0 \rightarrow 4_0 - A$	241.791	2.2e-01	3.2e+00	3.2e-01	1.8e+01
$5_4 \rightarrow 4_4 - A$	241.806	1.2e-05	4.7e-05	2.5e-02	9.4e-01
$5_4 \rightarrow 4_4 - E$	241.829	9.1e-07	7.9e-06	9.9e-03	4.0e-01
$5_3 \rightarrow 4_3 - A$	241.832	3.7e-01	5.3e-01	3.5e-01	7.6e+00
$5_3 \rightarrow 4_3 - E$	241.833	1.4e-03	1.5e-02	1.0e-01	5.3e+00
$5_2 \rightarrow 4_2 - A$	241.842	6.7e-04	7.9e-03	1.2e-01	6.3e+00
$5_3 \rightarrow 4_3 - E$	241.843	6.8e-05	5.6e-04	7.1e-02	3.1e+00
$5_{-3} \rightarrow 4_{-3} - E$	241.852	3.1e-05	3.0e-04	4.5e-02	2.1e+00
$5_1 \rightarrow 4_1 - E$	241.879	1.3e-02	1.5e-01	2.4e-01	1.2e+01
$5_2 \rightarrow 4_2 - A$	241.887	7.3e-04	7.6e-03	1.2e-01	6.3e+00
$5_{-2} \rightarrow 4_{-2} - E$	241.904	8.1e-04	7.8e-03	1.7e-01	7.6e+00
$5_2 \rightarrow 4_2 - E$	241.905	2.3e-02	2.8e-01	2.4e-01	1.1e+01

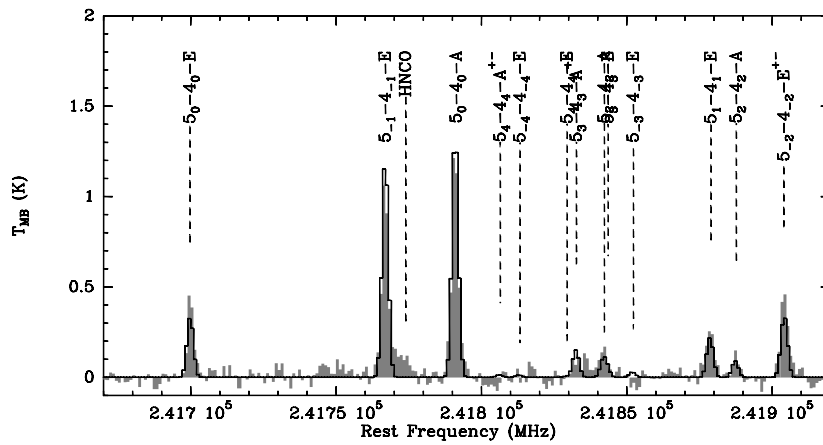
Table 3.13: Line parameters: IRAS 18151–1208 .



(a)



(b)

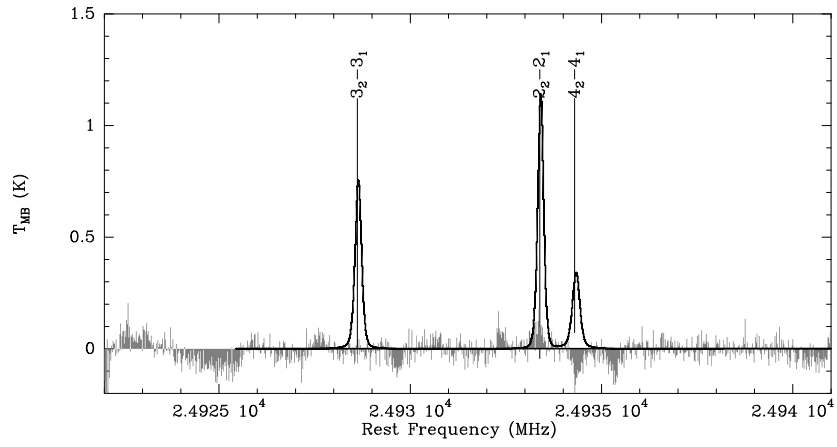


(c)

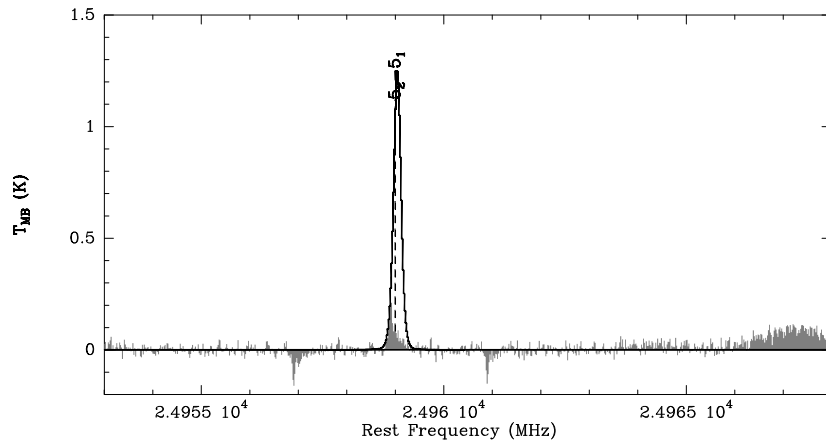
Figure 3.17: Spectra toward IRAS 18151–1208 taken with the IRAM 30 m telescope. The 1 mm and 2 mm data smoothed to the resolution of the 3 mm spectra (Fig. 3.17(a)). All observed lines are labelled. Overlaid in black the synthetic spectra resulting from the fit.

IRAM 18182–1433							
transition	ν (GHz)	τ	T_b	τ	T_b	τ	T_b
		1 comp.		2 comp.		3 comp.	
$3_2 \rightarrow 3_1 - E$	24.929	-1.9e-01	1.0e+00	-1.6e-02	6.8e-02	-2.2e+00	1.2e+02
$4_2 \rightarrow 4_1 - E$	24.934	-1.6e-01	7.9e-01	-1.8e-02	7.8e-02	-1.3e+00	4.3e+01
$2_2 \rightarrow 2_1 - E$	24.933	-1.8e-01	9.7e-01	-1.1e-02	4.5e-02	-2.7e+00	2.0e+02
$5_2 \rightarrow 5_1 - E$	24.959	-1.4e-01	7.5e-01	-5.1e-03	2.1e-02	-2.8e+00	2.2e+02
$6_2 \rightarrow 6_1 - E$	25.018	-1.0e-01	5.1e-01	-1.9e-03	8.0e-03	-2.7e+00	1.9e+02
$7_2 \rightarrow 7_1 - E$	25.125	-6.1e-02	0.0e+00	-5.8e-04	0.0e+00	-2.3e+00	0.0e+00
$2_1 \rightarrow 1_1 - E, v_t=1$	96.492	0.0e+00	0.0e+00	0.0e+00	0.0e+00	0.0e+00	0.0e+00
$2_0 \rightarrow 1_0 - E, v_t=1$	96.494	0.0e+00	0.0e+00	0.0e+00	0.0e+00	0.0e+00	0.0e+00
$2_{-1} \rightarrow 1_{-1} - E, v_t=1$	96.501	0.0e+00	0.0e+00	0.0e+00	0.0e+00	0.0e+00	0.0e+00
$2_{-1} \rightarrow 1_{-1} - A, v_t=1$	96.589	0.0e+00	0.0e+00	0.0e+00	0.0e+00	0.0e+00	0.0e+00
$2_{-1} \rightarrow 1_{-1} - E$	96.739	1.2e-01	3.6e+00	6.6e-02	8.0e-01	1.3e+00	4.3e+01
$2_0 \rightarrow 1_0 - A$	96.741	2.7e-01	5.3e+00	1.1e-01	1.3e+00	1.5e+00	4.9e+01
$2_0 \rightarrow 1_0 - E$	96.744	2.8e-01	1.3e+00	6.2e-02	1.6e-01	2.0e+00	3.3e+01
$2_1 \rightarrow 1_1 - E$	96.755	3.7e-02	5.9e-01	7.6e-03	4.2e-02	1.0e+00	3.1e+01
$6_0 \rightarrow 6_{-1} - E$	157.048	7.3e-01	1.1e+00	4.3e-02	7.2e-03	8.9e+00	2.2e+01
$5_0 \rightarrow 5_{-1} - E$	157.179	1.0e+00	1.5e+00	1.1e-01	2.7e-02	1.0e+01	2.2e+01
$4_0 \rightarrow 4_{-1} - E$	157.246	1.2e+00	1.9e+00	2.1e-01	8.1e-02	1.0e+01	2.2e+01
$1_0 \rightarrow 1_{-1} - E$	157.270	5.4e-01	3.3e+00	2.0e-01	5.8e-01	4.4e+00	2.8e+01
$3_0 \rightarrow 3_{-1} - E$	157.272	1.2e+00	2.2e+00	2.9e-01	1.9e-01	9.6e+00	2.3e+01
$2_0 \rightarrow 2_{-1} - E$	157.276	1.1e+00	2.3e+00	3.0e-01	3.4e-01	7.7e+00	2.3e+01
$5_0 \rightarrow 4_0 - E$	241.700	1.9e-01	3.4e+00	1.6e-02	1.0e-01	5.9e+00	5.0e+01
$5_{-1} \rightarrow 4_{-1} - E$	241.767	5.1e-01	1.0e+01	1.3e-01	1.1e+00	7.5e+00	5.0e+01
$5_0 \rightarrow 4_0 - A$	241.791	6.3e-01	1.1e+01	1.5e-01	1.2e+00	7.0e+00	5.2e+01
$5_4 \rightarrow 4_4 - A$	241.806	5.0e-04	2.6e-03	7.5e-07	2.0e-06	4.7e-01	1.8e+01
$5_4 \rightarrow 4_4 - E$	241.829	2.7e-05	0.0e+00	5.8e-08	0.0e+00	1.9e-01	0.0e+00
$5_3 \rightarrow 4_3 - A$	241.832	1.1e+00	2.3e+00	3.0e-01	3.4e-01	7.7e+00	2.3e+01
$5_3 \rightarrow 4_3 - E$	241.833	1.6e-02	2.3e-01	2.3e-04	1.6e-03	1.8e+00	4.2e+01
$5_2 \rightarrow 4_2 - A$	241.842	1.3e-02	1.8e-01	1.1e-04	7.6e-04	2.6e+00	4.7e+01
$5_3 \rightarrow 4_3 - E$	241.843	1.8e-03	1.9e-02	1.2e-05	6.4e-05	1.6e+00	3.6e+01
$5_{-3} \rightarrow 4_{-3} - E$	241.852	5.6e-04	0.0e+00	3.4e-06	0.0e+00	1.0e+00	0.0e+00
$5_1 \rightarrow 4_1 - E$	241.879	8.7e-02	1.6e+00	5.1e-03	3.3e-02	4.9e+00	4.8e+01
$5_2 \rightarrow 4_2 - A$	241.887	1.3e-02	1.8e-01	1.2e-04	7.3e-04	2.6e+00	4.7e+01
$5_{-2} \rightarrow 4_{-2} - E$	241.904	1.7e-02	2.2e-01	2.2e-04	1.3e-03	3.7e+00	4.6e+01
$5_2 \rightarrow 4_2 - E$	241.905	1.4e-01	2.4e+00	1.0e-02	6.7e-02	4.6e+00	4.8e+01
$7_{-3} \rightarrow 7_2 -^{13}A$	254.959	-2.3e-04	4.7e-03	-7.6e-07	1.3e-05	6.2e-04	2.1e+00
$6_{-3} \rightarrow 6_2 -^{13}A$	255.050	-1.2e-04	4.8e-03	-2.7e-08	1.1e-05	-3.3e-02	3.1e+00
$5_{-3} \rightarrow 5_2 -^{13}A$	255.121	-5.0e-04	1.2e-02	-3.7e-06	7.2e-05	-1.1e-02	3.0e+00
$4_{-3} \rightarrow 4_2 -^{13}A$	255.173	-7.7e-04	1.7e-02	-7.7e-06	1.5e-04	-3.5e-02	3.2e+00
$5_{-3} \rightarrow 5_{-2} -^{13}A$	255.192	-5.9e-04	1.2e-02	-4.8e-06	7.9e-05	2.9e-03	3.0e+00
$6_3 \rightarrow 6_{-2} -^{13}A$	255.194	-3.6e-04	8.0e-03	-1.8e-06	3.4e-05	-5.0e-03	2.7e+00
$4_3 \rightarrow 4_{-2} -^{13}A$	255.204	-7.8e-04	1.7e-02	-8.3e-06	1.5e-04	-3.0e-02	3.2e+00
$3_{-3} \rightarrow 3_2 -^{13}A$	255.211	-1.1e-03	2.0e-02	-1.4e-05	2.4e-04	-6.2e-02	2.8e+00
$7_3 \rightarrow 7_{-2} -^{13}A$	255.215	-2.0e-04	4.4e-03	-6.7e-07	1.2e-05	1.2e-02	2.0e+00
$3_3 \rightarrow 3_{-2} -^{13}A$	255.221	-1.9e-03	3.1e-02	-3.1e-05	4.7e-04	-1.1e-01	3.6e+00
$8_3 \rightarrow 8_{-2} -^{13}A$	255.266	-1.0e-04	2.2e-03	-2.3e-07	3.8e-06	4.8e-03	1.5e+00
$9_3 \rightarrow 9_{-2} -^{13}A$	255.356	-5.4e-05	9.0e-04	-6.2e-08	9.0e-07	-8.4e-03	9.4e-01

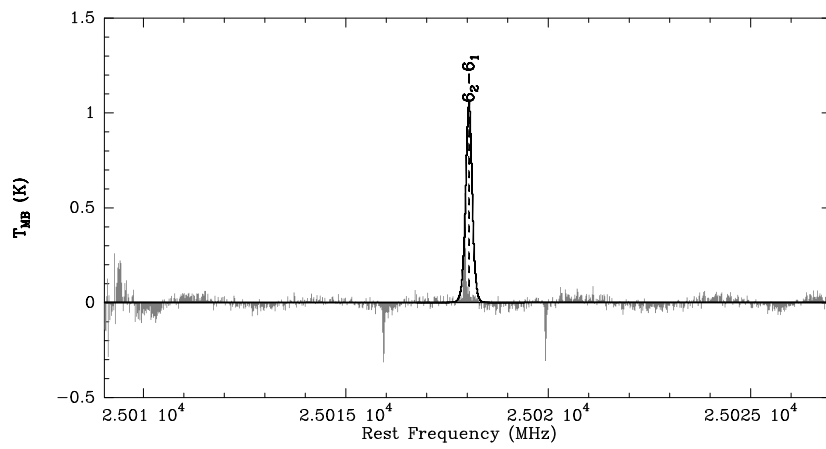
Table 3.14: Line parameters: IRAS 18182–1433.



(a)



(b)



(c)

Figure 3.18: Spectra toward IRAS 18182–1433 taken with the 100 m telescope, in frequency switching. All observed lines are labelled. Overlaid in black the synthetic spectra resulting from the fit.

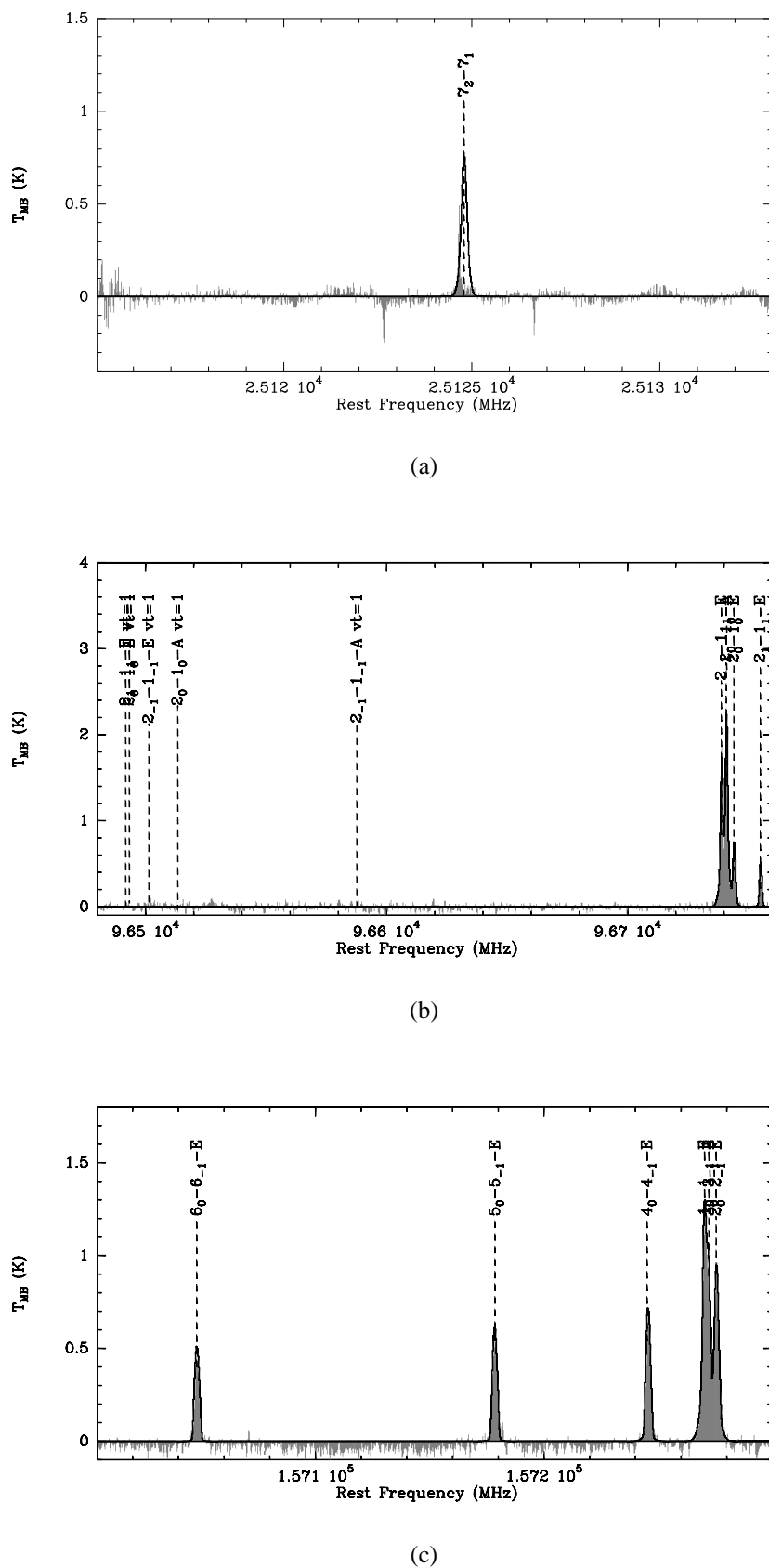
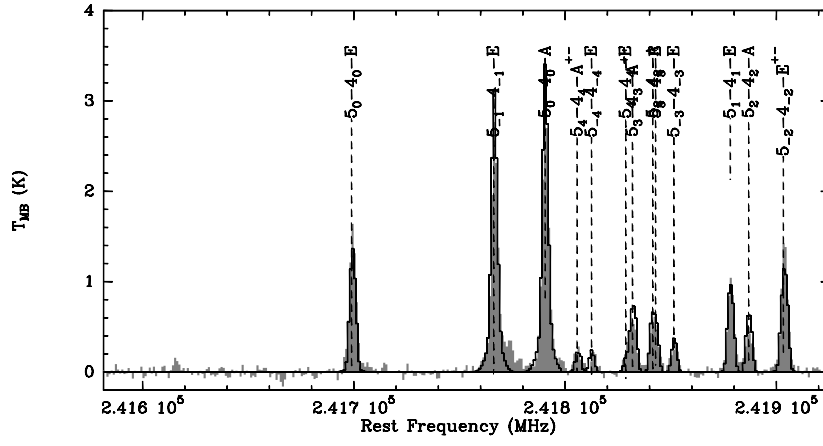
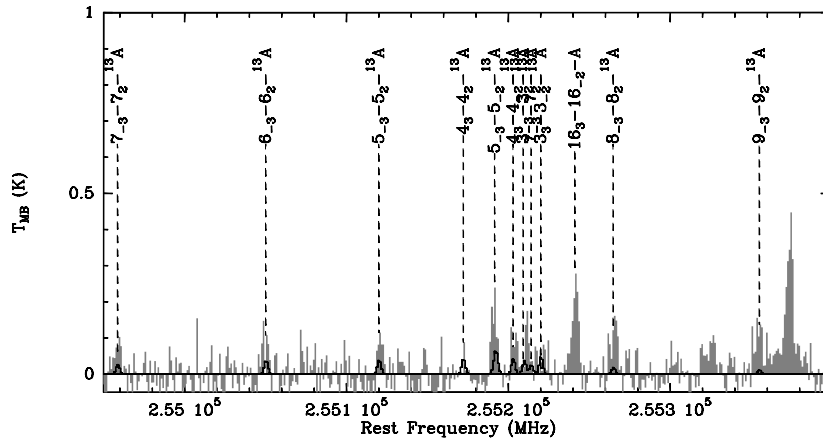


Figure 3.19: Spectra toward IRAS 18182–1433 taken with the 100 m telescope (3.19(a)), in frequency switching, and with the IRAM 30 m telescope (Fig. 3.19(b)-3.19(c)); the 2 mm data are smoothed to the resolution of the 3 mm spectra. All observed lines are labelled. Overlaid in black the synthetic spectra resulting from the fit.



(a)

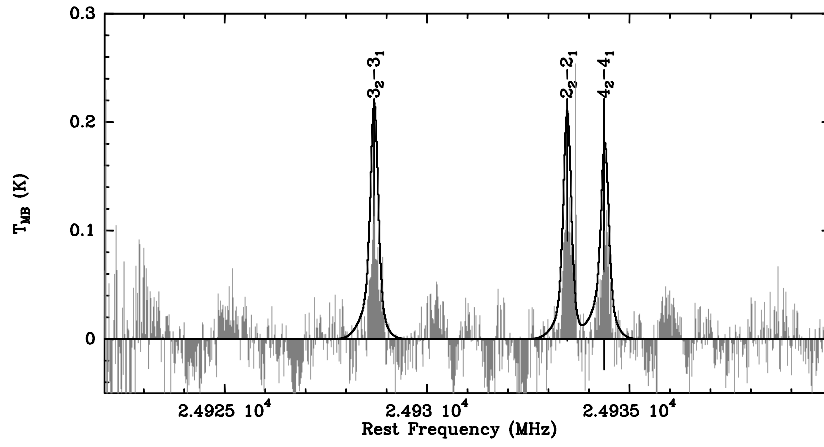


(b)

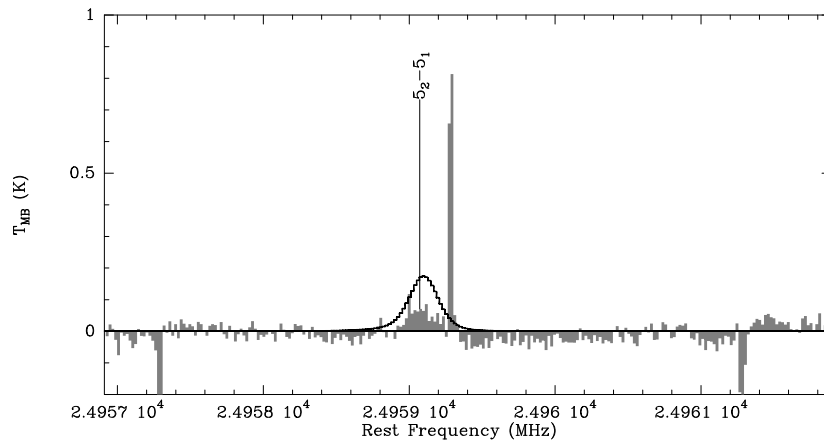
Figure 3.20: Spectra toward IRAS 18182–1433 taken with the IRAM 30 m telescope; data are smoothed to the resolution of the 3 mm spectra. All observed lines are labelled. Overlaid in black the synthetic spectra resulting from the fit.

IRAM 18264–1152							
transition	ν (GHz)	τ	T_b	τ	T_b	τ	T_b
		1 comp.		2 comp.		3 comp.	
$3_2 \rightarrow 3_1 - E$	24.929	-4.6e-02	2.0e-01	-4.1e-01	2.9e+00	-2.5e-01	4.4e+00
$4_2 \rightarrow 4_1 - E$	24.934	-5.4e-02	2.3e-01	-4.0e-01	2.4e+00	-1.4e-01	2.5e+00
$2_2 \rightarrow 2_1 - E$	24.933	-3.2e-02	1.4e-01	-3.6e-01	2.7e+00	-3.1e-01	5.7e+00
$6_2 \rightarrow 6_1 - E$	25.018	-6.7e-03	2.8e-02	-2.0e-01	1.4e+00	-3.1e-01	6.2e+00
$2_{-1} \rightarrow 1_{-1} - E$	96.739	1.7e-01	2.3e+00	2.7e-01	1.2e+01	8.1e-02	7.0e+00
$2_0 \rightarrow 1_0 - A$	96.741	3.4e-01	4.1e+00	5.0e-01	1.5e+01	5.7e-02	8.4e+00
$2_0 \rightarrow 1_0 - E$	96.744	1.9e-01	4.4e-01	8.5e-01	4.0e+00	1.2e-01	7.9e+00
$2_1 \rightarrow 1_1 - E$	96.755	2.1e-02	1.2e-01	8.0e-02	1.8e+00	7.6e-02	5.4e+00
$6_0 \rightarrow 6_{-1} - E$	157.048	1.8e-01	2.3e-02	3.7e+00	2.7e+00	6.6e-01	1.9e+01
$5_0 \rightarrow 5_{-1} - E$	157.179	4.2e-01	7.9e-02	4.6e+00	3.0e+00	6.6e-01	2.0e+01
$4_0 \rightarrow 4_{-1} - E$	157.246	7.3e-01	2.1e-01	4.9e+00	3.2e+00	6.2e-01	2.0e+01
$1_0 \rightarrow 1_{-1} - E$	157.270	5.8e-01	1.5e+00	1.9e+00	6.5e+00	2.3e-01	1.1e+01
$3_0 \rightarrow 3_{-1} - E$	157.272	9.3e-01	4.3e-01	4.7e+00	3.3e+00	5.3e-01	1.9e+01
$2_0 \rightarrow 2_{-1} - E$	157.276	9.1e-01	7.5e-01	3.8e+00	3.6e+00	4.0e-01	1.6e+01
$5_0 \rightarrow 4_0 - E$	241.700	5.2e-02	3.8e-01	6.2e-01	1.5e+01	5.4e-01	2.7e+01
$5_{-1} \rightarrow 4_{-1} - E$	241.767	4.1e-01	3.5e+00	1.6e+00	3.0e+01	5.7e-01	3.1e+01
$5_0 \rightarrow 4_0 - A$	241.791	5.7e-01	4.6e+00	1.7e+00	3.1e+01	4.5e-01	3.2e+01
$5_4 \rightarrow 4_4 - A$	241.806	5.3e-06	1.6e-05	1.9e-03	1.1e-02	4.9e-02	3.4e+00
$5_4 \rightarrow 4_4 - E$	241.829	2.6e-07	1.7e-06	7.1e-05	9.3e-04	4.2e-02	2.6e+00
$5_3 \rightarrow 4_3 - A$	241.832	9.1e-01	7.5e-01	3.8e+00	3.6e+00	4.0e-01	1.6e+01
$5_3 \rightarrow 4_3 - E$	241.833	1.0e-03	8.3e-03	3.9e-02	6.9e-01	1.7e-01	1.2e+01
$5_2 \rightarrow 4_2 - A$	241.842	5.2e-04	4.2e-03	4.9e-02	8.7e-01	2.2e-01	1.6e+01
$5_3 \rightarrow 4_3 - E$	241.843	4.1e-05	2.3e-04	5.8e-03	6.4e-02	1.9e-01	1.1e+01
$5_{-3} \rightarrow 4_{-3} - E$	241.852	1.4e-05	1.0e-04	1.8e-03	2.7e-02	1.4e-01	8.3e+00
$5_1 \rightarrow 4_1 - E$	241.879	1.5e-02	1.1e-01	2.7e-01	5.9e+00	4.6e-01	2.5e+01
$5_2 \rightarrow 4_2 - A$	241.887	5.6e-04	4.0e-03	5.1e-02	8.2e-01	2.1e-01	1.6e+01
$5_{-2} \rightarrow 4_{-2} - E$	241.904	9.1e-04	5.5e-03	8.9e-02	1.5e+00	3.7e-01	1.9e+01
$5_2 \rightarrow 4_2 - E$	241.905	3.0e-02	2.1e-01	3.7e-01	6.5e+00	4.4e-01	2.3e+01

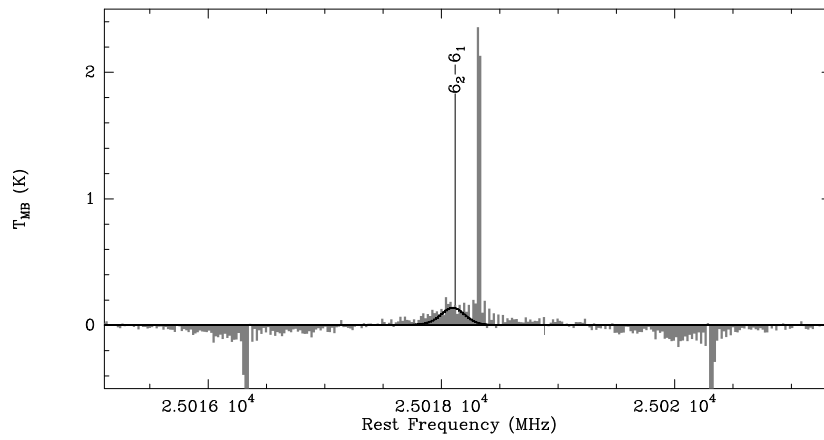
Table 3.15: Line parameters: IRAS 18264–152 .



(a)

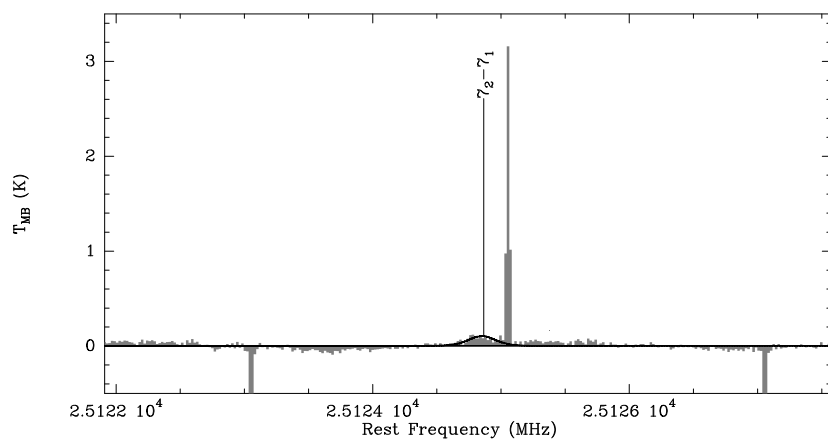


(b)

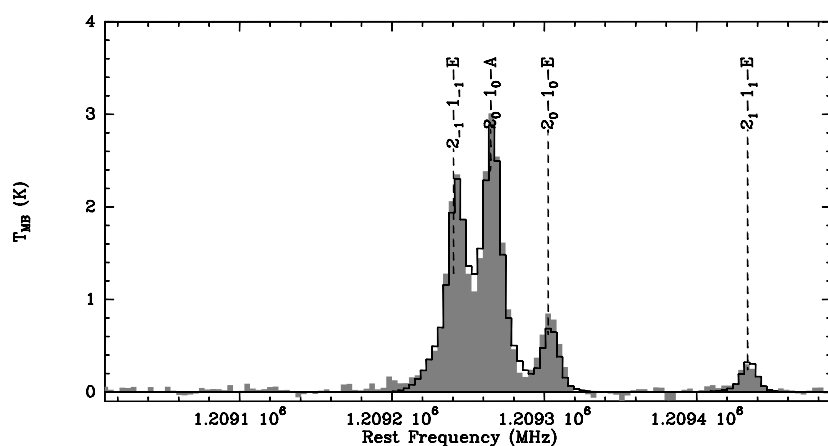


(c)

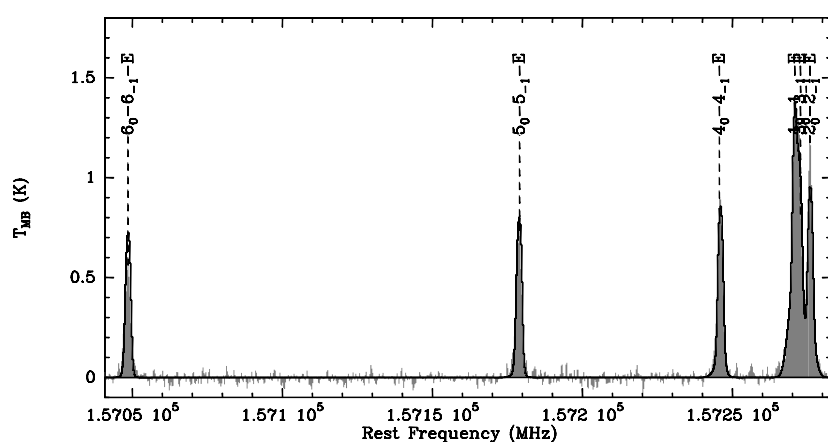
Figure 3.21: Spectra toward IRAS 18264–1152 taken with the 100 m telescope, in frequency switching. All observed lines are labelled. Overlaid in black the synthetic spectra resulting from the fit.



(a)

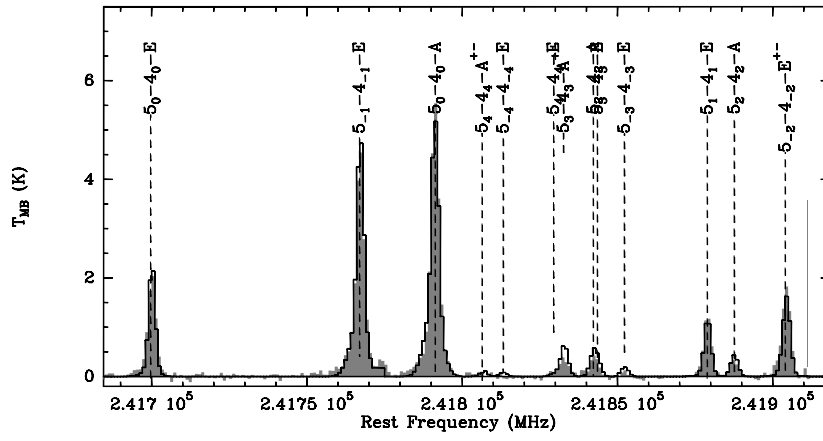


(b)



(c)

Figure 3.22: Spectra toward IRAS 18264–1152 taken with the 100 m telescope (3.22(a)), in frequency switching, and with the IRAM 30 m telescope (Fig. 3.22(b)-3.22(c)); the 2 mm data are smoothed to the resolution of the 3 mm spectra. All observed lines are labelled. Overlaid in black the synthetic spectra resulting from the fit.

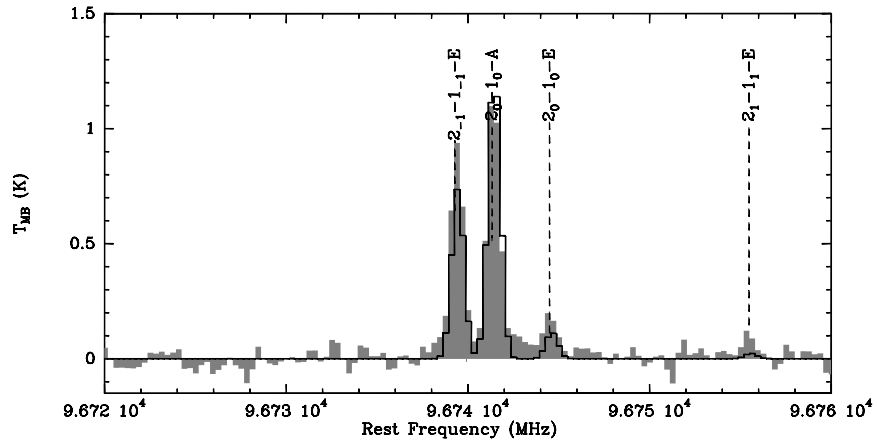


(a)

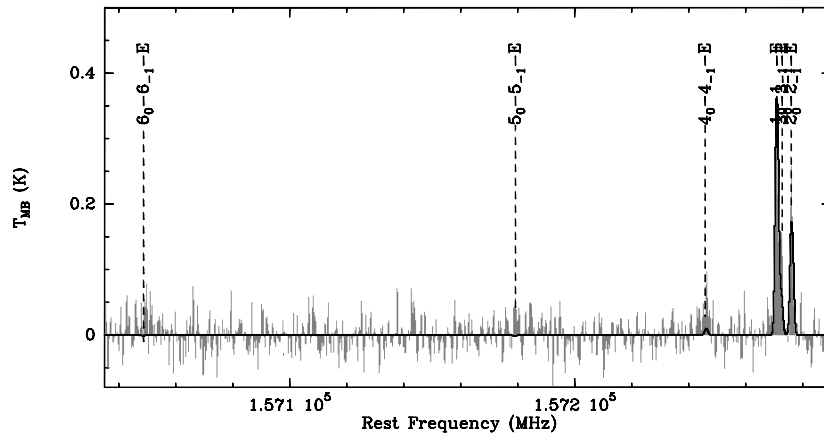
Figure 3.23: 1 mm spectrum toward IRAS 18264–1152 taken with the IRAM 30 m telescope; data are smoothed to the resolution of the 3 mm spectra (Fig. 3.22(b)). All observed lines are labelled. Overlaid in black the synthetic spectra resulting from the fit.

IRAM 18310–0825			
transition	ν (GHz)	τ	T_b
		1 comp.	
$2_{-1} \rightarrow 1_{-1} - E$	96.739	2.9e-01	2.3e+00
$2_0 \rightarrow 1_0 - A$	96.741	5.0e-01	3.9e+00
$2_0 \rightarrow 1_0 - E$	96.744	1.9e-01	3.6e-01
$2_1 \rightarrow 1_1 - E$	96.755	2.2e-02	7.5e-02
$6_0 \rightarrow 6_{-1} - E$	157.048	6.1e-02	-3.8e-03
$5_0 \rightarrow 5_{-1} - E$	157.179	2.2e-01	-5.5e-03
$4_0 \rightarrow 4_{-1} - E$	157.246	5.4e-01	3.2e-02
$1_0 \rightarrow 1_{-1} - E$	157.270	8.2e-01	1.1e+00
$3_0 \rightarrow 3_{-1} - E$	157.272	9.0e-01	1.9e-01
$2_0 \rightarrow 2_{-1} - E$	157.276	1.1e+00	5.3e-01
$5_0 \rightarrow 4_0 - E$	241.700	2.9e-02	1.2e-01
$5_{-1} \rightarrow 4_{-1} - E$	241.767	3.7e-01	1.8e+00
$5_0 \rightarrow 4_0 - A$	241.791	5.0e-01	2.3e+00
$5_4 \rightarrow 4_4 - A$	241.806	5.5e-07	1.2e-06
$5_4 \rightarrow 4_4 - E$	241.829	2.4e-08	1.2e-07
$5_3 \rightarrow 4_3 - A$	241.832	1.1e+00	5.3e-01
$5_3 \rightarrow 4_3 - A$	241.833	2.3e-04	1.3e-03
$5_2 \rightarrow 4_2 - A$	241.842	1.1e-04	6.1e-04
$5_3 \rightarrow 4_3 - E$	241.843	9.7e-06	3.8e-05
$5_{-3} \rightarrow 4_{-3} - E$	241.852	2.3e-06	1.2e-05
$5_1 \rightarrow 4_1 - E$	241.879	6.6e-03	2.7e-02
$5_2 \rightarrow 4_2 - A$	241.887	1.2e-04	5.8e-04
$5_{-2} \rightarrow 4_{-2} - E$	241.904	3.8e-04	1.5e-03
$5_2 \rightarrow 4_2 - E$	241.905	1.5e-02	6.5e-02

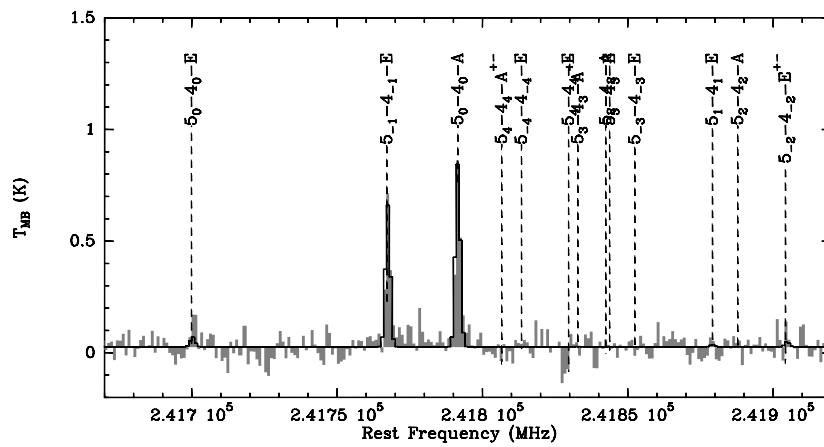
Table 3.16: Line parameters: IRAS 18310–0825.



(a)



(b)

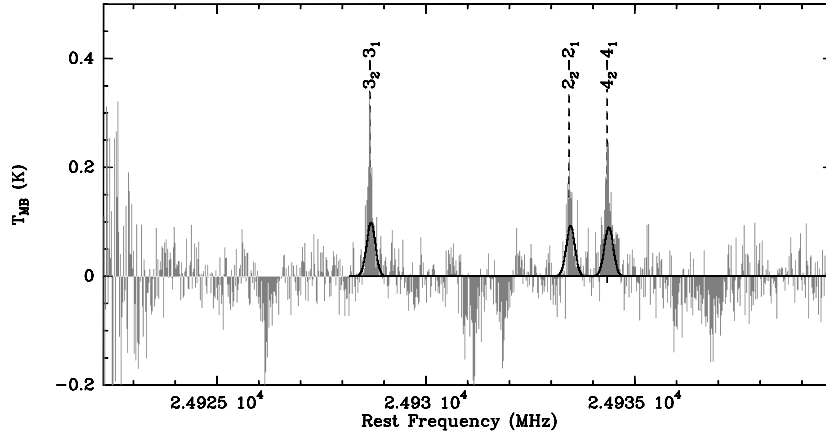


(c)

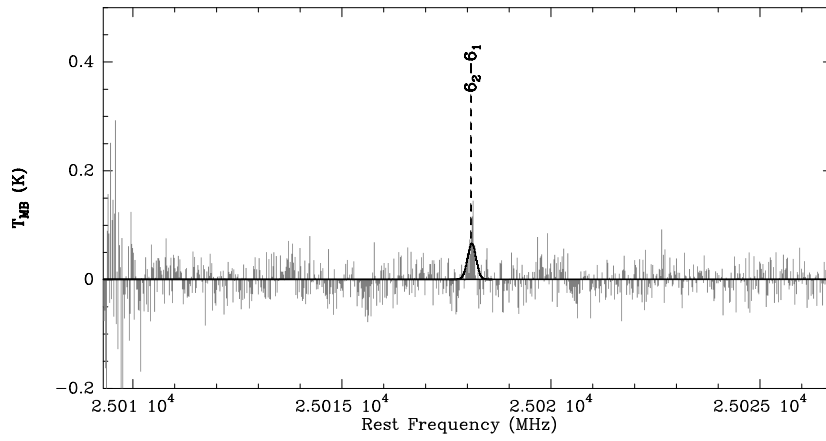
Figure 3.24: Spectra toward IRAS 18310–0825 taken with the IRAM 30 m telescope. The 1 mm and 2 mm data smoothed to the resolution of the 3 mm spectra (Fig. 3.24(a)). All observed lines are labelled. Overlaid in black the synthetic spectra resulting from the fit.

IRAM 19410+2336					
transition	ν (GHz)	τ	T_b	τ	T_b
		1 comp.		2 comp.	
$3_2 \rightarrow 3_1 - E$	24.929	-4.2e-02	1.8e-01	-4.2e-01	4.1e+00
$4_2 \rightarrow 4_1 - E$	24.934	-6.0e-02	2.5e-01	-2.9e-01	2.6e+00
$2_2 \rightarrow 2_1 - E$	24.933	-2.4e-02	9.8e-02	-4.6e-01	4.7e+00
$6_2 \rightarrow 6_1 - E$	25.018	-2.8e-03	1.1e-02	-4.0e-01	4.1e+00
$2_{-1} \rightarrow 1_{-1} - E$	96.739	3.6e-01	3.1e+00	1.2e-01	7.4e+00
$2_0 \rightarrow 1_0 - A$	96.741	5.7e-01	4.9e+00	2.0e-01	9.1e+00
$2_0 \rightarrow 1_0 - E$	96.744	2.7e-01	4.9e-01	2.4e-01	5.4e+00
$2_1 \rightarrow 1_1 - E$	96.755	3.0e-02	1.1e-01	8.4e-02	3.5e+00
$6_0 \rightarrow 6_{-1} - E$	157.048	1.1e-01	-5.2e-03	1.6e+00	6.4e+00
$5_0 \rightarrow 5_{-1} - E$	157.179	3.8e-01	-2.0e-03	1.8e+00	7.0e+00
$4_0 \rightarrow 4_{-1} - E$	157.246	8.5e-01	6.5e-02	1.8e+00	7.4e+00
$1_0 \rightarrow 1_{-1} - E$	157.270	1.1e+00	1.5e+00	7.6e-01	6.8e+00
$3_0 \rightarrow 3_{-1} - E$	157.272	1.3e+00	2.7e-01	1.7e+00	7.5e+00
$2_0 \rightarrow 2_{-1} - E$	157.276	1.4e+00	6.7e-01	1.4e+00	7.3e+00
$5_0 \rightarrow 4_0 - E$	241.700	4.7e-02	2.2e-01	5.1e-01	1.7e+01
$5_{-1} \rightarrow 4_{-1} - E$	241.767	5.5e-01	2.8e+00	8.1e-01	2.5e+01
$5_0 \rightarrow 4_0 - A$	241.791	7.2e-01	3.4e+00	7.9e-01	2.6e+01
$5_4 \rightarrow 4_4 - A$	241.806	1.3e-06	3.2e-06	2.7e-02	5.3e-01
$5_4 \rightarrow 4_4 - E$	241.829	5.9e-08	3.2e-07	4.7e-03	1.2e-01
$5_3 \rightarrow 4_3 - A$	241.832	1.4e+00	6.7e-01	1.4e+00	7.3e+00
$5_3 \rightarrow 4_3 - E$	241.833	4.3e-04	2.7e-03	1.4e-01	4.6e+00
$5_2 \rightarrow 4_2 - A$	241.842	2.1e-04	1.3e-03	1.8e-01	6.2e+00
$5_3 \rightarrow 4_3 - E$	241.843	1.8e-05	7.7e-05	7.0e-02	2.1e+00
$5_{-3} \rightarrow 4_{-3} - E$	241.852	5.1e-06	2.8e-05	3.3e-02	1.0e+00
$5_1 \rightarrow 4_1 - E$	241.879	1.1e-02	4.9e-02	4.0e-01	1.4e+01
$5_2 \rightarrow 4_2 - A$	241.887	2.2e-04	1.2e-03	1.8e-01	6.1e+00
$5_{-2} \rightarrow 4_{-2} - E$	241.904	7.1e-04	2.9e-03	2.4e-01	7.7e+00
$5_2 \rightarrow 4_2 - E$	241.905	2.4e-02	1.1e-01	4.3e-01	1.4e+01

Table 3.17: Line parameters: IRAS 19410+2336.

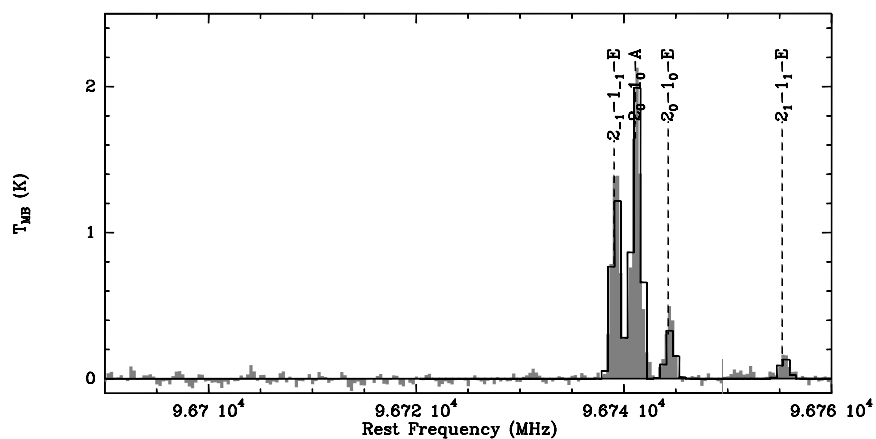


(a)

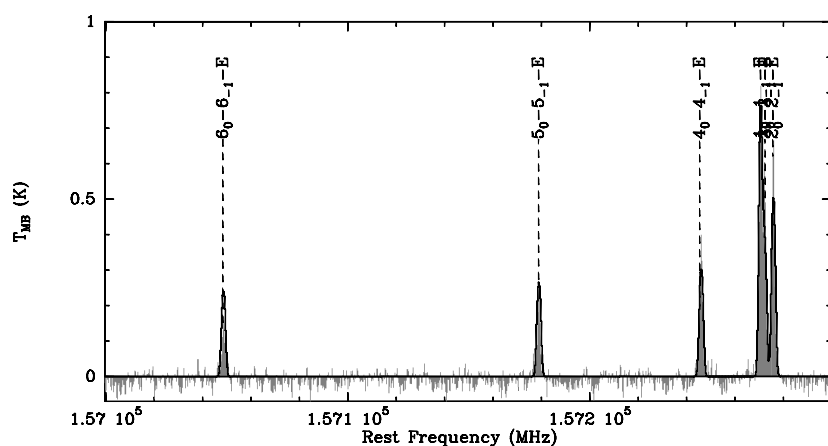


(b)

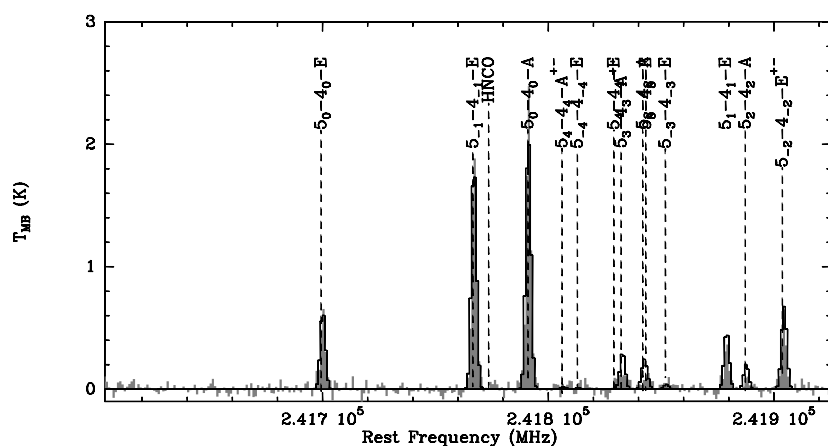
Figure 3.25: Spectra toward IRAS 19410+2336 taken with the 100 m telescope, in frequency switching,. All observed lines are labelled. Overlaid in black the synthetic spectra resulting from the fit.



(a)



(b)



(c)

Figure 3.26: Spectra toward IRAS 19410+2336 taken with the IRAM 30 m telescope. The 1 mm and 2 mm data smoothed to the resolution of the 3 mm spectra (Fig. 3.26(a)). All observed lines are labelled. Overlaid in black the synthetic spectra resulting from the fit.

IRAM 20126+4104					
transition	ν (GHz)	τ	T_b	τ	T_b
		1 comp.		2 comp.	
$2_{-1} \rightarrow 1_{-1} - E$	96.739	2.2e-02	7.6e-01	7.0e-01	3.8e+01
$2_0 \rightarrow 1_0 - A$	96.741	6.0e-02	1.5e+00	8.3e-01	4.7e+01
$2_0 \rightarrow 1_0 - E$	96.744	5.4e-02	2.6e-01	8.7e-01	4.1e+01
$2_1 \rightarrow 1_1 - E$	96.755	6.2e-03	1.1e-01	6.5e-01	3.1e+01
$6_0 \rightarrow 6_{-1} - E$	157.048	1.8e-01	2.6e-01	4.2e+00	4.4e+01
$5_0 \rightarrow 5_{-1} - E$	157.179	2.4e-01	3.9e-01	4.3e+00	4.5e+01
$4_0 \rightarrow 4_{-1} - E$	157.246	2.8e-01	5.0e-01	4.2e+00	4.5e+01
$1_0 \rightarrow 1_{-1} - E$	157.270	1.2e-01	7.2e-01	1.8e+00	4.0e+01
$3_0 \rightarrow 3_{-1} - E$	157.272	2.7e-01	5.7e-01	3.7e+00	4.5e+01
$2_0 \rightarrow 2_{-1} - E$	157.276	2.3e-01	5.8e-01	2.9e+00	4.4e+01
$5_0 \rightarrow 4_0 - E$	241.700	3.2e-02	7.0e-01	3.9e+00	6.3e+01
$5_{-1} \rightarrow 4_{-1} - E$	241.767	1.0e-01	2.8e+00	4.3e+00	6.4e+01
$5_0 \rightarrow 4_0 - A$	241.791	1.6e-01	3.8e+00	4.3e+00	6.6e+01
$5_4 \rightarrow 4_4 - A$	241.806	1.2e-04	7.2e-04	5.3e-01	2.9e+01
$5_4 \rightarrow 4_4 - E$	241.829	7.3e-06	8.6e-05	3.9e-01	2.2e+01
$5_3 \rightarrow 4_3 - A$	241.832	2.3e-01	5.8e-01	2.9e+00	4.4e+01
$5_3 \rightarrow 4_3 - E$	241.833	4.3e-03	7.3e-02	1.5e+00	5.3e+01
$5_2 \rightarrow 4_2 - A$	241.842	2.6e-03	4.6e-02	2.2e+00	5.8e+01
$5_3 \rightarrow 4_3 - E$	241.843	2.8e-04	3.6e-03	1.5e+00	5.1e+01
$5_{-3} \rightarrow 4_{-3} - E$	241.852	1.3e-04	1.8e-03	1.2e+00	4.5e+01
$5_1 \rightarrow 4_1 - E$	241.879	1.5e-02	3.5e-01	3.5e+00	6.2e+01
$5_2 \rightarrow 4_2 - A$	241.887	2.8e-03	4.6e-02	2.2e+00	5.8e+01
$5_{-2} \rightarrow 4_{-2} - E$	241.904	2.1e-03	3.0e-02	2.8e+00	6.0e+01
$5_2 \rightarrow 4_2 - E$	241.905	2.6e-02	5.7e-01	3.0e+00	6.2e+01

Table 3.18: Line parameters: IRAS 20126+4104.



Figure 3.27: Spectra toward IRAS 20126+4104 taken with the IRAM 30 m telescope. The 1 mm and 2 mm data smoothed to the resolution of the 3 mm spectra (Fig. 3.27(a)). All observed lines are labelled. Overlaid in black the synthetic spectra resulting from the fit.

IRAS 23139+5939					
transition	ν (GHz)	τ	T_b	τ	T_b
		1 comp.		2 comp.	
$2_{-1} \rightarrow 1_{-1} - E$	96.739	9.3e-02	8.5e-01	1.9e-01	5.9e+00
$2_0 \rightarrow 1_0 - A$	96.741	1.7e-01	1.6e+00	4.7e-01	8.8e+00
$2_0 \rightarrow 1_0 - E$	96.744	5.0e-02	1.1e-01	3.9e-01	3.0e+00
$2_1 \rightarrow 1_1 - E$	96.755	6.1e-03	2.0e-02	9.1e-02	1.6e+00
$6_0 \rightarrow 6_{-1} - E$	157.048	1.9e-02	-2.0e-03	1.0e+00	1.4e+00
$5_0 \rightarrow 5_{-1} - E$	157.179	6.8e-02	-6.0e-03	1.6e+00	2.2e+00
$4_0 \rightarrow 4_{-1} - E$	157.246	1.7e-01	-4.5e-03	1.9e+00	3.0e+00
$1_0 \rightarrow 1_{-1} - E$	157.270	2.8e-01	3.6e-01	8.0e-01	5.4e+00
$3_0 \rightarrow 3_{-1} - E$	157.272	3.0e-01	3.8e-02	1.9e+00	3.7e+00
$2_0 \rightarrow 2_{-1} - E$	157.276	3.6e-01	1.7e-01	1.5e+00	4.4e+00
$5_0 \rightarrow 4_0 - E$	241.700	7.6e-03	3.4e-02	4.4e-01	5.4e+00
$5_{-1} \rightarrow 4_{-1} - E$	241.767	1.2e-01	6.1e-01	9.7e-01	1.3e+01
$5_0 \rightarrow 4_0 - A$	241.791	1.7e-01	8.7e-01	1.2e+00	1.6e+01
$5_4 \rightarrow 4_4 - A$	241.806	1.6e-07	3.8e-07	4.6e-04	5.1e-03
$5_4 \rightarrow 4_4 - E$	241.829	8.2e-09	4.2e-08	1.1e-04	1.7e-03
$5_3 \rightarrow 4_3 - A$	241.832	3.6e-01	1.7e-01	1.5e+00	4.4e+00
$5_3 \rightarrow 4_3 - E$	241.833	8.3e-05	4.9e-04	1.8e-02	2.4e-01
$5_2 \rightarrow 4_2 - A$	241.842	3.7e-05	2.2e-04	2.6e-02	3.7e-01
$5_3 \rightarrow 4_3 - E$	241.843	2.5e-06	1.1e-05	5.0e-03	8.3e-02
$5_{-3} \rightarrow 4_{-3} - E$	241.852	7.7e-07	4.1e-06	1.4e-03	2.9e-02
$5_1 \rightarrow 4_1 - E$	241.879	1.8e-03	7.8e-03	2.6e-01	3.3e+00
$5_2 \rightarrow 4_2 - A$	241.887	4.0e-05	2.1e-04	2.6e-02	3.6e-01
$5_{-2} \rightarrow 4_{-2} - E$	241.904	8.3e-05	3.9e-04	3.7e-02	6.7e-01
$5_2 \rightarrow 4_2 - E$	241.905	4.4e-03	1.9e-02	2.4e-01	3.0e+00

Table 3.19: Line parameters: IRAS 23139+5939.



Figure 3.28: Spectra toward IRAS 23139+5939 taken with the IRAM 30 m telescope. The 1 mm and 2 mm data smoothed to the resolution of the 3 mm spectra (Fig. 3.28(a)). All observed lines are labelled. Overlaid in black the synthetic spectra resulting from the fit.

Chapter 4

IRAS 05358+3543: a high mass star forming cluster.

The content of this chapter is based on Leurini, S., Schilke, P., Beuther, H., et al. to be submitted to A&A

4.1 Introduction

IRAS 05358+3543, also known in literature as S233IR, is part of a sample of 69 high-mass protostellar objects (HMPOs) studied in great detail in recent years (Sridharan et al. 2002; Beuther et al. 2002b,c,d). At a distance of 1.8 kpc (Snell et al. 1990), IRAS 05358+3543 has a luminosity of $6300 L_{\odot}$ and a dust temperature of 47 K (Sridharan et al. 2002); strong high mass star formation activity is evidenced by emission in Class II CH_3OH (Minier et al. 2000) and H_2O (Tofani et al. 1995) masers. Outflow activity has been first reported by Snell et al. (1990) in CO; more recently, Beuther et al. (2002a) have found at least three highly-collimated outflows in CO and SiO, the most prominent of which is more than a parsec in length and massive ($M > 10 M_{\odot}$). Two of them form a quadrupolar system, most likely originating from adjacent protostars; PdBI continuum data (Beuther et al. 2002a) resolve the mm core at the center of the quadrupolar outflow in three massive ($75 M_{\odot} < M < 100 M_{\odot}$) condensations. A number of other outflows is seen by McCaughrean et al. (2005) in H_2 , confirming the intense star formation activity associated with IRAS 05358+3543.

In this chapter, we present an interferometric analysis of the region at mm wavelengths in several molecular transitions and in the continuum. While the former study by Beuther et al. (2002a) was aimed at the large scale outflow structure, our analysis will be particularly dedicated to the understanding of the physical conditions at the very center part of the region, close to the massive protostars.

4.2 Observations with the Plateau de Bure Interferometer (PdBI)

IRAS 05358+3543 was observed with the IRAM Plateau de Bure Interferometer (Guilloteau et al. 1992) in four tracks between January and October 2003 in one frequency setup in the B and D configurations of the array. Two observations, in January and October, were performed with only 5 antennae. The 3mm receivers were used in single side mode and tuned to 96.6 GHz; the 1mm receivers, in double side mode, were tuned to 241.85 GHz, (USB). The C^{34}S and the torsionally excited CH_3OH quartet ($2_k \rightarrow 1_k$)¹ were covered using two correlator units of 80 MHz bandwidth. One 320 MHz unit was placed to obtain a continuum measurement at 3mm. The CH_3OH $5_k \rightarrow 4_k$ band, the HDO ($2_{1,1} \rightarrow 2_{1,2}$) and the SO_2 ($5_{2,4} \rightarrow 4_{1,3}$) lines were observed with four units of 160 MHz bandwidth, which were also used to obtain a continuum measurement at 1.3mm. The same configuration of the correlator units allowed the observation of CH_3CN $13_K \rightarrow 12_K$ band in the LSB at 239 GHz. The observations were performed in the MOSAIC mode, with seven fields covering the whole source in a hexagonal pattern with a center field. The reference center is RA[2000] 05:19:13.0 and Dec[2000] 34:45:54; the v_{LSR} is -17.6 km s^{-1} . Details on the system temperatures, resolutions and synthesized beam sizes are given in Table 4.1.

Molecular transition	Rest freq. (GHz)	HPBW (")	T_{sys} (K)	Res. (kms^{-1})
$\text{C}^{34}\text{S}(2 \rightarrow 1)$	96.412	4.42×3.2	100–150	0.48
$\text{CH}_3\text{OH}(2_{k,v_t=1} \rightarrow 1_{k,v_t=1})$	96.500	4.35×3.14	100–150	0.48
$\text{CH}_3\text{CN}(13_K \rightarrow 12_K)$	239.100	3.13×1.9	300–600	0.625
$\text{HDO}(2_{1,1} \rightarrow 2_{1,2})$	241.561	2.76×1.43	300–500	0.77
$\text{SO}_2(5_{2,4} \rightarrow 4_{1,3})$	241.616	2.67×1.37	300–500	0.77
$\text{CH}_3\text{OH}(5_{k,v_t=0} \rightarrow 4_{k,v_t=0})$	241.800	2.58×1.35	300–500	0.77

Table 4.1: Observational parameters of spectral lines observations.

4.3 Observational results

Continuum emission

A continuum map at mm wavelengths of the main core of IRAS 05358+3543 has been already presented by Beuther et al. (2002a). They resolve the region into three sub-sources, with angular separation between $4''$ and $6''$, and label them mm1, mm2 and mm3. However, due to poor summer weather conditions, their analysis was based only on the 3mm data with

¹The projection of the angular momentum quantum number k runs from $-J$ to $+J$ for E -type CH_3OH . For A -type CH_3OH a capital K is used, with $0 < K \leq J$. When referring in one expression to levels from both species, lowercase k is used.

a resolution of $4'' \times 3''$ (7200×5400 AU). While at 3mm we reached a similar resolution (see Table.4.1), we can zoom deeper into the core at 241 GHz, with a resolution $1.26'' \times 0.84''$ (2200×1500 AU), PA(-127°) in uniform weighting.

At higher resolution, the data reveal two other millimeter condensations (see Fig. 4.1(a)), whose positions and sizes have been determined by fitting two-dimensional Gaussians to the data and which we label mm4 and mm5; source mm2 splits up into two condensations, mm2a and mm2b. Source mm2b, mm4 and mm5 are associated, within less than $1''$, with H_2O maser spots detected by Tofani et al. (1995). In 1999, Beuther et al. (2002d) detected only one of the known maser features. Minier et al. (2000) detected three clusters of methanol masers at 6.7 GHz; the detection indicated in Fig. 4.1(a) consists of several features along an elongated structure of 40 mas (100 AU) and with a clear velocity gradient, which they interpret as associated to a disk. This structure is perpendicular to one of the outflows in the region (see Fig. 4.1(a)).

With our resolution, the main core, mm1, seems to be extended and just at the verge of splitting up; for this reason, given the high signal-to-noise ratio in our data, we have restored the Clean components with a smaller clean beam ($0.7'' \times 0.7''$) than that used in Fig. 4.1(a). This is justified by the fact that the data from the longest baseline reach a resolution of $0.48''$. With a beam of $0.7'' \times 0.7''$, the condensation splits up in two sources, mm1a and mm1b, whose parameters are given in Table 4.3; the data also reveal another millimeter condensation which we label mm6 (see Table 4.3). We believe the new feature, mm6, is real, and not an artifact of super-resolution used in restoring the Clean components, since the rms in the map is 0.004 Jy/beam and mm6 is a 3σ detection. Moreover mm1b coincides with the CH_3OH maser emission detected by Minier et al. (2000) and mm6 with the H_2O maser emission reported by Tofani et al. (1995). However, higher resolution is needed to confirm these results and here after the values obtained with a Clean beam of $1.26'' \times 0.84''$ will be discussed. Observations with the Submillimeter Array (SMA) on top of Mauna Kea, at 340 GHz, are scheduled for the winter 2004 observing period with which a angular resolution below $1''$ will be reached.

Assuming optically thin dust emission, masses and column densities have been calculated using the formulae 3.3-3.4, for a dust temperature of 50 K; a value of two is used for β . Visual extinctions are calculated using $A_v = N_{\text{H}_2} / 0.94 \times 10^{21}$ (Frerking et al. 1982). Results are listed in Table 4.3. Mass and column density associated with mm5 are higher than what expected from the millimeter peak flux because of the extended emission associated to it.

Our results differ significantly from the values found by Beuther et al. (2002a), who derived masses ranging between 100 and $73 M_\odot$. This can be attributed to the stronger spatial filtering effect of the interferometer at shorter wavelengths. Column densities are, on the other hand, similar or bigger than their results, which is due to our smaller beam. Moreover, at 1 mm the continuum emission could start being optically thick.

Uncertainties on the derived parameter are hard to quantify as they depend on the dust opacity index and dust-to-gas ratio assumed in the calculations. As already discussed in § 3.4, the

source	R.A. [J2000]	Dec. [J2000]	maj.×min. [″]	peak [mJy beam ⁻¹]	flux [mJy]	M [M _⊙]	N _{H₂} [10 ²⁴]	A _v
resolution: 1.26″×0.84″ ^a								
mm1	05:39:13.09	35:45:50.79	2.15×1.84	57	203	22	6	6000
mm2a	05:39:12.74	35:45:51.16	2.14×1.57	33	80	9	3	2800
mm2b	05:39:12.82	35:45:50.58	1.30×1.30	30	20	2	1	1400
mm3	05:39:12.50	35:45:54.93	1.80×1.40	40	50	5	2	2300
mm5	05:39:13.11	35:45:48.47	3.59×1.69	19	50	5	1	1000
mm4	05:39:12.93	35:45:49.10	1.80×1.56	27	40	4	2	1900
super-resolution: 0.7″×0.7″ ^b								
source	R.A. [J2000]	Dec. [J2000]	maj.×min. [″]	peak [mJy beam ⁻¹]	flux [mJy]	M [M _⊙]	N _{H₂} [10 ²⁴]	A _v
mm1a	05:39:13.07	35:45:51.16	1.02×0.84	44	513	5	7	7000
mm1b	05:39:13.12	35:45:50.52	1.50×0.70	28	583	6	6	6500
mm2a	05:39:12.75	35:45:51.30	1.76×0.90	25	45	5	4	3300
mm2b	05:39:12.82	35:45:50.32	1.20×0.80	18	31	3	4	3800
mm3	05:39:12.49	35:45:54.84	1.14×0.90	36	40	4	4	4600
mm5	05:39:13.04	35:45:48.56	1.26×0.98	18	24	3	2	2300
mm4	05:39:12.91	35:45:49.28	1.53×1.12	20	35	4	2	2400
mm6	05:39:13.00	35:45:49.96	1.10×0.79	18	20	2	3	2700

^a see Fig. 4.1(a)

^b see Fig. 4.1(b)

Table 4.2: Core parameters derived from the PdBI continuum observations.

opacity index β is assumed to be close to 2 in massive star forming regions, but values lower than this are found (Natta et al. 2004). Also, the dust temperature for the condensations might be higher than 50 K. From the 3 mm and 1 mm data, values of β can be derive from

$$\frac{S_{\nu_{241} \text{ GHz}}}{S_{\nu_{96} \text{ GHz}}} = \left(\frac{241}{96}\right)^{3+\beta} \times \frac{\exp\left(\frac{h\nu_{96} \text{ GHz}}{kT_d}\right) - 1}{\exp\left(\frac{h\nu_{241} \text{ GHz}}{kT_d}\right) - 1} \quad (4.1)$$

β ranges between 1, at the outer edge of the cores, and 0.3, at the dust condensations; however, the 1 mm data are severely affected by spatial filtering and results are not reliable. A detailed modelling of the continuum emission in the cluster is necessary once more frequency points are collected.

Masses and column densities are derived here with the assumption that all emission comes from the dust, as no centimeter emission at 3.6 cm is detected down to 1 mJy with the Very Large Array (Sridharan et al. 2002). However, hypercompact HII regions (≤ 2000 AU, Tieftrunk et al. 1997) can have a very weak flux at centimeter wavelengths but still contribute significantly to the total emission in the millimeter range (Keto 2003) if their emission is still

optically thick at these frequencies. The millimeter condensation mm1 is the most massive and probably more evolved in the cluster; therefore, at least for this case, it is better to investigate different scenarios and give limits to the values listed in Table 4.3. From the observed fluxes at 241 GHz and 115 GHz (Beuther et al. 2002a), one can derive the contribution to the total flux due to free-free emission and to the dust, assuming an optically thick free-free emission; this is the worst scenario and leads to a maximum contribution by free-free emission to give range to the masses and column densities derived.

$$\begin{aligned} S_{\text{obs}241\text{GHz}} &= S_{\text{ff}241\text{GHz}} + S_{\text{dust}241\text{GHz}} \\ S_{\text{obs}115\text{GHz}} &= S_{\text{ff}115\text{GHz}} + S_{\text{dust}115\text{GHz}} \end{aligned} \quad (4.2)$$

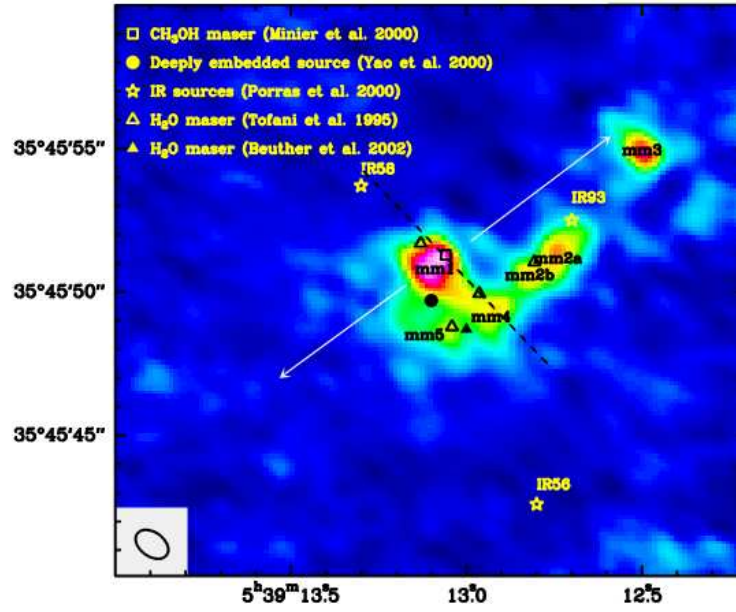
and

$$\begin{aligned} S_{\text{obs}241\text{GHz}} &= S_{\text{ff}115\text{GHz}} \times \left(\frac{\nu_{241\text{ GHz}}}{\nu_{115\text{ GHz}}} \right)^2 + S_{\text{dust}115\text{GHz}} \times \left(\frac{\nu_{241\text{ GHz}}}{\nu_{115\text{ GHz}}} \right)^{3+\beta} \\ S_{\text{obs}115\text{GHz}} &= S_{\text{ff}115\text{GHz}} + S_{\text{dust}115\text{GHz}} \end{aligned} \quad (4.3)$$

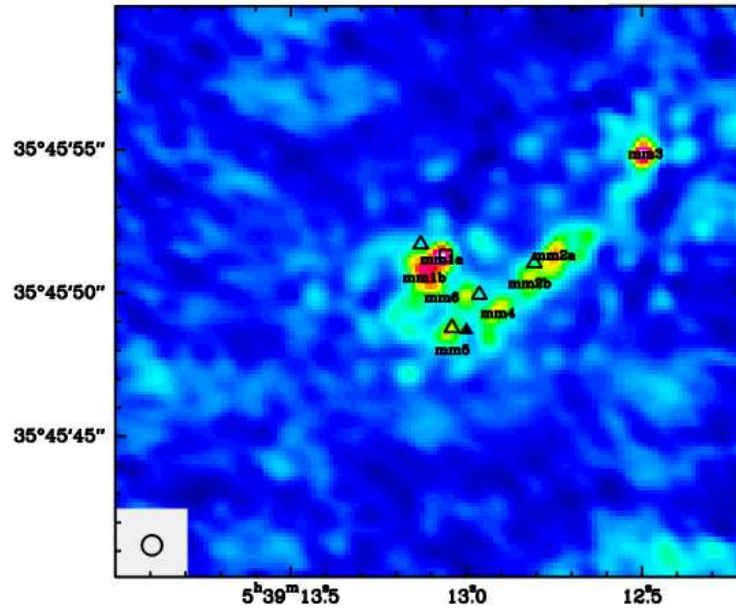
Solving equation 4.3 leads to a dust flux of 114 mJy at 241 GHz; then the gas mass of mm1 is $12 M_{\odot}$, the column density $6 \times 10^{24} \text{ cm}^{-2}$ and the visual extinction 6000. The true values of these quantities are therefore in between those derived in Table 4.3, under the assumption that all the flux at 1 mm is due to the dust, and the values just derived assuming that the free-free emission at 1 mm is still in the optically thick regime.

Molecular emission

While the 1 mm continuum data have a very high signal-to-noise ratio and allow us to reduce the data in uniform weighting, natural weighting is used for the line data, thus reaching lower spatial resolution. We detected several complex (CH_3OCH_3 , $\text{C}_2\text{H}_5\text{CN}$, CH_3CN , CH_3OH $v_t=0,1$, HNCO) and deuterated (HDO) molecular species (see Fig. 4.2) towards the main millimeter condensation of the cluster (see Fig. 4.3- 4.4); however, given the low resolution of the line data at 3 mm and 1 mm, compared to the continuum map at 1 mm, an exact location of the emitting region is not possible. Methanol and methyl cyanide (CH_3CN) transitions show double peaked line profiles towards mm1; however the low linear resolution of the data ($\sim 4600 \times 2400 \text{ AU}$) does not allow us to perform any kinematic studies on the source.



(a)



(b)

Figure 4.1: The colour scale shows the 1.3 mm continuum emission towards IRAS 05358+3543 as observed with the PdBI with a Clean beam of $1.26'' \times 0.84''$ (a) and $0.7'' \times 0.7''$ (b). In Fig. 4.1(a) the white arrows outline the high velocity outflow detected in CO by Beuther et al. (2002a), while the black, dashed line depicts (not to scale) the structure along which the 6.7 GHz CH_3OH maser features are found by Minier et al. (2000).

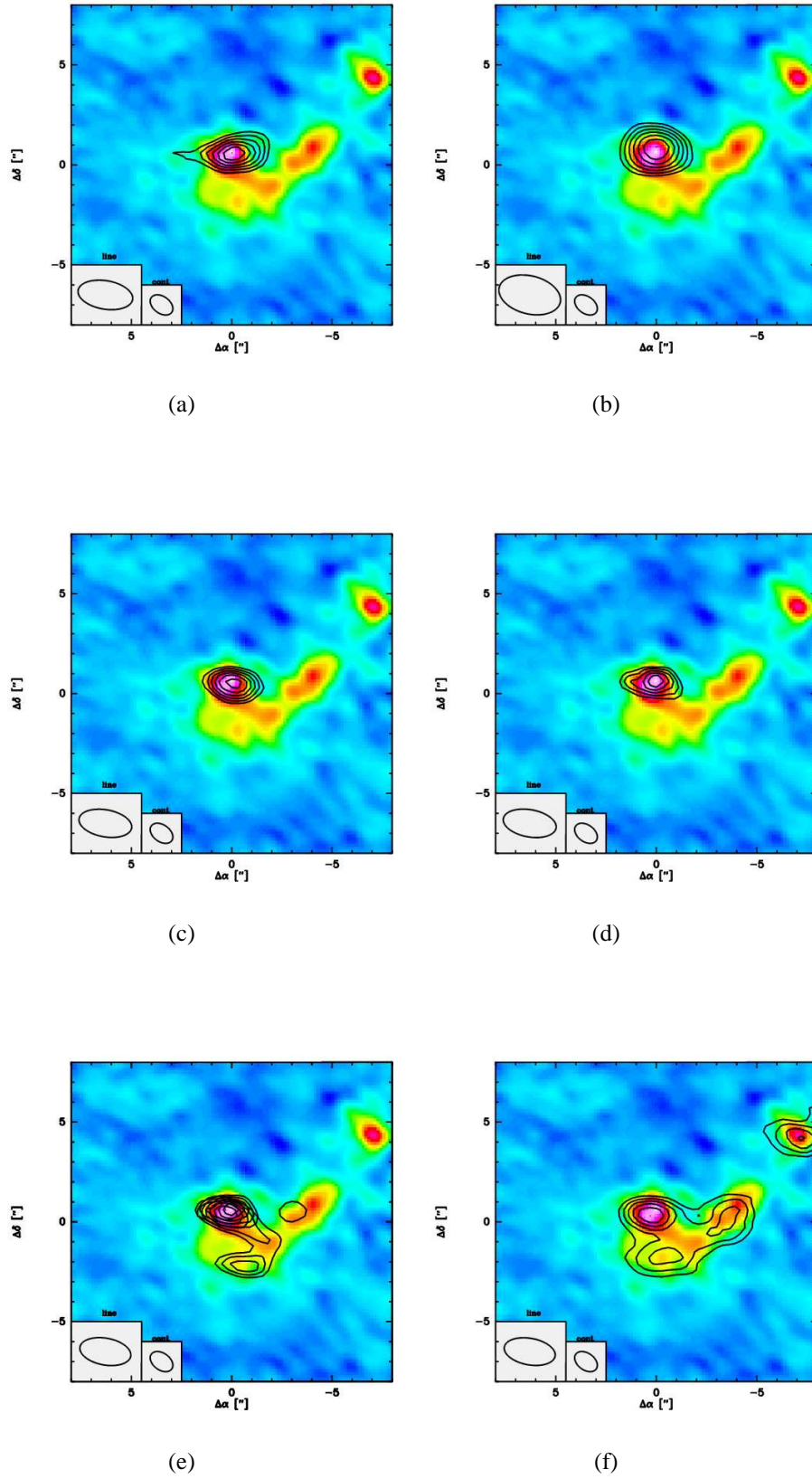


Figure 4.2: In colour scale the 1 mm continuum emission. The black contours show the integrated line intensity of the $2_{1,1} \rightarrow 2_{1,2}$ HDO transition (a), of the $13_2 \rightarrow 12_2$ CH₃CN (b), the $11_0 \rightarrow 10_0$ HNCO (c), of the $5_{2,4} \rightarrow 4_{1,3}$ SO₂ (d), of the CH₃OCH₃ ($13_{1,13} \rightarrow 12_{0,12}$) (e) and of the C₂H₅CN ($27_{8,20} \rightarrow 26_{8,19}$) (f). Level contours are arbitrary.

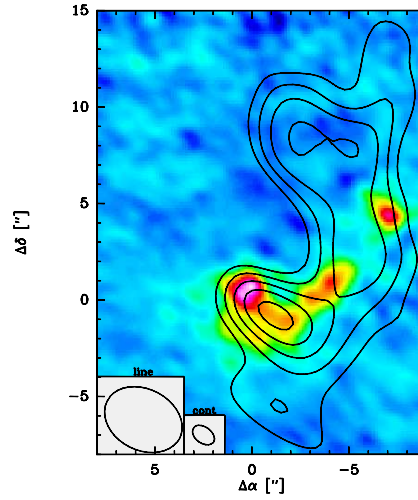


Figure 4.2: continued: In colour scale the 1 mm continuum emission. The black contours show the integrated line intensity of the $\text{C}^{34}\text{S}(2 \rightarrow 1)$. Level contours are arbitrary.

Only the less excited CH_3OH lines, $|k| = 0, 1 - A, E$, $|k| = 2 - E$, and C^{34}S show extended emission. Fig. 4.5(a) shows the map of the integrated intensity of the $5_0 \rightarrow 4_0 - A$ CH_3OH line, overlaid on the 1 mm continuum emission. The line clearly peaks at the position of the main millimeter condensation mm1, even if the spatial resolution in the spectral data is not high enough to give definitive proof, at the methanol maser position, which, in the continuum analysis we labelled mm1a. The emission is then extended towards mm2 but the second emission peak is shifted from mm2 by $(-1.6'', 0.5'')$. Therefore, we label the methanol peak positions $\text{CH}_3\text{OH} -1$, the one coinciding with mm1a, and $\text{CH}_3\text{OH} -2$, the one offset by mm2. Two other emission peaks are found at $(-11.1'', 5.1'')$ and $(5.4'', -7.8'')$, which we label $\text{CH}_3\text{OH} -\text{NW}$ and $\text{CH}_3\text{OH} -\text{SE}$ respectively; these two features seem to be associated with the outflows detected by Beuther et al. (2002a) (see Fig. 4.5(b)). However, CH_3OH emission does show almost no shift from the system velocity of the source (Table 4.4) and, in $\text{CH}_3\text{OH} -\text{SE}$, linewidths are not broad as expected in outflows (Fig. 4.9(a)-4.9(b)). A 11 km s^{-1} broad component is detected in the $5_0 \rightarrow 4_0 - A$ and $5_{-1} \rightarrow 4_{-1} - E$ transitions towards the $\text{CH}_3\text{OH} -\text{NW}$ position. However, also SiO does not show broad linewidths or shift in velocity at these positions ($\Delta v \sim 2.7 \text{ km s}^{-1}$ at both positions; $v = 1.3 \text{ km s}^{-1}$ at $(-11.1'', 5.1'')$, $v = -2.4 \text{ km s}^{-1}$ at $(5.4'', -7.8'')$). However, spatial filtering affects severely the data at 1 mm and any analysis on the extended emission needs the zero spacing information; a proposal to map the region in the $5_k \rightarrow 4_k$ CH_3OH lines was accepted for the summer 2004 observing period at the IRAM 30 m telescope but not performed due to poor weather conditions. The project has been now accepted again for the the winter 2004 observing period. The $\text{CH}_3\text{OH} -\text{SE}$ emission position is found at the tip of the south-eastern lobe of the high velocity outflow

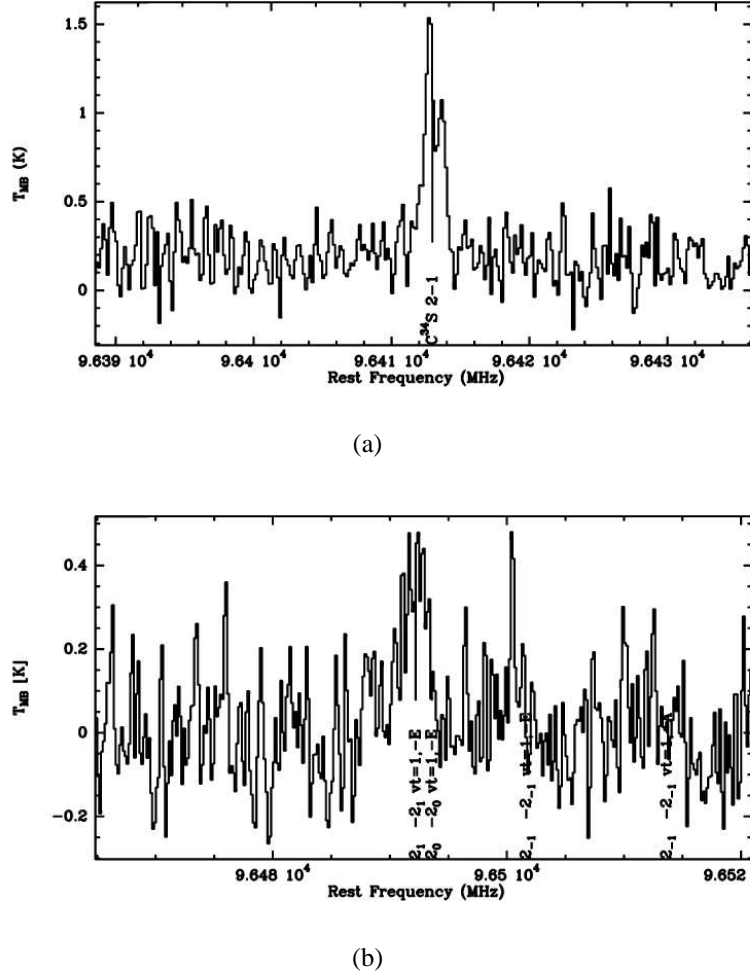
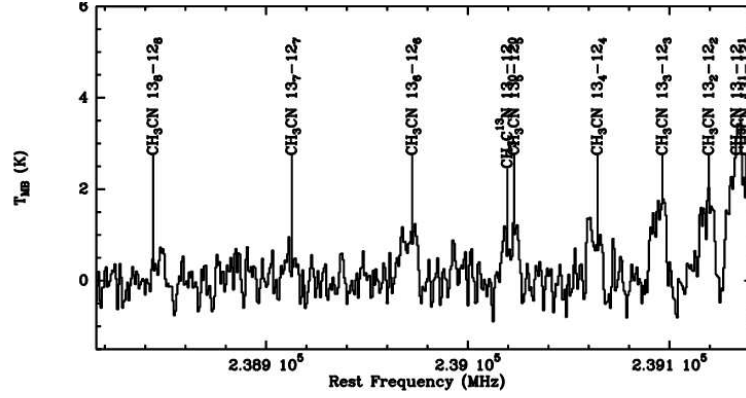


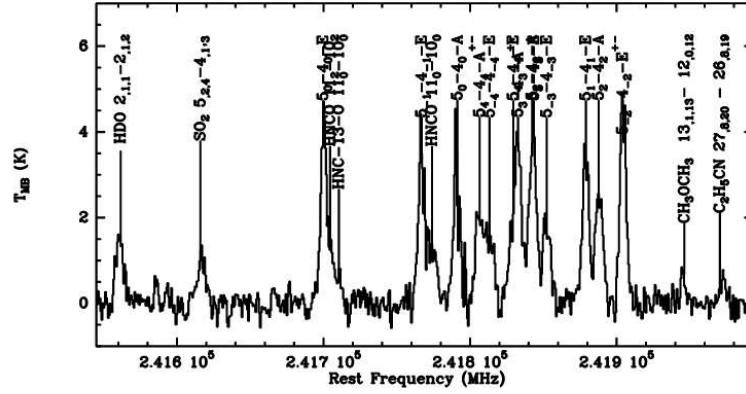
Figure 4.3: $2_k \rightarrow 1_k$ $v_t = 1$ CH_3OH (a) and C^{34}S (b) spectra towards mm1.

in CO (indicated by black arrows in Fig. 4.5(b)), where also shocked SiO is observed. The CH_3OH -NW position is also associated with SiO emission; whether SiO and CH_3OH at this position belong to the outflow detected in SiO by Beuther et al. (2002a) (white arrows on the right side of Fig. 4.5(b)) or to the high velocity outflow in CO has to be further investigated. As discussed by McCaughrean et al. (2005), ambiguity is also found in the H_2 emission: Porras et al. (2000) suggest that knots N4A and N3A (see Fig. 4.5(b)) are possibly related to the high velocity CO outflow, while McCaughrean et al. (2005) interpret N3A as belonging to the SiO outflow.

The association of CH_3OH and SiO emission is however interesting as both molecular species reside in dust grains. Since methanol is believed to be found in the mantles (Grim et al. 1991; Dartois et al. 1999a) and SiO in the cores (Caselli et al. 1997; Schilke et al. 1997), a possible, tempting interpretation of the spatial distribution of the two species is that CH_3OH is tracing less energetic events than SiO in the same outflow or that its emission is a tracer of fossil



(a)



(b)

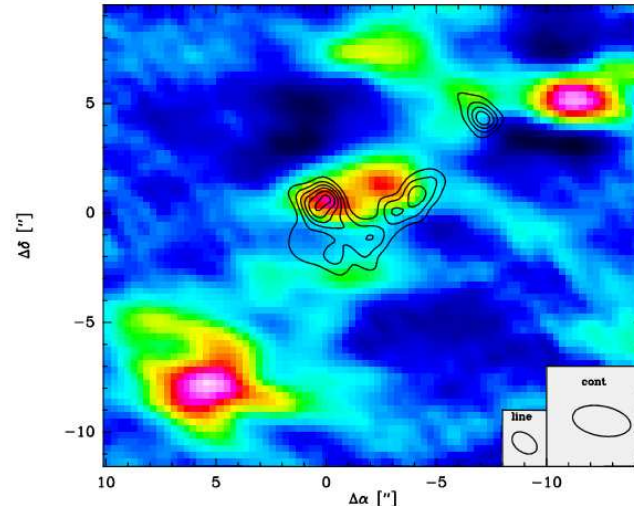
Figure 4.4: $\text{CH}_3\text{CN } 13_K \rightarrow 12_K$ (a) and $5_K \rightarrow 4_K$ CH_3OH (b) spectra towards mm1.

outflow in the region. Our data are, however, heavily corrupted by negative features caused by missing spacings and any further interpretation of the extended emission needs the zero spacing information.

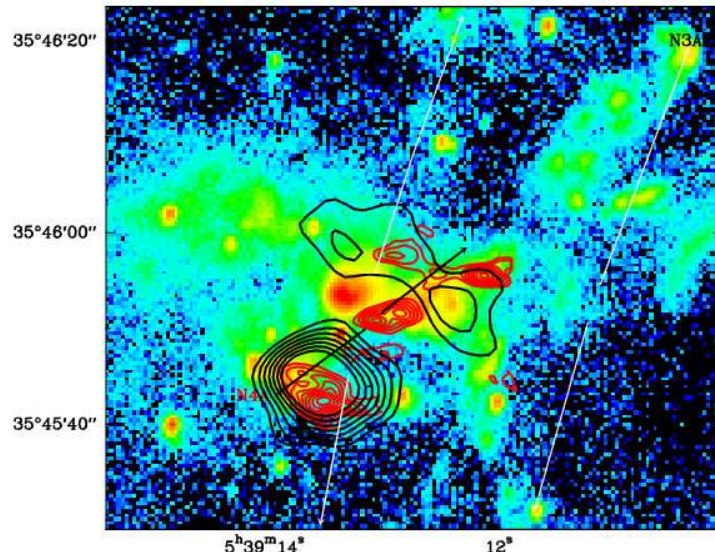
The $\text{CH}_3\text{OH } 2_{k,v_{l=1}} \rightarrow 1_{k,v_{l=1}}$ distribution seems similar to the continuum distribution, being, together with the $\text{C}_2\text{H}_5\text{CN } (27_{8,20} \rightarrow 26_{8,19})$ transition, the only line possibly showing up at mm3 as well as at the other cores. However, given the relatively low resolution of the 3 mm data, compared to the one at 1 mm, and the low signal-to-noise ratio, this is a tentative detection (1σ) and needs high resolution and high signal-to-noise $v_l=1$ data to be confirmed. From the linewidths of the CH_3OH observed transitions and the clump sizes, virial masses for mm1 and mm2 can be estimated using the relation (see e.g. MacLaren et al. 1988)

$$M_{\text{vir}} = 0.509 \left(\frac{d}{\text{kpc}} \right) \left(\frac{\Theta_s}{\text{arcsec}} \right) \left(\frac{\Delta v_{1/2}^2}{\text{kms}^{-1}} \right) [M_\odot] \quad (4.4)$$

where $\Delta v_{1/2}$ is the line FWHM as from Table 4.3. Here, Θ_s is the continuum source size, as



(a)



(b)

Figure 4.5: **(a)** In colour scale the $5_0 \rightarrow 4_0 - A$ CH_3OH line integrated intensity. Levels go from $0.027 \text{ mJy beam}^{-1}$ (3σ) to 0.20 by step of 2σ . Overlaid in contours the continuum emission at 1 mm (levels: $0.015 \text{ mJy beam}^{-1}$ to 0.056 by step of 0.006 (3σ)). **(b)** In color scale the H_2 data (McCaughrean et al. 2005) towards IRAS 05358; white arrows show the CO and SiO outflows detected by Beuther et al. (2002a); the black arrows the high velocity CO outflow. Black contours show the SiO shocked emission and the red one the $5_0 \rightarrow 4_0 - A$ CH_3OH integrated intensity.

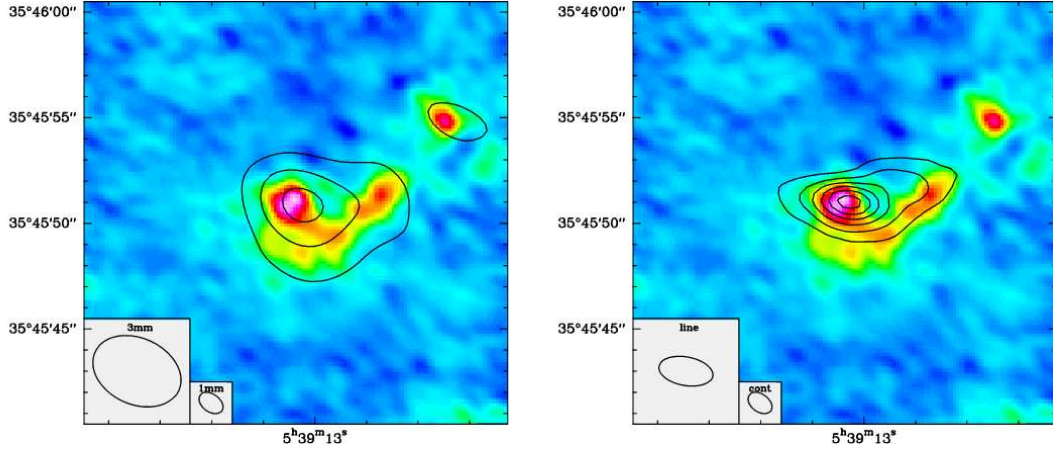


Figure 4.6: In grey scale we present the 1 mm continuum map of IRAS 05358, while thick contours show the integrated intensity (1σ , 2σ , 3σ contours) of the $2_1 \rightarrow 1_1$ $v_t=1$ $\text{CH}_3\text{OH}-E$ line (a) and the integrated intensity (contours are by step of 6σ) of the $5_2 \rightarrow 4_2$ $\text{CH}_3\text{OH}-A$ line (b). At the bottom left, the beam sizes of the PdBI data are shown.

the methanol emitting region are unresolved with our beam. Results are shown in Table 4.3; they are in good agreement with the values found from the dust emission (Table 4.3). The dust condensation mm3 is not analysed because, even if methanol is present at that position too, data are too contaminated by spatial filtering effect to be analysed.

core	$\Delta v_{1/2}$ km s^{-1}	Θ_s "	M_{vir} M_{\odot}	M_{dust} M_{\odot}
$\text{CH}_3\text{OH}-1$	6.0	1	33	22
$\text{CH}_3\text{OH}-2$	3.8	1	13	16

Table 4.3: Virial masses estimated from CH_3OH transitions.

4.4 Physical parameters

Methanol excitation

In chapter 1, the diagnostic properties of CH_3OH have been investigated over a range of physical parameters typical of high-mass star-forming regions, finding CH_3OH to be a good tracer of high-density environments and sensitive to the kinetic temperature. In chapter 3, the initial level dataset (up to $(J,k)=9$), incomplete in energy above 100 K, has been extended to include all the levels up to $(J=14, k=13)$ in the torsional ground state and up to $(J,k)=9$ for the first torsionally excited state, in order to apply the analysis of methanol spectra to sources

in more evolved stages of star formation, where high temperatures are expected. The main results of the calculations on this new dataset are

- IR vibrational pumping is shown to mimic the effect of excitation by collisions (see Fig. 3.3(a));
- a promising way to break the degeneracy is by observation of vibrationally or torsionally excited methanol lines and reliable determinations of density **and** kinetic temperature are possible only when $v_t=1$ bands are observed.

The fitting procedure used to analyse the CH₃OH data is described in Leurini et al. (2004); free parameters are the kinetic temperature and the spatial density of the gas, the CH₃OH-*E* and -*A* column densities and source size. A single component model is used to fit the data towards CH₃OH -1, CH₃OH -2, CH₃OH -NW and CH₃OH -SE. Source sizes are estimated from the line maps and are bigger than the 1 mm beam for all the four positions. An external radiation field, described by a diluted grey-body (equation 3.1) has been included in the model for CH₃OH -1 and CH₃OH -2. The dust optical depth at 100 μ m is derived from our 1 mm continuum data using equation 3.2 and assuming that the emission at 1 mm is optically thin; values obtained are $\tau_{1\text{mm}} = 0.018$ and $\tau_{100\mu\text{m}} = 2.8$ towards CH₃OH -1 and $\tau_{1\text{mm}} = 0.001$ and $\tau_{100\mu\text{m}} = 0.19$ towards CH₃OH -2, assuming $\beta = 2$ and a dust temperature of 240 K. β and T_{dust} are uncertain and the following analysis on the CH₃OH data depends on them. As already discussed in § 3.4, degeneracy happens between the dilution factor w , the dust temperature T_d , the spectral index β and the reference optical depth of the dust at 100 μ m in the external radiation field (eq. 3.1): changing these parameters in the model has the only physical meaning of changing the number of photons which excite the torsional levels. (Beuther et al. 2002a). Following Krügel & Walmsley (1984), dust and gas are assumed to be coupled at high density, ($n > 10^5 \text{ cm}^{-3}$).

	$\Delta v_{l/2}$ km s ⁻¹	v_{lsr} km s ⁻¹
CH ₃ OH -1	6.5	-15.6
CH ₃ OH -2	3.9	-15.4
CH ₃ OH -NW (-11.1 ", 5.1 ")		
narrow comp.	2.5	-16.5
broad comp.	11.9	-14.3
CH ₃ OH -SE (5.4 ", -7.8 ")	2.3	-16.6

Table 4.4: Methanol line parameters.

CH₃OH -1

The methanol spectrum towards mm1 is typical of a hot core, with detection of highly excited lines in both the torsional ground state and in the first torsionally excited state; linewidths

are broad (see Table 4.4).

The $2_k \rightarrow 1_k$ $v_t=1$ CH₃OH band at 96.4 GHz and the $5_k \rightarrow 4_k$ band at 241 GHz have been included in our analysis; the source size is estimated from the data on the $2_1 \rightarrow 1_1$ $v_t=1$ CH₃OH-*E* line. Emission from this line seems to be extended (see Fig. 4.3) but, since the resolution at 3 mm is $4.35'' \times 3.14''$ and the separation between mm1 and mm2a is almost $5''$ in RA, contamination from CH₃OH -2 cannot be excluded. Therefore we have also restored the Clean components with a smaller clean beam ($2.3'' \times 2.3''$), which corresponds to the resolution of the most extended baselines; at this spatial resolution the bulk emission splits up into two components, mm1 and mm2a, with sizes smaller than the beam. Therefore, in our analysis, the continuum source size has been used as input parameter.

The best fit results of our analysis are given in Table 4.5 and the synthetic spectrum, overlaid on the data, in Fig. 4.7. While the 1 mm lines are pretty well reproduced by our model, the torsionally excited transitions at 3 mm are not and line intensities are a factor of 2 smaller than what observed. We believe the low signal to noise ratio in this band, the degeneracy between collisions and infrared pumping and the uncertainties in the collisional rates within the torsionally excited levels and with the ground state to be the cause of this discrepancy.

CH₃OH -2

The CH₃OH spectrum towards CH₃OH -2 is typical of low-mass star forming regions, with narrow linewidths (see Table 4.4). However, given that there is no association between methanol emission at this position and the continuum, the very nature of this molecular emission is unknown. All the lines in the $5_k \rightarrow 4_k$ band are detected, with a possible 2σ detection of the $2_1 \rightarrow 1_1 - E$ $v_t=1$ lines. The best fit results of our analysis are given in Table 4.5 and the synthetic spectrum, overlaid on the data, in Fig. 4.8. As in the case of CH₃OH -1, the model does not reproduce the emission in the torsionally excited lines which are, however, affected by a low signal to noise ratio.

CH₃OH -NW

The CH₃OH spectrum towards this position is characterized by red non Gaussian wings in the $5_0 \rightarrow 4_0 - A$ and $5_{-1} \rightarrow 4_{-1} - E$ lines, shifted by 2km s^{-1} in velocity from the parental cloud velocity; emission from the other lines comes from a narrower component. As discussed in § 4.3, there is no clear evidence for association between the outflows detected by Beuther et al. (2002a) and the emission at this position, modelling the spectrum towards CH₃OH -NW is done only on the narrow component. The 1 mm beam is used as source size. The best fit results and the quantities derived by it are listed in Table 4.5.

CH₃OH -SE

The CH₃OH spectrum towards this position is characterized by narrow linewidths with a shift in velocity of 1km s^{-1} from the parental cloud. The 1 mm beam is used as source size.

The best fit results and the quantities derived by it are listed in Table 4.5.

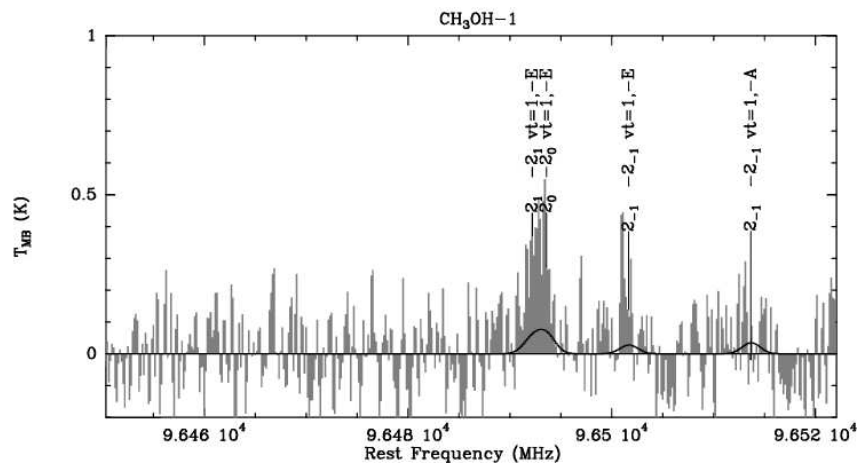
	CH ₃ OH -1	CH ₃ OH -2	CH ₃ OH -SE	CH ₃ OH -NW
T _K (K)	240	113	25	40
n(H ₂) (cm ⁻³)	5×10 ⁷	2.3×10 ⁶	6×10 ⁶	6×10 ⁶
N(CH ₃ OH-E) (cm ⁻²)	6.6× 10 ¹⁶	1.8× 10 ¹⁶	1× 10 ¹⁵	1× 10 ¹⁵
N(CH ₃ OH-A)(cm ⁻²)	6.6× 10 ¹⁶	1.8× 10 ¹⁶	1× 10 ¹⁵	1× 10 ¹⁵
size (″)	0.7	0.7	2.2	2.2
L (10 ⁴ L _⊙)	5.52	0.3	0.006	0.04
M (M _⊙)	0.3	0.03	1.1	1.1
N(H ₂)(10 ²³ cm ⁻²)	10	2	4	3.5
[CH ₃ OH]/[H ₂]	1× 10 ⁻⁷	7× 10 ⁻⁷	6× 10 ⁻⁹	6× 10 ⁻⁹

Table 4.5: CH₃OH model results.

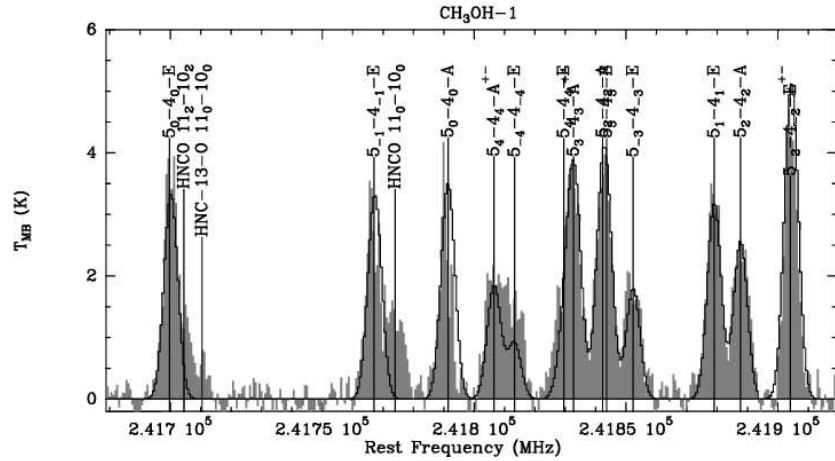
4.5 Conclusion

We have presented a high resolution study of the High Mass Protostellar Object IRAS 05358+3543 based on 3 mm and 1 mm data from the Plateau de Bure Interferometer. At our resolution, the previously known three millimeter dust condensations split up in several other condensations, whose masses, column densities and visual extinction have been derived by analysing the continuum data. The main dust condensation, mm1, shows several indicator of hot core formation going on, with the detection of several complex molecules and very excited transitions. A preliminary analysis on the $2_k \rightarrow 1_k$ CH₃OH series at 3 mm and of the $5_k \rightarrow 4_k$ CH₃OH band at 1 mm indicates high temperature (240 K) and density (5×10^7 cm⁻³) in the gas surrounding mm1; methanol abundance is typical of a hot core. The same analysis has been performed on other three positions successfully leading to derive their physical parameters. Emission from the less excited methanol lines shows an extended pattern and it is probably associated to the several outflows detected in the region, in CO, SiO and H₂. Our data are, however, heavily corrupted by negative features caused by missing spacings and any further interpretation of the extended emission needs the zero spacing information.

This preliminary analysis of methanol in IRAS 05358+3543 has shown that, when other data on highly excited transitions will be available and the zero spacing information recovered, a measure of the temperature and density distributions of the gas in the region, around the inner core **and** in the outflows, will be possible. This will result in one the first unambiguously separated temperature and density maps of very young massive star-forming regions and will establish CH₃OH as a unique tool to study the physical parameters density and temperature simultaneously. Observations of the $7_k \rightarrow 6_k$ band at 338 GHz, in both the ground state and the first torsionally excited level, are planned for the next winter with the Submillimeter Array, on Mauna Kea; the $5_k \rightarrow 4_k$ $v_t = 1$ band at 241 GHz will be observed with the PdBI. Single-dish observations with the IRAM 30 m telescope are also scheduled for the winter 2004, to recover the zero spacing information filtered out in the PdBI data.

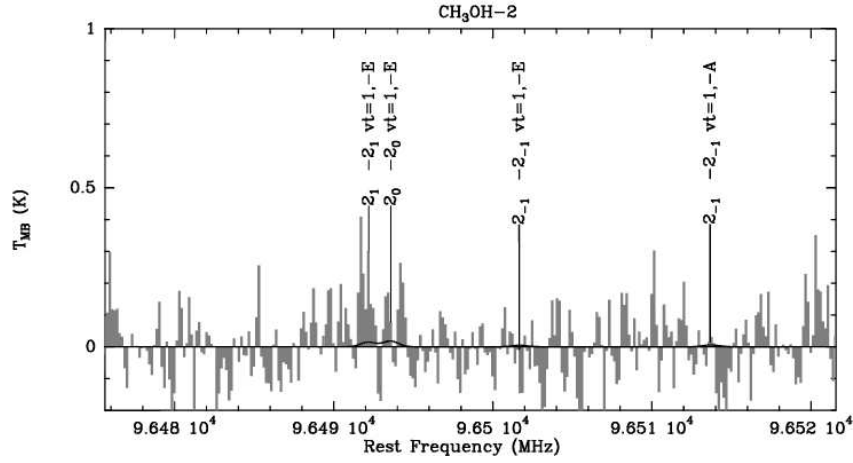


(a)

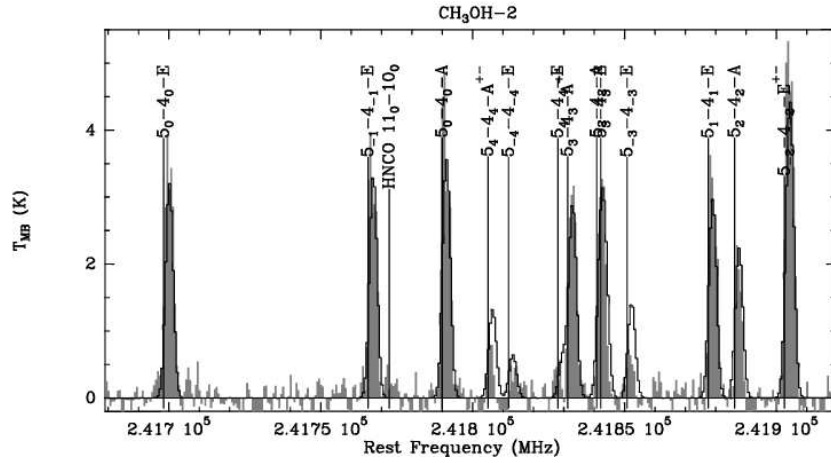


(b)

Figure 4.7: Spectra of the $2_k \rightarrow 1_k$ $v_t=1$ CH₃OH band at 96.4 GHz **(a)** and of the $5_k \rightarrow 4_k$ band at 241 GHz **(b)** toward mm1. Overlaid in black the synthetic spectra resulting from the fit.

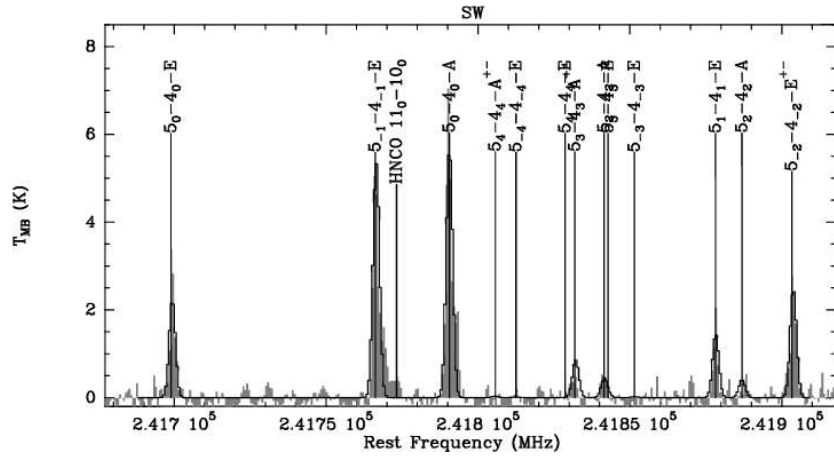


(a)

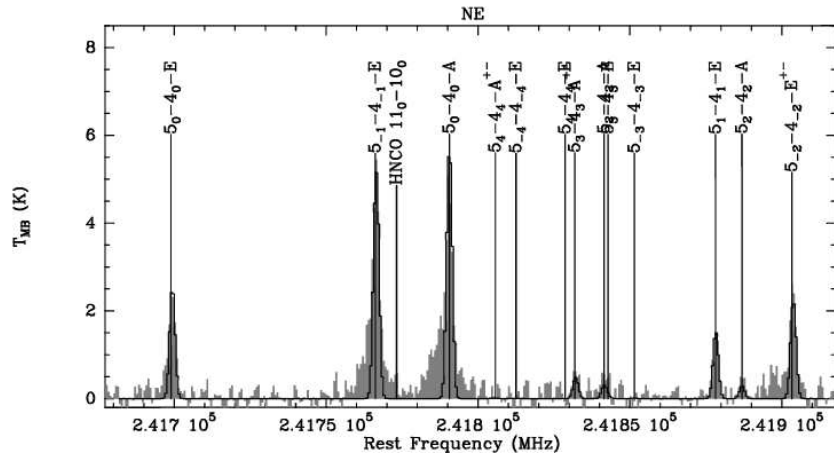


(b)

Figure 4.8: Spectra of the $2_k \rightarrow 1_k$ (a) band at 96 GHz and the $5_k \rightarrow 4_k$ (b) band at 241 GHz toward CH₃OH-2. Overlaid in black the synthetic spectra resulting from the fit.



(a)



(b)

Figure 4.9: Spectra of the $5_k \rightarrow 4_k$ band at 241 GHz toward (5.4'', -7.8'') (b) and (-11.1'', 5.1'') (c). Overlaid in black the synthetic spectra resulting from the fit.

Chapter 5

Highlights and prospects

5.1 Summary

This thesis has been a pilot study dedicated to the analysis of the excitation condition of methanol in the interstellar medium and to its tracing properties in the centimeter, millimeter and submillimeter spectra. Since methanol is ubiquitously found in different regimes of star formation and it is associated not only to the inner region of the clouds, close to the proto-stars, but also to the outflows, it is particularly well suited to study high mass star forming regions, whose physical conditions during the early evolutionary stages are still poorly understood.

A diagnostic tool of interstellar clouds. In Chapter 1, we have selected four bands of CH₃OH transitions in the millimeter and submillimeter regime and shown that when several CH₃OH lines, in different excitation ranges, are observed towards the same region, the analysis on the spectra lead to estimates of both kinetic temperature and spatial density, thus avoiding problems of different spatial distributions which are known to happen when relying on different molecules. We found that many millimeter line ratios are mainly sensitive to spatial density in the range 10^5 – 10^8 cm⁻³, while in the submillimeter range a strong dependence on kinetic temperature up to 150 K is found. When infrared pumping is taken into account and torsionally excited lines included in the calculations, reliable determinations of temperature are possible by observing $v_t=1$ lines. For complex sources and for lines surveys or multi-frequency studies of a molecule, the traditional approach of deriving physical parameter from a spectrum by “by-hand” Gaussian fitting of the lines with multiple components is impractical. Therefore, we have extended the innovative technique to handle the problem proposed by Schilke et al. (1999) to the Large Velocity Gradient approximation. This is based on the simultaneous fit of all the lines in a spectrum with a synthetic spectrum; it handles multiple components along the line of sight and can simultaneously fit up to 100 000 lines, in different frequency windows and from different telescopes. Local line overlap is taken into account.

Chapter 2 is dedicated to the analysis of the pumping mechanism of Class I CH₃OH masers

and to the information on the physical parameters of an interstellar cloud that can be derived by observing these transitions: the simultaneous observations of Class I masers in the $J_2 \rightarrow J_1 - E$ band **and** in other transitions allow a reliable estimate of the H_2 density, as the $J_2 \rightarrow J_1 - E$ transitions arise at high density (10^7 cm^{-3}) and the others at lower values ($10^4 - 10^6 \text{ cm}^{-3}$).

High mass star forming regions in their early evolutionary stages. In chapter 3, a sample of 13 sources in the early stages of star formation is analysed by single dish observations of centimeter, millimeter and some submm CH_3OH lines. The analysis and the technique discussed in the first two chapters are applied to high-mass star forming regions, chosen among the sample of High Mass Protostellar Objects studied by Sridharan et al. (2002) and the Infrared dark clouds by Carey et al. (1998). Methanol has been successfully detected in all the sources of our sample; non-Gaussian profiles have been found in several sources, probably due to outflows. Among the HMPOs, a variety of different methanol spectra has been detected, with linewidths ranging from 2.4 km s^{-1} to 5 km s^{-1} and with very different excitation conditions. Therefore, our analysis confirms methanol to be a good indicator of the physical conditions in star forming regions. Our models usually reproduce the observations well.

For each source, temperature, H_2 density and CH_3OH column density are derived by a simultaneously fitting of all the observed transitions. Errors on these quantities are given by a χ^2 analysis. Luminosities, H_2 masses, column densities and methanol abundances are also given. The derived CH_3OH abundance ranges between 10^{-9} and 10^{-7} , values in good agreement with the results reported by other authors (Menten et al. 1986; Friberg et al. 1988; van der Tak et al. 2000). In some sources, a jump in the CH_3OH abundance is required, from low values at low densities and temperature to three orders of magnitude higher for high temperatures and densities. This jump is usually attributed to be due to evaporation of methanol from ice mantles. High values of the reduced χ^2 are sometimes found, but they are probably mainly due to the complexity of the sources, which is not really represented by our geometrically simple model; moreover, calibration uncertainties can still play a role in our analysis.

IRAS 05358+3543: a case study. The High Mass Protostellar Object IRAS 05358+3543 has been studied at high resolution with the Plateau de Bure Interferometer, in the $5_k \rightarrow 4_k$ CH_3OH band at 1 mm. In the continuum, with the resolution of $1.26'' \times 0.84''$, the previously known three millimeter dust condensations split up in at least two other cores, thus revealing a cluster of at least five cores. H_2 masses range between $39 M_\odot$ and $4 M_\odot$. A first analysis of the methanol data, although affected by the degeneracy between collisions and the IR radiation field in the pumping of the energy levels, indicates hot core physical conditions in the surroundings of the main mm core. Highly excited CH_3OH lines (lower level energy $\sim 80 \text{ K}$) are detected in the region and a simultaneous fit of all the lines in the $5_k \rightarrow 4_k$ CH_3OH $v_t=0$ and in the $2_k \rightarrow 1_k$ CH_3OH $v_t=1$ series at 96.5 GHz gives typical hot-core pa-

parameter: $T=240$ K, $N(\text{CH}_3\text{OH})=1.2 \times 10^{17} \text{ cm}^{-2}$, $n(\text{H}_2)=5 \times 10^7 \text{ cm}^{-3}$ and $[\text{CH}_3\text{OH}]/[\text{H}_2]$ values of 10^{-7} . Other hot core molecular species (CH_3OCH_3 , $\text{C}_2\text{H}_5\text{CN}$, CH_3CN , HNCO) are also detected.

Emission from the less excited methanol lines shows an extended pattern which probably is associated to the several outflows detected in the region, in CO, SiO and H_2 . Particularly interesting is the association between CH_3OH and SiO emission: since both molecular species reside in dust grains, methanol in the mantles and SiO in the cores, a possible, tempting interpretation of the spatial distribution of the two species is that CH_3OH is tracing less energetic events than SiO in the same outflow or that its emission is a tracer of fossil outflow in the region. Our data are, however, heavily corrupted by negative features caused by missing spacings and any further interpretation of the extended emission needs the zero spacing information.

5.2 Future plans

Despite the observational effort to identify the very earliest stages in the evolution of massive stars and study their physical conditions, several questions on the physical processes involved in their formation are still to be addressed. High resolution and high frequency are essential, to solve the confusion of the clustered mode and zoom in the innermost regions of high mass star forming cluster. Interferometric millimeter and submillimeter observations are therefore ideal to investigate the individual protostellar dust condensations in the continuum and the hot, dense gas within the evolving cores in molecular line emission, as shown by our highly successful study of IRAS 05358.

In that respect, in chapter 3, we have selected a sample of high mass star forming regions in earliest evolutionary stages well suited for interferometric follow-up observations, since the two election criteria have been that they show strong methanol emission and that are at distances less than 4 kpc. Millimeter methanol observations with the Plateau de Bure Interferometer are currently scheduled for the winter 2004 observing period towards the infrared dark cloud G11.11–0.12 P1. Indirect evidences of a disk and an outflow in the region are found in the detection of CH_3OH and H_2O masers and in the non-Gaussian wings detected in the thermal methanol. However, with the PdBI data at 1 mm, we expect to image the disk and probe the kinematics and the morphology of the outflow. By analysing the CH_3OH line intensities, a map of the density of the region around G11.11 can be derived.

We have also started a chemical and kinematical study of the Cep-A hot core, based on high-resolution, high-sensitivity data acquired with the PdBI. The analysis on the velocity structure of CH_3OH lines at 1 mm suggests the presence of a massive protostellar disk, which is resolved by the PdBI in extended configuration.

In this thesis, high-resolution observations of IRAS 05358+3543 have already been discussed. However, with the data we collected so far, a satisfying analysis on the source is not yet possible. Our PdBI methanol data leave open two intriguing questions: *is methanol*

tracing a less energetic event than SiO in the outflows?; which are the physical conditions of the inner gas around the main millimeter dust condensation?. To address the first question, single-dish observations with the IRAM 30 m telescope are scheduled for the winter 2004, to recover the zero spacing information filtered out in the PdBI data. These data will shed light on the morphology of the extended methanol emission and will allow us to investigate the association of CH₃OH and SiO. Moreover, a study on the physical conditions in the outflows will be possible.

To investigate the inner region around the protostars, observations of the $7_k \rightarrow 6_k$ band at 338 GHz, in both the ground state and the first torsionally excited level, are scheduled for the next winter with the Submillimeter Array, on Mauna Kea; the $5_k \rightarrow 4_k$ $v_t = 1$ band at 241 GHz will be observed with the PdBI. Zooming down to 0.7'' at both the frequencies and combining the information from all the observed bands, we plan to measure the temperature distribution of the sources and resolve the density structure of the individual protostellar. This will result in one the first unambiguously separated temperature and density maps of very young massive star-forming regions and will establish CH₃OH as a unique tool to study the physical parameters density and temperature simultaneously. Moreover, our data could also test the *jump* model for the methanol abundance and reveal at which temperature and distance from the inner core evaporation of CH₃OH from the ice mantles happens.

Additional information on the source comes from the observations of class II methanol masers at 6.7 GHz by Minier et al. (2000), which show that the single emission centers (maser spots) are very well aligned perpendicularly to one of the outflow in the region. Several studies have suggested that CH₃OH and H₂O maser emission can be a powerful tool to study outflows and disks in high mass star forming regions, as, with the high intensity and spatial compactness (~ 1 AU) of the maser spots, they are well suited to be observed with the VLBI networks, thus zooming in the inner region close to the protostars (< 100 AU) and allowing proper motion studies. However, ambiguous results are found, with motions which can be interpreted as rotation around a disk, expansion about the axis or infall (Cesaroni 2004). A general conclusion is that proper motion studies of masers features is useful when additional information on the source, such as the morphology of the outflows, is available. Therefore, we also plan to combine the information from our millimeter interferometric data with proper motion and kinematics studies of CH₃OH and H₂O maser features with the VLBI and the EVN. The 22.2 GHz H₂O and 6.7 GHz CH₃OH VLBI observations will offer a good case where the information on the gas kinematics and the physical conditions extracted with the maser observations at linear scales of $10 - 100$ AU, can be connected with the information on the environment harbouring the maser emission deduced with thermal tracers at scales ≥ 1000 AU. Therefore, the analysis on the kinematics of the class II CH₃OH masers has the potential to discriminate between the disk and the outflows scenarios of the structure outlined by the 6.7 GHz masers by Minier et al. (2000).

In the next decade submillimeter astronomy will become routine: the APEX telescope on the Atacama plane in Chile will be operational in 2005 with receivers covering all atmo-

spheric windows up to 1 THz and some selected windows above it; the Herschel satellite, whose launch is scheduled for 2007, with its HIFI instrument, will collect data on the molecular spectrum in the THz region. SMA is already routinely operating on Mauna Kea at frequencies up to 345 GHz.

Methanol has been shown to be the most prolific species in the $350\mu\text{m}$, in the line survey by Comito et al. (2004) on Orion-KL. Therefore a proper understanding of its excitation condition in the interstellar medium will be extremely useful in the near future.

Moreover, with SMA and PdBI, and with the Atacama Large Millimeter Array (ALMA) in the near future, sub-millimeter interferometry will be decisive in the study of very young massive star forming regions and produce copious amounts of spectral data. A major role in the analysis of 2-dimensional interferometric spectral data can be played by the LVG analysis tool described in chapter 1; however, in its current version, the fitting program is meant for single dish data. We therefore plan to implement this tool to easily handle interferometric data, including simple geometries for the sources and introducing a Monte Carlo method to solve the radiative transfer problem. Moreover the program, in its current version, can be easily adapted to work with other molecules.

Appendix A

CH₃OH-para H₂ collisional rates.

The relative abundance of H₂ and He in the molecular gas phase in the interstellar medium ($\sim 5 : 1$) implies that H₂ is the dominant collisional partner: in order to have a proper understanding of the excitation of CH₃OH, as well as of other molecules, the corresponding rate collisional coefficients are required. Para-H₂ has several similarities to helium as a collider: they both have a spherical symmetry and neither possesses finite electrostatic multipole moments. Therefore, it is usually assumed that para-H₂ and He behave similarly in low energy collisions. Ortho-H₂, on the other hand, is expected to behave differently from both para-H₂ and He. An extreme case of such a different behaviour is found by Flower et al. (1990) in the inversion of the NH₃ (J,k)=(3,3) line: collisional excitation of the levels by para-H₂ might lead to a maser action in the transition, while collisions with ortho-H₂ tend to inhibit inversion in the line. However, up to now (e.g. Walmsley et al. 1988; Menten et al. 1988b; Kalenskii et al. 1997; Leurini et al. 2004), all statical equilibrium calculations performed on the CH₃OH molecule have been done making use of CH₃OH-He collisional coefficients. Very recently, collisional rate coefficients for CH₃OH with para-H₂ have been computed by Pottage et al. (2004a), in the range $5 \leq T_{kin} \leq 200$ K, for levels up to (J,k)=9. These authors find that the two datasets of collisional rates (CH₃OH-He from Pottage et al. (2001, 2002) and CH₃OH-para-H₂) are qualitatively similar; however, they also find that the propensity rules are less pronounced when the collider is para-H₂ than when it is He: the $\Delta k = 0$ collisional transitions, for example, are preferred to the others, but the contrast with the $|\Delta k| = 1$ is less pronounced. Similar results are found in all the other collisional transitions with different K ladder.

Since H₂ is the main gas-phase collider, we performed test calculations for a set of physical parameters typical of the interstellar medium, to verify whether or not our previous calculations with the CH₃OH-He collisional rates (Leurini et al. 2004) are consistent with the results one would get using para-H₂ as main collider. Only calculations for CH₃OH –E have been done, but no different results are expected for CH₃OH –A. Fig. A.1-A.2 show that in the millimeter regime, energy levels are populated in a qualitatively very similar way by collisions with He or para-H₂, with deviations at low density. Major deviations are found at submillimeter wavelengths (see Fig. A.3) at low CH₃OH column densities; however, at

higher column densities (see Fig. A.3(d)-A.3(c)) results of the calculations with the CH₃OH-He collisional rates and with the CH₃OH-para-H₂ converge to common values.

In chapter 2, class I masers have been discussed. As already suggested by other authors in the past (Lees 1973; Lees & Haque 1974), class I CH₃OH masers are found in our calculations to be pumped by collisions. However, what differentiates our model from others is the pumping mechanism of the $J_2 \rightarrow J_1 - E$ maser series: Johnston et al. (1992) explain the masing action in these lines with an additional preference for the $\Delta k = 3$ collisions and the assumption that $\Delta k = 2$ collisions are forbidden. Our calculations show that collisions equally populate the upper and lower levels of these transitions ($\Delta k = 2$ collisions are almost as strong as the $\Delta k = 3$ with the CH₃OH-He collisional rates from Pottage et al. (2001, 2002)), while spontaneous decays more fastly depopulate the lower levels, thus leading to inversion.

Therefore, the new CH₃OH-para-H₂ collisional coefficients could indeed affect the pumping mechanism in class I masers, particularly in the $J_2 \rightarrow J_1 - E$ band, as $\Delta k = m$, $m \leq 3$ have comparable intensities. Fig. A.4(a)-A.4(d) show line optical depths of several class-I maser transitions with the two datasets of collisional rates. No major deviations are seen: collisions with He produce slightly more intense masers and the opposite is seen in the $J_2 \rightarrow J_1 - E$ band. Moreover these lines do mase and are quenched at lower densities.

As discussed above, no major deviations are found in computing the level populations for methanol using collisional rates with He or with para-H₂, at least for those physical conditions for which the analysed transitions are accessible to observations. However, as discussed at the beginning of this section, ortho-H₂ is expected to behave differently from both He and para-H₂ with possible consequences on the CH₃OH populations, when governed by collisions, as in the case of NH₃ (Flower et al. 1990). If this is the case, changes in the ortho to para ratio, known to be 3 in warm ($T \geq 170$ K) sources in LTE, while ranging between 9 and very low values in cold clouds, depending on the chemical history and state of the region (Flower & Watt 1984; Le Boulbot 2000; Takahashi 2001), would also affect the results.

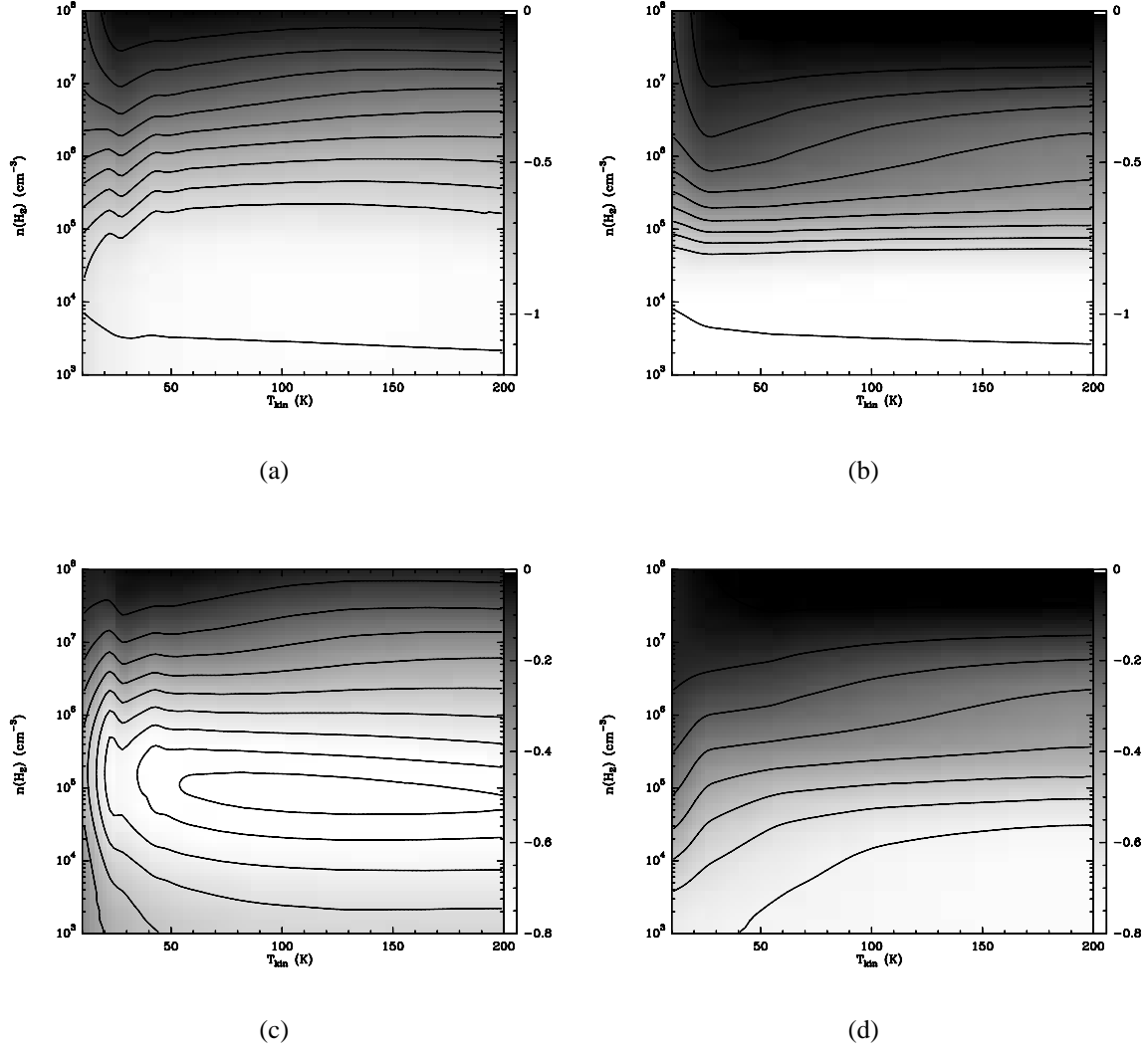


Figure A.1: Results of statistical equilibrium calculations for $\text{CH}_3\text{OH-E}$. The $T_R(2_0 \rightarrow 1_0)/T_R(2_{-1} \rightarrow 1_{-1})$ line ratio is shown in logarithmic scale, as function of H_2 density and temperature at $N(\text{CH}_3\text{OH})/\Delta\nu = 10^{13} \text{ cm}^{-2}/(\text{km s}^{-1})$, **a)** with $\text{CH}_3\text{OH-He}$ collisional rates, **b)** with $\text{CH}_3\text{OH-para-H}_2$; same calculations are shown in **c)** with $\text{CH}_3\text{OH-He}$ collisional rates and **d)** with $\text{CH}_3\text{OH-para-H}_2$, at $N(\text{CH}_3\text{OH})/\Delta\nu = 10^{15} \text{ cm}^{-2}/(\text{km s}^{-1})$.

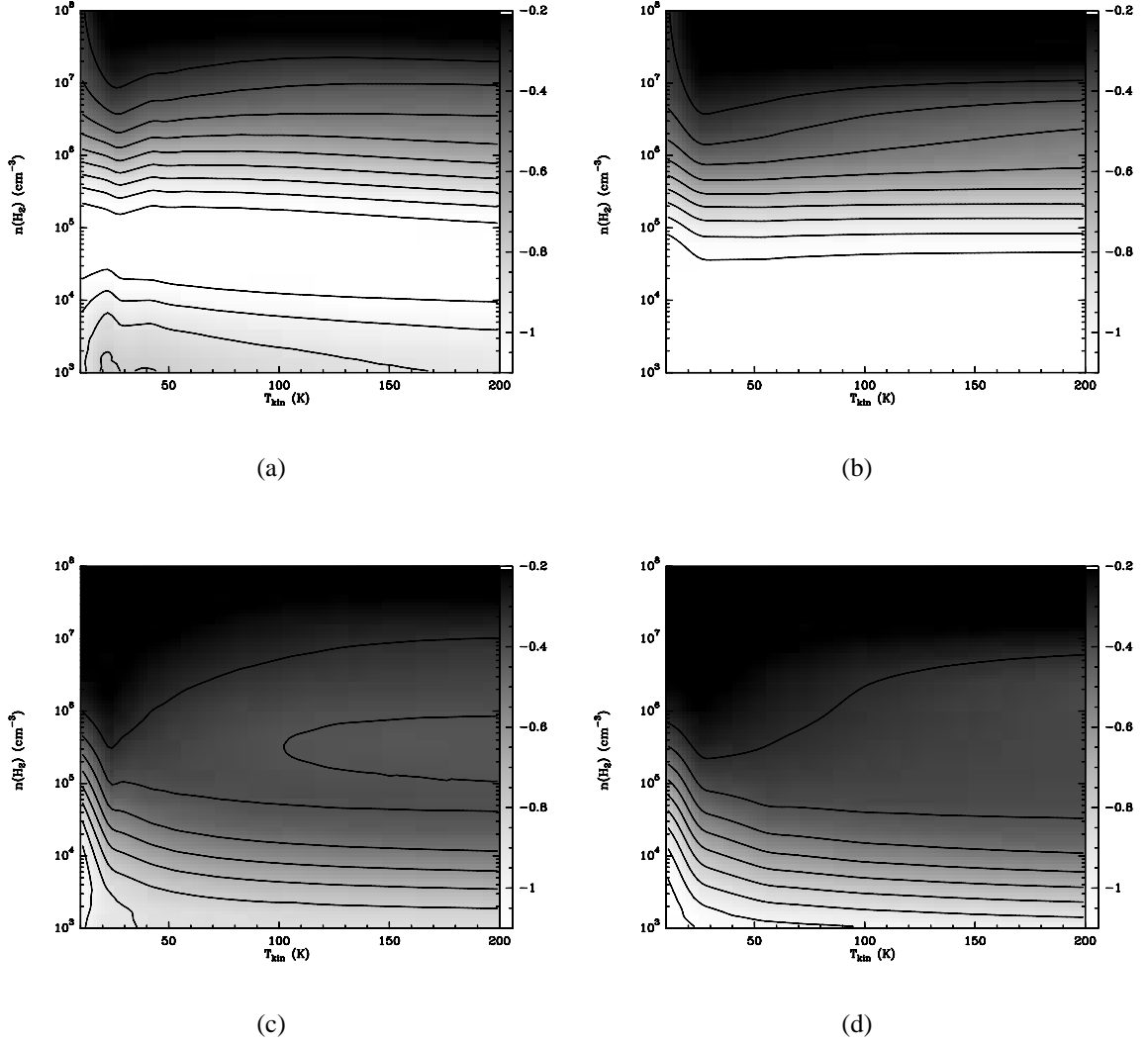


Figure A.2: Results of statistical equilibrium calculations for CH₃OH-*E*. The $T_R(5_0 \rightarrow 4_0) / T_R(5_{-1} \rightarrow 4_{-1})$ line ratio is shown in logarithmic scale, as function of H₂ density and temperature at $N(\text{CH}_3\text{OH})/\Delta v = 10^{13}$ cm⁻²/(km s⁻¹), **a)** with CH₃OH-He collisional rates, **b)** with CH₃OH-para-H₂; same calculations are shown in **c)** with CH₃OH-He collisional rates and **d)** with CH₃OH-para-H₂, at $N(\text{CH}_3\text{OH})/\Delta v = 10^{15}$ cm⁻²/(km s⁻¹).

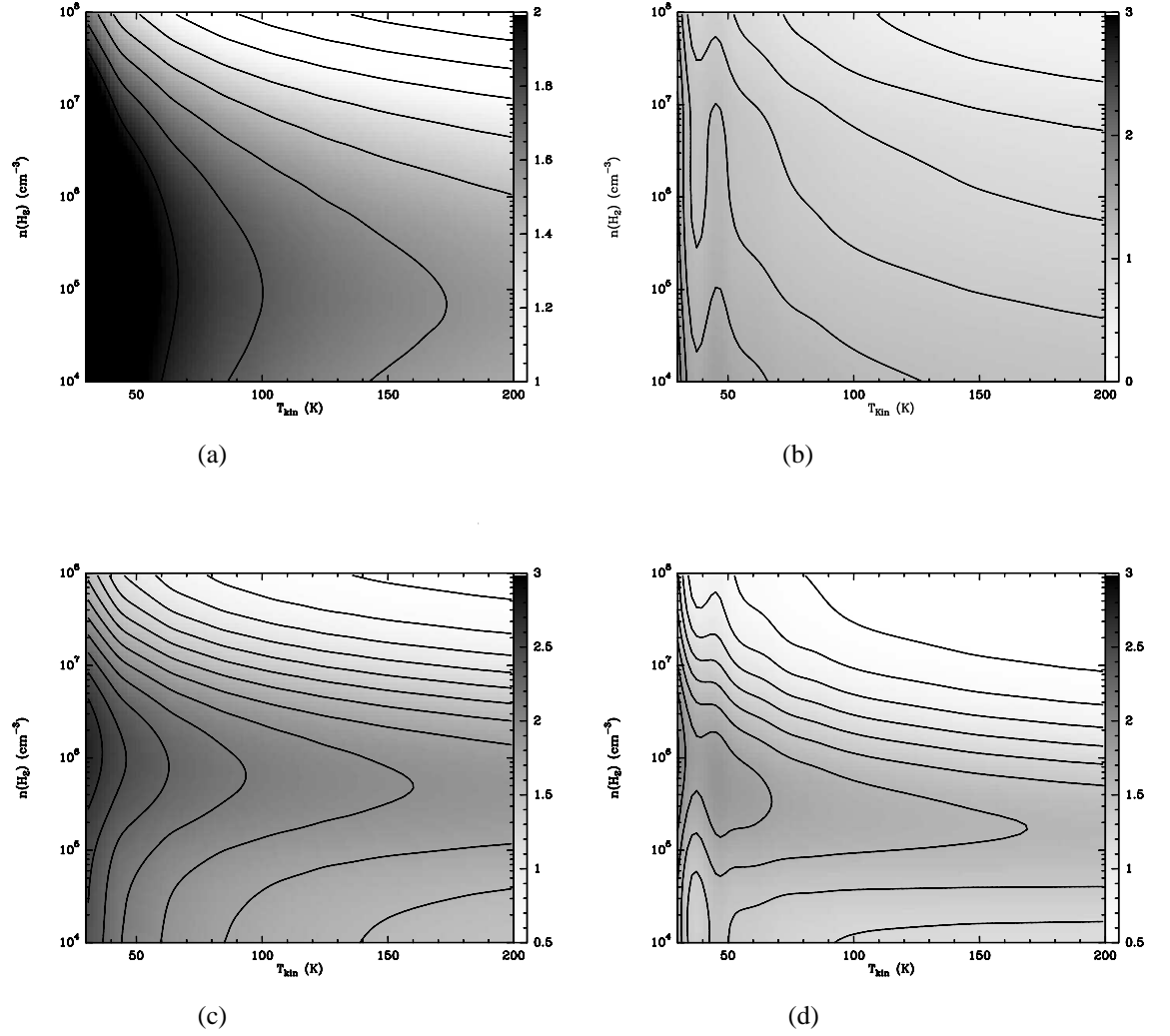


Figure A.3: Results of statistical equilibrium calculations for CH₃OH-*E*. The $T_R(7_{-3} \rightarrow 6_{-3}) / T_R(7_5 \rightarrow 5_5)$ line ratio is shown in logarithmic scale, as function of H₂ density and temperature at $N(\text{CH}_3\text{OH})/\Delta v = 10^{15} \text{ cm}^{-2}/(\text{km s}^{-1})$, **a)** with CH₃OH-He collisional rates, **b)** with CH₃OH-para-H₂; same calculations are shown in **c)** with CH₃OH-He collisional rates and **d)** with CH₃OH-para-H₂, at $N(\text{CH}_3\text{OH})/\Delta v = 10^{16} \text{ cm}^{-2}/(\text{km s}^{-1})$.

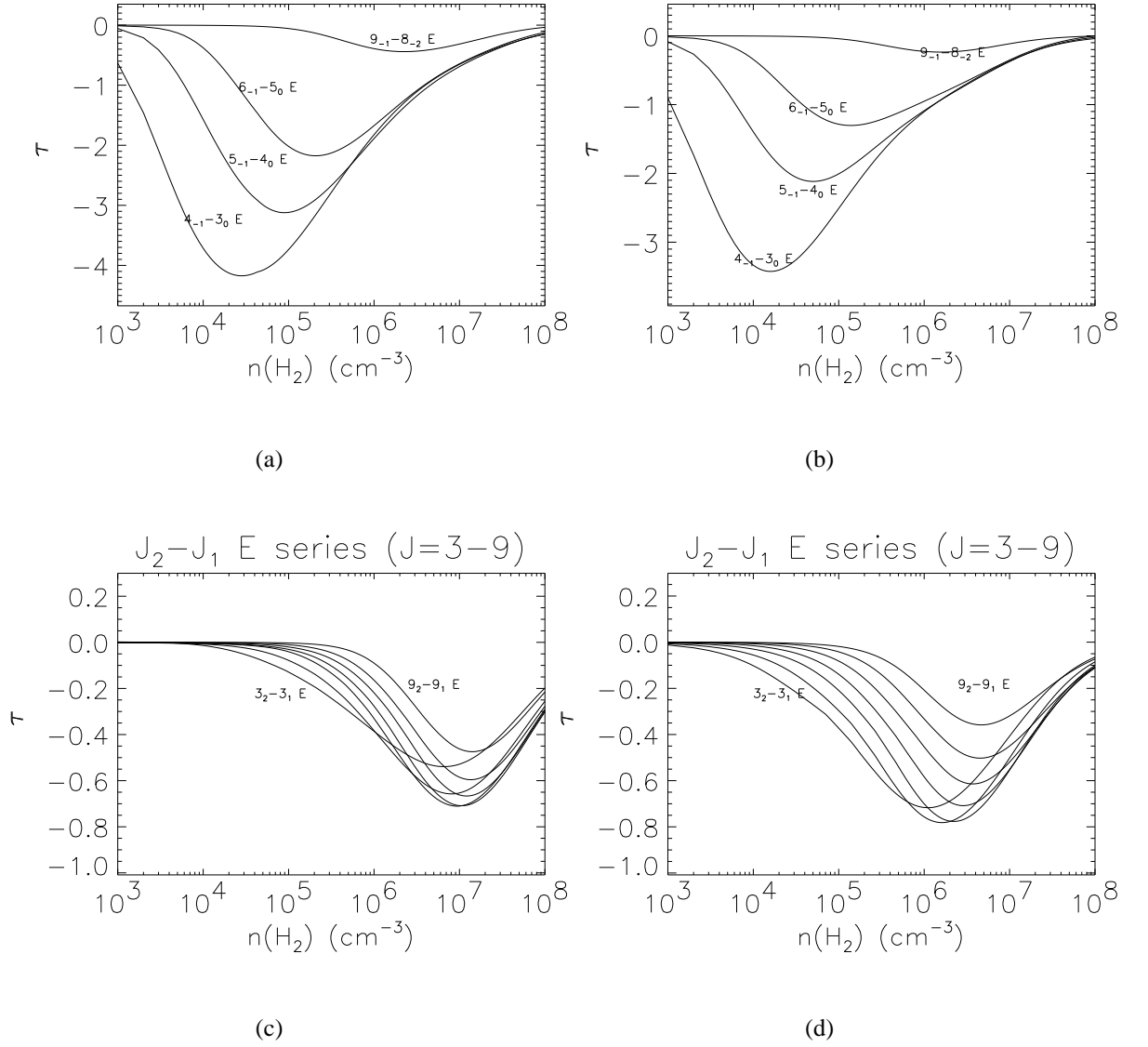


Figure A.4: Line optical depths of several class-I maser transitions of *E*-type: **a, c** with the CH₃OH-He collisional rates, **b, d** with the CH₃OH-para-H₂ collisional rates, at $N(\text{CH}_3\text{OH})/\Delta\nu = 10^{15} \text{ cm}^{-2} \text{ km s}^{-1}$, $T_{\text{kin}}=80 \text{ K}$.

Acknowledgements

This thesis was written at the Max Planck für Radioastronomie between November 2001 and December 2004. First of all, I thank Karl Menten for giving me the opportunity to work in the Millimeter and Submillimeter Astronomy group, for his guidance and support in many aspects of my work. From astronomy to comics and James Bond movies, our discussions have been very refreshing during several nights at Pico Veleta. Many thanks go to my supervisor Peter Schilke, who had the original idea behind this project and who followed me step by step during these three years despite his demanding involvement with APEX. I especially thank him for having faced all my *Sinnkrisen* with encouragement and patience. I acknowledge fruitful discussions with David Flower from Durham University; I am grateful to him and James Pottage for carrying out the collisional rates calculations.

The observations discussed in the thesis are based on data acquired with the IRAM facilities, the Effelsberg telescope and the Caltech Submillimeter Observatory. For this, I wish to thank Tom Phillips for the financial support for my travel to Hawaii and for my visit to Caltech. I am also grateful to Alex Kraus for many discussions on the calibration of the Effelsberg data and for calibrating the November 2002 dataset. I am also indebted to Friedrich Wyrowski who found my thesis interesting enough to spend a week with me at Pico Veleta and to help me with my first experience with a telescope.

A special thank you is for Luca Moscadelli, who suggested me for a Ph.D. position in this group. Without his email to Karl Menten, maybe I would have worked on some other project, missing out on the fun (and frustration) of methanol. I also wish to thank Malcolm Walmsley, with whom I discussed several aspects of this thesis; his comments and questions have really improved my thesis and my understanding of the problem.

Working in the Millimeter and Submillimeter Astronomy group at the MPIfR has been a great experience. I would like to thank the whole group for the stimulating working atmosphere and for the fruitful discussions we had. For having shared their knowledge of my sample of sources, I thank Henrik Beuther, Friedrich Wyrowski, Peter Schilke and Thushara Pillai.

Finally, many people warmly supported me during these three years and especially in the last months. My gratitude is to my parents, who accepted all my choices and me being so far away. I am also grateful to my *extended family* Silvia, Laura and Alessandra. Violetta, Giorgio, Claudia, Thushara, Jens, Ed, Maria, Hauke, Dirk, Carolin, Manolis and many others, I am sure, who have supported and encouraged me in so many situations; some of them have

also taken care of my cat when I was observing somewhere else! For all this, I thank you all.

List of publications

Refereed papers

Schilke, P., Leurini, S., Menten, K. M., Alcolea, J. 2003 , *Astronomy & Astrophysics*, 412, L15: *Interstellar SiN*

Leurini, S., Schilke, P., Menten, K. M., Flower, D. R., Pottage, J. T., Xu, L.-H. 2004, *Astronomy & Astrophysics*, 422, 573L: *Methanol as a diagnostic tool of interstellar clouds. I. Model calculations and application to molecular clouds*

In preparation

Leurini, S., Menten, K. M., Schilke, P., *Methanol as a diagnostic tool of interstellar clouds. II. Class I methanol masers*, in prep.

Leurini, S., Schilke, P., Wyrowski, F., Menten, K. M., *Methanol as a diagnostic tool of interstellar clouds. III. Modelling of high mass star forming regions*, in prep.

Leurini, S., Schilke, P., Beuther, H., *IRAS 05358+3543: a high mass star forming cluster*, in prep.

Conference proceedings

Leurini, S., Schilke, P., Menten, K. M., Flower, D. R., Pottage, J. T., Xu, L.-H. 2004 ,in *The Dense Interstellar Medium in Galaxies Proceedings of the 4th Cologne-Bonn-Zermatt-Symposium*, eds. S. Pfalzner, C. Kramer, C. Straubmeier, & A. Heithausen (Springer: Berlin), *Methanol: A Diagnostic Tool for High-Mass Star-Forming Regions*

Bibliography

- André, P., Ward-Thompson, D., & Barsony, M. 2000, *Protostars and Planets IV*, 59
- Bachiller, R., Codella, C., Colomer, F., Liechti, S., & Walmsley, C. M. 1998, *A&A*, 335, 266
- Bachiller, R., Gomez-Gonzalez, J., Barcia, A., & Menten, K. M. 1990, *A&A*, 240, 116
- Bachiller, R., Liechti, S., Walmsley, C. M., & Colomer, F. 1995, *A&A*, 295, L51+
- Barrett, A. H., Ho, P., & Martin, R. N. 1975, *ApJ*, 198, L119
- Barrett, A. H., Hot, P. T. P., Martin, R. N., et al. 1976, *Astrophys. Lett.*, 18, 13
- Barrett, A. H., Schwartz, P. R., & Waters, J. W. 1971, *ApJ*, 168, L101+
- Batrla, W., Matthews, H. E., Menten, K. M., & Walmsley, C. M. 1987, *Nature*, 326, 49
- Batrla, W. & Menten, K. M. 1988, *ApJ*, 329, L117
- Beckwith, S., Persson, S. E., Neugebauer, G., & Becklin, E. E. 1978, *ApJ*, 223, 464
- Beuther, H., Hunter, T. R. Q., Zhang, Q., et al. 2004a, *American Astronomical Society Meeting*, 204,
- Beuther, H., Schilke, P., Gueth, F., et al. 2002a, *A&A*, 387, 931
- Beuther, H., Schilke, P., Menten, K. M., et al. 2002b, *ApJ*, 566, 945
- Beuther, H., Schilke, P., Sridharan, T. K., et al. 2002c, *A&A*, 383, 892
- Beuther, H., Schilke, P., & Stanke, T. 2003, *A&A*, 408, 601
- Beuther, H., Schilke, P., & Wyrowski, F. 2004b, *ApJ*, in press
- Beuther, H., Walsh, A., Schilke, P., et al. 2002d, *A&A*, 390, 289
- Beuther, H., Zhang, Q., Hunter, T. R. Q., et al. 2004c, *American Astronomical Society Meeting*, 204,

- Breckenridge, S. M. & Kukolich, S. G. 1995, *ApJ*, 438, 504
- Buxton, R. B., Barrett, A. H., Ho, P. T. P., & Schneps, M. H. 1977, *AJ*, 82, 985
- Carey, S. J., Clark, F. O., Egan, M. P., et al. 1998, *ApJ*, 508, 721
- Carey, S. J., Feldman, P. A., Redman, R. O., et al. 2000, *ApJ*, 543, L157
- Carroll, T. J. & Goldsmith, P. F. 1981, *ApJ*, 245, 891
- Caselli, P., Hartquist, T. W., & Havnes, O. 1997, *A&A*, 322, 296
- Caselli, P., Hasegawa, T. I., & Herbst, E. 1993, *ApJ*, 408, 548
- Cesaroni, R. 2004, *ApJS*, in press
- Cesaroni, R., Felli, M., Jenness, T., et al. 1999, *A&A*, 345, 949
- Cesaroni, R., Felli, M., Testi, L., Walmsley, C. M., & Olmi, L. 1997, *A&A*, 325, 725
- Cesaroni, R. & Walmsley, C. M. 1991, *A&A*, 241, 537
- Charnley, S. B., Tielens, A. G. G. M., & Millar, T. J. 1992, *ApJ*, 399, L71
- Chui, M. F., Cheung, A. C., Matsakis, D., Townes, C. H., & Cardasmenos, A. G. 1974, *ApJ*, 187, L19+
- Comito, C., Schilke, P., Phillips, T., et al. 2004, in press
- Cragg, D. M., Johns, K. P., Godfrey, P. D., & Brown, R. D. 1992, *MNRAS*, 259, 203
- Cragg, D. M., Sobolev, A. M., & Godfrey, P. D. 2002, *MNRAS*, 331, 521
- Danby, G., Flower, D. R., Valiron, P., Schilke, P., & Walmsley, C. M. 1988, *MNRAS*, 235, 229
- Dartois, E., Demyk, K., d'Hendecourt, L., & Ehrenfreund, P. 1999a, *A&A*, 351, 1066
- Dartois, E., Schutte, W., Geballe, T. R., et al. 1999b, *A&A*, 342, L32
- Davis, C. J., Varricatt, W. P., Todd, S. P., & Ramsay Howat, S. K. 2004, accepted
- de Jong, T., Dalgarno, A., & Chu, S.-I. 1975, *ApJ*, 199, 69
- Dickens, J. E., Irvine, W. M., Snell, R. L., et al. 2000, *ApJ*, 542, 870
- Egan, M. P., Shipman, R. F., Price, S. D., et al. 1998, *ApJ*, 494, L199+
- Feldman, P. A., Redman, R. O., Avery, L. W., et al. 2004, *Can. J. Chem.*, 82, 740

- Flower, D. R., Offer, A., & Schilke, P. 1990, MNRAS, 244, 4P
- Flower, D. R. & Watt, G. D. 1984, MNRAS, 209, 25
- Frerking, M. A., Langer, W. D., & Wilson, R. W. 1982, ApJ, 262, 590
- Friberg, P., Hjalmarson, A., Madden, S. C., & Irvine, W. M. 1988, A&A, 195, 281
- Grim, R. J. A., Baas, F., Greenberg, J. M., Geballe, T. R., & Schutte, W. 1991, A&A, 243, 473
- Guilloteau, S., Delannoy, J., Downes, D., et al. 1992, A&A, 262, 624
- Haschick, A. D. & Baan, W. A. 1989, ApJ, 339, 949
- Haschick, A. D., Menten, K. M., & Baan, W. A. 1990, ApJ, 354, 556
- Hauschildt, H., Gusten, R., Phillips, T. G., et al. 1993, A&A, 273, L23+
- Henkel, C., Guesten, R., & Gardner, F. F. 1985, A&A, 143, 148
- Hildebrand, R. H. 1983, QJRAS, 24, 267
- Hills, R., Pankonin, V., & Landecker, T. L. 1975, A&A, 39, 149
- Hogerheijde, M. R. & van der Tak, F. F. S. 2000, A&A, 362, 697
- Johnston, K. J., Gaume, R., Stolovy, S., et al. 1992, ApJ, 385, 232
- Johnston, K. J., Gaume, R. A., Wilson, T. L., Nguyen, H. A., & Nedoluha, G. E. 1997, ApJ, 490, 758
- Jones, B. F. & Walker, M. F. 1985, AJ, 90, 1320
- Kalenskii, S. V., Bachiller, R., Berulis, I. I., et al. 1992, AZh, 69, 1002
- Kalenskii, S. V., Dzura, A. M., Booth, R. S., Winnberg, A., & Alakoz, A. V. 1997, A&A, 321, 311
- Kalenskii, S. V., Liljestroem, T., Val'tts, I. E., et al. 1994, A&AS, 103, 129
- Kalenskii, S. V., Slysh, V. I., Val'Tts, I. E., Winnberg, A., & Johansson, L. E. 2001, Astronomy Reports, 45, 26
- Keto, E. 2003, ApJ, 599, 1196
- Kogan, L. & Slysh, V. 1998, ApJ, 497, 800
- Krügel, E. & Walmsley, C. M. 1984, A&A, 130, 5

- Le Bourlot, J. 2000, *A&A*, 360, 656
- Lee, H.-H., Bettens, R. P. A., & Herbst, E. 1996, *A&AS*, 119, 111
- Lees, R. M. 1973, *ApJ*, 184, 763
- Lees, R. M. & Baker, J. 1968, *J. Chem. Phys.*, 48, 5299
- Lees, R. M. & Haque, S. 1974, *Canadian J. Phys.*, 52, 2250
- Lees, R. M. & Oka, T. 1969, *J. Chem. Phys.*, 51, 3027
- Laurini, S. & Schilke, P. 2005, in preparation
- Laurini, S., Schilke, P., Menten, K. M., et al. 2004, *A&A*, 422, 573
- Liechti, S. & Walmsley, C. M. 1997, *A&A*, 321, 625
- Liechti, S. & Wilson, T. L. 1996, *A&A*, 314, 615
- Lis, D. C., Serabyn, E., Keene, J., et al. 1998, *ApJ*, 509, 299
- Müller, H. S. P., Thorwirth, S., Roth, D. A., & Winnewisser, G. 2001, *A&A*, 370, L49
- MacLaren, I., Richardson, K. M., & Wolfendale, A. W. 1988, *ApJ*, 333, 821
- Mangum, J. G. & Wootten, A. 1993, *ApJS*, 89, 123
- Maret, S. 2004, in *The dusty and molecular universe, A Prelude to Herschel and ALMA, meeting held in Paris, France, October 27-29, 2004*, Eds.: A. Wilson. To be published in ESA Conference Series.
- Matsakis, D. N., Wright, M. C. H., Townes, C. H., et al. 1980, *ApJ*, 236, 481
- McCaughrean, M. J., Stanke, T., Andersen, M., Beuther, H., & Quirrenbach, A. 2005, in preparation
- Mehringer, D. M. & Menten, K. M. 1997, *ApJ*, 474, 346
- Mekhtiev, M. A., Godfrey, P. D., & Hougen, J. T. 1999, *J. Mol. Spectrosc.*, 194, 171
- Menten, K. 1991a, in *ASP Conf. Ser. 16: Atoms, Ions and Molecules: New Results in Spectral Line Astrophysics*, 119–+
- Menten, K. M. 1991b, *ApJ*, 380, L75
- Menten, K. M. & Batrla, W. 1989, *ApJ*, 341, 839
- Menten, K. M., Walmsley, C. M., Henkel, C., & Wilson, T. L. 1986, *A&A*, 157, 318

- Menten, K. M., Walmsley, C. M., Henkel, C., & Wilson, T. L. 1988a, A&A, 198, 267
- Menten, K. M., Walmsley, C. M., Henkel, C., & Wilson, T. L. 1988b, A&A, 198, 253
- Minier, V., Booth, R. S., & Conway, J. E. 2000, A&A, 362, 1093
- Minier, V., Ellingsen, S. P., Norris, R. P., & Booth, R. S. 2003, A&A, 403, 1095
- Molinari, S., Brand, J., Cesaroni, R., & Palla, F. 1996, A&A, 308, 573
- Molinari, S., Brand, J., Cesaroni, R., & Palla, F. 2000, A&A, 355, 617
- Molinari, S., Brand, J., Cesaroni, R., Palla, F., & Palumbo, G. G. C. 1998, A&A, 336, 339
- Morimoto, M., Kanzawa, T., & Ohishi, M. 1985, ApJ, 288, L11
- Moscadelli, L., Cesaroni, R., & Rioja, M. J. 2000, A&A, 360, 663
- Mundy, L. G., Evans, N. J., Snell, R. L., & Goldsmith, P. F. 1987, ApJ, 318, 392
- Nakano, M. & Yoshida, S. 1986, PASJ, 38, 531
- Natta, A., Testi, L., Neri, R., Shepherd, D. S., & Wilner, D. J. 2004, A&A, 416, 179
- Nomura, H. & Millar, T. J. 2004, A&A, 414, 409
- Olmi, L., Cesaroni, R., & Walmsley, C. M. 1993, A&A, 276, 489
- Pelling, M. 1975, MNRAS, 172, 41
- Pillai, T., Wyrowski, F., Carey, S., & Egan, M. 2005, in preparation
- Pillai, T., Wyrowski, F., & Menten, K. M. 2004, submitted
- Plambeck, R. L. & Menten, K. M. 1990, ApJ, 364, 555
- Plambeck, R. L. & Wright, M. C. H. 1988, ApJ, 330, L61
- Pontoppidan, K. M., van Dishoeck, E. F., & Dartois, E. 2004, A&A, 426, 925
- Porrás, A., Cruz-González, I., & Salas, L. 2000, A&A, 361, 660
- Pottage, J. T., Flower, D. R., & Davis, S. L. 2001, J. Phys. B: At. Mol. Phys., 34, 3313
- Pottage, J. T., Flower, D. R., & Davis, S. L. 2002, J. Phys. B: At. Mol. Phys., 35, 2541
- Pottage, J. T., Flower, D. R., & Davis, S. L. 2004a, MNRAS, 352, 39
- Pottage, J. T., Flower, D. R., & Davis, S. L. 2004b, Journal of Physics B Atomic Molecular Physics, 37, 165

- Press, W., Teukolsky, S., Vetterling, W., & Flannery, B. 1992, *Numerical Recipes in Fortran (The Art of Scientific Computing)* (Cambridge University Press)
- Ray, B. 1932, *Zeitschrift für Physik*, 78, 74
- Redman, R. O., Feldman, P. A., Wyrowski, F., et al. 2003, *ApJ*, 586, 1127
- Sandford, S. A. & Allamandola, L. J. 1993, *ApJ*, 417, 815
- Sastry, K. V. L. N., Lees, R. M., & Van der Linde, J. 1981, *J. Mol. Spectrosc.*, 88, 229
- Schaller, G., Schaerer, D., Meynet, G., & Maeder, A. 1992, *A&AS*, 96, 269
- Schilke, P., Phillips, T. G., & Mehringer, D. M. 1999, in *The Physics and Chemistry of the Interstellar Medium, Proceedings of the 3rd Cologne-Zermatt Symposium, 1998*, Eds.: V. Ossenkopf, J. Stutzki, and G. Winnewisser, GCA-Verlag Herdecke, 330–+
- Schilke, P., Walmsley, C. M., Pineau des Forets, G., & Flower, D. R. 1997, *A&A*, 321, 293
- Shepherd, D. S. & Churchwell, E. 1996, *ApJ*, 472, 225
- Shu, F. H., Adams, F. C., & Lizano, S. 1987, *ARA&A*, 25, 23
- Slysh, V. I., Kalenskii, S. V., Val'tts, I. E., & Golubev, V. V. 1997, *ApJ*, 478, L37+
- Slysh, V. I., Kalenskii, S. V., Val'tts, I. E., Golubev, V. V., & Mead, K. 1999, *ApJS*, 123, 515
- Slysh, V. I., Kalenskii, S. V., Val'tts, I. E., & Otrupcek, R. 1994, *MNRAS*, 268, 464
- Slysh, V. I., Kalenskij, S. V., & Val'tts, I. E. 1993, *ApJ*, 413, L133
- Snell, R. L., Dickman, R. L., & Huang, Y.-L. 1990, *ApJ*, 352, 139
- Snell, R. L., Goldsmith, P. F., Erickson, N. R., Mundy, L. G., & Evans, N. J. 1984, *ApJ*, 276, 625
- Snell, R. L., Loren, R. B., & Plambeck, R. L. 1980, *ApJ*, 239, L17
- Sobolev, A. M., Cragg, D. M., & Godfrey, P. D. 1997, *A&A*, 324, 211
- Sobolev, A. M. & Deguchi, S. 1994a, *ApJ*, 433, 719
- Sobolev, A. M. & Deguchi, S. 1994b, *A&A*, 291, 569
- Sobolev, A. M. & Strel'nitskii, V. S. 1983, *Soviet Astronomy Letters*, 9, 12
- Sobolev, A. M., Wallin, B. K., & Watson, W. D. 1998, *ApJ*, 498, 763

- Sridharan, T. K., Beuther, H., Schilke, P., Menten, K. M., & Wyrowski, F. 2002, *ApJ*, 566, 931
- Strelnitskii, V. S. & Sunyaev, R. A. 1972, *AZh*, 49, 704
- Sutton, E. C., Sobolev, A. M., Salii, S. V., et al. 2004, *ApJ*, 609, 231
- Swade, D. 1989, *ApJ*, 345, 828
- Tafalla, M., Myers, P. C., Caselli, P., Walmsley, C. M., & Comito, C. 2002, *ApJ*, 569, 815
- Takahashi, J. 2001, *ApJ*, 561, 254
- Tieftrunk, A. R., Gaume, R. A., Claussen, M. J., Wilson, T. L., & Johnston, K. J. 1997, *A&A*, 318, 931
- Tofani, G., Felli, M., Taylor, G. B., & Hunter, T. R. 1995, *A&AS*, 112, 299
- Torrelles, J. M., Patel, N. A., Anglada, G., et al. 2003, *ApJ*, 598, L115
- Townes, C. & Schawlow, A. 1996, *Microwave Spectroscopy* (Dover Pub. New York)
- Val'Tts, I. E., Dzyura, A. M., Kalenskii, S. V., et al. 1995, *Astronomy Reports*, 39, 18
- Val'tts, I. E., Ellingsen, S. P., Slysh, V. I., et al. 2000, *MNRAS*, 317, 315
- van der Tak, F. F. S., van Dishoeck, E. F., & Caselli, P. 2000, *A&A*, 361, 327
- Walmsley, C. M., Menten, K. M., Batrla, W., & Matthews, H. E. 1988, *A&A*, 197, 271
- Walmsley, C. M. & Ungerechts, H. 1983, *A&A*, 122, 164
- Walsh, A. J., Burton, M. G., Hyland, A. R., & Robinson, G. 1998, *MNRAS*, 301, 640
- Whiteoak, J. B. & Peng, R.-S. 1989, *MNRAS*, 239, 677
- Wilking, B. A., Blackwell, J. H., Mundy, L. G., & Howe, J. E. 1989, *ApJ*, 345, 257
- Wilson, T. L. & Rood, R. 1994, *ARA&A*, 32, 191
- Wilson, T. L., Zeng, Q., Huettmeister, S., & Dahmen, G. 1996, *A&A*, 307, 209
- Wouterloot, J. G. A., Henkel, C., & Walmsley, C. M. 1989, *A&A*, 215, 131
- Wouterloot, J. G. A., Walmsley, C. M., & Henkel, C. 1988, *A&A*, 203, 367
- Wyrowski, F. 2005, in preparation
- Wyrowski, F., Schilke, P., Menten, K. M., Beuther, H., & Sridharan, T. K. 2005, in preparation

Xu, L.-H. & Hougen, J. T. 1995, *J. Mol. Spectrosc.*, 137, 540

Xu, L.-H. & Lovas, F. L. 1997, *J. Phys. Chem. Ref. Data*, 26, 17

Yao, Y., Ishii, M., Nagata, T., Nakaya, H., & Sato, S. 2000, *ApJ*, 542, 392

Zeng, Q., Lou, G. F., & Li, S. Z. 1987, *Ap&SS*, 132, 263

Zhang, Q., Hunter, T. R., Brand, J., et al. 2001, *ApJ*, 552, L167

Curriculum vitae

Personal details:

Name: Silvia Leurini
Date of birth: 1976
Place of birth: Roma, Italy
Nationality: Italian

Academic degrees and working experience

- **1990–1995:** High-school student at the *Liceo Classico* in Quartu S.E., Italy. Final grades: 60/60.
- **1995–2000:** Undergraduate student in Physics at the University of Cagliari, Italy. *Laurea* degree in Physics achieved in October 2000, final grades: 110/110 summa cum laude.
 - December 1999 to October 2000: *Laurea* thesis carried out at the University of Cagliari (supervisor: Prof. P. Benvenuti), in collaboration with the Osservatorio Astronomico di Cagliari (advisor: Dr. I. Porceddu). Thesis title: “*Studio della curva di estinzione galattica e extragalattica con dati del Faint Object Spectrograph a bordo del Telescopio Spaziale Hubble*” (*Analysis of galactic and extragalactic extinction curves with data from the Faint Object Spectrograph on board HST*).
- **2000–2001:** “*Tutor*” teaching assistant, *Fisica per il corso di Laurea in Scienze Naturali*, University of Cagliari.
- **2001:** six months post-laurea fellow at the Osservatorio Astronomico di Cagliari (advisor: Dr. L. Moscadelli), *Theoretical calculations of thermal excitation of methanol in the Interstellar Medium*.
- **2001–today:** Graduate student at the *Max-Planck-Institut für Radioastronomie* in Bonn (Germany).
 - Ph.D. thesis carried out in the *Millimeter and Submillimeter Astronomy Group*, under the supervision of Prof. Dr. K. M. Menten (MPIfR) and Prof. Dr. U. Klein (University of Bonn). Advisor: Dr. P. Schilke. Thesis title: “*Methanol: a diagnostic tool for star formation*”
 - April 2002–today: enrolled in the *International Max-Planck Research School* at the MPIfR, Bonn.